

# Single Particle and Collective Excitations near $Z = 50$

*by*

**Ranabir Banik**

Enrolment No: PHYS04201404012

*Variable Energy Cyclotron Centre, Kolkata*

*A thesis submitted to*

*The Board of Studies in Physical Sciences*

*in partial fulfillment of requirements*

*for the Degree of*

**DOCTOR OF PHILOSOPHY**

*of*

**HOMI BHABHA NATIONAL INSTITUTE**

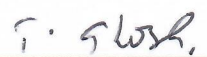


December, 2020

# Homi Bhabha National Institute

## Recommendation of the Viva Voce Board

As members of the Viva Voce Board, we certify that we have read the dissertation prepared by Shri Ranabir Banik entitled "Single particle and collective excitations near  $Z = 50$ " and recommend that it may be accepted as fulfilling the dissertation requirement for the degree of Doctor of Philosophy.

 Chairman- Prof. C. Bhattacharya	Date: 7.5.2021
 Supervisor- Dr. S. Bhattacharyya	Date: 7-5-2021
 External examiner- Prof. Gautam Gangopadhyay	Date: 7.5.2021
 Member 1- Prof. M. Saha Sarkar	Date: 12/5/2021
 Member 2- Dr. D. Sanyal	Date: 07/05/2021
 Member 3- Dr. T. K. Ghosh	Date: 07/05/2021

Finally approval and acceptance of this dissertation is contingent upon the candidate's submission of the final copies of the dissertation to HBNI.

I hereby certify that I have read this dissertation prepared under my direction and recommend that it may be accepted as fulfilling the dissertation requirement.

Date: 07-05-2021

Place: VECC, KOLKATA.

  
Dr. Sarmishtha Bhattacharyya  
Guide

## STATEMENT BY AUTHOR

This dissertation has been submitted in partial fulfillment of requirements for an advanced degree at Homi Bhabha National Institute (HBNI) and is deposited in the Library to be made available to borrowers under rules of the HBNI.

Brief quotation from this dissertation are allowable without special permission, provided that accurate acknowledgement of source is made. Requests for permission for extended quotation from or reproduction of this manuscript in whole or in part may be granted by the Competent Authority of HBNI when in his or her judgement the proposed use of the material is in the interests of scholarship. In all other instances, however, permission must be obtained from the author.

*Ranabir Banik*  
Ranabir Banik

## DECLARATION

I, hereby declare that the investigation presented in the thesis has been carried out by me. The work is original and has not been submitted earlier as a whole or in part for a degree/diploma at this or any other Institution/University.

*Ranabir Banik*

Ranabir Banik

# List of Publications arising from the thesis

## (A) Relevant to the present Thesis

### Journals :

1. **Observation of signature partner bands in  $^{117}\text{Sb}$ .**

**R. Banik**, S. Bhattacharyya, Soumik Bhattacharya, G. Mukherjee, R. Goswami, D. Choudhury, S. Das, S. Samanta, S. S. Ghugre, R. Raut, and A. Goswami.  
Phys. Rev. C, (2020), Vol. **101**, 014322.

2. **Revealing multiple band structures in  $^{131}\text{Xe}$  from  $\alpha$ -induced reactions.**

**R. Banik**, S. Bhattacharyya, S. Biswas, Soumik Bhattacharya, G. Mukherjee, S. Rajbanshi, Shabir Dar, S. Nandi, Sajad Ali, S. Chatterjee, S. Das, S. Das Gupta, S. S. Ghugre, A. Goswami, A. Lemasson, D. Mondal, S. Mukhopadhyay, H. Pai, S. Pal, D. Pandit, R. Raut, Prithwijita Ray, M. Rejmund, and S. Samanta.  
Phys. Rev. C, (2020), Vol. **101**, 044306.

3. **High spin states above the isomers in neutron rich Iodine nuclei near  $N = 82$ .**

**R. Banik**, S. Bhattacharyya, M. Rejmund, A. Lemasson, S. Biswas, A. Navin, Y. H. Kim, C. Michelagnoli, I. Stefan, P. Bednarczyk, Soumik Bhattacharya, E. Clement, H. L. Crawford, G. de France, P. Fallon, G. Fremont, J. Goupil, B. Jacquot, H. J. Li, J. Ljungvall, A. Maj, L. Menager, V. Morel, G. Mukherjee, R. Palit, R. M. Perez-Vidal, J. Ropert, and C. Schmitt.  
Phys. Rev. C, (2020), Vol. **102**, 044329.

## Conferences/Symposia :

1. **Exploring the structure of Xe isotopes in A~130 region: Single particle and collective excitations**

**R. Banik**, S. Bhattacharyya, S. Biswas, S. Bhattacharya, G. Mukherjee, S. Rajbanshi, S. Dar, S. Nandi, S. Ali, S. Chatterjee, S. Das, S. Das Gupta, S. S. Ghugre, A. Goswami, D. Mondal, S. Mukhopadhyay, H. Pai, S. Pal, D. Pandit, R. Raut, P. Ray, and S. Samanta  
EPJ Web of Conferences, (2020), Vol. **232**, 04001.

2. **Observation of Magnetic Rotational band in  $^{131}\text{Xe}$**

**R. Banik**, S. Rajbanshi, S. Bhattacharyya, G. Mukherjee, S. Bhattacharya  
Proceedings of the DAE Symp. on Nucl. Phys., (2019), Vol. **64**, A94.

3.  **$\gamma$ -ray spectroscopy of  $^{131}\text{Xe}$  from  $\alpha$ -induced reaction**

**R. Banik**, S. Bhattacharyya, S. Biswas, Soumik Bhattacharya, G. Mukherjee, Shabir Dar, S. Das Gupta, S. Nandi, Sajad Ali, P. Ray, S. Chatterjee, S. Samanta, S. Das, A. Goswami, S. S. Ghugre, R. Raut, H. Pai, A. Lemasson, A. Navin, M. Rejmund, D. Mondal, S. Mukhopadhyay, S. Pal, D. Pandit, S. Rajbanshi  
Proceedings of the DAE International Symp. on Nucl. Phys., (2018), Vol. **63**, 82.

4. **Identification of new partner bands based on  $\pi g_{7/2}$  in  $^{117}\text{Sb}$**

**R. Banik**, S. Bhattacharyya, Soumik Bhattacharya, R. Raut, S. S. Ghugre, R. Goswami, D. Choudhury, S. Das, A. Dhal, A. Goswami, G. Mukherjee, S. Samanta  
Proceedings of the DAE International Symp. on Nucl. Phys., (2018), Vol. **63**, 80.

5. **Band Structures and Single particle excitations in  $^{117}\text{Sb}$**

**R. Banik**, S. Bhattacharyya, Soumik Bhattacharya, R. Raut, S. S. Ghugre, S. Das, A. Dhal, A. Goswami, G. Mukherjee, S. Samanta

Proceedings of the DAE Symposium on Nucl. Phys., (2017), Vol. **62**, 124.

6. **Spectroscopy of low lying states of  $^{132,134}\text{Xe}$  from  $\beta$ -Decay**

**R. Banik**, S.Bhattacharyya, Soumik Bhattacharya, D.Banerjee, S.K.Das, R.Guin, G. Mukherjee, Sangeeta Das, T. Bhattacharjee, A. Choudhury, P. Das, A. Saha  
Proceedings of the DAE Symposium on Nucl. Phys., (2016), Vol. **61**, 76.

7. **Decay Spectroscopy of  $^{134}\text{I}$**

**R. Banik**, S. Bhattacharyya, Soumik Bhattacharya, D. Banerjee, S. K. Das, G. Mukherjee, T. Bhattacharjee, A. Choudhury, P. Das, R. Guin, A. Saha  
Proceedings of the DAE Symposium on Nucl. Phys., (2015), Vol. **60**, 244.

**(B) Other publications (in Journals)**

1. **Investigation of different possible excitation modes in neutron-rich  $^{78}\text{As}$**

A. K. Mondal, A. Chakraborty, K. Mandal, U. S. Ghosh, Aniruddha Dey, Saumyajit Biswas, B. Mukherjee, S. Rai, Krishichayan, S. Chatterjee, S. K. Das, S. Samanta, R. Raut, S. S. Ghugre, S. Rajbanshi, **R. Banik**, S. Bhattacharyya, S. Nandi, S. Bhattacharya, G. Mukherjee, S. Ali, A. Goswami, R. Chakrabarti, S. Mukhopadhyay, A. K. Sinha, V. Kumar and A. Kumar  
Phys. Rev. C, (2020), Vol. **102**, 064311.

2. **First Observation of Multiple Transverse Wobbling Bands of Different Kinds in  $^{183}\text{Au}$**

S. Nandi, G. Mukherjee, Q. B. Chen, S. Frauendorf, **R. Banik**, Soumik Bhattacharya, Shabir Dar, S. Bhattacharyya, C. Bhattacharya, S. Chatterjee, S. Das, S. Samanta, R. Raut, S. S. Ghugre, S. Rajbanshi, Sajad Ali, H. Pai, Md. A. Asgar, S. Das Gupta, P.

Chowdhury, and A. Goswami

Phys. Rev. Letters, (2020), Vol. **125**, 132501.

3. **Prompt-delayed  $\gamma$ -ray spectroscopy of neutron-rich  $^{119,121}\text{In}$  isotopes**

S. Biswas, A. Lemasson, M. Rejmund, A. Navin, Y. H. Kim, C. Michelagnoli, I. Stefan, **R. Banik**, P. Bednarczyk, Soumik Bhattacharya, S. Bhattacharyya, E. Clement, H. L. Crawford, G. de France, P. Fallon, G. Fremont, J. Goupil, B. Jacquot, H. J. Li, J. Ljungvall, A. Maj, L. Menager, V. Morel, R. Palit, R. M. Perez-Vidal, and J. Ropert  
Phys. Rev. C, (2020), Vol. **102**, 014326.

4. **Quasi- $\gamma$  band in  $^{114}\text{Te}$**

Prithwijita Ray, H. Pai, Sajad Ali, Anjali Mukherjee, A. Goswami, S. Rajbanshi, Soumik Bhattacharya, **R. Banik**, S. Nandi, S. Bhattacharyya, G. Mukherjee, C. Bhattacharya, S. Chakraborty, G. Gangopadhyay, Md. S. R. Laskar, R. Palit, G. H. Bhat, S. Jehangir, J. A. Sheikh, A. K. Sinha, S. Samanta, S. Das, S. Chatterjee, R. Raut, and S. S. Ghugre  
Phys. Rev. C, (2020), Vol. **101**, 064313.

5. **Effects of one valence proton on seniority and angular momentum of neutrons in neutron-rich  $^{122,131}_{51}\text{Sb}$  isotopes**

S. Biswas, A. Lemasson, M. Rejmund, A. Navin, Y. H. Kim, C. Michelagnoli, I. Stefan, **R. Banik**, P. Bednarczyk, S. Bhattacharya, S. Bhattacharyya, E. Clement, H. L. Crawford, G. de France, P. Fallon, G. Fremont, J. Goupil, B. Jacquot, H. J. Li, J. Ljungvall, A. Maj, L. Menager, V. Morel, R. Palit, R. M. Perez-Vidal, J. Ropert, D. Barrientos, G. Benzoni, B. Birkenbach, A. J. Boston, H. C. Boston, B. Cederwall, J. Collado, D. M. Cullen, P. Desesquelles, C. Domingo-Pardo, J. Dudouet, J. Eberth, V. Gonzalez, L. J. Harkness-Brennan, H. Hess, A. Jungclaus, W. Korten, M. Labiche, A. Lefevre, R. Menegazzo, D. Mengoni, B. Million, D. R. Napoli, A. Pullia, B. Quintana, D. Ralet, F. Recchia, P. Reiter, F. Saillant, M. D. Salsac, E. Sanchis, O. Stezowski, Ch. Theisen, J. J. Valiente-Dobn, and M. Zielinska  
Phys. Rev. C, (2019), Vol. **99**, 064302.

6. **Effect of neutron alignments on the structure of  $^{197}\text{Tl}$**

S. Nandi, G. Mukherjee, T. Roy, **R. Banik**, A. Dhal, Soumik Bhattacharya, S. Bhattacharyya, C. Bhattacharya, Md. A. Asgar, H. Pai, S. Rajbanshi, Pratap Roy, T. K. Ghosh, K. Banerjee, T. K. Rana, Samir Kundu, S. Manna, R. Pandey, A. Sen, S. Pal, S. Mukhopadhyay, D. Pandit, D. Mandal, and S. R. Banerjee  
Phys. Rev. C, (2019), Vol. **99**, 054312.

7. **Yrast and non-yrast spectroscopy of  $^{199}\text{Tl}$  using  $\alpha$ -induced reactions**

Soumik Bhattacharya, S. Bhattacharyya, **R. Banik**, S. Das Gupta, G. Mukherjee, A. Dhal, S. S. Alam, Md. A. Asgar, T. Roy, A. Saha, S. Nandi, T. Bhattacharjee, A. Choudhury, Debasish Mondal, S. Mukhopadhyay, P. Mukhopadhyay, S. Pal, Deepak Pandit, I. Shaik, and S. R. Banerjee  
Phys. Rev. C, (2018), Vol. **98**, 044311.

8. **A Compton suppressed detector multiplicity trigger based digital DAQ for gamma-ray spectroscopy**

S. Das, S. Samanta, **R. Banik**, R. Bhattacharjee, K. Basu, R. Raut, S.S. Ghugre, A.K. Sinha, S. Bhattacharya, S. Imran, G. Mukherjee, S. Bhattacharyya, A. Goswami, R. Palit, H. Tan  
Nuclear Inst. and Methods A, (2018), Vol. **893**, 138.

9. **Prompt-delayed  $\gamma$ -ray spectroscopy with AGATA, EXOGAM and VAMOS++.**

Y. H. Kim, A. Lemasson, M. Rejmund, A. Navin, S. Biswas, C. Michelagnoli, I. Stefan, **R. Banik**, P. Bednarczyk, S. Bhattacharya, S. Bhattacharyya, E. Clment, H. L. Crawford, G. De France, P. Fallon, J. Goupil, B. Jacquot, H. J. Li, J. Ljungvall, A. O. Macchiavelli, A. Maj, L. Mnager, V. Morel, R. Palit, R. M. Prez-Vidal, J. Ropert and C. Schmitt.  
Eur. Phys. J. A, (2017), Vol. **53**, 162.

10. **Deformed band structures at high spin in  $^{200}\text{Tl}$**

Soumik Bhattacharya, S. Bhattacharyya, S. Das Gupta, H. Pai, G. Mukherjee, R. Palit,

F. R. Xu, Q. Wu, A. Shrivastava, Md. A. Asgar, **R. Banik**, T. Bhattacharjee, S. Chanda, A. Chatterjee, A. Goswami, V. Nanal, S. K. Pandit, S. Saha, J. Sethi, T. Roy, and S. Thakur

Phys. Rev. C, (2017), Vol. 95, 014301.

Ranabir Banik  
(RANABIR BANIK)

*Dedicated to my 'Family (Baba, Maa and Bhai)'.*

# ACKNOWLEDGMENTS

I would like to express my deep and sincere gratitude to my Ph.D thesis supervisor Dr. Sarmishtha Bhattacharyya for her constant and unconditional support, both academically and personally, throughout my thesis work. Her dynamic nature, vision and dedication towards research always motivates me. She has provided me all the basic requirements towards carrying out my work and groomed me in my early days of Ph.D. I also acknowledge her for her guidance and concern at every stage of my work. I deeply appreciate her knowledge and understanding in the field of research which played a defining role in shaping the present thesis. I really fortunate enough to have her as my guide as well as my mentor during this journey. Thank you madam.

I am also extremely grateful to Dr. Gopal Mukherjee from the bottom of my heart for his uncomparable support in every step of my thesis. It is a privilege to have him in the same lab during my work. All the enthusiastic discussion, I have with him in this tenure of my thesis, always eases all the difficulties. I am really thankful to him for his unconditional help. Thank you, sir.

I am grateful to Prof. Dinesh Kumar Srivastava, former Director, Variable Energy Cyclotron Centre (VECC), Prof. Alok Chakraborty, former Director, VECC and Shri. Amitava Roy, former Director, VECC, for their kind support. I also sincerely acknowledge Dr. Sumit Som, Director, VECC, for providing lively working atmosphere and for the facilities.

I am also indebted to Prof. Sailajananda Bhattacharya, former Head, Physics Group, VECC, Prof. S. R. Banerjee, former Head, Experimental Nuclear Physics Division, VECC, for providing me their kind support. I am also grateful to our present Physics Group head and former Dean of Academics (Physical Sciences), Prof. Jane Alam for his unconditional help and encouragement at every stage of my work. I also express my sincere gratitude to Dr. Chandana Bhattacharya, Head, Experimental Nuclear Physics Division for being extremely caring and helpful during the course of my work. I am very much indebted to Dr. Parnika Das, Dean Aca-

demics (Physical Sciences) for her encouragement during this period. I am extremely grateful to all the members of Experimental Nuclear Physics Division and Physics Group of VECC.

A special thanks to Prof. Maitreyee Saha Sarkar, Saha Institute of Nuclear Physics, for her suggestions and critical advises. It helps me a lot to improve my work. I would like to thank late Prof. Asimananda Goswami from SINP, for his encouragements. His suggestions and discussions were always helpful in course of my research. I also thank my collaborator Dr. Ranjana Goswami for her help to carry out this thesis work. I would also like to thank Prof. Partha Chowdhury, University of Massachusetts Lowell, for his guidance towards various analysis procedures. A special thanks to Prof. Ranjan Kumar Bhowmik, who taught me the preliminary analysis techniques and helped me to grow interest in  $\gamma$ -ray spectroscopy.

I also thank Dr. Rajarshi Raut and Dr. Sandeep S. Ghugre from UGC, DAE-CSR, Kolkata Center for their encouragement and kind support. I have really enjoyed the discussion with them on various physics issues.

I sincerely thank all the collaborators of the INGA and VENUS campaign. The effort of the operators of the accelerator group at VECC are also acknowledged.

I also thank all the members of the Radio-chemistry department of VECC for their help during the experiments.

I would like to express my special thanks to Dr. Navin Alahari, Director, GANIL, France for hosting me at GANIL to carry out my research and for allowing me to use their advanced facilities to its extent. I am also thankful to Dr. Maurycy Rejmund and Dr. Antoine Lemasson for fruitful discussion and guidance for analysis of data of experiment at GANIL. I also acknowledge all international collaborators involved in the experiment using AGATA and VAMOS++ at GANIL, France. I am also thankful to Kim and Sayani di, former Post Docs at GANIL for their guidance during this period. I also thank the accelerator support team of GANIL.

I would also like to acknowledge CEFIPRA (Project number 5604-4) for their financial support towards my visit to GANIL, France. Without which, it will be impossible for me to carry out my research work at France.

A special mention is for Soumik da for his constant help and support throughout this period my research work. I thank him from the bottom of my heart for his help in almost every area including academic and private. The mental support he provided is appreciable. I am really thankful to God having such a nice senior like you. Thank you.

It is my great pleasure to thank Hari Da and Shinjinee Di for their encouragement and kind support throughout my thesis work. Their guidance at the early stage is very much helpful to understand the field of research. I also thank my juniors Shabir and Soumen for every support they provided.

I also acknowledge my 'Physics lab' members, Mrs. Anindita Chowdhury, Mr. Pulak Mukhopadhyay and Imran Seikh, for their help and support.

I am really grateful to Arindam da, Santu da, Chandrasekhar da, Chiranjib da, Debasish da, Pratanu da, Arup da for their encouragement and inspiration. I have spent a lot of joyful moments with them during this period.

I am very much indebted to all my teachers throughout different parts of my life, without whom it would never been possible to start the journey of physics for me. I would also like to mention a special thanks to all of my close friends from my school, college and university.

I thank my Ph.D mates and close friends Homnath, Dipak, Shabnam, Nachiketa, Safikul, Ajit, Ashik and Samrangy for their encouragements and friendly discussions. In this connections I would like to acknowledge all my senior and junior research colleagues at VECC for their friendly behaviours.

At last I would like to thank my parents and brother, who gave me love and all kinds of supports from my childhood. Without them, I would not be able to achieve anything.

I sincerely apologize if I missed someone unintentionally in the above list of acknowledgment.

Ranabir Banik

# Contents

Summary	viii
List of Publications	x
List of Figures	xxiv
List of Tables	xxvi
<b>1 Introduction</b>	<b>1</b>
<b>2 Nuclear Models</b>	<b>14</b>
2.1 The Liquid Drop Model . . . . .	14
2.2 Shell Model . . . . .	16
2.3 Nuclear shapes . . . . .	19
2.4 Deformed Shell Model: Nilsson Model . . . . .	22
2.5 Cranking Model . . . . .	26
2.6 Various quantities related to rotational bands . . . . .	28
2.7 Shell Model Calculations . . . . .	30
2.8 Particle Rotor Model (PRM) calculations . . . . .	32
2.9 Total Routhian Surface (TRS) calculations . . . . .	33
2.10 SPAC calculations and Magnetic Rotational band . . . . .	34

<b>3</b>	<b>Experimental techniques and data analysis procedures</b>	<b>41</b>
3.1	Reaction mechanisms to populate nuclei in excited states . . . . .	41
3.1.1	Fusion evaporation reaction . . . . .	42
3.1.2	Nuclear Fission . . . . .	43
3.1.3	$\beta$ -decay . . . . .	43
3.2	Detection of the $\gamma$ -radiation . . . . .	44
3.2.1	Photoelectric effect . . . . .	44
3.2.2	Compton scattering . . . . .	45
3.2.3	Pair production . . . . .	45
3.3	High-Purity Germanium (HPGe) detectors . . . . .	46
3.3.1	Clover detectors . . . . .	47
3.3.2	Low Energy Photon Spectrometer (LEPS) . . . . .	48
3.3.3	BGO detectors as anti-Compton shield . . . . .	49
3.3.4	AGATA detectors . . . . .	50
3.4	Experimental Setups . . . . .	52
3.4.1	VECC Array for Nuclear Spectroscopy (VENUS) . . . . .	52
3.4.2	Indian National Gamma Array (INGA) . . . . .	53
3.4.3	Set up consisting of VAMOS++, AGATA and EXOGAM . . . . .	54
3.5	Offline Data Analysis . . . . .	56
3.5.1	Calibration . . . . .	56
3.5.2	Efficiency determination . . . . .	57
3.5.3	$E_\gamma$ - $E_\gamma$ coincidence analysis . . . . .	57
3.5.4	Angular Correlations . . . . .	58
3.5.5	DCO measurements . . . . .	59
3.5.6	Polarization measurements . . . . .	59
3.6	Analysis procedures using VAMOS++ . . . . .	61
3.6.1	Trajectory reconstruction . . . . .	61
3.6.2	Identification of $Z$ . . . . .	62

3.6.3	Identification of mass and charge state . . . . .	62
<b>4</b>	<b>High spin spectroscopy of <math>^{117}\text{Sb}</math>: Observation of signature partner bands</b>	<b>66</b>
4.1	Introduction . . . . .	66
4.2	Experiment and Data Analysis . . . . .	68
4.3	Results . . . . .	69
4.4	Discussion . . . . .	85
4.5	PRM calculations . . . . .	89
4.6	Shell model calculations . . . . .	90
4.7	Summary . . . . .	93
<b>5</b>	<b>Yrast and non-yrast band structures in <math>^{131}\text{Xe}</math></b>	<b>96</b>
5.1	Introduction . . . . .	96
5.2	Experiment and Data Analysis . . . . .	98
5.3	Results . . . . .	99
5.4	Discussion . . . . .	111
5.5	TRS calculations . . . . .	118
5.6	SPAC and semi-empirical calculations of the Shears band . . . . .	121
5.7	Shell Model calculations . . . . .	124
5.8	Summary . . . . .	125
<b>6</b>	<b>Prompt-delayed spectroscopy of neutron-rich Iodine nuclei near <math>N = 82</math></b>	<b>129</b>
6.1	Introduction . . . . .	129
6.2	Experiment and Data Analysis . . . . .	131
6.3	Results . . . . .	133
6.3.1	$^{130}\text{I}$ . . . . .	133
6.3.2	$^{131}\text{I}$ . . . . .	135
6.3.3	$^{132}\text{I}$ . . . . .	141

6.3.4	$^{133}\text{I}$	146
6.3.5	$^{134}\text{I}$	151
6.4	Discussion	154
6.4.1	Systematics	154
6.4.2	Shell Model Calculations	155
6.5	Summary	162
<b>7</b>	<b>Low lying level structure of <math>^{134}\text{Xe}</math> from decay spectroscopy of fission fragments</b>	<b>167</b>
7.1	Introduction	167
7.2	Experiment and Data Analysis	169
7.3	Results	171
7.3.1	Identification	171
7.3.2	Coincidence Analysis	172
7.3.3	Spin assignments	178
7.4	Discussion	181
7.4.1	Shell Model Calculations	181
7.4.2	Summary	185
<b>8</b>	<b>Summary and Future scope</b>	<b>188</b>
8.1	Summary	188
8.2	Future scope	191

# List of Figures

2.1	Energy states as obtained using Simple Harmonic Oscillator (S.H.O) (left column), same as obtained after introducing $l^2$ term (middle column). Right column is the same but obtained from more realistic potential with another extra $ls$ term. Fig is taken from Ref. [9]. . . . .	18
2.2	Shapes of the multipoles as the perturbations of a sphere. From left to right: dipole ( $\lambda = 1$ ), quadrupole ( $\lambda = 2$ ), octupole ( $\lambda = 3$ ) and hexadecapole ( $\lambda = 4$ ). Fig is taken from Ref. [12]. . . . .	20
2.3	Various collective nuclear shapes described in the $\beta$ - $\gamma$ plane. (Lund convention). The $\gamma$ value for the prolate and oblate shapes are also indicated in the figure. This figure is taken from Ref. [14]. . . . .	21
2.4	Nilsson diagram of single particle levels, calculated from equation 2.19 for neutrons ( $50 \leq N \leq 82$ ) as a function of deformation. The solid lines correspond to positive parity orbitals and the dashed lines correspond to negative parity orbitals. Figure is taken from Ref. [19]. . . . .	24
2.5	Nilsson diagram of single particle levels, calculated from equation 2.19 for protons ( $50 \leq Z \leq 82$ ) as a function of deformation. The solid lines correspond to positive parity orbitals and the dashed lines correspond to negative parity orbitals. Figure is taken from Ref. [19]. . . . .	25
2.6	The nucleon has orbital angular momentum $l$ and spin angular momentum $s$ . The total angular momentum is $j$ so that $j = l + s$ . The projection of the orbital angular momentum ( $l$ ) and spin angular momentum ( $s$ ) on the symmetry axis is represented by $\Lambda$ and $\Sigma$ respectively. Projection of a single valance particle total angular momenta $j$ on the symmetry axis of a deformed nucleus is represented by. $\Omega = \Lambda + \Sigma$ . . . . .	26
2.7	Schematic diagram showing the proton and neutron angular momenta vectors. . . . .	34
3.1	Schematic diagram of formation and decay of the compound nucleus in fusion-evaporation reactions. . . . .	42

3.2	Picture of a Clover detector used for the experiments in the present thesis. . . .	47
3.3	Comparison of efficiency of a LEPS detector and a Clover detector in addback mode. . . . .	48
3.4	(a) Schematic diagram of an AGATA crystal displaying central core contact and its segments. The picture is taken from Ref. [28]. (b) The AGATA clusters are mounted in front of the VAMOS++ spectrometer at GANIL, picture is taken from AGATA website. (c) The AGATA $1\pi$ array, drawing made by STFC Daresbury. . . . .	50
3.5	Relative efficiency for a AGATA triple cluster obtained from its core signal (Sum Core) and the same obtained after $\gamma$ -ray tracking. . . . .	51
3.6	VENUS set up at channel 3 beam line at VECC. . . . .	53
3.7	INGA set up channel 3 beam line at VECC. . . . .	54
3.8	Schematic experimental setup of VAMOS++, AGATA and EXOGAM at GANIL. The figure is taken from Ref. [13]. . . . .	55
3.9	Variation of the asymmetry parameter $a(E_\gamma)$ as a function of incident $\gamma$ -ray energy ( $E_\gamma$ ), as obtained for (a) VENUS and (b) INGA set up using standard unpolarized radioactive sources. The linear fitting of $a(E_\gamma)$ as a function of $\gamma$ -ray energy ( $E_\gamma$ ) is also shown. . . . .	60
3.10	Flow chart of various steps required in isotopic fragment identification using VAMOS++. . . . .	62
4.1	Total projection of the $E_\gamma$ - $E_\gamma$ matrix, as obtained in the present experiment. All the $\gamma$ rays marked in the figure are from $^{117}\text{Sb}$ . The spectrum is shown in two parts, (a) upto 680 keV and (b) beyond 680 keV. The newly observed transitions from the present work are marked with ‘*’. The insets show some of the new transitions in an expanded scale. The 159 keV, marked with ‘#’, is from $^{117}\text{Sn}$ which is populated from the decay of $^{117}\text{Sb}$ . . . . .	69
4.2	Proposed level scheme of $^{117}\text{Sb}$ , as obtained from the present work. The new $\gamma$ rays observed from the present work are marked with ‘*’ on the right side of the $\gamma$ -ray energy label. . . . .	70
4.3	DCO ratio ( $R_{DCO}$ ) <i>vs.</i> $\Delta_{PDCO}$ plot of various new (black) and known (red) transitions observed in $^{117}\text{Sb}$ obtained in the present work. The dotted lines at X-axis are to guide the eye for the DCO ratios corresponding to the pure dipole and quadrupole transitions, respectively. The dotted line at Y-axis is to guide the eye for $\Delta_{PDCO}$ values corresponding to the electric (+ve) and magnetic (-ve) nature of the transitions. . . . .	72

4.4	Angular distributions of various transitions of $^{117}\text{Sb}$ , observed in the present work. The panels (a), (c), (e) and (g) represent the distribution for the quadrupole transitions and the panels (b), (d), (f) and (h) represent distribution corresponding to the dipole transitions in $^{117}\text{Sb}$ , as obtained in the present work.	73
4.5	Coincidence spectra corresponding to the (a) 817 keV gate of the band B1, (b) 1183 keV gate of the band B1 and (c) 1045 keV gate of the band B1(a). The insets of (a) and (b) show the expanded view of the coincidence spectra of the 817 and 1183 keV gates respectively. The newly observed transitions are marked with '*'. . . . .	74
4.6	Coincidence spectra corresponding to the gates of (a) 877 keV $\gamma$ ray of band B2 and (b) 571 keV $\gamma$ ray of band B3. . . . .	75
4.7	The coincidence spectra corresponding to the double gates of (a) 208 & 303 keV $\gamma$ rays of B4, (b) 1160 & 387 keV $\gamma$ rays of B5 and (c) 1001 & 202 keV $\gamma$ rays of B6 from the $E_\gamma$ - $E_\gamma$ - $E_\gamma$ cube. The new transitions observed in the current work are marked with '*'. The 159 keV, marked with '#', is from $^{117}\text{Sn}$ . . . . .	76
4.8	Coincidence spectra corresponding to the gates of (a) 457 keV $\gamma$ ray of B6(a), (b) 552 keV $\gamma$ ray of B6(b) and (c) 426 keV $\gamma$ ray of B2. The new $\gamma$ rays observed in the present work are marked with '*'. . . . .	77
4.9	Coincidence spectra corresponding to the gate of 1160 keV transition of the band B5, (a) upto 625 keV; (b) above 625 keV. All the newly observed transitions are marked with '*'. . . . .	78
4.10	Excitation energy ( $E(I)$ ) as a function of level spin ( $I$ ) for the bands of $^{117}\text{Sb}$ . . . . .	85
4.11	Aligned angular momentum ( $i_x$ ) of (a) various band structures in $^{117}\text{Sb}$ and (b) the band B5(b) of $^{117}\text{Sb}$ and same band of similar configurations in odd mass Sb isotopes as a function of rotational frequency $\hbar\omega$ . Harris reference parameters of $J_0 = 17$ and $J_1 = 12$ have been taken from Ref. [11]. . . . .	86
4.12	Kinematic moment of inertia ( $\vartheta^{(1)}$ ) of various band structures in $^{117}\text{Sb}$ as a function of rotational frequency $\hbar\omega$ . . . . .	88
4.13	Comparison of the experimental (a) energy levels and (b) the energy staggering of the band B1 and B1(a) with that obtained from present PRM calculations. The energy levels are plotted with respect to the $13/2^+$ state. . . . .	89
4.14	Comparison of the experimentally observed low-lying states with that of the Shell Model calculation. . . . .	90

5.1	Total projection of the symmetric $E_\gamma$ - $E_\gamma$ matrix. Energy of the observed $\gamma$ -rays are marked and the new transitions of $^{131}\text{Xe}$ , are marked with ‘*’. Energy upto 710 keV is shown in (a) and above 710 keV is shown in (b). The transitions of neighbouring nuclei produced in the same reaction are marked as ‘#’ and the $\gamma$ rays marked with ‘c’ are the contaminant $\gamma$ rays coming from the reactions with Mylar backing and Al frame. . . . .	100
5.2	Proposed level scheme of $^{131}\text{Xe}$ , as obtained from the present work. The new $\gamma$ rays observed in the present work are marked in red. . . . .	101
5.3	(a) The DCO ratio ( $R_{DCO}$ ) and (b) the polarization asymmetry ( $\Delta_{PDCO}$ ) of the new $\gamma$ rays (in red), and those of some of the known $\gamma$ rays (in black), as obtained in the present work, are plotted as a function of $\gamma$ -ray energy. The dotted lines at Y-axis in (a) are to guide the eye for the DCO ratio corresponding to pure dipole and quadrupole transitions respectively. The dotted line at Y-axis in (b) is to guide the eye for $\Delta_{PDCO}$ values corresponding to the electric (+ve) and magnetic (-ve) nature of the transitions. . . . .	102
5.4	Coincidence spectra corresponding to the double gates of (a) 642 & 902 keV, (b) 642 & 663 keV and (c) 642 & 682 keV transitions of band $B1$ from $E_\gamma$ - $E_\gamma$ - $E_\gamma$ cube. The new transitions observed in the present work are marked with ‘*’. . .	103
5.5	Coincidence spectra corresponding to the double gates of (a) 642 & 444 keV and (b) 642 & 389 keV transitions from the $E_\gamma$ - $E_\gamma$ - $E_\gamma$ cube. The new transitions observed in the present work are marked with ‘*’. . . . .	104
5.6	Coincidence spectra corresponding to the gates of (a) 993 and (b) 1021 keV transitions of band $B4$ obtained from the $E_\gamma$ - $E_\gamma$ matrix. The new transitions observed in the present work are marked with ‘*’. . . . .	105
5.7	Coincidence spectra corresponding to the gate of 177 keV transition of sequence $B5$ from the $E_\gamma$ - $E_\gamma$ matrix. The new transitions observed in the present work are marked with ‘*’. The $\gamma$ -ray marked with ‘#’ is the contaminant $\gamma$ -ray coming from reactions with the Mylar backing. . . . .	110
5.8	Coincidence spectra corresponding to the added gates of 365 and 638 keV transitions of band $B6$ obtained from the $E_\gamma$ - $E_\gamma$ matrix. The new transitions observed in the present work are marked with ‘*’. . . . .	111
5.9	Evolution of the low-lying 1-qp states in Xe isotopes. . . . .	112
5.10	Alignment plot of the $\nu h_{11/2}$ band of Xe ( $Z = 54$ ) isotopes. The Harris parameters of $J_0 = 16 \hbar^2/\text{MeV}$ and $J_1 = 7 \hbar^4/\text{MeV}^3$ are used [15]. Filled and open circles are used for two different signatures. . . . .	113

5.11	Alignment plot of the $\nu h_{11/2}$ band of the $N = 77$ isotones and the ground state band (g.s.b) of neighbouring even-even nuclei. The Harris parameters of $J_0 = 16 \hbar^2/\text{MeV}$ and $J_1 = 7 \hbar^4/\text{MeV}^3$ are used [15]. Filled and open circles are used for two different signatures. . . . .	114
5.12	Staggering of the $11/2^-$ band in $^{131}\text{Xe}$ are plotted as a function of spin, I, and compared with the same band of other isotopes (a) and isotones (b). Filled and open circles are used for two different signatures. . . . .	115
5.13	The staggering, $S(I)$ , plot as a function of spin, I, for the low-lying positive parity band $B6$ of $^{131}\text{Xe}$ along with the neighbouring isotopes and isotone. Filled and open circles are used for two different signatures. . . . .	116
5.14	The staggering, $S(I)$ , plot as a function of spin, I, for the band $B4$ of $^{131}\text{Xe}$ along with the similar bands in the neighbouring isotope and isotone. Filled and open circles are used for two different signatures. . . . .	117
5.15	Contour plots of total Routhian surfaces in the $\beta_2 - \gamma$ deformation mesh calculated for the lowest negative parity configuration corresponding to the $\nu h_{11/2}$ band (band B1) in $^{131}\text{Xe}$ at the rotational frequencies ( $\hbar\omega$ ) = 0.11 MeV (left) and 0.26 MeV (right). . . . .	118
5.16	Plot of total Routhian surface energies ( $E_{TRS}$ ) as a function of the deformation parameter, $\gamma$ calculated for the 1-qp, negative parity configuration corresponding to the $\nu h_{11/2}$ band in $^{131}\text{Xe}$ at different values of rotational frequencies ( $\hbar\omega$ ). . .	119
5.17	Same as Figure 5.15 but for the lowest positive parity configuration, corresponding to the $\nu d_{3/2}$ band (band B6) in $^{131}\text{Xe}$ at rotational frequencies ( $\hbar\omega$ ) = 0.16 MeV (a) and 0.36 MeV (b). . . . .	120
5.18	(a) Same as Figure 5.15 but for the 3-qp configuration, corresponding to the band $B4$ in $^{131}\text{Xe}$ . (b) The TRS energies as a function of the deformation parameter $\gamma$ for $\beta_2$ value around the minimum of the TRS. . . . .	121
5.19	(a) Variation of the observed $\gamma$ -ray energy with spin (I), which is compared with the SPAC calculation (solid line). (b) Variation of $\theta_1$ and $\theta_I$ with spin (I) as obtained from the present SPAC calculations. Inset shows the variation of core angular momentum contribution (R) with spin. . . . .	122
5.20	Variation of $V[I(\theta)]$ as a function of the shears angle ( $\theta$ ) for the MR band in $^{131}\text{Xe}$ . The solid line is the fit to the data points from which the effective interaction ( $V_2$ ) between the proton and neutron angular momentum vectors has been obtained. . . . .	123
5.21	Comparison of the calculated energy levels (red) using the shell model calculations with the experimental levels (black) in $^{131}\text{Xe}$ . . . . .	124

6.1	Charge state ( $Q$ ) as a function of the mass over charge ( $M/Q$ ) after the selection of Iodine ( $Z = 53$ ). The Iodine isotopes are obtained from various charge states and the identification of $A = 130$ and $134$ are marked for charge state $Q = 40$ .	132
6.2	Level scheme of $^{130}\text{I}$ above the ( $8^-$ ) isomeric level, as obtained in the present work. The newly observed $\gamma$ rays are displayed in red. The thickness of the $\gamma$ rays represents their relative intensities.	134
6.3	(a) The prompt singles $\gamma$ -ray spectrum ( $\gamma_P$ ) of $^{130}\text{I}$ . (b) Prompt $\gamma$ rays ( $\gamma_P$ ) in coincidence with added gates of $\gamma_P = 748 + 922 + 971$ keV. (c) Prompt $\gamma$ rays ( $\gamma_P$ ) in coincidence with $\gamma_P = 588$ keV. (d) Prompt $\gamma$ rays ( $\gamma_P$ ) in coincidence with $\gamma_P = 922$ keV. (e) Prompt $\gamma$ rays ( $\gamma_P$ ) in coincidence with $\gamma_P = 630$ keV. The new $\gamma$ -transitions are marked with ‘*’ in all the cases.	136
6.4	Level scheme of $^{131}\text{I}$ as obtained in the present work. The newly observed $\gamma$ rays are displayed in red. Isomeric state is indicated with a thick line and the half-life remeasured in this work is underlined by a red line. The thickness of the $\gamma$ rays represent their relative intensities.	137
6.5	(a) The prompt singles $\gamma$ -ray spectrum of $^{131}\text{I}$ . (b) Prompt $\gamma$ rays ( $\gamma_P$ ) in coincidence with added gates of $\gamma_P = 773 + 782$ keV. The inset shows the expanded energy range of 300-400 keV. (c) Prompt $\gamma$ rays ( $\gamma_P$ ) in coincidence with added gates of $\gamma_P = 201 + 491 + 564 + 692$ keV. The new $\gamma$ -transitions are marked with ‘*’.	139
6.6	(a) The delayed singles $\gamma$ -ray ( $\gamma_D$ ) spectrum of $^{131}\text{I}$ for $t_{Decay} < 75 \mu\text{s}$ . The inset shows the decay curve of $\gamma_D = 122 + 331$ keV delayed transitions with exponential fit. (b) Delayed $\gamma$ rays ( $\gamma_D$ ) within the time window $t_{Decay} < 75 \mu\text{s}$ in coincidence with $\gamma_P = 949$ keV. (c) Prompt $\gamma$ rays ( $\gamma_P$ ) in coincidence with $\gamma_D = 122$ keV. The new $\gamma$ -transitions are marked with ‘*’.	140
6.7	Level scheme of $^{132}\text{I}$ above the ( $8^-$ ) isomeric level, as obtained in the present work. The newly observed $\gamma$ rays are displayed in red. Isomeric state is indicated with a thick line and the newly measured half-life has been marked with a red box. The thickness of the $\gamma$ rays represents their relative intensities with respect to the 762 keV doublet.	142
6.8	(a) The prompt singles $\gamma$ -ray spectrum of $^{132}\text{I}$ . (b) Prompt $\gamma$ rays ( $\gamma_P$ ) in coincidence with $\gamma_P = 762$ keV. (c) Prompt $\gamma$ rays ( $\gamma_P$ ) in coincidence with $\gamma_P = 605$ keV. The new $\gamma$ -transitions are marked with ‘*’.	144

6.9	(a) The delayed singles $\gamma$ -ray ( $\gamma_D$ ) spectrum of $^{132}\text{I}$ in the time window $t_{Decay} < 3 \mu\text{s}$ . The inset shows the decay pattern of delayed $\gamma$ -ray 762 keV with exponential fitting. (b) Delayed $\gamma$ rays ( $\gamma_D$ ) within the time window $t_{Decay} < 3 \mu\text{s}$ in coincidence with $\gamma_P = 605$ keV. (c) Delayed $\gamma$ rays ( $\gamma_D$ ) within the time window $t_{Decay} < 3 \mu\text{s}$ in coincidence with $\gamma_D = 762$ keV. (d) Delayed $\gamma$ rays ( $\gamma_D$ ) within the time window $t_{Decay} < 3 \mu\text{s}$ in coincidence with $\gamma_D = 912$ keV of $^{133}\text{I}$ . The new $\gamma$ -transitions are marked with ‘*’. . . . .	145
6.10	Level scheme of $^{133}\text{I}$ as obtained in the present work. The newly observed $\gamma$ rays are displayed in red. Isomeric state is indicated with a thick line and the half-life remeasured in this work has been underlined by a red line. The thickness of the $\gamma$ rays represents their relative intensities. . . . .	147
6.11	(a) The prompt singles $\gamma$ -ray spectrum of $^{133}\text{I}$ . The higher energy part of this spectrum is shown in an expanded scale in the inset. (b) Prompt $\gamma$ rays ( $\gamma_P$ ) in coincidence with the added gate of $\gamma_P = 912 + 647 + 874$ keV. (c) Prompt $\gamma$ rays ( $\gamma_P$ ) in coincidence with added gate of $\gamma_P = 614 + 714 + 629$ keV. (d) Prompt $\gamma$ rays ( $\gamma_P$ ) in coincidence with added gate of $\gamma_P = 956 + 729 + 536$ keV. The new $\gamma$ -transitions are marked with ‘*’ in all the cases. . . . .	149
6.12	(a) Delayed $\gamma$ -ray ( $\gamma_D$ ) spectrum of $^{133}\text{I}$ within time window $t_{Decay} < 3 \mu\text{s}$ . Inset of the figure shows the decay pattern of delayed $\gamma$ rays $\gamma_D = 874 + 353 + 1168$ keV with exponential fitting. (b) Delayed $\gamma$ rays ( $\gamma_D$ ) in coincidence with the added prompt gate of $\gamma_P = 614 + 714 + 629 + 786$ keV. . . . .	150
6.13	Level scheme of $^{134}\text{I}$ as obtained in the present work. The newly observed $\gamma$ rays are displayed in red. The thickness of the $\gamma$ rays represents their relative intensity. . . . .	152
6.14	(a) The prompt singles $\gamma$ -ray spectrum of $^{134}\text{I}$ . (b) Prompt $\gamma$ rays ( $\gamma_P$ ) in coincidence with added gate of $\gamma_P = 962 + 640 + 244 + 752 + 785$ keV. (c) Prompt $\gamma$ rays ( $\gamma_P$ ) in coincidence with $\gamma_P = 952$ keV. The new $\gamma$ -transitions are marked with ‘*’ in all the cases. . . . .	153
6.15	Systematics of experimental energy differences for the lowest states with $\Delta I = 2$ for: (a) even- $N$ isotopes of Sn ( $E(2^+) - E(0^+)$ ), Sb ( $E(11/2^+) - E(7/2^+)$ ), Te ( $E(2^+) - E(0^+)$ ) and I ( $E(11/2^+) - E(7/2^+)$ ). (b) odd- $N$ isotopes of Sn ( $E(15/2^-) - E(11/2^-)$ ), Sb ( $E(10^-) - E(8^-)$ ), Te ( $E(15/2^-) - E(11/2^-)$ ) and I ( $E(10^-) - E(8^-)$ ). The new states observed in the present measurements are shown by filled symbols. . . . .	155
6.16	The comparison of experimental ((Exp) shown in black) and theoretical ((SM) shown in red) level schemes for even- $A$ $^{130,132,134}\text{I}$ (a-c) and odd- $A$ $^{131,133}\text{I}$ (d-e) isotopes for both positive and negative parities. The experimental and shell model states of the same spin-parity have been joined with dotted lines to guide the eye. . . . .	156

6.17	The variation in average hole occupancy (for neutron) and particle occupancy (for proton) in all the available orbitals for even mass $^{130,132,134}\text{I}$ isotopes. . . . .	157
6.18	The variation in average hole occupancy (for neutron) and particle occupancy (for proton) in all the available orbitals for odd mass $^{131,133}\text{I}$ isotopes. . . . .	158
6.19	<b>(Left)</b> (a) Probability of neutron hole occupancy in $\nu h_{11/2}$ orbital for $^{130,132}\text{I}$ as a function of the total spin ( $J$ ) of the negative parity states, (b) Average spin contribution of proton ( $2J_\pi$ ) and neutron ( $2J_\nu$ ) to the total spin ( $J$ ) of the negative parity states in $^{130}\text{I}$ for different number of hole occupancy in the $\nu h_{11/2}$ orbital and (c) Same as (b), but for $^{132}\text{I}$ . <b>(Right)</b> (a) Probability of neutron hole occupancy in $\nu h_{11/2}$ orbital for $^{131,133}\text{I}$ as a function of the total spin ( $2J$ ) of the negative parity states, (b) Average spin contribution of proton ( $2J_\pi$ ) and neutron ( $2J_\nu$ ) to the total spin ( $2J$ ) of the negative parity states in $^{131}\text{I}$ for different number of hole occupancy in the $\nu h_{11/2}$ orbital and (c) Same as (b), but for $^{133}\text{I}$ . . . . .	161
7.1	Variation of $E_{4+}/E_{2+}$ with neutron number ( $N$ ) for Te, Xe and Ba. . . . .	168
7.2	Total projected spectrum from the $\gamma$ - $\gamma$ matrix as obtained in the present experiment indicating various $\gamma$ -transitions coming from the corresponding excited nuclei. $\gamma$ rays for different nuclei are indicated with different colour code. . . .	170
7.3	<b>(Left)</b> Decay half-life plots of (a) 1131 keV of $^{135}\text{Xe}$ ( $t_{1/2} = 398(6)$ min) (b) 847 keV of $^{134}\text{Xe}$ ( $t_{1/2} = 52.5(2)$ min) (c) 954 keV of $^{132}\text{Xe}$ ( $t_{1/2} = 149(3)$ min) produced from ground state decay of $^{132}\text{I}$ and (d) 175 keV of $^{132}\text{Xe}$ ( $t_{1/2} = 94(9)$ min) populated from isomeric decay of $^{132}\text{I}$ . Their deduced half-lives are in good agreement with the reported values. <b>(Right)</b> Decay plots of various newly observed $\gamma$ -rays. Deduced half lives confirms them as decaying from $^{134}\text{I}$ to $^{134}\text{Xe}$ . . . . .	172
7.4	Proposed level scheme of $^{134}\text{Xe}$ , as obtained from the present work. New transitions are marked with '*'. . . . .	173
7.5	Coincidence spectra corresponding to the gate of 848 keV $\gamma$ -ray of $^{134}\text{Xe}$ . The newly observed transitions in the present work are marked with '*'. (a)low energy part, (b) higher energy part. . . . .	174
7.6	Coincidence spectra corresponding to the newly observed $\gamma$ rays of energy (a)2313, (b)1655 and (c)1542 keV. . . . .	179
7.7	Coincidence spectra corresponding to the $\gamma$ rays of energies (a)1455 keV and (b)1073 keV. . . . .	180
7.8	Variation of intensities of different transitions as a function of angle. These intensities are fitted with angular correlation function. . . . .	181

7.9	Comparison between experimental $a_{kk}$ coefficients with the theoretical calculations. The contours shown are plotted for varying $\delta$ values. (a) 1806, (a) 766, (a) 1073, (a) 817, (a) 622, (a) 678 and (a) 541 keV transitions are shown in the figure. . . . .	182
7.10	Evolution of the lower lying levels in Xe ( $Z = 54$ ) isotonic chain. . . . .	183
7.11	Comparison of the experimental results with the theoretical calculations for the low lying spins only. . . . .	185

# List of Tables

4.1	The energies ( $E_\gamma$ ) and relative intensities ( $I_\gamma$ ) of the $\gamma$ rays observed in $^{117}\text{Sb}$ along with the spin and parity of the initial ( $J_i^\pi$ ) and the final ( $J_f^\pi$ ) states and the energy of the initial state ( $E_i$ ). The measured values of $R_{DCO}$ and $\Delta_{PDCO}$ are also shown along with the multipolarity of the $\gamma$ rays. . . . .	79
4.2	Experimental excitation energy ( $E_x$ ), spin ( $J^\pi$ ) and their calculated configurations with % contribution of the positive parity low lying states in $^{117}\text{Sb}$ , as obtained from the shell model calculations. Contributions above 10% of the configurations are only tabulated. . . . .	91
5.1	The energies ( $E_\gamma$ ) and relative intensities ( $I_\gamma$ ) of the $\gamma$ rays observed in $^{131}\text{Xe}$ along with the spin and parity of the initial ( $J_i^\pi$ ) and the final ( $J_f^\pi$ ) states and the energy of the initial state ( $E_i$ ). The measured values of $R_{DCO}$ and $\Delta_{PDCO}$ are also shown along with the proposed multipolarity of the $\gamma$ rays. . . . .	105
6.1	Energies ( $E_\gamma$ ) and relative intensities ( $I_\gamma$ ) of the $\gamma$ rays observed in $^{130}\text{I}$ along with tentative spin and parity of the initial ( $J_i^\pi$ ) and the final ( $J_f^\pi$ ) states and the energy of the initial state ( $E_i$ ). . . . .	135
6.2	Energies ( $E_\gamma$ ) and relative intensities ( $I_\gamma$ ) of the $\gamma$ rays observed in $^{131}\text{I}$ along with tentative spin and parity of the initial ( $J_i^\pi$ ) and the final ( $J_f^\pi$ ) states and the energy of the initial state ( $E_i$ ). The top and bottom panels, separated by a line, are for the prompt and delayed transitions, respectively. The low energy transitions which could not be detected with the present setup are adopted from Ref.[18] and are put within parenthesis. . . . .	138
6.3	Energies ( $E_\gamma$ ) and relative intensities ( $I_\gamma$ ) of the $\gamma$ rays observed in $^{132}\text{I}$ along with probable spin and parity of the initial ( $J_i^\pi$ ) and the final ( $J_f^\pi$ ) states and the energy of the initial state ( $E_i$ ). The total intensity of the 762 keV doublet (d) is normalized to 100. . . . .	143

6.4	Energies ( $E_\gamma$ ) and relative intensities ( $I_\gamma$ ) of the $\gamma$ rays observed in $^{133}\text{I}$ along with probable spin and parity of the initial ( $J_i^\pi$ ) and the final ( $J_f^\pi$ ) states and the energy of the initial state ( $E_i$ ). The top and bottom panels, separated by a line, are for the prompt and delayed transitions, respectively. The low energy transitions which could not be detected with the present setup are adopted from Ref.[18] and are put within parenthesis. . . . .	148
6.5	Energies ( $E_\gamma$ ) and relative intensities ( $I_\gamma$ ) of the $\gamma$ rays observed in $^{134}\text{I}$ along with probable spin and parity of the initial ( $J_i^\pi$ ) and the final ( $J_f^\pi$ ) states and the energy of the initial state ( $E_i$ ). . . . .	153
7.1	The $\gamma$ -ray energies ( $E_\gamma$ ) observed in the decay of $^{134}\text{I}$ to $^{134}\text{Xe}$ and their relative intensities ( $I_\gamma$ ) along with the corresponding angular correlation coefficients ( $a_{kk}$ ) and the energy of the initial state ( $E_i$ ). The new observed $\gamma$ rays are marked with ‘*’. . . . .	175
7.2	Configurations of various states as obtained from the present shell model calculations. Contribution greater than 10 % is only mentioned. . . . .	184

# Chapter 8

## Summary and Future scope

### 8.1 Summary

In this thesis work, yrast and near-yrast states of  $^{117}\text{Sb}$  ( $Z = 51$ ),  $^{131,134}\text{Xe}$  ( $Z = 54$ ) and  $^{130-134}\text{I}$  ( $Z = 53$ ) are investigated via high resolution  $\gamma$ -ray spectroscopy techniques. These nuclei provide the opportunity to explore the different structural phenomenon around the  $Z = 50$  magic shell closure as a function of the neutron number. The isotopes are also chosen in such a way that the neutron number varies from the middle of the  $N = 50 - 82$  shell to the neutron-rich side near  $N = 82$ .

The rotational band structures as well as the low-lying single-particle excitations in  $^{117}\text{Sb}$  have been studied using the reaction  $^{115}\text{In}(\alpha, 2n)^{117}\text{Sb}$  at the beam energy of 28 MeV and the VENUS setup. The existing level scheme of  $^{117}\text{Sb}$  is extended with the placement of 31 new  $\gamma$ -ray transitions. The signature partner of the band, based on the  $\pi g_{7/2}$  configuration coupled to the 2p-2h structure of the  $^{116}\text{Sn}$  core, has been established for the first time in  $^{117}\text{Sb}$ , from the observation of the connecting M1 transitions and the firm assignment of the spin and parity to the states in these bands. The spin-parity of most of the states are also assigned, based on the measured DCO ratio, polarization asymmetry measurements. The rotational nature, and thereby the deformed structure of bands  $B1$  and  $B1(a)$ , has been established above the  $11/2^+$

state by comparing with the rotational model. A  $\pi g_{7/2}$  configuration has been assigned to this decoupled band having large signature splitting. The level energies and the signature splitting have been well reproduced by the Particle Rotor Model (PRM) calculations and indicate a low- $\Omega$   $\pi 1/2[431]$  Nilsson configuration for this band, which is consistent with its large signature splitting. Several new non-yrast levels have been identified at the low and medium spin. The low-lying positive-parity states have been interpreted in terms of the large scale shell model calculations.

Excited states in  $^{131}\text{Xe}$  have been investigated by populating them using the reaction  $^{130}\text{Te}(\alpha, 3n)^{131}\text{Xe}$  at 38 MeV of beam energy and with the INGA detectors. A much improved and extended level scheme with several new band structures has been obtained with the observation of 72 new  $\gamma$  rays in this work. Different varieties of yrast and non-yrast band structures have been observed in this nucleus. The identification of these bands, based on different quasi-particle configurations, reveals the existence of different structures in the  $N = 77$  transitional nucleus  $^{131}\text{Xe}$ . The new data on the signature splitting and the single-particle alignment of the lowest negative-parity band (B1), having the  $\nu h_{11/2}$  character, indicate a triaxial shape with the involvement of a high-Nilsson orbital. The lowest positive parity band [B6 - B6(a)] has also been substantially extended. This band shows a signature inversion at moderate spin, which, along with a large signature splitting after the inversion, indicates a change in the structure at higher spins. Two new band structures, a 3 quasi-particle (qp) band having configuration  $\pi(g_{7/2}h_{11/2}) \otimes \nu f_{7/2}$  (B4) with large staggering and a 5-qp dipole band having configuration  $\pi(g_{7/2}d_{5/2})^3 h_{11/2} \otimes \nu h_{11/2}$  (B3), have been identified. The configurations of the different bands have been assigned from the systematics of the neighbouring odd-A and even-even nuclei and considering the available orbitals near the Fermi levels. Theoretical TRS calculations for the 1-qp and 3-qp configuration bands suggest interesting structural evolution, which corroborates well with the experimental findings. Triaxial shape and  $\gamma$ -softness are obtained for the 3-qp configurations. New sets of states have been identified, which have been found to decay to these 3-qp, negative- and positive-parity bands. This gives interesting prospects of the observation of  $\gamma$  bands, which needs to be further investigated. Magnetic Rotational band is also identified in this nucleus and discussed using the SPAC model calculations.

The prompt-delayed spectroscopy of the neutron-rich iodine isotopes  $^{130,132,134}\text{I}$  have been carried out after producing the nuclei in fusion-fission and transfer induced fission via reaction  $^9\text{Be}(^{238}\text{U},f)$  at a beam energy of 6.2 MeV/u. The VAMOS++ spectrometer coupled with the AGATA tracking array and the EXOGAM segmented clover detector array were used for measurement. The prompt  $\gamma$ -ray transitions above the isomers in odd-odd  $^{130,132}\text{I}$  are identified for the first time and a new isomer in  $^{132}\text{I}$  is also reported. The level structure of  $^{134}\text{I}$  is also extended with the observation of a new transition. The high-spin level structures of  $^{131,133}\text{I}$  are also extended with the placement of the new prompt transitions above the known isomers from the prompt-delayed coincidence technique. The proposed level schemes are interpreted in terms of systematics and the large scale shell model calculations using NuShellX code. It is found that, the hole occupancy in the  $\nu h_{11/2}$  orbital plays a dominant role in generating the high-spin negative parity states in these neutron-rich iodine isotopes. An additional feature, that the hole occupation in the  $\nu h_{11/2}$  orbital varies strongly in certain iodine isotopes, could also be observed. In even mass iodine isotopes, it is seen that only the  $\pi g_{7/2}$ ,  $\pi d_{5/2}$  and  $\nu h_{11/2}$  orbitals are active in the spin generation. For the states above the  $19/2^-$  isomer, in odd mass iodine, the same set of orbitals are again found to be responsible in the high spin generation. From the shell model calculations, it is also observed that, for  $^{132}\text{I}$ , dominant contribution comes from  $\nu h_{11/2}^{-1}$ , which goes to  $\nu h_{11/2}^{-3}$  at higher spin. Similar scenario is also observed for  $^{130}\text{I}$ . In odd mass  $^{133}\text{I}$ , the  $\nu h_{11/2}^{-1}$  configuration is found to be almost pure. But in  $^{131}\text{I}$ , the  $\nu h_{11/2}^{-1}$  configuration dominates only upto  $25/2^-$  spin, beyond that, proton excitation to the  $\pi h_{11/2}$  orbital takes place.

The low lying excited levels of  $^{134}\text{Xe}$  have also been studied after populating from the  $\beta$ -decay of  $^{134}\text{I}$ . This iodine isotope is produced by the  $\alpha$  induced fission of  $^{Nat}\text{U}$  at the beam energy of 32 MeV and then radio-chemically separated from other fission fragments. The  $^{134}\text{Xe}$  has been studied with an offline setup of four clovers and 2 LEPS detectors. A total of 17 new  $\gamma$ -ray transitions are observed and placed in the new proposed level scheme. Spin assignments to the excited levels are carried out on the basis of the angular correlation measurements. The observed levels are interpreted using the large scale shell model calculations using OXBASH and it is found that the low lying states are highly fragmented.

Nuclei, having atomic number near the 50 shell closure, both near the stability line and towards the neutron-rich side, have been studied in the present thesis work. The new results, manifesting various new structural phenomena in the nuclei around  $Z = 50$ , are reported for the first time. The competition between the collective and single particle degrees of freedom is explored in detail. Though, such competitions are expected in the mid-shell nuclei only (such as, in  $^{117}\text{Sb}$ ), the same is also observed in  $^{131}\text{Xe}$  isotope, which is nearer to the  $^{132}\text{Sn}$  shell closure. The coupling natures of the valence orbital outside the  $Z = 50$  with the core are also explored from the observation of the strongly coupled  $g_{9/2}$  and weakly coupled  $g_{7/2}$  bands in  $^{117}\text{Sb}$ . It is also observed from this thesis work that, for  $^{131}\text{Xe}$ , deformation is being induced by the high- $j$ , unique parity  $h_{11/2}$  orbital. This orbital plays the crucial role in generation of the high spins in near spherical systems, as seen in  $^{131}\text{Xe}$  and in  $^{130-134}\text{I}$ . The involvement of the  $h_{11/2}$  orbital gives rise exotic excitation modes, such as Magnetic Rotational (MR) bands as observed in  $^{131}\text{Xe}$ . Towards the neutron rich side, around  $^{132}\text{Sn}$ , as in  $^{130-134}\text{I}$ , the single particle excitations are found to dominate the states both below and above the high spin isomers. It is also found that, the hole occupancy in the  $h_{11/2}$  orbital plays the dominant role in generating the high spin negative parity states in these neutron rich iodine isotopes.

## 8.2 Future scope

The new and exciting results of these nuclei obtained in the present thesis work open up new physics interests to look for in the neighbouring nuclei, both experimentally and theoretically.

In this work, the coupling nature of the  $g_{7/2}$  orbital with the underlying core is explored in  $^{117}\text{Sb}$ . But such coupling nature of this orbital with the core is not studied in neighbouring lower odd mass Sb isotopes. It is also interesting to inspect the involvement of the  $\Omega$ -component of the  $g_{7/2}$  orbital in order to explain the staggering of such band in the lower mass Sb isotopes.

The present data indicates the presence of the  $\gamma$  vibrational band in  $^{131}\text{Xe}$ , which needs to be investigated further. It is worth to mention that,  $\gamma$  band is reported in Xe isotopes in the  $A < 130$  region, but not in the heavier Xe isotopes. TRS calculations also support the presence

of such bands. Thus, it becomes an open question to look for the existence of  $\gamma$  vibrational band in  $^{131}\text{Xe}$ , as well as in the odd mass Xe isotopes beyond  $A = 130$ . Observation of MR band in  $^{131}\text{Xe}$  also makes this mass region interesting to look for MR bands in the neighbouring isotopes.

The nuclei near the  $N = 82$  shell closure is known for the presence of low lying high spin isomers, as found in the iodine isotopes. A new isomer is identified in  $^{132}\text{I}$  from the present measurements. Thus, neighbouring even mass iodine isotopes must be investigated to search for such isomers, having similar configurations. The prompt-delayed coincidence techniques, as utilized in the present thesis, will be helpful while investigating these isomers.

All the isotopes, studied in the present thesis, have atomic number above the  $Z = 50$  shell closure. Thus, the effect of the orbitals, situated above the  $Z = 50$  shell closure, are explored. In the present study, the various coupling of the valence orbitals occupied by the proton particles above  $Z = 50$  have been investigated. It will be interesting to compare similar excitations in the nuclei having same neutron number, as studied in present thesis, with proton holes in the  $Z = 50$  shell closure. Such nuclei would obviously be situated in the neutron-rich side of the stability line and therefore would be challenging to investigate experimentally also.

# SUMMARY

The present thesis reports the single particle and collective excitations of nuclei, both near stability as well as towards the neutron-rich side, having atomic number around the  $Z = 50$  shell closure. Nuclei, having few proton particles above  $Z = 50$ , with few neutron holes in the  $N = 82$  shell provide valuable information about the effective nucleon-nucleon interactions and various coupling schemes between the valance protons and neutrons. The presence of the unique parity, high- $j$   $h_{11/2}$  orbital, in both  $Z, N = 50 - 82$  shell, makes these nuclei more fascinating in order to explore the shape driving effects of the  $h_{11/2}$  orbital over a chain of isotopes from near stability to neutron-rich side of the nuclear chart. The  $h_{11/2}$  orbital results into deformed bands in the neutron mid-shell nuclei, whereas, this orbital is responsible to generate the high spin in near spherical nuclei in the mass 130 region. The contribution of this orbital in the high spin generation mechanism is also one of the major interests of this thesis. The study of the nuclei, having proton number near  $Z = 50$ , also helps to understand the competition between the collective and the single particle excitations. On the contrary, if one moves towards  $N \geq 82$ , with  $Z \sim 50$ , the exciting domain of neutron rich nuclei around  $^{132}\text{Sn}$  becomes accessible. The present thesis also aims to explore the deformation driving behaviour of the  $\nu h_{11/2}$  orbital in the neutron rich domain.

This thesis reports the results from the study of the excited level structures of  $^{117}\text{Sb}$  ( $Z = 51$ ), having single proton above  $Z = 50$  and neutron in mid-shell of  $N = 50 - 82$ , and  $^{131,134}\text{Xe}$  ( $Z = 54$ ),  $^{130-134}\text{I}$  ( $Z = 53$ ) which have few neutron holes in the  $N = 82$  shell closure. It, therefore, helps to understand the evolution of the  $\nu h_{11/2}$  orbital over a mass region. In this work, different reactions mechanisms, such as fusion evaporation, fission and  $\beta$ -decay have been employed to populate the nuclei in its excited states. The measurements, related to the present thesis, are carried out using four different high resolution HPGe detector arrays, namely, VECC Array for Nuclear Spectroscopy (VENUS) at VECC, India, Indian National Gamma Array (INGA) at VECC, India and Advanced Gamma Ray Tracking Array (AGATA), coupled with VAMOS++ magnetic spectrometer and segmented clover HPGe detectors (EXOAM), at GANIL, France.

The new results, obtained for the first time, manifest various new structural phenomena in the nuclei of interest. The competition between the collective and single particle degrees of freedom is explored in detail. Such competition is observed in both mid shell nucleus  $^{117}\text{Sb}$  ( $N = 66$ ) and near shell closure nucleus  $^{131}\text{Xe}$  ( $N = 77$ ). The core polarizing effects, leading to the deformation originating from the effect of the mid shell neutrons, are also explored from the observation of strongly coupled  $g_{9/2}$  and weakly coupled  $g_{7/2}$  bands in the same nucleus  $^{117}\text{Sb}$ . The weak coupling scheme of the  $g_{7/2}$  orbital with the core, due to the involvement of the low- $\Omega$  component, is established, for the first time, from the observation of its signature partner band and Particle Rotor Model (PRM) calculation. The deformation driving effect of the high- $j$   $h_{11/2}$  orbital is also studied from the observation of rotational band based on this orbital in  $^{131}\text{Xe}$ . Triaxial nature of this band at higher spin is also observed. The involvement of this orbital, both in proton and neutron valence space, gives rise to exotic excitation modes, such as Magnetic Rotational (MR) band, as observed in  $^{131}\text{Xe}$ , in the present work. The  $\gamma$ -soft nature of  $^{131}\text{Xe}$  at the higher spin is established from the observation of new 3 quasi-particle band and several new states, along with Total Routhian Surface (TRS) calculation. The orbital  $h_{11/2}$  is also found to be responsible for generation of high spin states in the near spherical neutron-rich systems,  $^{130-134}\text{I}$ . Towards the neutron rich side, the single particle excitations are found to dominate, as is seen in  $^{130-134}\text{I}$ , above the high spin isomers and in the low lying structures of  $^{134}\text{Xe}$ . It is found that, the hole occupancy in the  $\nu h_{11/2}$  orbital plays a crucial role in generating the high spin negative parity states as a function of the increasing neutron number in these neutron rich Iodine isotopes.

# Chapter 1

## Introduction

Atomic nuclei are considered to be one of the fascinating quantal many body systems, the complete microscopic behaviour of which is extremely difficult to understand. It should be mentioned that the existence of the subatomic world was unknown until the discovery of electron by J. J. Thomson in 1897 [1] and the discovery of the radioactivity by Henri Becquerel [2], and Pierre and Marie Curie [3, 4]. It was Ernest Rutherford in 1911, who first proposed the existence of nucleus inside an atom from his experiment of  $\alpha$  scattering from a thin gold foil [5]. The first description of the nucleus, which could explain Rutherford's experiment, was by Bohr [6]. Although, initially the atomic nucleus was conjectured as a spherical one, but in 1924, Pauli suggested that a variety of shapes is possible for a nucleus, when it is excited. Since then, the study of the nuclear shapes in its ground states as well as in its excited states became one of the prime interest of nuclear physics. One of the ways to study the shapes and structures of a nucleus is by exciting it to higher energy states and then by detecting the de-exciting  $\gamma$  rays, as prescribed by Bohr and Fritz Kalckar [7]. The study of the nuclear structures by determining the energies, multipolarities, electromagnetic properties and transition probabilities of the decaying  $\gamma$  rays is known to be one of the front-line techniques and commonly known as the high resolution  $\gamma$ -ray spectroscopy.

The first step towards the theoretical study of the nuclear structure starts with modelling of a nucleus by probing its properties. Theoretically, the nuclear structure study starts with a simple

model called Liquid Drop Model as proposed by Niels Bohr [8] in 1939 and then it evolved into Nuclear Shell Model [9, 10] in 1949. Aage Bohr, Ben Mottelson, and James Rainwater also proposed a model to describe the collective motion of a nucleus around 1950. According to this theory, the collectivity of a nucleus actually results from the deformation of the core [11, 12, 13]. Interestingly, after almost 100 years of the discovery of the nucleus, new modes of structural phenomenon, as a function of high excitation energy and angular momentum, are manifested by the nucleus. And, thus, it becomes necessary to explore such new phenomena in the nucleus in order to characterise it properly. It will not be an exaggeration to mention that such studies of the nuclear shapes and its various decay modes can be efficiently carried out using the  $\gamma$ -ray spectroscopic measurements.

The main focus of the contemporary experimental nuclear structure physics is to obtain the structural information about the nucleus in its high excitation and angular momentum states. There exist two modes of excitation in a nucleus, one is the single particle excitation and the other one is called the collective excitation. In single particle excitation mode, the nucleons inside a nucleus act independently and get excited to the higher lying nuclear levels. This kind of excitation results into complex and irregular excitation pattern of the observed nuclear levels. Usually nucleus, having few nucleons outside the magic core, exhibits such single particle excitations. Single particle excitations indicate spherical or near spherical shapes of the nucleus. The other kind of nuclear excitation is the collective one, where all the nucleons behave collectively or coherently as it gets excited. A regular sequence of excited levels is observed in this case of the collective excitation. Observation of such excited level structure in a nucleus manifests the well deformed shape of the nucleus. The deformed shapes are the usual characteristics of the nuclei, which are away from the shell closure, specifically in the mid shell region. The deformations, observed in an atomic nucleus, can also be classified in two categories, axial and non axial (or triaxial). Apart from these, there exist many other nuclear shapes originating from the interplay of single particle and collective degrees of freedom. This leads to various exotic nuclear shapes such as super-deformation, magnetic rotation, chiral symmetry breaking, wobbling motion *etc.*, which can be observed at different angular momentum regime.

The present thesis work is aimed to study the nuclear structures of the nuclei around the doubly magic shell closure  $^{132}\text{Sn}$  having  $Z$  near 50. The study of these nuclei, having both proton and neutron numbers in the vicinity of the respective magic shell closures, can provide valuable information about the single particle level energies outside the magic core, effect of the valence orbitals and the interactions of the doubly magic core with the available valance particles or holes. The nuclei around the doubly magic shell closure  $^{132}\text{Sn}$  ( $Z = 50, N = 82$ ) can provide important information about the single particle levels and excitations towards the neutron rich side, which in turn helps us to understand the underlying effective nucleon-nucleon shell model interactions. The study of neutron rich nuclei is of contemporary interest because it provides us interesting inputs about the shell structure near the neutron-rich magic core and also helps us to characterize the available orbitals. It is also essential to note that, a competition may arise between the collective and the single particle degrees of freedom, as one moves away from neutron mid-shell to the  $N = 82$  shell closure. Presence of the high- $j$   $h_{11/2}$  orbital and the possible excitations in the same major shell ( $50 - 82$ ) for both proton and neutron make  $A = 130$  region as a fertile ground to study the different shape driving effects of the orbital and also the evolution of deformation. The present thesis work aims to explore such physics aspects in the nuclei around  $Z = 50$ , both near stability and towards the neutron-rich side, by studying their structures using the  $\gamma$ -ray spectroscopic techniques. This helps to understand the effect of the variation of the neutron numbers on the nuclear shape having fixed proton number near to the magic shell. The systematic study of different kinds of band structures in this mass region has revealed the multi-quasi-particle (qp) excitation to the intruder  $h_{11/2}$  orbital as well as particle alignments in this orbital. On the contrary, the low spin structures in this mass region are dominantly contributed by the available  $g_{7/2}$ ,  $d_{5/2}$  and  $s_{1/2}$  orbitals with few proton particles and neutron holes occupying these orbitals. Such excitations in the low spin regime and involvement of the valence orbitals in spin generation help to examine the configurations of the levels using the nuclear shell model. The spin generation mechanism in the neutron rich sides is important to understand as it gives the insight of the contributions of the available orbitals in microscopic level.

The presence of the unique parity high- $j$   $h_{11/2}$  orbital in the both proton and neutron shell, makes the mass 130 region more fascinating to researchers to identify the effect of this orbital on the core polarization uniquely. Being an intruder one, this orbital possess a significant shape driving effect on the expected structures of the nuclei. This shape driving effect of an orbital can only be well studied if its contribution is understood over a long mass chain. This orbital may also leads to deformed bands in the nuclei having neutron number near shell closure, instead of the fact that the near shell closure nuclei possess less deformation. This is because near the shell closure, only few valence nucleons outside the core are available to deform the core. It is also interesting to note that this orbital is solely responsible to generate the high spin in the near spherical systems in the mass 130 region. Neutron rich nuclei in the mass  $A \approx 130$  region are also known for the presence of high spin isomers at the low excitation energies, which also result from the involvement of the  $h_{11/2}$  orbital. Thus it becomes necessary to characterise the  $h_{11/2}$  orbital to understand its effect in the nuclei having neutron number from the mid-shell to the neutron rich side.

As discussed above, nucleus near the shell closures, as in case of the present thesis, where nuclei are near to the  $Z = 50$  proton shell closure, usually exhibits single particle structures, but the presence of the deformation driving high- $j$  orbital induces collectivity in the system. Collective excitation, in form of rotation, in a nucleus is observed in the mid shell nuclei, because of the dominant core polarizing effect of the valence nucleons. Thus the study of the nuclei having nucleon number at the mid-shell to the near shell closure always provide us complementary information about the involved orbitals. It is also worth to mention that the nuclei with proton number near  $Z = 50$  and neutron number in the mid-shell of  $N = 50 - 82$  are interesting candidates to study the competitive behavior of the single particle excitations and collective behaviours [14, 15]. A good example of observation of such different kinds of excitations in nuclei depending on the position of neutron Fermi surface can be Sn ( $Z = 50$ ) isotope. A regular collective level structure is obtained for  $^{112}\text{Sn}$  ( $Z = 50, N = 62$ ) [16], where the neutron number is in the middle of the  $N = 50 - 82$  shell. On the other hand, complete irregular structure is observed in the case of  $^{131}\text{Sn}$  [17], which has both its proton and neutron number near to the shell closure. Study of the mid-shell nuclei and that near to the shell closure is,

therefore, a fertile testing ground of various collective models and shell models, respectively. The high spin generation mechanisms in these near spherical systems can also be understood by studying these nuclei.

The nuclei near the mass region  $A \approx 130$  show various exotic phenomenon, although they are near the doubly magic shell closure. Only conventional collective behaviours due to the deformation driving high- $j$  orbitals ( $g_{9/2}$ ,  $h_{11/2}$  *etc.*) can not account for the high spin generation mechanism in this region. The availability of the  $\pi h_{11/2}$  and  $\nu h_{11/2}$  orbitals in the  $A \approx 130$  region and their mutual interactions drive the nuclei towards triaxial deformation. The signature of triaxiality in nuclei is the chiral symmetry breaking or wobbling motion. Chiral symmetry breaking has been observed in  $^{132}\text{Cs}$  [18, 19], whereas,  $^{134}\text{Cs}$  [20] has shown Magnetic Rotational (MR) band. This is a manifestation of transition from non-planar to planar geometry of the angular momentum blades as a function of the increasing neutron number. Magnetic Rotational bands occur in the those nuclei, which has small deformation and high- $j$  orbitals involved in their structures. Therefore, it is evident that the position of the Fermi level plays an important role in determining the structure of the nucleus in this region. Similarly, in this mass region, triaxiality has also been manifested by wobbling motions [21]. Occurrence of MR band is also seen in the nuclei having  $A \leq 130$ , such as in  $^{123}\text{Xe}$  (mixed MR band). This band originates from various multi-nucleon excitations involving the  $\pi h_{11/2}$  and  $\nu h_{11/2}$  orbitals. Thus, it is evident that mass 130 region is always a suitable region to look for the exotic phenomenon. The importance of this region also comes from its proximity to the  $^{132}\text{Sn}$ , which makes it a fertile ground to search for the shell model inputs. Various works have been carried out to understand the behaviours of the orbitals and the residual interactions between the nucleons using the shell model [23, 23]. So, this region can always be investigated in order to increase the understanding about the nuclear shell model interactions. Thus, the study of nuclei in these mass regions are fruitful to get interesting results regarding nuclear structures.

The study of the excited states of the nucleus  $^{117}\text{Sb}$  ( $Z = 51, N = 66$ ) can provide us the required information about the behaviour of the available single particle orbitals around the  $Z = 50$  core and collective nature originating from the various angular momentum couplings among the valence nucleons and the core. This nucleus is also the ideal candidate to explore

the expected competition between the collectivity and single-particle yrast and near-yrast excitations. Because of the proximity of neutron mid-shell, these Sb isotopes in mass  $\approx 110$ -120 are known to exhibit various deformed band structures. A well established deformed  $2p - 2h$  band structure built on the  $9/2^+$  state is systematically observed in the Sb mass chain [8, 25], which manifests the deformation driving nature of the  $g_{9/2}$  orbital. Other than this, coupling of the odd proton with the underlying core gives rise to the various deformed band structures. Such bands, based on the  $h_{11/2}$ ,  $g_{7/2}$  and  $d_{5/2}$  orbitals, are experimentally observed and studied [26, 27, 28, 29] in these isotopes. So, in  $^{117}\text{Sb}$ , bands based on both  $g_{9/2}$  and  $g_{7/2}$  are seen but in case of the  $g_{7/2}$  band, the nature of the particle coupling is unknown. The presence of the signature partner of any deformed band and the characteristics of the same provide information about the nature of the coupling of the valence particle with the underlying core. This also helps to understand the involvement and effect of the Nilsson component of the available orbital. The observed signature splitting of the partner bands depends on the  $\Omega$  value of the orbital. Therefore, the effect of the involved  $\Omega$ -component of the Nilsson orbital can be understood. Such signature partner bands are reported in the odd- $A$  I ( $Z = 53$ ) [13] and Cs ( $Z = 55$ ) isotopes [14], but similar investigations are yet to be carried out for odd- $A$  Sb isotopes. It is important to note that, Sb isotopes have just a single proton outside the  $Z = 50$  core, thus, the characteristics of the partner bands give the unique feature of the valence proton orbital and the interaction of it with the core. The primary focus of the study of  $^{117}\text{Sb}$  is, therefore, to look for such partner bands of the established rotational bands and to characterize them. The results on this coupling scheme will also highlight the core polarizing effect of the valence proton orbitals in the vicinity of  $Z = 50$ . Other than this,  $^{117}\text{Sb}$  is a good candidate to understand the single particle structures originating from the occupancy of the single proton in various available orbitals. The low spin structures of this nucleus is dominated by such kind of excitations as it has only one valence proton.

It is apparent from the structure of the  $^{117}\text{Sb}$  isotope, that the rotational band structures can be seen in the mid shell nuclei. But, the presence of the deformation driving orbitals near the doubly magic shell closure can also give rise to the collective rotational structures. In such situation, again there exists competition between collective and single particle excitations. To

understand such phenomenon, the excited states of  $^{131}\text{Xe}$  ( $Z = 54, N = 77$ ) are studied under the present thesis work. This nucleus has proton and neutron number near the  $Z = 50$  and  $N = 82$  major shell closures, respectively. The transitional nuclei in the  $A \approx 130$  region, are known to provide a rich variety of single-particle and collective structures and their co-existences. Although, this region is known for its spherical structures, but, deformation can arise with the inclusion of several number of neutron holes in the  $N = 82$  shell. This is because the structure of these transitional nuclei largely depends on the shape driving effect of the involved orbitals. It is also seen that most of the even-even nuclei in this region depict softness towards the  $\gamma$  deformation [32]. It is, therefore, interesting to look for the effect of the addition of extra odd neutron holes on top of the even-even core. In this context, the  $^{131}\text{Xe}$  ( $Z = 54, N = 77$ ) isotope, with four proton particles beyond the  $Z = 50$  core and few neutron holes in the  $N = 82$  core, is suitable candidate to study the various interesting features from its band structures. Other than deformed band structures, there is also a probability of occurrence of Magnetic Rotational (MR) band due to its near spherical shape arising from its proximity to the closed shell and involvement of the  $\pi h_{11/2}$  and  $\pi h_{11/2}$  high- $j$  orbitals. Therefore, in order to understand the systematic of the different multi-quasi-particle configurations in the  $^{131}\text{Xe}$  isotopes, it is necessary to have detailed spectroscopic information of the both yrast and non-yrast states.

The study of the nuclei near the doubly magic shell closure enhances our knowledge about the properties of the available single particle orbitals along with the various coupling schemes between the valence nucleons. The nuclei with either odd- $Z$  or odd- $N$  near a major shell closure are of contemporary interest to obtain the single particle level energies and the nucleon-nucleon effective interaction. To explore such aspects of the neutron rich nuclei, the excited states of  $^{130-134}\text{I}$  and  $^{134}\text{Xe}$  are studied in this thesis work. The nuclei with a few odd valence protons outside the  $Z = 50$  shell closure, like Iodine ( $Z = 53$ ) and Xenon ( $Z = 54$ ), can give the required information about the proton single particle energies and also the multiplets of various particle-hole configurations, with valence odd proton and odd neutron. The presence of the high- $j$ , unique parity  $h_{11/2}$  orbital in both the  $Z, N = 50 - 82$  shell plays a major role in generating the high spin states for nuclei in the  $A = 130$  region and in the neutron rich side.

Configurations involving  $\nu h_{11/2}$  holes are found to be responsible for systematic occurrence of isomers in the odd- $A$  as well as in the odd-odd nuclei in this region [33, 34, 35]. It would be, thus, interesting to investigate the level structure above these isomers and to understand the relative contributions of protons and neutrons in generating those states. In this context, it can be noted that, the involvement of the  $h_{11/2}$  orbital in  $^{131}\text{Xe}$  leads deformed band structures. To study the effect of the unique parity  $h_{11/2}$  orbital in both proton and neutron space in this mass region is one of the primary concerns of this work. The higher spin generation mechanism in these nuclei is greatly affected by the high- $j$   $h_{11/2}$  orbital, which has a tendency to induce deformation in near-spherical systems. It is also worth to mention that only the study of high spin structures does not always provide the complete nuclear structure information. The low-lying excitations are also important to have complementary information and to characterize a nucleus completely. The non- and near-yrast states in a nucleus in this mass region also help to understand the various coupling schemes responsible in generation of the excited states in these nuclei in detail.

There exist various reaction mechanisms to excite a nucleus in the higher energy, such as, fusion evaporation reaction, Coulomb excitation, transfer reaction,  $\beta$ -decay, fission *etc.*. Fusion-evaporation and fission reactions are known to populate the nuclei at more high angular momentum states, whereas the spin population and excitation energy in case of the  $\beta$ -decay is limited by the reaction Q-value. In a conventional fusion-evaporation reaction, the projectile (heavy or light) fuses with the target and the compound nucleus gets excited to higher energy and angular momentum. Depending upon the excitation energy, the compound nucleus evaporates few particle until it comes below the particle threshold energy and after that no particle evaporation is possible due to the energy constraint. Then the nucleus de-excites to its ground state by decaying  $\gamma$  rays. In case of fission also, the fission products are populated in its higher excited states and decays to the ground state via  $\gamma$ -ray emissions. In this process, one of the fission partner is produced in the neutron rich side. In the process of the  $\beta$ -decay, the excited states of the daughter nuclei are populated by the  $\beta$ -decay of the parent nuclei. But in this case, the angular momentum population as well as the excitation energy of the daughter nuclei is limited by the angular momentum of the decaying level and the reaction Q-value. As a matter

of fact, in the process of the  $\beta$ -decay, usually low spin, non- or near-yrast levels are populated and, thus, it is one of the efficient way to study the non-yrast states. This present thesis utilizes fusion-evaporation, fission and  $\beta$ -decay followed by fission, in order to populate the nuclei in its excited states of different excitation energy and angular momentum. As one of the primary aim of the present work is to study the nuclei near  $^{132}\text{Sn}$  and towards the neutron-rich side, the problem arises due to the unavailability of the stable target-projectile combinations to produce those nuclei. Fission is known to be one of the way out to produce the nucleus in neutron rich side. Other than this, light-ion induced fusion-evaporation reactions is also used in this thesis work to produce the yrast and non-yrast states of the nuclei near  $^{132}\text{Sn}$  as well as, near the stability line.

With the increase in interest in the nuclear structure physics, the requirement of more advanced experimental tools also arises in order to probe the nucleus at its high excitation energy, high angular momentum states. The combination of high resolution, high efficiency  $\gamma$ -ray multi-detector array, coupled with various other ancillary detectors and the modern accelerators facilities gives the essential boost to explore new exotic and often unexpected nuclear structure phenomena. The theoretical predictions can only be verified by studying the nuclear structure using this kind of state of art detector arrays. This thesis work uses the state of art  $\gamma$ -ray detector arrays to detect the decaying  $\gamma$  rays. This is worth to mention that different kinds of detector arrays in India, as well as new generation detectors at international laboratories are utilized in the present thesis work. Measurements are carried out using arrays of Compton suppressed Clover HPGe detectors, such as, Indian National Gamma Array (INGA), VECC array for NUClear Structure (VENUS) and ADavance Gamma ray Tracking Array (AGATA) coupled with the VAMOS++ magnetic spectrometer and the EXOGAM segmented Clover detectors. An in-house offline set-up, consisting of Clover detectors and Low Energy Photon Spectrometer (LEPS) detectors, is also used in the offline  $\beta$ -decay studies. It is also necessary to determine the multipolarity and the electromagnetic nature of the decaying transitions in order to uniquely characterize the states associated with it. The determination of the spin and parity of the excited states are really important to explain the structure and the underlying symmetry. A Compton suppressed Clover HPGe detector array is, therefore, not only necessary

for such studies but becomes an inseparable part. Other than this, the arrangement (angular orientation) of the detectors is equally important to obtain the information of the multipolarity and polarization of the transitions.

Various nuclear shapes, structures and nuclear models are discussed in the second chapter of this thesis. The theoretical model calculations, used in this work, are also discussed in the same chapter. This work employs different kinds of reaction mechanisms, such as fusion evaporation, fission,  $\beta$ -decay to populate the nuclei in its excited states. These are discussed in detail in Chapter 3. Details about the different detector arrays connected with the present work are also in the third chapter. It also includes various data reduction, sorting and analysis techniques, which are used to analyze the recorded data. This thesis work reports the experimental study of the level structures of eight nuclei, those are  $^{117}\text{Sb}$ ,  $^{131}\text{Xe}$ ,  $^{130-134}\text{I}$  and  $^{134}\text{Xe}$  using the  $\gamma$ -ray spectroscopic techniques. This thesis work tries to integrate the results on the various observable structural phenomenon arising from their different positions of the neutron Fermi surface with few proton particles above the  $Z = 50$  core. It reports the excited level structures of  $^{117}\text{Sb}$ , which has neutron in the mid-shell of  $N = 50 - 82$ . Whereas,  $^{131}\text{Xe}$ ,  $^{130-134}\text{I}$  and  $^{134}\text{Xe}$  have only few neutron holes in the  $N = 82$  shell closure. Thus the effect of the variation in the neutron number from mid shell to the shell closure is studied under this work. Involvement and contribution of various available orbitals in the high spin generation are also well understood by using the shell model calculations. A detailed study of the aforesaid nuclei is carried out following various experimental techniques and the results of these measurements give important inputs for the single particle excitations and collective structures of nuclei near the stability as well as neutron-rich nuclei around  $Z = 50$ . Experimental findings are also interpreted using different theoretical models to have a better understanding of their structures.

# Bibliography

- [1] J. J. Thomson. *Philosophical Magazine*, 44:293, (1897).
- [2] H. Becquerel. *Comptes Rendus*, 122:420, (1896).
- [3] M. Curie. *Comptes Rendus*, 126:1101, (1898).
- [4] M. Curie and P. Curie. *Comptes Rendus*, 127:175, (1898).
- [5] E. Rutherford. *Philosophical Magazine, Sixth Series*, 21:669, (1911).
- [6] N. Bohr. *Philosophical Magazine*, 26:1, (1913).
- [7] N. Bohr and F. Kalckar. *Mat.-Fys. Medd.*, 14:10, (1937).
- [8] A. Bohr and B. R. Mottelson, “Nuclear structure, vol. II”, Benjamin Reading, Massachusetts (1975).
- [9] M. G. Mayer. On Closed Shells in Nuclei II. *Physical Review*, 75:19691970, (1949).
- [10] O. Haxel J. H. D. Jensen and H. E. Suess. On the Magic Numbers in Nuclear Structure. *Physical Review*, 75:1766, (1949).
- [11] L. J. Rainwater. *Phys. Rev.*, 79:432, (1950).
- [12] A. Bohr and B. R. Mottelson. *Dan. Mat.-Fys. Medd.*, 27:16, (1953).
- [13] A. Bohr and B. R. Mottelson. *Collective Nuclear Motion and the Unified Model in Beta and Gamma Ray Spectroscopy*. North Holland, Amsterdam, first edition, 1955.

- [14] K. Heyde, Phys. Rep., **102**, 291 (1983).
- [15] K. Heyde, Phys. Lett., **64B**, 135 (1976).
- [16] S. Ganguly *et al.* Nucl. Phys. A **789**, 1 (2007).
- [17] P. Bhattacharyya *et.al.*, Phys. Rev. Lett., **87**, No. 6 (2001).
- [18] C. W. Beausang *et al.*, Nucl. Phys. A **682**, 394 (2001).
- [19] G. Rainovski *et al.*, Phys. Rev. C **68**, 024318 (2003).
- [20] H. Pai *et al.*, Phys. Rev. C **84**, 041301(R) (2011).
- [21] Matta *et al.*, Phys. Rev. Lett. **114**, 082501 (2015).
- [22] B. A. Brown Progress in Particle and Nuclear Physics **47**, 517 (2001).
- [23] J.P. Schiffer and W.W. True, Rev. of Mod. Phys. **48**, 191 (1976)
- [24] R. E. Shroy *et al.*, Phys. Rev. C **19**, 1324 (1979).
- [25] A. K. Gaigalas *et al.*, Phys. Rev. Lett. **35**, 555 (1975).
- [26] D. R. LaFosse *et al.*, Phys. Rev. C **50**, 1819 (1994).
- [27] P. Banerjee *et al.*, Phys. Rev. C **87**, 034321 (2013).
- [28] R. S. Chakrawarthy and R. G. Pillay, Phys. Rev. C **54**, 2319 (1996).
- [29] D. R. LaFosse *et al.*, Phys. Rev. C **56**, 760 (1997).
- [30] S. Tormanen *et al.*, Nucl. Phys. A **613**, 282 (1997).
- [31] S. Ohya, Nucl. Data Sheets **111**, 1619 (2010).
- [32] N. V. Zamfir and R. F. Casten, Phys. Lett. B **260**, 265 (1991).
- [33] S. Biswas *et al.*, Phys. Rev. C **99**, 64302 (2019).
- [34] A. Astier *et al.*, Phys. Rev. C **85**, 054316 (2012).

[35] H. Watanabe *et al.*, Phys. Rev. C **79**, 024306 (2009).

# Chapter 2

## Nuclear Models

The excited states of an atomic nucleus, made up of  $Z$  protons and  $N$  neutrons, can be characterized by their excitation energies, angular momenta and parities. These nuclear energy states can also be well described by their shapes. The positions of the proton and neutron Fermi surfaces and the accessibility of various available nuclear orbitals by the valence nucleons, together determine the shape of a nucleus. In general, the shell closures lead to spherical shapes, whereas the residual interactions between the valence nucleons try to deform it. Various nuclear models are developed in order to describe the different shapes of a nucleus as a function of excitation energy and angular momentum. This chapter discusses the nuclear models relevant to this thesis work.

### 2.1 The Liquid Drop Model

The liquid drop model [1] is a simplified description of the nuclei, where the atomic nucleus is treated as a drop of an incompressible fluid. It is, historically the first model proposed for a nucleus. The atomic nucleus can be compared with a liquid drop due to its saturation property and the fact that nucleus has a very low compressibility. The observed Binding Energy per nucleon of a nucleus for  $A \geq 12$  is almost constant with a value  $\sim -8.5$  MeV,

which highlights its saturation property. The best known semi-empirical mass formula for the Binding Energy ( $B(N, Z)$ ) is given by Bethe-Weizsäcker [2, 3], and is written as,

$$B(N, Z) = a_V A + a_S A^{\frac{2}{3}} + a_C \frac{Z^2}{A^{\frac{1}{3}}} + a_I \frac{(N - Z)^2}{A} + \delta(A) \quad (2.1)$$

The first term of Eq. 2.1 is called the volume term because it is proportional to the mass number (*i.e.*, volume as the mass number of a nucleus is proportional to the  $r^3$  or volume) of the nucleus. The second term in that expression is proportional to  $A^{\frac{2}{3}}$  *i.e.*, to the surface area of the nucleus and therefore is called the surface term. This term originates from the surface tension of the nuclear surface and thus reduces the total binding energy. The third term of Eq. 2.1 is called the Coulomb term and it takes into account the Coulomb repulsion between the charged protons inside a nucleus. The contribution of this term can be calculated approximately by assuming the nucleus to be an uniformly charged sphere. The fourth term is called the symmetry term, which balances the difference between the number of protons and neutrons inside a nucleus. This term is therefore proportional to the relative difference between the neutron number and proton number (N-Z). Contribution of this term becomes significant at higher mass region where, this difference (N-Z) is reasonably higher. The  $\delta(A)$  term is the pairing term, which accounts for the pairing between the various nucleons. Contribution from this term makes the even-even nuclei to be more bound than the odd-odd one. The coefficients of all the terms can be obtained from fitting the experimental data points using this mass formula. The values for those coefficients are obtained as [4]  $a_V = -15.68$  MeV;  $a_S = 18.56$  MeV;  $a_C = 0.717$  MeV and  $a_I = 28.1$  MeV. The pairing term,  $\delta(A)$  in Eq. 2.1 is given by,

$$\begin{aligned} \delta(A) &= 34. A^{-\frac{3}{4}} \text{ MeV} \quad \text{for even - even nuclei} \\ &= 0 \quad \text{MeV} \quad \text{for even - odd nuclei} \\ &= -34. A^{-\frac{3}{4}} \text{ MeV} \quad \text{for odd - odd nuclei} \end{aligned}$$

This simple Liquid Drop Model is capable of explaining few nuclear properties, such as, its binding energy curve, fission probability, saturation property *etc.*. But this model fails miser-

ably to explain the two proton separation energies, magnetic moments, generation of the magic numbers *etc.*.

## 2.2 Shell Model

The necessity to develop the nuclear shell model, where the nucleons are treated as independent particles, was the occurrences of so-called magic numbers (2, 8, 20, 28, 50, 82 and 126) in the nuclear chart. Nuclei having magic numbers of proton and neutrons are found to be more stable compared to its neighbours. They also have larger nucleon separation energies. Such observations allowed to treat the nucleons as independent particles moving in a mean potential field. The nuclear shell model was first proposed by Mayer [5] and Haxel, Jensen and Suess [6], independently. This proposition is able to explain the first few magic numbers, magnetic moments, spins and energies of the levels *etc.* [7, 8].

The shell model Hamiltonian of a nucleus, having  $A$  number of nucleons, consists of one body kinetic energy term and a two body potential energy term and is represented as:

$$\mathcal{H} = T + V = \sum_{i=1}^A -\frac{\hbar^2}{2m_i} \nabla_i^2 + \frac{1}{2} \sum_{i,j=1}^A V_{i,j} \quad (2.2)$$

The first term of Eq. 2.2 is the kinetic energy term of each nucleon and the  $V_{i,j}$  is the two body potential energy term originating from the nucleon-nucleon interactions. Since the exact form of the nuclear potential energy inside a nucleus is unknown, we, therefore, introduce an average one body potential,  $U(r_i)$ , which is experienced by all the ( $A$ ) nucleons. Hence, the Hamiltonian can be rewritten by adding and subtracting  $U(r_i)$  as,

$$\mathcal{H} = \sum_{i=1}^A [T_i + U(r_i)] + \left( \frac{1}{2} \sum_{i,j=1}^A V_{i,j} - \sum_{i=1}^A U(r_i) \right) = \mathcal{H}_0 + \mathcal{H}_{res} = \sum_{i=1}^A h_0(i) + \mathcal{H}_{res} \quad (2.3)$$

where,  $\mathcal{H}_0$  is the one body part of the total Hamiltonian and  $\mathcal{H}_{res}$  is the residual interaction, which is the two body part of the Hamiltonian. The  $\mathcal{H}_0$  describes the motion of all the nucleons

in the mean field  $U(r_i)$ . Usually,  $\mathcal{H}_0$  is chosen in such a way that the residual interaction part becomes so small that it can be treated as a non-relativistic perturbation.

An analytic 'Woods-Saxon' potential is used extensively as a mean field potential  $U(r_i)$ , which is given by,

$$V_{WS}(r) = -\frac{V_0}{1 + \exp[(r - R)/a]} \quad (2.4)$$

where,  $V_0$  is the depth of the potential ( $\approx 50$  MeV),  $R$  is the nuclear radius given as  $R \approx 1.2A^{1/3}$  fm and 'a' is the surface thickness ( $\approx 0.5$  fm). In the above equation, the potential  $V(r)$  depends only on 'r', thus the potential is radially or spherically symmetric. For simplicity, we take the spherically symmetric Harmonic Oscillator potential as  $V(r)$ , which also depends only on the radius 'r' and is given by,

$$V_{HO}(r) = \frac{1}{2}m\omega_0^2(r^2 - R_0^2) \quad (2.5)$$

where,  $R_0$  is the mean radius of the nucleus,  $m$  is the mass of a nucleon, and  $\omega_0$  is the oscillator frequency of the nucleon.

The Schrodinger equation of the three dimensional spherically symmetric harmonic oscillator potential is written as,

$$\mathcal{H}\Phi_{nlm}(r, \theta, \phi) = \left[ \frac{-\hbar^2}{2m}\nabla^2 + V_{HO}(r) \right] \Phi_{nlm}(r, \theta, \phi) = E_N\Phi_{nlm}(r, \theta, \phi) \quad (2.6)$$

where, the wave function  $\Phi(r, \theta, \phi)$  is divided in radial part  $R_{nl}(r)$  and spherical harmonics  $Y_{lm}(\theta, \phi)$ . The  $E_N$ s are the energy eigen-values corresponding to the major oscillator quantum numbers 'N'. The solution of this equation is given by,

$$E_N = \left( N + \frac{3}{2} \right) \hbar\omega_0 \quad (2.7)$$

with,

$$N = 2(n - 1) + l, \quad n = 1, 2, 3, \dots \quad \text{and} \quad l = 0, 1, 2, \dots \quad (2.8)$$

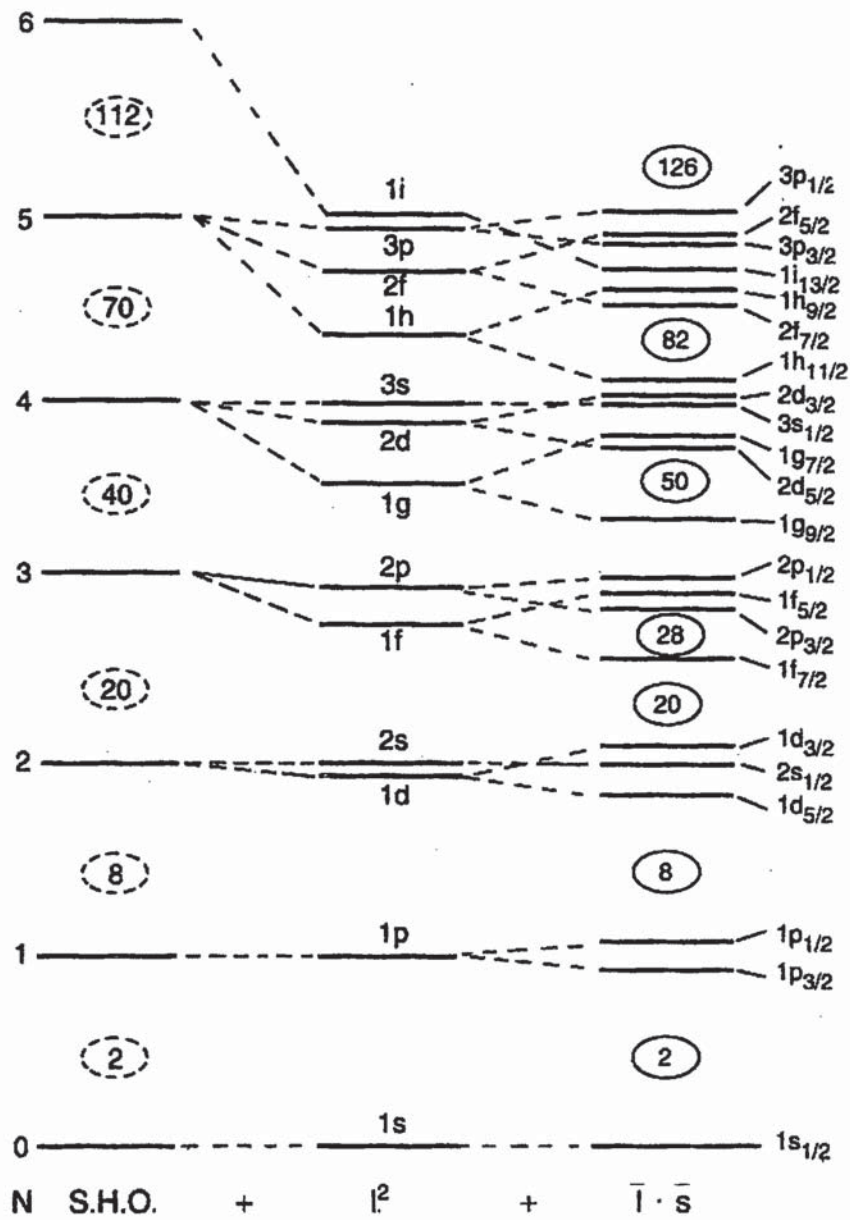


Figure 2.1: Energy states as obtained using Simple Harmonic Oscillator (S.H.O) (left column), same as obtained after introducing  $l^2$  term (middle column). Right column is the same but obtained from more realistic potential with another extra  $l \cdot s$  term. Fig is taken from Ref. [9].

Here, ‘ $N$ ’ is the principal quantum number and  $n$ ,  $l$ ,  $m$  are the radial, orbital and magnetic quantum numbers, respectively. Each ‘ $N$ ’ shell contains a maximum number of  $(N+1)(N+2)$  nucleons. The parity ( $\pi$ ) of the levels for a particular shell is given by  $\pi = (-1)^l = (-1)^N$ .

With this Harmonic oscillator potential, existence of the magic numbers can be reproduced only upto 20. For the higher magic numbers, this simple potential needs modification. The first attempt to modify this mean potential was made by introducing a  $l^2$  term into this potential, which makes this potential more attractive one. Though this slight modification makes this potential more realistic, but still it is not able to reproduce all the magic numbers. For correct description of the observed magic numbers, Maria Geopart Mayer [5] and Haxel, Jensen, Suess [6] introduces an extra spin-orbit coupling term in the form of  $f(r) \vec{l} \cdot \vec{s}$  to the Hamiltonian. This  $f(r)$  is called the strength of the spin orbit coupling and ‘ $s$ ’ (for single nucleon  $s = 1/2$ ) is the intrinsic spin angular momentum. Both the orbital and spin angular momentum now coupled to generate the total angular momentum  $\vec{j}$  as,

$$\vec{j} = \vec{l} + \vec{s} \quad (2.9)$$

Inclusion of this  $\vec{l} \cdot \vec{s}$  term splits the levels into two components corresponding to  $j = l \pm \frac{1}{2}$ . The  $j = l + \frac{1}{2}$  states become lower in energy compared to the  $j = l - \frac{1}{2}$  states. This lowering in energy becomes more significant in high angular momentum states, where the  $j + \frac{1}{2}$  levels intrude in the lower major shell and the observed magic numbers are reproduced. Each single particle states in shell model can contain  $(2j + 1)$  number of nucleons. Hence a state can uniquely be characterized by its  $n$ ,  $l$  and  $j$  values. The shell model is well capable to explain the ground state properties of many nuclei. Fig. 6.16 shows the single particle energy states using the S.H.O. potential and modified forms of it. It is also evident from the figure that only after addition of the  $\vec{l} \cdot \vec{s}$  term to the potential, the magic numbers are reproduced.

## 2.3 Nuclear shapes

Simple nuclear model, such as, shell model is able to explain the features of the nucleus near shell closures. As one goes away from the shell closure, some regular band structures arise.

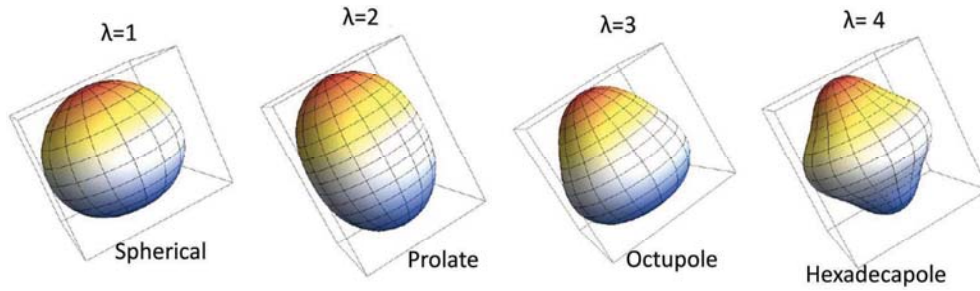


Figure 2.2: Shapes of the multipoles as the perturbations of a sphere. From left to right: dipole ( $\lambda = 1$ ), quadrupole ( $\lambda = 2$ ), octupole ( $\lambda = 3$ ) and hexadecapole ( $\lambda = 4$ ). Fig is taken from Ref. [12].

These structures, in the mid shell regime, indicate that the nucleons act collectively to generate angular momentum in that domain. Such collectivity in an atomic nucleus can occur if the nucleons undergo collective rotation or vibration. These collective models are first described by Bohr and Motelsson [11]. This model is based on the simple paramaterization of the nuclear surface. In this formalism, the radius of the nucleus ( $R$ ) is expressed as,

$$R(\theta, \phi) = R_0 \left[ 1 + \sum_{\lambda=0}^{\infty} \sum_{\mu=-\lambda}^{\lambda} \alpha_{\lambda\mu}^* Y_{\lambda\mu}(\theta, \phi) \right] \quad (2.10)$$

Where, the  $\alpha_{\lambda\mu}^*$  term represents the shape parameter and  $\lambda$  term is the order of the multipole. The  $Y_{\lambda\mu}(\theta, \phi)$ s are the spherical harmonics where, the  $(\theta, \phi)$  are measured with respect to the three axes of the spherical coordinate system. The  $\lambda = 0$  term in the expression can be ignored assuming the nucleus to be incompressible *i.e.*, its volume is conserved. Similarly, the  $\lambda = 1$  (dipole) term can also be discarded by assuming the translational symmetry of the nucleus. The  $\lambda = 2, 3, 4$  terms correspond to the quadrupole, octupole and hexadecapole deformations, respectively as shown in Fig. 2.2. The quadrupole term ( $\lambda = 2$ ) describes nuclear shapes of two kinds. One is oblate (which has two semi major axes equal) and the other is prolate (which has two semi minor axes equal) ellipsoid.

The quadrupole ( $\lambda = 2$ ) term involves five  $\alpha_{2\mu}$  coefficients, among them three are simply Euler angles describing the orientation of the nuclei in space. The  $\alpha_{2\mu}$ s are chosen such a way that it

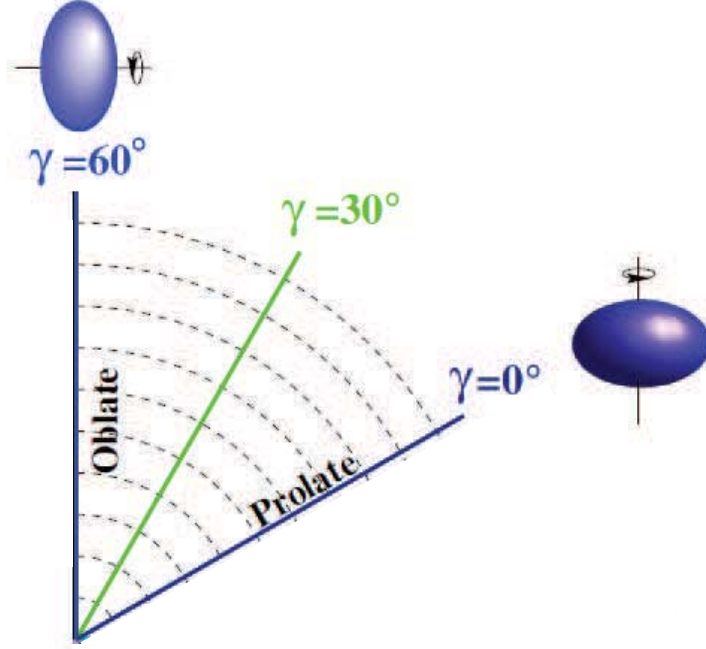


Figure 2.3: Various collective nuclear shapes described in the  $\beta - \gamma$  plane. (Lund convention). The  $\gamma$  value for the prolate and oblate shapes are also indicated in the figure. This figure is taken from Ref. [14].

satisfy  $\alpha_{21} = \alpha_{2-1} = 0$  and  $\alpha_{22} = \alpha_{2-2}$ . Now, two new shape parameters, called the Hill-Wheeler coordinates [13],  $\beta$  and  $\gamma$ , are introduced to simplify these formulation. The remaining  $\alpha_{20}$  and  $\alpha_{22}$  coefficients are converted to polar coordinates as,

$$\alpha_{20} = \beta_2 \cos\gamma \quad (2.11)$$

$$\alpha_{22} = \frac{1}{\sqrt{2}}\beta_2 \sin\gamma \quad (2.12)$$

Using these paramaterization, Eq. 2.10 can be written upto the quadrupole deformation as,

$$R(\theta, \phi) = R_0 \left[ 1 + \beta_2 \sqrt{\frac{5}{16\pi}} \left( \cos\gamma(3\cos^2\theta - 1) + \sqrt{3}\sin\gamma \sin^2\theta \cos 2\phi \right) \right] \quad (2.13)$$

The parameter,  $\beta_2$ , is called the quadrupole deformation parameter, whereas,  $\gamma$  is called the triaxiality parameter.  $\gamma$  represents the deviation from the axial symmetric shape of the nucleus. The different nuclear shapes depending on the different values of  $\beta_2$  and  $\gamma$  are shown in Fig. 2.3. According to the Lund convention, the axially deformed nuclei can be categorized in three categories. One is prolate shape for which  $\gamma$  values are  $\gamma=0^\circ, 120^\circ, 240^\circ$ , and the second one is oblate shape which has  $\gamma=60^\circ, 180^\circ, 300^\circ$ . Nuclei having  $\gamma$  values other than these are called the triaxially deformed nuclei, in which three major axes are not equal. In general, the  $\gamma=30^\circ$  value is recognized as maximum triaxially deformed one. Various shapes, as described using the Lund convention, is illustrated in Fig 2.3.

## 2.4 Deformed Shell Model: Nilsson Model

In order to describe the experimentally observed levels in a deformed nucleus, introduction of the deformed potential is needed where, the core is considered to be deformed and the valence nucleons are moving in that deformed potential. This kind of deformity in the nuclear potential can be explained considering the harmonic oscillator with anisotropy in it [15, 16, 17, 18]. The anisotropic harmonic oscillator potential can be written as,

$$V(r) = \frac{1}{2}m (\omega_x^2 x^2 + \omega_y^2 y^2 + \omega_z^2 z^2) \quad (2.14)$$

where,  $\omega_x$ ,  $\omega_y$ , and  $\omega_z$  are the three frequencies of the oscillators along the three mutually perpendicular axes. For nuclei, which are axially symmetric about the  $z$ -axis, it is simplified as  $\omega_x = \omega_y = \omega_\perp$  and these are expressed in terms of the deformation parameter  $\delta$  (or  $\epsilon_2$ ) as

$$\begin{aligned} \omega_\perp &= \omega_0(\delta) \sqrt{1 + \frac{2}{3}\delta} \\ \omega_z &= \omega_0(\delta) \sqrt{1 - \frac{4}{3}\delta}, \end{aligned} \quad (2.15)$$

Now, as the volume of the nucleus is conserved, we get,

$$\omega_0(\delta) = \tilde{\omega}_0 \left( 1 + \frac{2}{3}\delta^2 \right). \quad (2.16)$$

where,  $\tilde{\omega}_0$  can be obtained from,

$$\omega_x \omega_y \omega_z = \text{constant} = \tilde{\omega}_0^3. \quad (2.17)$$

The deformation parameter  $\delta$ , as defined in this equation, is directly related to the deformation term,  $\beta$ , which is defined in the collective model of the nuclear shape by,

$$\delta \approx \frac{3}{2} \sqrt{\frac{5}{4\pi}} \beta \approx 0.95\beta. \quad (2.18)$$

The Nilsson model Hamiltonian can be written as,

$$H = -\frac{\hbar^2}{2m} \nabla^2 + \frac{1}{2} m \omega_0^2 r^2 - \beta_0 m \omega_0^2 r^2 Y_{20}(\theta, \phi) - \kappa \hbar \tilde{\omega}_0 2\hat{\ell} \cdot \hat{s} + \mu \left( \hat{\ell}^2 - \langle \hat{\ell}^2 \rangle_N \right) \quad (2.19)$$

where,  $\kappa$  and  $\mu$  determine the strength of the spin-orbit and  $\ell^2$  interaction terms, respectively. The value of  $\kappa$  and  $\mu$  are different for different nuclear shell [24] because they have different interactions. The Nilsson levels are labeled by their asymptotic quantum numbers  $\Omega^\pi [N n_z \Lambda]$ , where,  $\Omega$  ( $= \Lambda + \Sigma$ ),  $N$  is the principle quantum number and  $n_z$  is the projection of  $N$  on the symmetry axis ( $n_z = 0, 1, 2, \dots, N$ ).  $\Lambda$ ,  $\Sigma$  and  $\Omega$  are the projections of the orbital ( $\ell$ ), the spin ( $s$ ) and the total angular momentum ( $j$ ) of the odd nucleon on the symmetry axis of the nucleus, respectively. In the Nilsson model, the  $\ell$  and  $j$  are no longer remain a good quantum number, rather the quantum numbers  $N$ ,  $\pi$  and  $\Omega$  becomes the good quantum numbers. Also asymptotically  $n_z$  and  $\Lambda$  become good quantum numbers. Thus  $\Omega^\pi [N n_z \Lambda]$  can label the Nilsson model states, uniquely. The energy levels (in unit of  $\hbar\omega_0$ ), calculated using the Eq. 2.19 as a function of the deformation parameter  $\epsilon_2$ , are shown separately for the neutron ( $50 \leq N \leq 82$ ) and for the proton ( $50 \leq N \leq 82$ ) in Fig. 2.4 and 2.5, respectively. From the definition, for  $\epsilon_2 > 0$ , the nucleus is said to be of prolate shape and for  $\epsilon_2 < 0$ , it is of oblate shape. In presence of the deformation, each spherical level splits into  $(2j+1)$  doubly degenerate states, according to the  $\pm\Omega$  degeneracy. The Nilsson model can successfully describe the deformed shape of the nuclei.



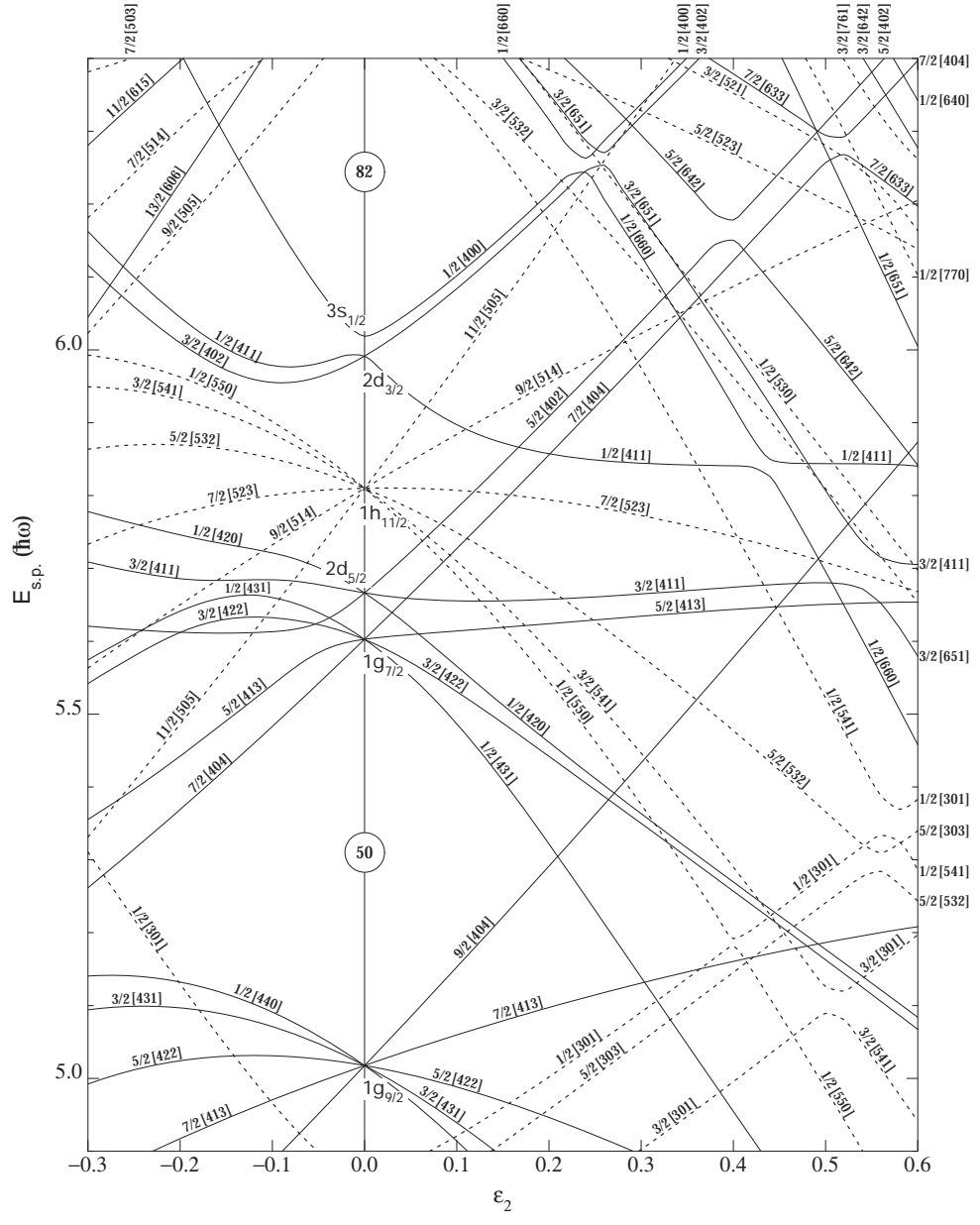


Figure 2.5: Nilsson diagram of single particle levels, calculated from equation 2.19 for protons ( $50 \leq Z \leq 82$ ) as a function of deformation. The solid lines correspond to positive parity orbitals and the dashed lines correspond to negative parity orbitals. Figure is taken from Ref. [19].

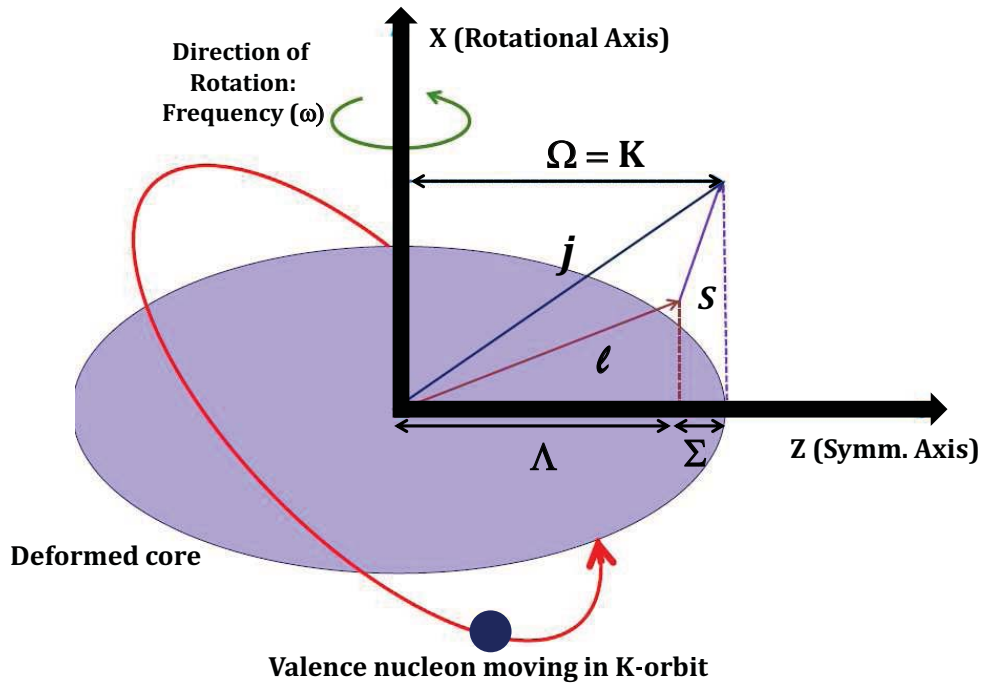


Figure 2.6: The nucleon has orbital angular momentum  $l$  and spin angular momentum  $s$ . The total angular momentum is  $j$  so that  $j = l + s$ . The projection of the orbital angular momentum ( $l$ ) and spin angular momentum ( $s$ ) on the symmetry axis is represented by  $\Lambda$  and  $\Sigma$  respectively. Projection of a single valance particle total angular momenta  $j$  on the symmetry axis of a deformed nucleus is represented by  $\Omega = \Lambda + \Sigma$ .

## 2.5 Cranking Model

For a rotating nuclei, the cranking model is used to describe the motion of the single particle. This model deals with the effect of the rotating nucleus on the single particle behaviour. The cranking model first formulated by Inglis [20, 21] and further developed by Bengtsson and Frauendorf [22]. In this model, the rotation of the nucleus is described in terms of a body fixed frame, which is assumed to rotate with constant angular velocity ( $\omega$ ) with respect to the laboratory fixed frame. The rotation of the nucleus is treated classically and it is assumed that the independent nucleons move in an average rotating potential.

If the intrinsic coordinates in the body fixed frame rotate about an axis perpendicular to the symmetry axis (say,  $x_3$ ) and the other intrinsic axis,  $x_1$ , coincides with the laboratory fixed axis  $x$ , then the total cranking Hamiltonian for  $N$  particle can be written as,

$$H_\omega = H^0 - \omega J_x = \sum_{\nu=1}^N h_\nu^0 - \omega j_{x\nu} \quad (2.20)$$

where,  $H_\omega$  is the total Hamiltonian in the body fixed frame (rotating frame),  $H_0$  is total Hamiltonian in the laboratory fixed frame and  $J_x$  is the projection of the total angular momentum on the rotational axis. The  $h_\nu^\omega = h_\nu^0 - \omega j_{x\nu}$  term is the single particle Hamiltonian in the rotating frame,  $h_\nu^0$  is the single particle Hamiltonian in the laboratory fixed frame and  $j_{x\nu}$  is the projection of the single particle total angular momentum on the rotational axis. The  $-\omega j_{x\nu}$  term consists of the centrifugal force and the Coriolis force, which align the angular momentum of the nucleons along the rotational axis. The eigen-values of  $H_\omega$  are called the Routhians. After solving this Hamiltonian in Eq. 2.20 in terms of eigen-functions  $|\nu^\omega\rangle$ , the energy in the laboratory frame (E) is given as,

$$E = \sum_{\nu=1}^N e_\nu^\omega + \omega \sum_{\nu=1}^N \langle \nu^\omega | j_x | \nu^\omega \rangle \quad (2.21)$$

where,  $e_\nu^\omega$  is the single particle Routhians in the rotating frame. Using this cranking model, one can calculate the projection of the total angular momentum ( $I_x$ ) and the aligned angular momentum ( $i_x$ ) by following the formula,

$$I_x = \sum_{\nu=1}^N \langle \nu^\omega | j_x | \nu^\omega \rangle \quad (2.22)$$

The slope of the Routhian is related to the single particle alignment ( $i_x$ ) as,

$$i_x = -\frac{de_\nu^\omega}{d\omega} \quad (2.23)$$

Due to the presence of the Coriolis term ( $-\omega j_x$ ), the time reversal symmetry in the nucleus gets broken and as a result of that, the Nilsson quantum number ( $\Omega$ ) does not remain a good

quantum number anymore. Only the parity ( $\pi$ ), which describes the reflection symmetry, and the signature quantum number ( $\alpha$ ) [23] remain the good quantum numbers. The symmetry under a  $180^\circ$  rotation of the nucleus about the rotation axis is described by the signature quantum number. So, these two quantum numbers can be utilized to define the nuclear states uniquely. The rotation operator is defined as,

$$\mathcal{R}_x = \exp(-i\pi j_x) \quad (2.24)$$

with the eigen-values,

$$r = \exp(-i\pi\alpha) \quad (2.25)$$

Nucleus, having even number of nucleons, have  $\alpha = 0$  or  $1$ , while for odd number of nucleons,  $\alpha = \pm\frac{1}{2}$ . The signature quantum numbers of the favoured and unfavoured states are given by,

$$\alpha_f = \frac{1}{2}(-1)^{j-1/2} \quad \alpha_{uf} = \frac{1}{2}(-1)^{j+1/2} \quad (2.26)$$

$j$  is the single particle angular momentum of the system. For a system having multi-valence particle, the favoured signature is calculated by,

$$\alpha_f = \frac{1}{2} \sum_i (-1)^{j_i-1/2} \quad (2.27)$$

This model can predict the rotational effect of the nucleus on the single particle energy levels.

## 2.6 Various quantities related to rotational bands

The main characteristic of a deformed system is that, it can rotate about any axis perpendicular to its symmetry axis, which leads to the observation of the rotational bands. The presence of rotational bands are the experimental signatures of the deformation in a nucleus. The energy states of a rotational band ( $E_{rot}(I)$ ) are represented by the following equation,

$$E_{rot}(I) = \frac{\hbar^2}{2\mathcal{J}} I(I+1) \quad (2.28)$$

where,  $I$  is the rotational angular momentum (spin) of the state and  $\mathcal{J}$  is the rigid moment of inertia. The above expression is similar to the energy of a classical symmetric top. The rotational energies for the first few states can be obtained as  $E_{2+} = 6\hbar^2/2\mathcal{J}$ ,  $E_{4+} = 20\hbar^2/2\mathcal{J}$ ,  $E_{6+} = 42\hbar^2/2\mathcal{J}$ , which give  $E_{4+}/E_{2+} = 1.33$ . This ratio is one of the best signature for the rotation and deformation [25]. This expression also helps to determine the rigid moment of inertia of a deformed nucleus. The level scheme of a deformed nucleus usually has several rotational bands, based on different microscopic configurations.

The rigid moment of inertia needs not to be necessarily constant for a single rotational band. If a band has a higher  $\mathcal{J}$  at higher energy, the energy levels of that band at higher energy, become yrast. Eventually, at higher spin, states of that excited band become yrast rather than the states of the ground state band. This phenomenon is called band-crossing. Such crossing of bands occurs when a pair of valence nucleon aligns to the direction of the rotation and thus increases the moment of inertia. The change in the moment of inertia in a single band directly indicates a change in the intrinsic structure.

The aligned angular momentum ( $i_x$ ) of a rotational band is defined as the single particle angular momentum contribution to the total angular momentum ( $I_x$ ). This  $i_x$  can be determined using the equation,

$$i_x = I_x(I) - I_x^{ref}(I). \quad (2.29)$$

where,

$$I_x^{ref}(I) = \mathfrak{S}_0\omega + \omega^3\mathfrak{S}_1 \quad (2.30)$$

is the angular momentum of the core and is calculated in terms of the Harris parameters [26].  $\mathfrak{S}_0$  and  $\mathfrak{S}_1$  are the Harris parameters. These Harris parameters, can be determined from the  $I_x$  vs  $\omega$  plot for the even-even core.

Determination of the rotational frequency, moments of inertia (both kinematic and dynamic), aligned angular momentum *etc.* are very essential part to characterize a rotational band of a nucleus. The rotational frequency ( $\hbar\omega$ ), for an axially symmetric deformed nucleus, which

rotates about an axis ( $x$ ) perpendicular to the symmetry axis is given by [27],

$$\hbar\omega(I) = \frac{dE(I)}{dI_x} \approx \frac{E(I+1) - E(I-1)}{I_x(I+1) - I_x(I-1)}, \quad (2.31)$$

where,  $I_x$  is the projection of the total angular momentum on the rotation axis and is given by,

$$I_x(I) = \sqrt{I(I+1) - K^2} \approx \sqrt{\left(I + \frac{1}{2}\right)^2 - K^2}. \quad (2.32)$$

with,  $K$  is the projection of the total angular momentum on the symmetry axis, called the band head.

The Kinematic moment of inertia of a rotational band of a rotating nucleus is defined as,

$$J^{(1)} = \frac{\hbar I_x(I)}{\omega(I)}. \quad (2.33)$$

and the Dynamic moment of inertia is defined as,

$$J^{(2)} = \frac{\hbar dI_x(I)}{d\omega(I)}, \quad (2.34)$$

This dynamic moment of inertia,  $J^{(2)}$ , is independent of spin,  $I$ .

## 2.7 Shell Model Calculations

In the present thesis work, the excited states of a near spherical nucleus (*i.e.* nucleus near the shell closure) are characterized using the theoretical framework of the large scale Shell Model (SM) calculations. Shell model calculations, for nuclei having large number of valence nucleons, are carried out numerically using the well known SM calculation codes. With the recent advancement in computational power, it is now feasible to carry out such SM calculations for nuclei having few valence nucleons outside the magic core around  $^{132}Sn$ . The aim of such computationally intense calculations is to obtain a detailed understanding of the intrinsic configurations of the observed levels of the concerned nucleus. There are number of SM codes available, such as, OXBASH [28], NuShellX [29], Antoine [30, 31] to carry out such extensive calculations. Using these codes, it is possible to obtain the complete basis states to solve the

eigen-value equation,  $H|\Phi\rangle = E|\Phi\rangle$  by the matrix diagonalization method. The eigen-value solutions of this equation give the required energy states and the resultant eigen-vectors can be used to obtain other nuclear observables, such as, transition strengths, spectroscopic factors *etc.*

Ideally, in order to obtain the exact energy eigen-values and eigen-vectors, the Schrödinger equation must be solved using the exact nuclear potential assuming all the nucleons as free. However, in reality, such calculations are computationally extensive and almost impossible. Practically, these eigen-value equations are solved assuming an effective Hamiltonian  $\mathcal{H}$ , instead of the proper Hamiltonian  $H$  and a truncated model space  $|\phi\rangle$ , which is a subset of the complete Hilbert space  $|\Phi\rangle$ . It is considered such a way that they satisfy the  $\mathcal{H}|\phi\rangle = E|\phi\rangle$  eigen-value equation. Hence, all the practical SM calculations utilize the effective Hamiltonian procedure. This effective Hamiltonian, which deals with the effective interactions, can be obtained from the available experimental data and such interaction is called the empirical interaction. Usually, such data are obtained from the binding energies and nucleon separation energies. The schematic interactions are obtained from the least square fitting of the experimental information where, a large number of nucleons are involved. In the mass 130 region, empirical interactions are hard to get.

In the present thesis, the SM calculations have been carried out using the codes NuShellX [29] and OXBASH [28]. The main advantage of NuShellX over OXBASH is that the former can diagonalize about 100 times more dimensional matrix. NuShellX is written in J-scheme formalism, whereas OXBASH is in M-scheme. The basic procedure of these two codes are as follows: (i) first identify the inert core of the nucleus, (ii) then the available valence orbitals are identified, which will construct the model space, (iii) the two body matrix elements (TBME, deduced from the effective interactions) involving the valence orbitals are then identified. The model spaces and the interaction (matrix elements) are usually provided by the program. Available different model spaces include different orbitals and one particular model space may also have different interactions. Finally the code is run with the inputs and the code diagonalizes the matrix to obtain its eigen-values. The code gives the eigen-energies with the percentage contributions of the configurations to the wave-functions of the eigen-states as its output.

## 2.8 Particle Rotor Model (PRM) calculations

In this thesis, Particle Rotor Model (PRM) Calculations are carried out using the PRM code [32]. The Particle Rotor Model [32] is widely used to describe the structure of odd-A deformed nuclei. This model is built on the assumption that the core of the nucleus is axially deformed and the unpaired valence quasi-particle (qp) is coupled with this core via the Coriolis interaction. In this particle rotor model, the total Hamiltonian of the nucleus is taken as,

$$H = H_p + H_{rot} \quad (2.35)$$

where,  $H_p$  is the single particle Hamiltonian and  $H_{rot}$  is the Hamiltonian arising due to the rotation. This  $H_{rot}$  can be expressed as,

$$H_{rot} = \frac{\hbar^2}{2\mathcal{J}}(I - j)^2 = \frac{\hbar^2}{2\mathcal{J}}[I^2 + j^2 - 2I_3j_3 - (I_+j_- + I_-j_+)] \quad (2.36)$$

where, the components of  $I$  and  $j$  are written in the body fixed frame and the last term of this expression is the Coriolis term. Here, the 3<sup>rd</sup> axis is taken as the symmetry axis and  $\mathcal{J}$  is the moment of inertia (MoI). Now, Eq. 2.35 can be rewritten as,

$$H = H_0 + H_{cor} \quad (2.37)$$

where,

$$H_0 = H_p + \frac{\hbar^2}{2\mathcal{J}}[I^2 + j^2 - 2I_3j_3] \quad (2.38)$$

and,

$$H_{cor} = -\frac{\hbar^2}{2\mathcal{J}}[I_+j_- + I_-j_+] \quad (2.39)$$

This formalism can be carried out using both constant MoI and variable MoI [33, 34]. In this calculation, the shell model parameters,  $\mu$  and  $\kappa$ , are adjusted to match the single particle energies of the orbitals with no deformation [35]. This program also takes the pairing gap ( $\Delta$ ), Fermi level ( $\lambda$ ) and the MoI parameter as its input. These input parameters are determined from the available data for the nearby isotopes. Finally, the Coriolis mixing parameter and the deformation need to be tuned to get the best fitted match for the observed levels. These mixing parameter and deformation give the measure of the interaction of the valence nucleon with the core and the deformation of the core, respectively.

## 2.9 Total Routhian Surface (TRS) calculations

In the present thesis, the Total Routhian Surface (TRS) calculations have been carried out to describe the structure of nucleus and subsequently to obtain the deformation of the nucleus, as described by Nazarewicz *et.al.* [36, 37]. The total Routhian  $E^\omega(Z, N; \beta, \gamma)$  of a given nucleus as a function of its deformation  $(\beta, \gamma)$  can be calculated from the sum of the (i) liquid-drop energy  $E_{LD}^\omega(Z, N; \beta, \gamma)$ , (ii) the shell correction energy  $E_{shell}^\omega(Z, N; \beta, \gamma)$  and (iii) the pairing correction energy  $E_{pair}^\omega(Z, N; \beta, \gamma)$  within the cranked Woods-Saxon, Bogolyubov, Strutinsky model as:

$$E^\omega(Z, N; \beta, \gamma) = E_{LD}^\omega(Z, N; \beta, \gamma) + E_{shell}^\omega(Z, N; \beta, \gamma) + E_{pair}^\omega(Z, N; \beta, \gamma) \quad (2.40)$$

The liquid drop model energy  $E_{LD}^\omega$  is expressed in terms of the nuclear surface energy  $E_{surf}^\omega$ , Coulomb energy  $E_{Coul}^\omega$  and the nuclear rotational energy  $E_{rot}^\omega$ ,

$$E_{LD}^\omega(Z, N; \beta, \gamma) = E_{surf}^\omega(Z, N; \beta, \gamma) + E_{Coul}^\omega(Z, N; \beta, \gamma) + E_{rot}^\omega(Z, N; \beta, \gamma) \quad (2.41)$$

Again, the nuclear rotational energy can be calculated from,

$$E_{rot}^\omega(Z, N; \beta, \gamma) = \frac{\hbar^2 I(I+1)}{2J_{rig}} \quad (2.42)$$

where,  $J_{rig}$  is the rigid body moment of inertia at a given deformation. The shell correction term in the expression is calculated using the Strutinsky shell corrections procedures within a deformed Woods-Saxon potential. The Hartee-Fock-Bogoliubov code by Nazarewicz *et al.* [36, 37] has been used for the present TRS calculations. Each Routhian Surface has been calculated in the  $(\beta_2, \gamma, \beta_4)$  deformation mesh points obtained from the minimization of the  $\beta_4$ . The minima of the TRS contours involving the available orbitals give the ground state deformation of the given nucleus in terms of the  $\beta$  and  $\gamma$ . The details of the TRS calculation procedure is described in the Refs. [38, 39].

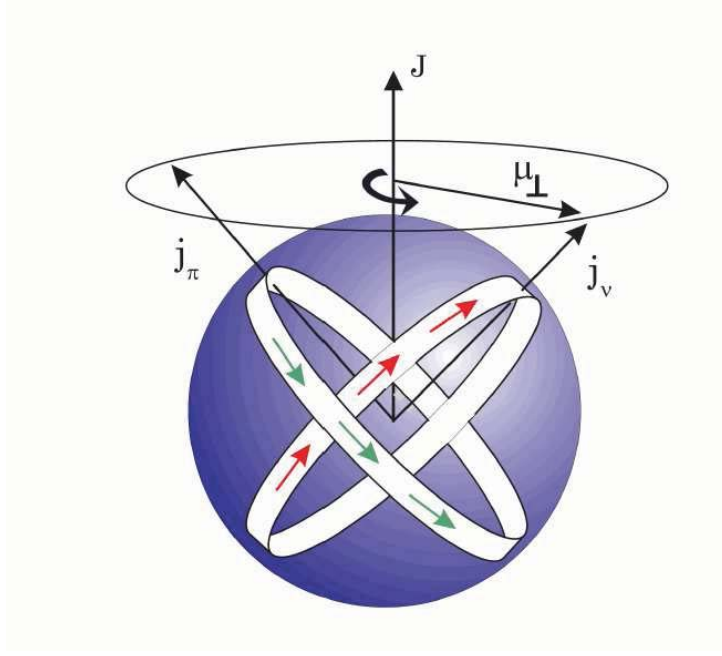


Figure 2.7: Schematic diagram showing the proton and neutron angular momenta vectors.

## 2.10 SPAC calculations and Magnetic Rotational band

Magnetic Rotation (MR) is a well known phenomenon in the weakly deformed systems which generates the high spin (see Fig. 2.7). In such rotation, the angular momentum of the system is generated by the gradual alignment of the high- $j$  particle and hole angular momenta towards the total angular momentum. This kind of closing of the proton and neutron angular momentum can be compared with a closing of a shear and, thus, it is often called a Shears' mechanism.

Magnetic rotational bands can be explained in terms of a semi classical description developed by Clark and Macchiavelli [40]. This description is based on the coupling of the proton angular momentum ( $\vec{j}_\pi$ ) and neutron angular momentum ( $\vec{j}_\nu$ ). The angle (called Shear's angle) between these two angular momenta is thus given by the relation,

$$\begin{aligned}
 \cos\theta &= \frac{\vec{j}_\nu \cdot \vec{j}_\pi}{|\vec{j}_\nu| |\vec{j}_\pi|} \\
 &= \frac{I_{shears}(I_{shears} + 1) - j_\nu(j_\nu + 1) - j_\pi(j_\pi + 1)}{2\sqrt{j_\nu(j_\nu + 1)j_\pi(j_\pi + 1)}}
 \end{aligned} \tag{2.43}$$

where,  $I_{shears}$  is the total angular momentum generated due to the Shear's mechanism.  $I_{shears}$  can be obtained by subtracting the core contribution ( $R_0$ ) from the observed total angular momentum ( $I$ ) as,

$$\vec{I}_{shears} = \vec{I} - \vec{R}_0,$$

According to this semi-classical model, the angular momentum vectors interact in the form of  $V_2 P_2(\cos\theta)$ , where,  $V_2$  determines the interaction strength. Thus, the level energies of a MR band with respect to the band head energy can be written as:

$$V(I(\theta)) = E(I) - E_b = (3/2)V_2 \cos^2\theta \quad (2.44)$$

where,  $E(I)$  is the level energy having spin  $I$  and  $E_b$  is the band head energy. The interaction strength ( $V_2$ ) can be obtained by fitting the experimentally observed energy levels of the Shears' band.

The MR band can also be well described in terms of the Shear's mechanism with the Principal Axis Cranking (SPAC) model. MR bands have been identified in the  $A \sim 100, 140$  and  $200$  mass regions [40] and explained within the framework of the Shear's mechanism [41, 42]. The SPAC model [43, 44, 45, 47, 46] is one of the successful models to explore and explain the intrinsic character of a Shear's sequence. In this model, the proton angular momentum ( $\vec{j}_\pi$ ) and the neutron angular momentum ( $\vec{j}_\nu$ ) couples with the core angular momentum vector ( $\vec{R}$ ) to generate the total angular momentum ( $I$ ). Thus, the total energy  $E(I)$  of an excited level is expressed as,

$$E(I) = \frac{R^2(I, \theta_1, \theta_2)}{2J(I)} + V_2 P_2(\cos(\theta_1 - \theta_2)) + constant \quad (2.45)$$

where, the first and second term represent the collective and Shear's contribution, respectively. And the  $\theta_1$  and  $\theta_2$  are the angles of  $\vec{j}_\pi$  and  $\vec{j}_\nu$  with respect to the rotational axis, respectively. The  $J(I)$  and  $V_2$  represent the core moment of inertia and the total particle-hole interaction energy, respectively. The  $I$ ,  $\theta_1$  and  $\theta_2$  can be found from the energy minimization condition,

$$\frac{\partial^2 E(I, \theta_1, \theta_2)}{\partial \theta_1 \partial \theta_2} = 0. \quad (2.46)$$

In normal aligned configuration [44], the  $\vec{j}_\nu$  is taken as directed along the rotational axis and thus the condition reduces to,

$$\frac{\partial E(I, \theta_1)}{\partial \theta_1} = 0 \quad (2.47)$$

which is then used to obtain  $\theta_1$  for the excited state ( $I$ ).

The contribution of the angular momentum due to the core rotation in the Shear's band can be obtained from the parameter  $\chi = \frac{J(I)}{j_\pi^2/3V_2}$ . Further details of the 'Magnetic Rotation' can be found in the articles [40, 53].

# Bibliography

- [1] G. Gamow Proceedings of the Royal Society of London, **126**:632, (1930).
- [2] C.F.Von Weizsäcker, Z. Phys. **96**, 431 (1936).
- [3] H.A. Bethe, Rev. Mod. Phys. **8**, 82 (1936).
- [4] P. Ring and P. Schuck, The Nuclear Many-Body Problem, Springer-Verlag Berlin Heidelberg (1980).
- [5] M. G. Mayer, Phys. Rev. **75**, 1969 (1949).
- [6] O. Haxel, J.H.D. Jensen and H.E. Suess, Phys. Rev. **75**, 1766 (1949).
- [7] M.G. Mayer and J.H.D. Jensen, Elementary Theory of Nuclear Shell Structure (John Wiley, 1955).
- [8] E. Feenberg, Shell Theory of the Nucleus (Princeton University Press, 1955).
- [9] Thesis of Rajarshi Raut.
- [10] A. Bohr, Mat. Fys. Medd. Dan. Vid. Selsk. **26** No. 14 (1952).
- [11] A. Bohr, Mat. Fys. Medd. Dan. Vid. Selsk. **26** No. 14 (1952).
- [12] Alvise Raccanelli et. al.,arXiv:1306.6646v2 [astro-ph.CO] 14 Aug 2013.
- [13] D. L. Hill and J. A. Wheeler, Phys. Rev. **89**, 1102 (1953).

- [14] P. A. Pipidis's Thesis (Structural behavior of  $^{157,158,159}\text{Dy}$  in the I=30-50l spin regime and the high-spin domain of  $^{158}\text{Er}$  up to and above band termination).
- [15] S. G. Nilsson. Binding States of Individual Nucleons in Strongly Deformed Nuclei. K. Dan Vidensk. Selsk. Mat. Fys. Medd.**29(16)**, (1955). 3.5, 3.7, 3.8
- [16] S. G Nilsson *et al.*, On the Nuclear Structure and Stability of Heavy and Superheavy Elements. Nucl. Phys. **A**, **131**, 1 (1969). 3.5, 4.5.
- [17] B. Nilsson, Inclusion of a P4 Term in the Deformed Shell Model Potential. Nucl. Phys. **A**, **129**, 445(1969) 3.5.
- [18] B. R. Mottelson and S. G. Nilsson. Clasification of the Nucleonic States in Deformed Nuclei. Phys. Rev. **99**, 1615 (1955). 3.5, 3.7, 3.8.
- [19] R. B. Firestone, et al., Table of Isotopes (John Wiley and Sons, Inc., New York (1999)).
- [20] D.R.Inglis, Phys. Rev. **96**, 1059 (1954).
- [21] D.R.Inglis, Phys. Rev. **97**, 701 (1955).
- [22] R. Bengtsson and S. Fraunendorf, Nucl. Phys. **A 327**, 139 (1979).
- [23] A. Bohr and B. R. Mottelson: Nuclear Structure, vol. II (W. A. Benjamin, Inc., New York, 1975)
- [24] T. Bengtsson and I. Ragnarsson, Nucl. Phys. **A 436**, 14 (1985).
- [25] R.F. Casten, Nuclear Structure from Simple Perspectives, Second Edition, Oxford.
- [26] S.M. Harris, Phys. Rev. **138** B509 (1965).
- [27] R. Bengtsson and S. Fraunendorf, Nucl. Phys. **A 327**, 139 (1979).
- [28] Oxbash for Windows, B. A. Brown *et al.*, MSU-NSCL report number 1289 (2004).
- [29] B.A. Brown *et al.*, Nucl. Data Sheets **120**, 115(2014).

- [30] E. Caurier *et al.*, Acta Physica Polonica B, **30**, 705 (1999).
- [31] E. Caurier *et al.*, Rev. of Mod. Phys., **77**, 427 (2005).
- [32] S. Bhattacharya *et al.*, Phys. Rev. C **32**, 1026 (1985).
- [33] H. A. Smith *et al.*, Phys. Rev. C **14**, 1946 (1976).
- [34] P. C. Simms *et al.* Nucl. Phys. A **347**, 205 (1980).
- [35] B. Reehal and R. Sorensen, Phys. Rev. C **2**, 819 (1970).
- [36] W. Nazarewicz *et al.*, Nucl. Phys. **A 512**, 61 (1990).
- [37] W. Nazarewicz *et al.*, Nucl. Phys. **A 435**, 397 (1985).
- [38] G. Mukherjee *et al.*, Phys. Rev. **C 64** (2001) 034316.
- [39] G. Mukherjee *et al.*, Nucl. Phys. **A 829**, 137 (2009).
- [40] R.M. Clark and A.O. Macchiavelli, Ann. Rev. Nucl. Part. Sci. **50** , 1 (2000).
- [41] A.O. Macchiavelli *et al.*, Phys. Rev. **C 58** R621 (1998).
- [42] A.O. Macchiavelli *et al.*, Phys. Rev. C **57**, R1073 (1998).
- [43] Amita, A. K. Jain, and B. Singh, At. Data and Nucl. Data Tables **74**, 283 (2000).
- [44] S. Frauendorf, Rev. Mod. Phy. **73**, 463 (2001).
- [45] R.M. Clark, A.O. Macchiavelli, Annu. Rev. Nucl. Part. Sci.**50**, 1 (2000).
- [46] A.A. Pasternak *et al.*, Eur. Phys. J. **A 23**, 191 (2005).
- [47] E.O. Podsvirova *et al.*, Eur. Phys. J. **A 21**, 1 (2004).
- [48] A.A.Pasternak *et al.*, Eur. Phys. J. **A 37**, 279 (2008).
- [49] S. Rajbanshi *et al.*, Phys. Rev. C **89**, 014315 (2014).
- [50] S. Rajbanshi *et al.*, Phys. Rev. C **90**, 024318 (2014).

- [51] A. A. Pasternak, E. O. Liedera, R. M. Liederb, Acta Phys. Pol. **B 40**, 647 (2009).
- [52] R.M. Clark *et al.* Phys. Rev. Lett. **82**, 3220(1999).
- [53] H. Hübel, Prog. Part. Nucl. Phys. **54**, 1 (2005).

# Chapter 3

## Experimental techniques and data analysis procedures

Nuclear structure studies at various angular momenta and excitation energies are based on the reaction mechanism used for the population of the nuclei at its excited states and the detection system employed. Unique analysis techniques are also used to extract various parameters of the decaying  $\gamma$  rays, such as energy, timing, intensity *etc.* from the experimental data to characterize the observed excited states. This chapter of the thesis focuses on the reaction mechanisms, detection systems and data analysis procedures used for  $\gamma$ -ray spectroscopic studies.

### 3.1 Reaction mechanisms to populate nuclei in excited states

Population of the nuclei in excited states depends on the reaction mechanism by which it is being populated. Various reactions, such as, fusion evaporation, fusion-fission, transfer induced reaction, Coulomb excitation,  $\beta$ -decay *etc.* can be utilized for populating the nuclei at different spin and excitation energy. Among these methods, fusion evaporation reaction, fission reaction and  $\beta$ -decay are used in the present thesis work and discussed in this chapter.

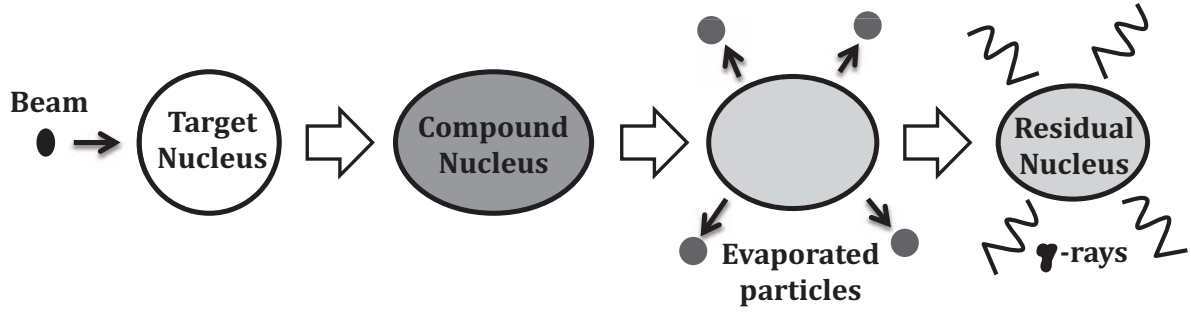


Figure 3.1: Schematic diagram of formation and decay of the compound nucleus in fusion-evaporation reactions.

### 3.1.1 Fusion evaporation reaction

Fusion evaporation reaction is one of the most efficient reaction mechanisms, widely used to populate the nuclei of interest. This method can populate the nuclei at low to high spin with reasonable cross section depending on the projectile used in the reaction. In this method, the projectile (or beam of particles) with sufficient energy to overcome the Coulomb barrier, fuses with the fixed target to form the Compound Nucleus (CN). This fast rotating CN then cools down by emitting statistical  $\gamma$  rays and evaporating particles, such as, alpha, protons and neutrons, depending upon its excitation energy. The schematic diagram of a fusion-evaporation reaction is shown in Fig. 3.1.

After losing substantial energy by the particle and statistical  $\gamma$ -ray emission, the residual nuclei enter the yrast line. The yrast line is a virtual line corresponding to the nuclear states with minimum excitation energy for a given spin. Here the residual nuclei do not possess much energy for particle emission thus, it goes for only  $\gamma$ -ray emission. The residual nuclei go to the ground state by only emitting  $\gamma$  rays along the yrast line. These  $\gamma$  rays are of discrete in nature. Other than the yrast states of the nucleus, fusion evaporation reaction can also populate non-yrast states. Non-yrast states are the states which are having less angular momentum but high

excitation energy. Mainly light ion induced (such as  $\alpha$ ) fusion-evaporation reactions can have direct feeding to the non-yrast states. The nucleus then goes to the ground state via  $\gamma$ -ray decay through many non-yrast states.

### 3.1.2 Nuclear Fission

Nuclear fission is the process by which a heavy nucleus splits into two lighter nuclei. This process is generally accompanied by release of large amount of energy as the fission products have higher values of binding energy per nucleon than that of the parent nucleus. The so called activation energy for fission is the minimum energy required by the nucleus to enable its fragments to just overcome the nuclear binding force. The requirement of the activation energy for the fission process depends on the force exerted by the Coulomb repulsion to overcome the nuclear binding force. Nuclear fission can either take place spontaneously or induced by another reaction. Fusion fission is one example of the induced fission where the target heavy nucleus is bombarded by a projectile and then these two nuclei fuse. The energy of this fused nucleus usually become very large to make this an unstable one. Thus the nucleus breaks into two parts as fission. Other than the fusion fission, transfer induced fission is another kind of nuclear fission. In this process, before fission, transfer of nucleons takes place. Then the fission products undergo particle emission, such as neutron, depending upon its excitation energy. The final products then cool down to its ground state via discrete  $\gamma$ -ray emissions as discussed in the case of fusion evaporation reaction. The nuclear fission mechanism is known to populate the neutron rich nuclei which is not possible in the fusion evaporation reaction.

### 3.1.3 $\beta$ -decay

Low lying states of a nucleus can be populated using  $\beta$ -decay. In this process, the ground state or any excited state of the parent nuclei, with a certain half-life, are populated in a nuclear reaction and then decay to the excited states of the daughter nuclei. These kind of studies are very effective since, these studies can be carried out at an off-beam set up. In these studies,

population of the excited states of the daughter nuclei via  $\beta$ -decay are guided by the spin difference of the excited levels of the parent and daughter and the Q-value of the reaction. Because of the selection rules, usually population of very high spin states is not possible in  $\beta$ -decay studies. However, the low lying non-yrast states can be efficiently populated and studied using this kind of decay study.

## 3.2 Detection of the $\gamma$ -radiation

Detection of the decaying  $\gamma$  rays is an integral part of the  $\gamma$ -ray spectroscopic studies. The information about the structure of nucleus can be understood by measuring the energies, timings, intensities and angular distributions of the decaying  $\gamma$  rays. For the detection of the  $\gamma$  rays in a detector, the  $\gamma$  rays must interact and lose its energy in the detector medium. The  $\gamma$  rays interact with the matter through the following three processes:

### 3.2.1 Photoelectric effect

A  $\gamma$ -ray may interact with a bound atomic electron in such a way that it loses all of its energy. Some of its energy is used to overcome the electron binding energy and the remain part of the energy is transferred to the emitted electron (called photo electron) as kinetic energy. This process of interaction is known as Photoelectric effect. The kinetic energy ( $E_{ke}$ ) of the emitted photo-electron is given by the expression:

$$E_{ke} = E_{\gamma} - E_b \quad (3.1)$$

where,  $E_{\gamma}$  is the incident  $\gamma$ -ray energy and  $E_b$  is the electron binding energy. The Photoelectric effect cross-section is inversely proportional to the incident  $\gamma$ -ray energy as  $\propto \frac{1}{E_{\gamma}^{3.5}}$  and is proportional to the atomic number  $Z$  of the detector material as  $\propto Z^N$ , where the value of  $N$  varies between 4 to 5.

### 3.2.2 Compton scattering

Compton scattering is the process, in which the incident  $\gamma$ -ray photon interacts with an almost free electron and transfers a part of its energy to the electron. From the energy and momentum conservation relations, the energy of the scattered photon ( $E'_\gamma$ ) is given by,

$$E'_\gamma = \frac{E_\gamma}{1 + (1 - \cos \theta)\left(\frac{E_\gamma}{m_0c^2}\right)} \quad (3.2)$$

where,  $\theta$  is the scattering angle of the photon,  $E_\gamma$  is the incident photon energy and  $m_0c^2$  is the rest mass energy of an electron. The kinetic energy of the emitted electron is thus given by,

$$E_{ke} = E_\gamma - E'_\gamma = \frac{E_\gamma^2(1 - \cos \theta)}{m_0c^2 + E_\gamma(1 - \cos \theta)} \quad (3.3)$$

The maximum energy transfer to the electron takes place when the scattering angle ( $\theta$ ) is  $180^\circ$ . That phenomenon is known as back scattering. It can be seen from the Eq. 3.3 that continuum of energy can be transferred to the electron corresponding to various possible  $\theta$  ( $0^\circ$  to  $180^\circ$ ) values. Hence a continuous Compton background can be observed in the energy spectrum, for the Compton scattering processes for different  $\theta$  values. The Compton scattering probability is proportional to the atomic number  $Z$  and inversely to the photon energy  $E_\gamma$  and mass number  $A$  of the detector material.

### 3.2.3 Pair production

The  $\gamma$  rays with energy greater than 1.022 MeV can create an electron-positron pair under the influence of a strong electromagnetic field in the vicinity of a nucleus. This process is called the pair production. In this interaction the  $\gamma$ -ray disappears completely and a pair of electron and positron is created. If the  $\gamma$ -ray energy exceeds 1.022 MeV, then the excess amount of energy is shared between the created electron and positron as their kinetic energies. This positron is annihilated in the detector medium to produce two annihilation  $\gamma$  rays having energy 0.511 MeV each. If the detector can detect both of these  $\gamma$  rays, then the full deposition

of the total energy of the primary  $\gamma$ -ray takes place. When one (or both) of the annihilation  $\gamma$  rays escapes from the detector medium, then it results into a single (or double) escape peak, located at 0.511 MeV (or 1.022 MeV) less than the photopeak energy in the spectrum. The probability of pair production process varies with the square of the atomic number  $Z$  of the detector medium.

Among these three processes, photoelectric effect is the most necessary and preferable one for the  $\gamma$ -ray detection in  $\gamma$ -ray spectroscopic experiments because of the full deposition of energy. Choosing a good detector material for  $\gamma$ -ray spectroscopy is also a very crucial part. This selection of detectors is mainly driven by the experimental measurements criteria, namely, high energy resolution, detection efficiency *etc.*. The new generation state of art detectors are used to detect the  $\gamma$  rays, in this present thesis. Next section discusses the variety of  $\gamma$ -ray detectors in context of the present thesis work.

### 3.3 High-Purity Germanium (HPGe) detectors

High-purity Germanium (HPGe) semiconductor detectors are known for its high energy resolution and moderate detection efficiency. The HPGe detector is made up of highly pure semiconductor material (Germanium) and operated in reverse bias to have maximum depletion region. For a semiconductor, the depletion depth is given by,

$$d = \left( \frac{2\epsilon V}{eN} \right)^{1/2} \quad (3.4)$$

where,  $V$  is the applied reverse bias voltage,  $N$  is the net impurity concentration,  $\epsilon$  is the dielectric constant of the material and  $e$  is the electronic charge. These HPGe detectors have an excellent energy resolution ( $\sim 2$  keV at 1 MeV) compared to the scintillator detectors. The HPGe detectors should be operated at a liquid nitrogen (LN2) temperature ( $\sim 77$  K) to reduce the leakage current. Depending upon the experimental need of better efficiency, HPGe detectors can be used in segmented versions. Current thesis includes the use of three kind of HPGe detectors which are discussed below.

### 3.3.1 Clover detectors

The Clover detector [1] is a composite detector of four coaxial HPGe crystals in a four-leaf clover geometry connected to a single cryostat [2]. It consists of four *n-type* Ge crystals of 50 mm diameter and 70 mm length. Usually radiation measurements require large volume detectors but production of such large volume crystals is very difficult. Thus, Clover detector, consisting of four smaller HPGe crystals, is a possible alternative. Picture of a Clover detector is shown in Fig. 3.2.



Figure 3.2: Picture of a Clover detector used for the experiments in the present thesis.

In a Compton scattering event, a partial energy deposition of the  $\gamma$ -ray takes place in any one of the crystals, and the remaining scattered energy can be absorbed by other neighbouring crystal of a Clover detector. For a Clover detector, it is possible to get back the full energy of the primary  $\gamma$ -ray by just adding the deposited energies in different crystals through Compton

scattering for a particular event. Thus, we can get back the Compton scattered events to the total photo peak area, which increases the total efficiency of the Clover detector. This process is called the addback. The addback factor of the Clover detector is defined as the ratio between the total photopeak counts of a particular energy obtained in addback mode and the total algebraic sum counts of the four crystals for that particular energy. In order to get the proper addback spectra, the data are stored in an event by event mode called LIST mode data and then the addback is carried out offline. This addback factor is close to unity in lower energy since low energy  $\gamma$  rays have less Compton scattering probabilities. Addback factor increases with incident  $\gamma$ -ray energy and achieves a value  $\sim 1.5$  at an energy 1.4 MeV.

### 3.3.2 Low Energy Photon Spectrometer (LEPS)

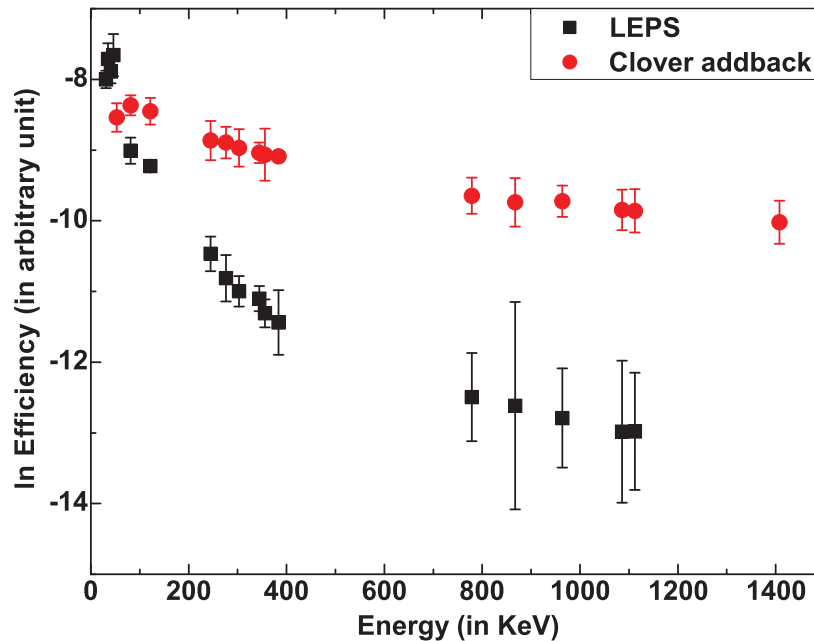


Figure 3.3: Comparison of efficiency of a LEPS detector and a Clover detector in addback mode.

Low Energy Photon Spectrometer (LEPS) are the detectors which has a very good efficiency in low energy regime. These kind of detectors are of planer configuration with a very thin Berilium

window at the entry point. The advantage of having Berilium window over the Aluminum one (used in Clover detectors) is that, it allows the low energy  $\gamma$  transitions to enter the detector medium, without much attenuation. The comparatively higher energy  $\gamma$  rays are simply pass through the detector medium without any interaction with the detector medium due to its planer geometry. These two properties together maximizes the low energy detection efficiency of the LEPS detectors.

The absolute efficiency in addback mode of a Clover detector is compared with that of a LEPS detector in Fig. 3.3. It can be clearly seen from the figure that the LEPS detector has comparatively higher efficiency in low energy and it falls rapidly with increasing energy in comparison with the Clover detectors.

### 3.3.3 BGO detectors as anti-Compton shield

A scintillation material  $Bi_4Ge_3O_{12}$ , also known as BGO, is used as an anti-Compton shield (ACS) in the  $\gamma$  spectroscopic experiments. Due to the high density and large atomic number, BGO is used, as it has better probability of photo-electric absorption. BGO is, therefore, chosen as anti-Compton shield, where the high detection efficiency is necessary, not the resolution. The BGO detector consists of the detector crystal, Photo Multiplier Tube (PMT) and 16 numbers of such detectors are clubbed together in a hollow configuration while used as shield. In the output part of this combinations of BGO detectors, there is only one logic OR signal, which is further used for signal processing.

In the interaction process between the incident  $\gamma$ -ray and the HPGe detector, the  $\gamma$ -ray can either deposit its full energy or it can be Compton scattered. In both the case, we get a signal out from the HPGe detector. Now, in case of Compton scattering, the scattered photon may escape the detector and can interact with the surrounded BGO detector acting as an ACS. And in this case, we get a signal from the ACS also. In the associated electronics, anti-coincidence condition is set (*i.e.*, when there is a signal from the ACS, reject that event) between the detector and ACS. In this process, the contributions coming from the Compton scattering is reduced

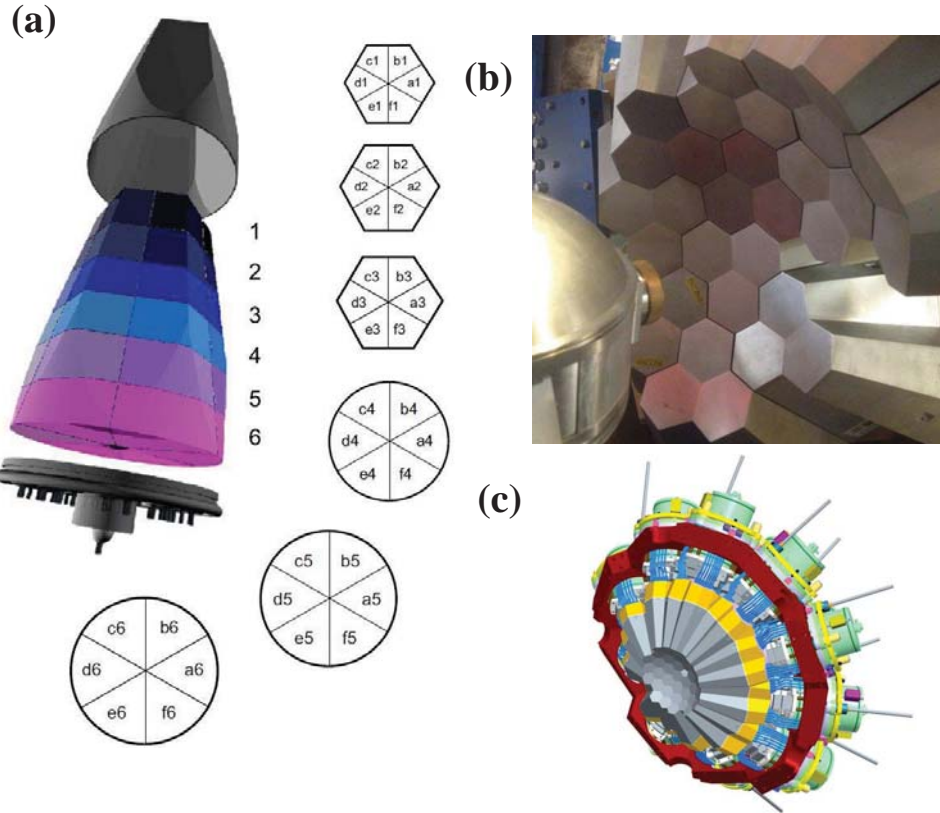


Figure 3.4: (a) Schematic diagram of an AGATA crystal displaying central core contact and its segments. The picture is taken from Ref. [28]. (b) The AGATA clusters are mounted in front of the VAMOS++ spectrometer at GANIL, picture is taken from AGATA website. (c) The AGATA  $1\pi$  array, drawing made by STFC Daresbury.

and, thus, it is called the Compton suppression. Such electronic condition of anti-coincidence reduce the background contribution almost by  $\sim 40\text{-}50\%$  compared to the unsuppressed data.

### 3.3.4 AGATA detectors

The knowledge of the  $\gamma$ -ray interaction point inside a detector medium is extremely necessary in order to reduce its Compton background, Doppler broadening and to increase detection effi-

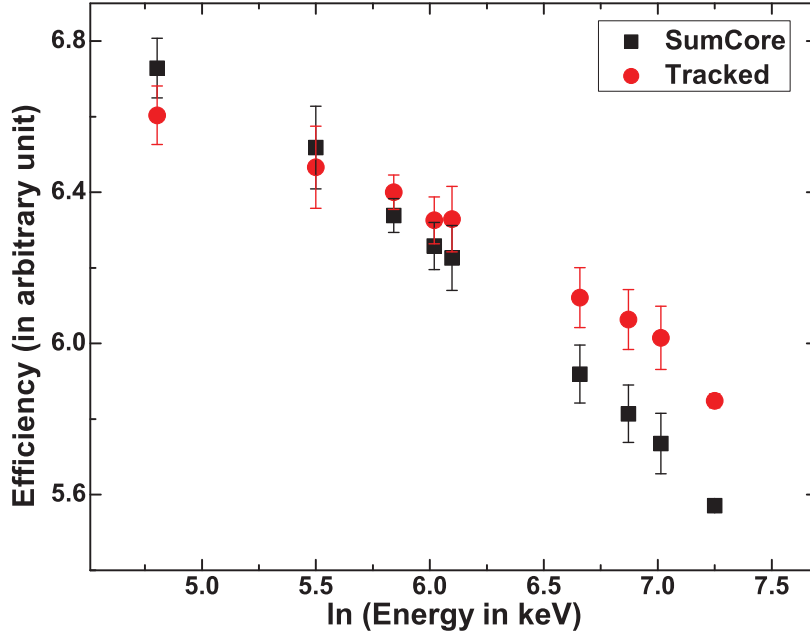


Figure 3.5: Relative efficiency for a AGATA triple cluster obtained from its core signal (Sum Core) and the same obtained after  $\gamma$ -ray tracking.

ciency. The Advanced GAMMA Tracking Array (AGATA) is a new generation granular detector, which employs the  $\gamma$ -ray tracking method to reconstruct the interaction points and hence the energy of the incident  $\gamma$ -ray. This  $\gamma$ -ray tracking procedure requires accurate determination of the interaction point along with its deposited energy and time of deposition. After knowing all the interaction points of an incident  $\gamma$ -ray inside the detector, the path and the total energy of the  $\gamma$ -ray is reconstructed in offline software, by Pulse Shape Analysis techniques. The detail of this tracking algorithm can be found in the Ref [28]. The AGATA detectors are electrically segmented coaxial  $n$  - *type* HPGe crystals. It has a triplet of crystals arranged in an triple cryostat. Each of the triple cluster detector contains 36 fold segmented crystals. This high granularity of a single crystal helps to identify the interaction points inside the detector very precisely. The detailed geometry and other details about AGATA can be found in Ref. [28, 4, 5]. The schematic and real picture of AGATA detector used during the experiment are shown in Fig. 3.4(a) and (b), respectively. Fig. 3.4(c) shows the  $1\pi$  geometry of AGATA array.

Comparison between the relative efficiency obtained from core signal (which is actually the sum of all the segments) with the tracked one is shown in Fig. 3.5. It is found that the efficiency is higher at higher energy when it is tracked. Which supports our claim that we gain in efficiency after  $\gamma$ -ray tracking.

## 3.4 Experimental Setups

Present thesis reports the spectroscopic studies carried out using the VECC Array for Nuclear Spectroscopy (VENUS) array, Indian National Gamma Array (INGA) at Variable Energy Cyclotron Centre, India and using coupled setup of magnetic spectrometer VAMOS++, detector arrays AGATA and EXOGAM at GANIL, France. Following subsections discuss about these experimental set ups.

### 3.4.1 VECC Array for Nuclear Spectroscopy (VENUS)

Light ion (like  $\alpha$ ) induced reactions can populate both yrast and non-yrast states. Such studies of yrast and non-yrast structures of a nucleus have been carried out using the  $\alpha$  beam delivered from the K-130 cyclotron at Variable Energy Cyclotron Centre (VECC), Kolkata using an array of HPGe Clover detectors. VECC array for Nuclear Spectroscopy (VENUS) [6], is a modular array at VECC for such studies. It consists of six Compton suppressed Clover detectors. These detectors are placed in a median plane ( $\phi = 0^\circ$ ) around the target position at a distance of 26 cm from the target. In this set up, two detectors are placed at  $90^\circ$ , two at backward  $30^\circ$  and one each at forward  $45^\circ$  and  $55^\circ$  with respect to the beam direction. This choice of the detector orientation (*i.e* angles) is made, depending upon various experimental needs and to extract various parameters relevant in the  $\gamma$  spectroscopic studies. The pulse processing and the data acquisition of this array is based on the PIXIE-16, 250 MHz, 12-bit digitizer modules from UGC-DAE CSR, Kolkata Centre [7]. Time stamped LIST mode data were acquired under the event trigger condition multiplicity ( $M_\gamma$ ), set either in singles ( $M_\gamma \geq 1$ ) or in coincidence ( $M_\gamma \geq 2$ ) mode.



Figure 3.6: VENUS set up at channel 3 beam line at VECC.

### 3.4.2 Indian National Gamma Array (INGA)

Indian National Gamma Array (INGA) is a national collaborative research facility of an array of Clover HPGe detectors. Indian National Gamma Array (INGA) consisting of seven Compton suppressed Clover detectors has been set up at channel 3 beam line at VECC for various  $\gamma$  spectroscopic studies. Four of those detectors are at  $90^\circ$  (at different  $\phi$  angles), two of them are at  $125^\circ$  and one detector is at  $40^\circ$  with respect to the incident beam direction. More number of detectors are placed in  $90^\circ$  to ensure better statistics in the polarization measurements. Detectors are kept at a distance of 25 cm from the target position. The current support structure is made up to accommodate upto ten detectors. Both analogue and Digital data acquisition system are available for the data recording. But the event by event LIST mode data acquisition used for the experiment relevant to the current thesis is same as used in the case of VENUS set up.

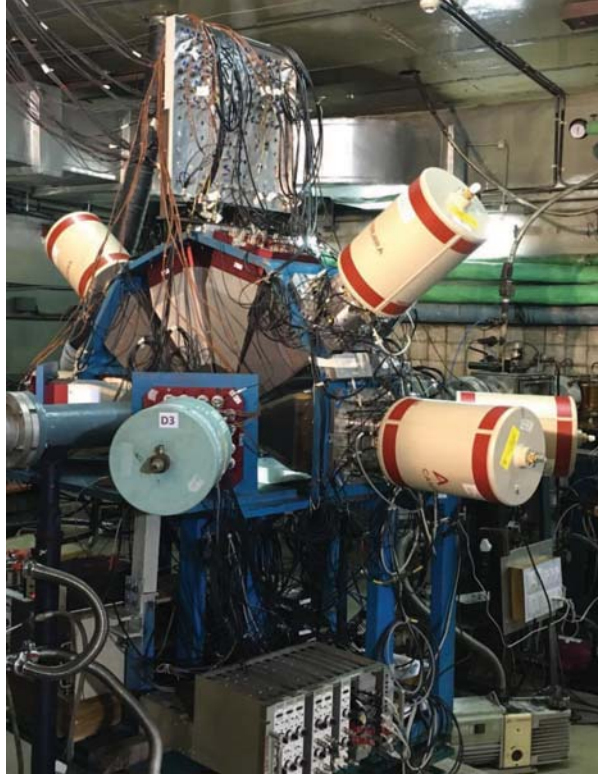


Figure 3.7: INGA set up channel 3 beam line at VECC.

### 3.4.3 Set up consisting of VAMOS++, AGATA and EXOGAM

Fission fragment spectroscopy using magnetic spectrometer VAMOS++ coupled with  $\gamma$ -ray tracking array AGATA and segmented HPGe detector EXOGAM is carried out at GANIL, France. In that experimental set up, fission fragments are isotopically identified using the VAMOS++ spectrometer [8, 9, 10, 11], which is placed at  $20^\circ$  relative to the beam axis. VAMOS++ actually consists of two quadrupole and one dipole magnets. The focal plane detectors of VAMOS++ consist of a Multi-Wire Proportional Counter (MWPC), two Drift Chambers (DC) and one segmented Ionization Chamber (IC). The IC has been operated with  $\text{CF}_4$  gas at 70 mbar. At the target position, a Dual Position-Sensitive MWPC (DPS MWPC) is placed which provides the start signal for the time-of-flight measurements and the recoiling

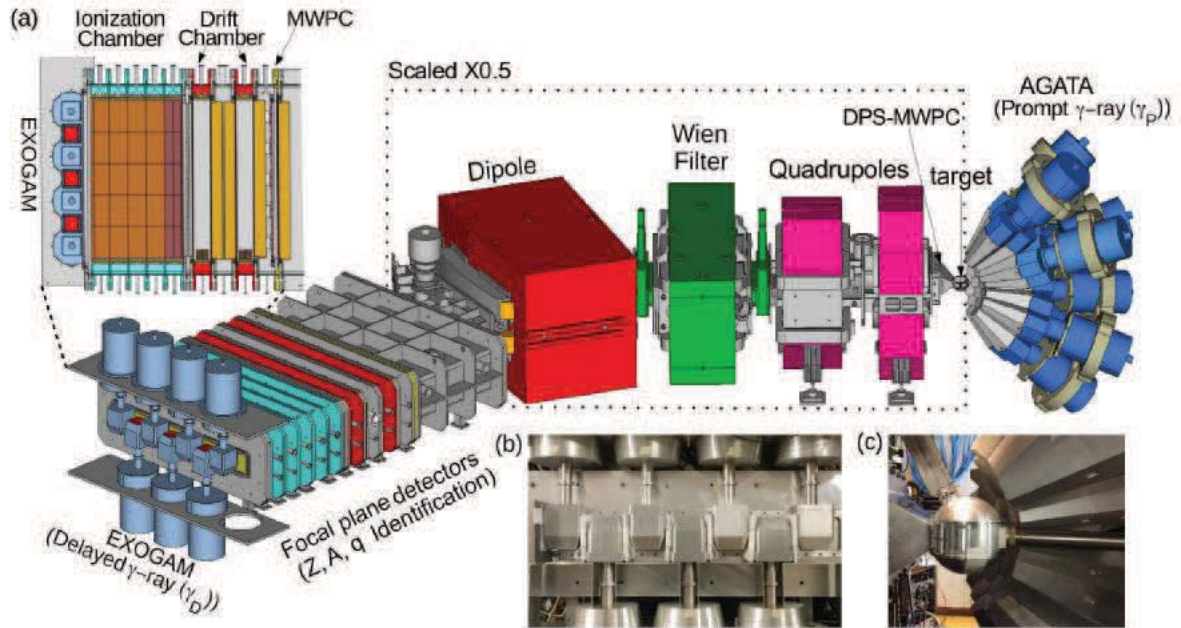


Figure 3.8: Schematic experimental setup of VAMOS++, AGATA and EXOGAM at GANIL. The figure is taken from Ref. [13].

angles of the reaction products. The focal plane MWPC and drift chambers are operated with isobutane gas at 6 mbar pressure.

The AGATA  $\gamma$ -ray tracking array [28] has been used to detect the prompt  $\gamma$  rays ( $\gamma_P$ ) emitted at the target position by the recoiling fission products. In the present set up, 32 of such AGATA crystals are used. The array is translated 10 cm towards the target compared to the nominal configuration of distance 23.5 cm. Seven EXOGAM [29] segmented Clover detectors are employed to detect the delayed  $\gamma$ -rays ( $\gamma_D$ ) at the end of the focal plane. Each crystal of the EXOGAM Clover detector has 4 segments resulting to higher position resolution compare

to that of a standard Clover detector. A 2 mm thick Aluminum window between the ionization chamber and the EXOGAM detectors is used to minimize the attenuation of the delayed  $\gamma$  rays. The prompt trigger of the data acquisition is generated when both AGATA and VAMOS++ events are present within 300 ns. The delayed trigger for detecting the delayed  $\gamma$  rays is generated within 200  $\mu$ s after the prompt trigger. The details of experimental setup can be found in the Ref. [13].

## 3.5 Offline Data Analysis

Offline data sorting and analysis has been carried out using the analysis packages LAMPS [14], RADWARE [15] and IUCPIX [7]. In case of the Clover detectors, the data from each detector are calibrated and gain matched and sorted event by event to form the symmetric two dimensional  $E_\gamma - E_\gamma$  matrix and three dimensional  $E_\gamma - E_\gamma - E_\gamma$  cube. The coincidence relationships between various  $\gamma$  rays and intensities are then used to construct the level structures of the nucleus. The Directional Correlation from Oriented states (DCO) ratio and Polarization asymmetry measurements of the decaying  $\gamma$  rays have been carried out for the spin-parity ( $J^\pi$ ) assignments to the levels. Different steps of the data analysis are discussed here.

### 3.5.1 Calibration

Calibration, *i.e.* converting the channel number to energy, is the first step of the data analysis of any  $\gamma$  spectroscopic study. The channel numbers of the photopeak are approximately proportional to the output voltage pulse of the detector. To determine the calibration parameters, a radioactive source is needed, which emits known  $\gamma$ -ray energies. Then by noting the channel numbers of the known detected  $\gamma$  rays in the spectrum and then fitting it, we can determine the calibration parameters. Once these parameters are known, the energy of any unknown  $\gamma$ -ray can easily be determined from the channel number of that unknown photopeak. Usually, these energies are fitted with a quadratic equation given by,  $E = P_2x^2 + P_1x + P_0$ , where, E implies the energy corresponding to the channel ( $x$ ) and  $P_i$  ( $i = 0 - 2$ ) are the calibration parameters.

### 3.5.2 Efficiency determination

In  $\gamma$ -ray spectroscopy, determination of the efficiency of individual detectors as well as, of the array is needed for determining the relative intensities of various detected  $\gamma$  rays. Efficiency of a detector determines how good a detector is to detect the particles falling on it *i.e.*, output/input. Efficiency of a detector is defined as following:

$$\text{Efficiency} = \frac{\text{No. of particles detected by the detector}}{\text{No. of particles emitted by the source}} \quad (3.5)$$

To obtain the relative efficiency of the detectors, we have used the standard  $^{152}\text{Eu}$  and  $^{133}\text{Ba}$  radioactive sources in the experiments. Relative efficiency of each of the Clover detectors have been extracted in the addback mode. The experimental data points of efficiency as a function of energy are fitted with the following equation,

$$\ln(\epsilon) = \{(A + Bx + Cx^2)^{-G} + (D + Ey + Fy^2)^{-G}\}^{1/-G}, \quad (3.6)$$

where,  $\epsilon$  is the efficiency,  $x = \ln(\frac{E_\gamma}{100})$ ,  $y = \ln(\frac{E_\gamma}{1000})$  and the  $\gamma$ -ray energy  $E_\gamma$ , is in keV.

### 3.5.3 $E_\gamma$ - $E_\gamma$ coincidence analysis

In  $\gamma$ -ray spectroscopic analysis, it is often necessary to identify the cascade of  $\gamma$  rays. This cascade identification can be carried out by coincidence analysis, creating two or higher dimensional histograms. These two (three) dimensional histograms are normally called matrix (cube). One  $E_\gamma$ - $E_\gamma$  matrix consists addback data from all the employed Clover detectors symmetrically in its two axes. Higher order histograms are the same but with higher number of axes. This matrix is then used for setting gates *i.e.*, specifying energies in one of the axis and then projecting the other one. This process helps to identify the  $\gamma$  rays which are in coincidence with each other.

It is also necessary to correct the data for background contributions, which is underlying the peaks in the gated spectrum. These background of a photopeak arises from Compton scattered  $\gamma$ -ray events. There are two methods of eliminating the background, which are used in the

present thesis. For gating from LAMPS software, we have selected the peak channels from the gated axis and then we have subtracted the contribution of the background events by subtracting the gated projection of the nearest backgrounds having same number of channels. In RADWARE compatible  $E_{\gamma}$ - $E_{\gamma}$  matrix format, background for a particular peak is subtracted by eliminating a common background from the 2D matrix having all possible correlations.

### 3.5.4 Angular Correlations

In general,  $\gamma$  rays are emitted isotropically in space because of the random initial orientation of the spin of the decaying nuclei. But, in an in-beam population, the spacial distribution of intensity of a decaying  $\gamma$ -ray becomes non-isotropic. Analogy of such non-uniformity of intensity distribution can also be achieved for a  $\gamma$ -ray cascade in off-beam measurements by fixing the spin orientation of the first  $\gamma$ -ray in one direction by gating on it. Now, by choosing the direction of the first  $\gamma$ -ray, the angular correlation function of the second  $\gamma$ -ray can be expressed as,

$$W(\theta) = A_{00}(1 + a_{22}P_{22}(\cos\theta) + a_{44}P_{44}(\cos\theta)) \quad (3.7)$$

where,  $\theta$  is the angle between the  $\gamma$  rays in cascade.  $P_{kk}(k = 0, 2, 4)$ 's are the Legendre Polynomial functions of  $k^{th}$  order and  $a_{kk}$  ( $=A_{kk}/A_{00}$ )s are called the angular correlation coefficients. Here,  $A_{00}$  is a normalization parameter. Again the values of the  $a_{kk}$  coefficients depend on the spins of the initial, intermediate and final states and also on the multipolarities of the transitions. Mathematically, this  $a_{kk}$  coefficients can be written as,

$$a_{kk}(j_i\lambda_1j\lambda_1j_f) = \frac{1}{1 + \delta^2}[F_{kk}(j_i\lambda_1\lambda_1j) + 2\delta F_{kk}(j_i\lambda_1\lambda'_1j) + \delta^2 F_{kk}(j_i\lambda'_1\lambda'_1j)]F_{kk}(j_f\lambda_2j) \quad (3.8)$$

with the assumption that the first transition is pure (*i.e.* pure quadrupole or dipole) but, the second one is of mixed multipole type. In this equation,  $j_i$ ,  $j$  and  $j_f$  are the spins of the initial, intermediate and final states, respectively.  $\lambda_i$  ( $i = 1, 2$ ) are the multipolarities and  $\delta$  is the mixing ratio of the second  $\gamma$ -ray [16]. Depending upon the multipolarity of the gating transition, these  $a_{kk}$  coefficients take some specific values, which can be calculated using Eq. 3.8, by putting the

relevant  $F_{kk}$  coefficients [16]. The values of this  $a_{kk}$  coefficients can also be extracted from the experimental data by fitting the intensities of the  $\gamma$ -ray (after gating) at various angles with Eq. 3.7. Then by comparing the experimental  $a_{kk}$  values with the corresponding theoretical ones, the mixing ratio ( $\delta$ ) of the transition can be extracted. In order to compare these two experimental and theoretically calculated values, usually the  $a_{22}$  vs  $a_{44}$  is plotted with varying  $\delta$ , for different possible spin sequences. Then the experimental  $a_{kk}$  values are compared to get the mixing ratio.

### 3.5.5 DCO measurements

Multipolarities of the  $\gamma$ -ray transitions have been determined from the procedure called Directional Correlation from the Oriented states (DCO) ratio, following the prescriptions of Krämer-Flecken *et al.* [17]. For the DCO ratio analysis, one asymmetric angle dependent matrix have been made having energy of the  $\gamma$  rays from the detectors at  $\theta_1$  in one axis, and the  $\gamma$  rays from the detectors at  $\theta_2$  on the other axis. The DCO ratio of a  $\gamma$ -ray ( $\gamma_1$ ) gated by the  $\gamma$ -ray of known multipolarity ( $\gamma_2$ ) is given by the ratio of intensities ( $I_{\gamma_1}$ ) of  $\gamma_1$  at two different angles  $\theta_1$  and  $\theta_2$  following the equation,

$$R_{DCO} = \frac{I_{\gamma_1} \text{ at } \theta_1, \text{ gated by } \gamma_2 \text{ at } \theta_2}{I_{\gamma_1} \text{ at } \theta_2 \text{ gated by } \gamma_2 \text{ at } \theta_1} \quad (3.9)$$

By putting gates on the transitions of known multipolarity along the two axes of the above matrix, the DCO ratios ( $R_{DCO}$ ) are obtained for the other unknown  $\gamma$ -ray. For stretched transitions, the value of  $R_{DCO}$  would be  $\sim 1$  for the same multipolarities of  $\gamma_1$  and  $\gamma_2$ . But when gated by known quadrupole (dipole) ( $\gamma_2$ ) transition, then the  $R_{DCO}$  value comes out to be  $\sim 0.5$  (2.0) for dipole (quadrupole) transition.

### 3.5.6 Polarization measurements

The close packed geometry of the Clover detectors can be utilized to measure the Polarization Directional Correlation (PDCO) asymmetry parameter, as described in [18, 19]. The PDCO

measurement gives the idea about the electromagnetic nature of the transitions (E/M). The PDCO asymmetry parameters can be obtained using the relation,

$$\Delta_{PDCO} = \frac{a(E_\gamma)N_\perp - N_\parallel}{a(E_\gamma)N_\perp + N_\parallel}, \quad (3.10)$$

where,  $N_\parallel$  and  $N_\perp$  are the counts of the Compton scattered  $\gamma$  rays in the planes parallel and perpendicular to the reaction plane, respectively. Here,  $a(E_\gamma) = \frac{N_\parallel}{N_\perp}$  is the geometrical asymmetry correction factor of the detector array. Ideally, this value should be close to unity. A positive value of  $\Delta_{PDCO}$  indicates an electric transition, whereas a negative value indicates a magnetic transition. To extract the  $\Delta_{PDCO}$  value two asymmetric matrices are made, containing parallel scattering events and perpendicular scattering events of the  $90^\circ$  detectors in one axis and the other axis contains the data from other detectors.

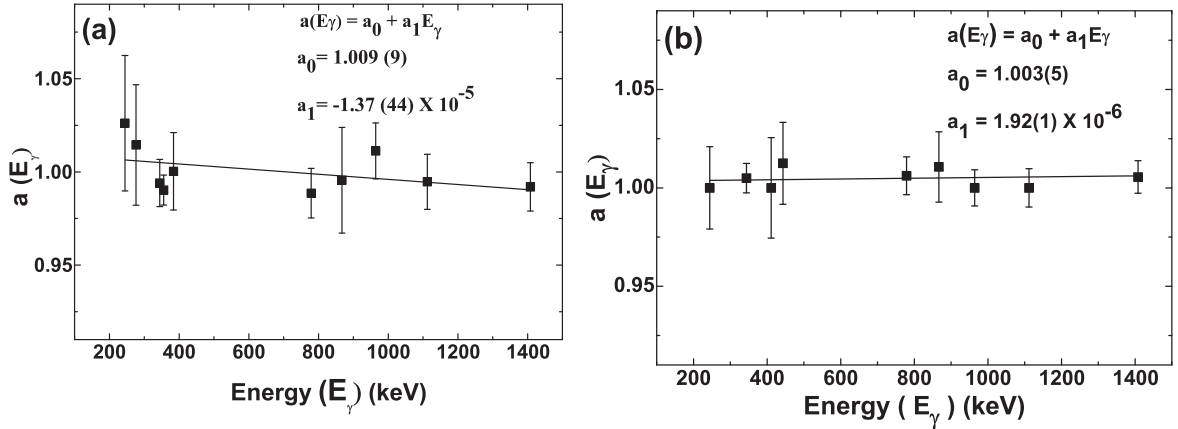


Figure 3.9: Variation of the asymmetry parameter  $a(E_\gamma)$  as a function of incident  $\gamma$ -ray energy ( $E_\gamma$ ), as obtained for (a) VENUS and (b) INGA set up using standard unpolarized radioactive sources. The linear fitting of  $a(E_\gamma)$  as a function of  $\gamma$ -ray energy ( $E_\gamma$ ) is also shown.

The variations of the asymmetry parameter  $a(E_\gamma)$  as a function of  $\gamma$ -ray energy ( $E_\gamma$ ), as obtained for the VENUS (top) and the INGA (below) set up are shown in Fig. 3.9. This variation is fitted with the equation  $a(E_\gamma) = a_0 + a_1 E_\gamma$ . For the present setups, this asymmetry value is deduced to be near unity.

## 3.6 Analysis procedures using VAMOS++

VAMOS++ is a large acceptance magnetic spectrometer, which is used in the present work, for complete isotopic ( $A$ ,  $Z$ ) identification of the fission fragments. A large number of nuclei are produced in fission, which de-excite to their ground states by emitting  $\gamma$  rays simultaneously. Thus it becomes extremely difficult and experimentally challenging to assign the  $\gamma$  transitions to specific nucleus only from  $\gamma - \gamma$  coincidence techniques. Using VAMOS++ spectrometer, direct tagging of the each fission fragments is possible with its  $A$ ,  $Z$  &  $Q$  identification uniquely and then look for the emitted  $\gamma$  rays in coincidence with particular fragment.

### 3.6.1 Trajectory reconstruction

The tracking of the total flight path of each fragment is reconstructed in the VAMOS++ spectrometer with the help of various parameters, determined from measurements using different detectors. The length of the flight path of the fragment inside the spectrometer is determined by measuring the position ( $X$ ,  $Y$ ) of the fragment at two different points, one is near the target (in DPS MWPC) and one is inside the focal plane (in DC). The transverse positions along with the recoiling angles are also determined using these detectors. These precise position information during the flight, along with the magnetic rigidity parameter ( $B\rho$ ), makes it possible to determine the whole flight trajectory of the fragment inside VAMOS++. Due to the non-uniform magnetic field of the dipole and quadrupoles, the trajectory of the fragment becomes complex and, thus, non-linear polynomials are used in the reconstruction algorithm. The Time of Flight (TOF) of the fragments are also measured by the time difference between the time signals just after the target position and at focal plane. The velocity vector ( $\mathbf{v}$ ) is, then, calculated using the flight length ( $l$ ) and ToF [9, 20].

### 3.6.2 Identification of $Z$

The atomic number ( $Z$ ) of the fragment is determined using the  $\Delta E$ - $E$  measurement. The segmented ionization chambers placed at the focal plane of the VAMOS++ are used in this purpose, which measures the energy loss ( $\Delta E$ ) of the fragment and also the total energy ( $E$ ). A two dimensional plot between  $\Delta E$  and  $E$  will give parallel separated curves corresponding to different  $Z$  in accordance to the Bethe-Bloch formula. This procedure is followed here to identify the atomic number of each fragment.

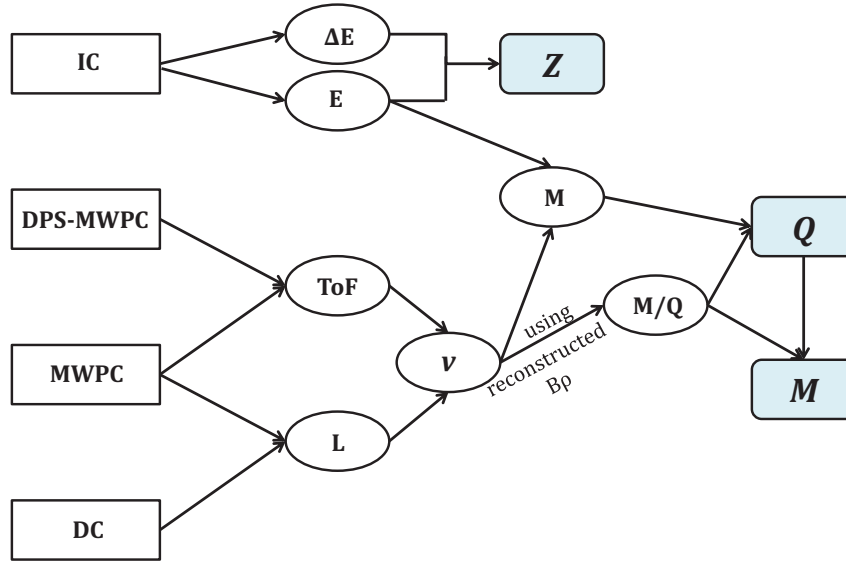


Figure 3.10: Flow chart of various steps required in isotopic fragment identification using VAMOS++.

### 3.6.3 Identification of mass and charge state

The trajectory of the fragments inside the magnetic field can be expressed in terms of applied magnetic field ( $B$ ) and radius of curvature ( $\rho$ ) as,

$$B\rho = \gamma \frac{M.v}{Q} \quad (3.11)$$

where  $\gamma$  is the Lorentz factor,  $B$  is the applied magnetic field of the dipole,  $M$  is the mass of the fragment,  $Q$  is the charge state of the fragment and  $\mathbf{v}$  is the velocity. The magnetic rigidity,  $B\rho$ , is so set in this experiment that the isotopes in mass  $\sim 130$  has maximum transmission through VAMOS++. The mass-over-charge ratio ( $M/Q$ ) is now calculated using  $B\rho$  and measured velocity ( $\mathbf{v}$ ) following Eq. 3.11. Again, the Mass of the fragment can be also estimated from the velocity and the total energy ( $E$ ) measured in ionization chamber using the equation,

$$M = \frac{E}{(\gamma - 1)c^2} \quad (3.12)$$

Thus, the mass ( $M$ ) and mass over charge ( $M/Q$ ) are measured independently. Therefore, the two dimensional plot between  $M$  and  $M/Q$  can be utilized to identify the charge state ( $Q$ ). More accurate mass and charge state identification is obtained by iterating this process a number of times. The schematic diagram of various steps in identification of each fragments using VAMOS++ is shown in Fig. 3.10.

# Bibliography

- [1] G. Duchene *et al.*, Nucl. Instrum. Methods **A 432**, 90 (1999).
- [2] S. L. Shepherd *et al.*, Nucl. Instrum. Methods in Phys. Res. **A 434**, 373 (1999).
- [3] S. Akkoyun *et al.*, Nucl. Instrum. Methods in Phys. Res. **A 668**, 26 (2012).
- [4] A. Wiens *et al.*, Nucl. Instrum. and Methods in Phys. Res. Section **A 618**, 223 (2010).
- [5] D. Lersch *et al.*, Nucl. Instrum. and Methods in Phys. Res. Section **A 640**, 133 (2011).
- [6] Soumik Bhattacharya *et al.*, Proc. DAE-BRNS Symp. Nucl. Phys. 61, 98 (2016).
- [7] S. Das *et al.*, Nucl. Instrum. and Methods in Phys. Res. **A**, 893, 138 (2018).
- [8] A. Navin, *et al.*, Phys. Lett. B **728**, 136 (2014).
- [9] M. Rejmund, *et al.*, Nucl. Instrum. Methods A **646**, 184 (2011).
- [10] N. Alahari and M. Rejmund, Gamma-ray spectroscopy of neutron-rich fission fragments,(2019).
- [11] M. Vandebrouck *et al.*, Nucl. Instr. and Meth. A 812, 112 (2016).
- [12] J. Simpson, *et al.*, Act. Phys. Hung. Ser. Heavy Ion Phys. **11**, 159 (2000).
- [13] Y. H. Kim *et al.*, Eur. Phys. J. A **53**, 162 (2017).
- [14] A. Chatterjee, Priv. comm. (2001); <http://www.tifr.res.in/~pell/lamps.html>.
- [15] D. C. Radford Nucl. Instrum. Methods Phys. Res. **A 361**, 297 (1995).

- [16] H. Morinaga and T. Yamazaki, In-beam gamma-ray spectroscopy (North-Holland Pub. Co., Amsterdam, 1976).
- [17] A. Krämer-Flecken et al., Nucl. Instrum. Methods Phys. Res. **A 275**, 333 (1989).
- [18] K. Starosta et al., Nucl. Instrum. Meth. Phys. Res. **A 423**, 16 (1999).
- [19] Ch. Droste et al., Nucl. Instrum. Meth. Phys. Res. **A 378**, 518 (1996).
- [20] S. Pullanhiotan *et al.*, Nucl. Inst. and Methods in Phys. Research A **593**, 343 (2008).

# Chapter 4

## High spin spectroscopy of $^{117}\text{Sb}$ :

## Observation of signature partner bands

### 4.1 Introduction

The nuclei having proton number near  $Z = 50$  but neutron number away from  $N = 82$  shell closure are known to exhibit single particle structures as well as collective bands based on different angular momentum couplings between the valence particle with the deformed core. Such kind of competitions between collective and single particle excitations can be studied in Sb isotopes ( $Z = 51$ ) of mass  $\sim 110 - 120$  region [1, 2]. The structure of Sb isotopes in this mass region gives us the idea about the evolution of nuclei from the spherical Sn to the transitional nuclei with  $Z \geq 52$ . Deformed structures in Sn nuclei originates from the proton two particle-two hole ( $2p - 2h$ ) excitations across the shell closure  $Z = 50$ , for example, in  $^{116}\text{Sn}$  [3]. Coupling of the valence proton with the spherical and deformed Sn core are systematically studied in odd-A Sb isotopes in this mass region [4, 5, 6, 7]. The lower lying states of odd-A Sb isotopes are understood as single-particle excitations. Also in all odd-A Sb nuclei, deformed bands based on two-particle one-hole ( $2p - 1h$ ) states, coming from a proton excitation beyond the  $Z = 50$ , are observed in  $A \sim 110 - 120$  region. Such kind of excitation of proton is possible since the

up-sloping high- $\Omega$  Nilsson orbital of the  $g_{9/2}$  from below  $Z = 50$  shell and the down-sloping components of the  $g_{7/2}$  and  $d_{5/2}$  orbitals from above  $Z = 50$  core come close with deformation. The  $9/2^+$  states are observed in all odd-A Sb isotopes and configured as deformed  $2p - 1h$  state  $((\pi g_{7/2})^2 \otimes (\pi g_{9/2})^{-1})$  [8, 9]. Strongly coupled rotational band structure based on this  $9/2^+$  state [6, 7, 10], thus, demonstrates the deformation driving effect of the  $g_{9/2}$  intruder orbital. On the other hand, rotational band based on the  $\pi h_{11/2}$  orbital indicates rather more enhanced deformation [11, 12].

The lowest states in the Sb isotopes are  $5/2^+$  and  $7/2^+$ , having  $\pi d_{5/2}$  and  $\pi g_{7/2}$  configurations, respectively. These states are situated very closeby and are expected to be of highly mixed nature. With increasing neutron number, the relative positions of these orbitals alter at  $A \geq 123$ . These single particle orbitals can also couple with the deformed  $2p - 2h$  states of Sn core to form rotational band structures at low energies. These bands are expected to have  $\Delta J = 2$  structure along with a signature partner, contrary to the strongly coupled  $g_{9/2}$   $2p - 1h$  band. These bands are also expected to possess large signature splitting due to the involvement of the low- $\Omega$  Nilsson components of these orbitals. The observed signature splitting of these bands helps us to understand the nature of the coupling of the odd particle to the core and hence the contribution of the involved Nilsson configuration of the band. These bands are identified and discussed in the odd-A Iodine ( $Z = 53$ ) [13] and Cesium ( $Z = 55$ ) isotopes [14] but are not well investigated in the odd-A Sb isotopes. The investigation of the band structures built on the  $\pi d_{5/2}$  and  $\pi g_{7/2}$  orbitals are thus important in the odd-A Sb isotopes to understand the shape polarizing effect of these orbitals on the  $Z = 50$  core. Though the indication of the band-like structures based on  $\pi g_{7/2}$  has been identified in  $^{117,119}\text{Sb}$  isotopes [7], but no signature partner bands has been observed. Thus detailed characterization of these bands still remain unexplored.

Initial studies on  $^{117}\text{Sb}$  are from  $\beta$ -decay of  $^{117}\text{Te}$  [15]. In-beam investigations have also been carried out using the  $\alpha$ , deuteron and proton induced fusion evaporation reactions with only a few Ge(Li) detectors [16, 17, 18, 19]. Shape coexistence in  $^{117}\text{Sb}$  is predicted from the presence of an isomer at  $23/2^-$  level [20]. The high spin states of  $^{117}\text{Sb}$  have been investigated by ( $^{11}\text{B}$ ,

4n) reaction with six Compton-suppressed HPGe detectors [7], but no polarization information of the observed  $\gamma$  rays are available.

In the present thesis work, the study of the excited states in  $^{117}\text{Sb}$  using  $\alpha$ -induced reaction is reported. The primary motivation of the present work is to identify and characterize the signature partner bands based on the  $g_{7/2}$  configuration in  $^{117}\text{Sb}$ , in order to investigate the shape driving effect of the  $g_{7/2}$  orbital.

## 4.2 Experiment and Data Analysis

The high spin excited states of  $^{117}\text{Sb}$  have been populated using the reaction  $^{115}\text{In}(\alpha, 2n)^{117}\text{Sb}$  at a beam energy of 28 MeV delivered from the K-130 cyclotron at Variable Energy Cyclotron Centre, Kolkata (India). A 4.1 mg/cm<sup>2</sup> thick  $^{nat}\text{In}$  self-supporting foil with a 95.7% abundance of  $^{115}\text{In}$  was used as target. The VEcc array for NUclear Spectroscopy (VENUS) [21, 22], consisting of six Compton suppressed HPGe Clover detectors, were used for  $\gamma$  ray detection. The PIXIE based digital data acquisition system [23] was used to record the list mode data. The details of the experimental setup is given in chapter 3.

The data were sorted using the IUCPIX package [23], to construct the  $E_\gamma$ - $E_\gamma$  matrices and the  $E_\gamma$ - $E_\gamma$ - $E_\gamma$  cube, and analyzed using the RADWARE [25] and LAMPS [26] analysis packages. Fig. 4.1 represents the total matrix projection of the data, as obtained in the present experiment. The source of the 159 keV transition, present in Fig. 4.1, is the electron capture decay of the  $^{117}\text{Sb}$  nucleus with 99% probability (intensity) to the 159 keV level of the  $^{117}\text{Sn}$  daughter nucleus and de-excitation therefrom. The half-life of  $^{117}\text{Sb}$  is 2.80 hours, sufficiently small to facilitate an equilibrated population of  $^{117}\text{Sb}$  during the progress of the experiment and thus, this acted as a source present during the experiment. The level structure of  $^{117}\text{Sb}$  is constructed from various coincidence relationships between the observed  $\gamma$ -rays and their relative intensities. The multiplicities of the  $\gamma$  rays are assigned from the measured  $R_{DCO}$  [27] and Polarisation asymmetry ( $\Delta_{PDCO}$ ) [28, 29] values. In the present measurement, the typical value of  $R_{DCO}$  is obtained as  $\sim 0.6$  (1.8) for a pure stretched dipole (quadrupole) transition when gated by a

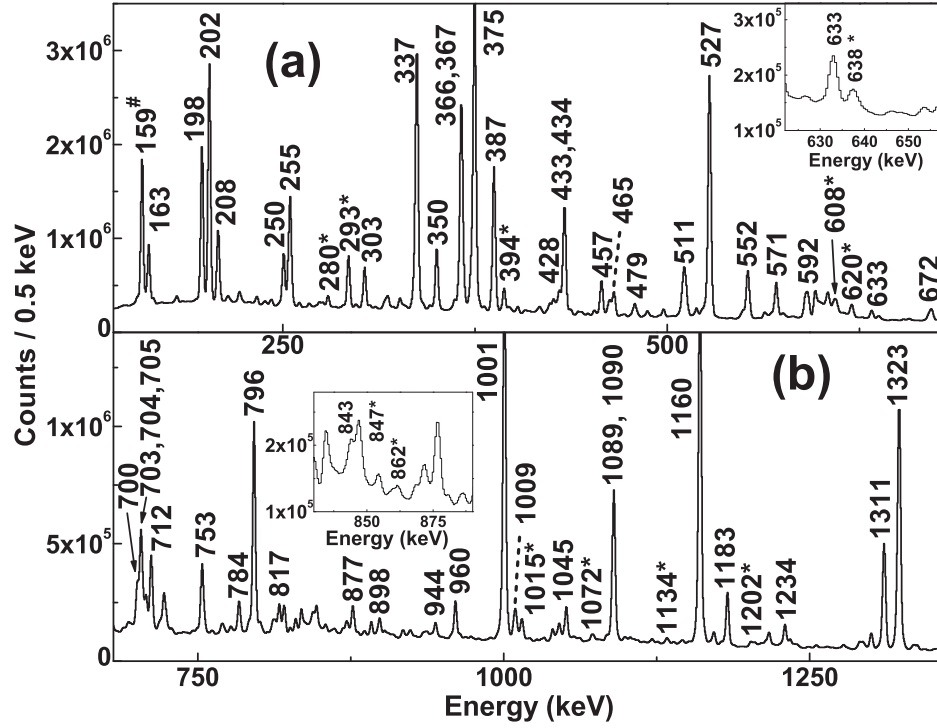


Figure 4.1: Total projection of the  $E_\gamma$ - $E_\gamma$  matrix, as obtained in the present experiment. All the  $\gamma$  rays marked in the figure are from  $^{117}\text{Sb}$ . The spectrum is shown in two parts, (a) upto 680 keV and (b) beyond 680 keV. The newly observed transitions from the present work are marked with ‘\*’. The insets show some of the new transitions in an expanded scale. The 159 keV, marked with ‘#’, is from  $^{117}\text{Sn}$  which is populated from the decay of  $^{117}\text{Sb}$ .

stretched pure quadrupole (dipole) transition. The angular distribution for some of the  $\gamma$  rays in  $^{117}\text{Sb}$  are also obtained from the singles data (*i.e.*, with event trigger set on Compton suppressed Clover detector multiplicity  $\geq 1$ ). For the polarisation measurements, the coefficients of the geometrical asymmetry factor are obtained as  $a_0 = 1.01(1)$  and  $a_1 = 1.37(4) \times 10^{-5}$ .

### 4.3 Results

The new level scheme of  $^{117}\text{Sb}$ , as obtained in the present work, is shown in Fig. 4.2. The band structures are marked as B1, B1(a), B1(b), B2, B3, B4, B5(a), B5(b), B6, B6(a) and

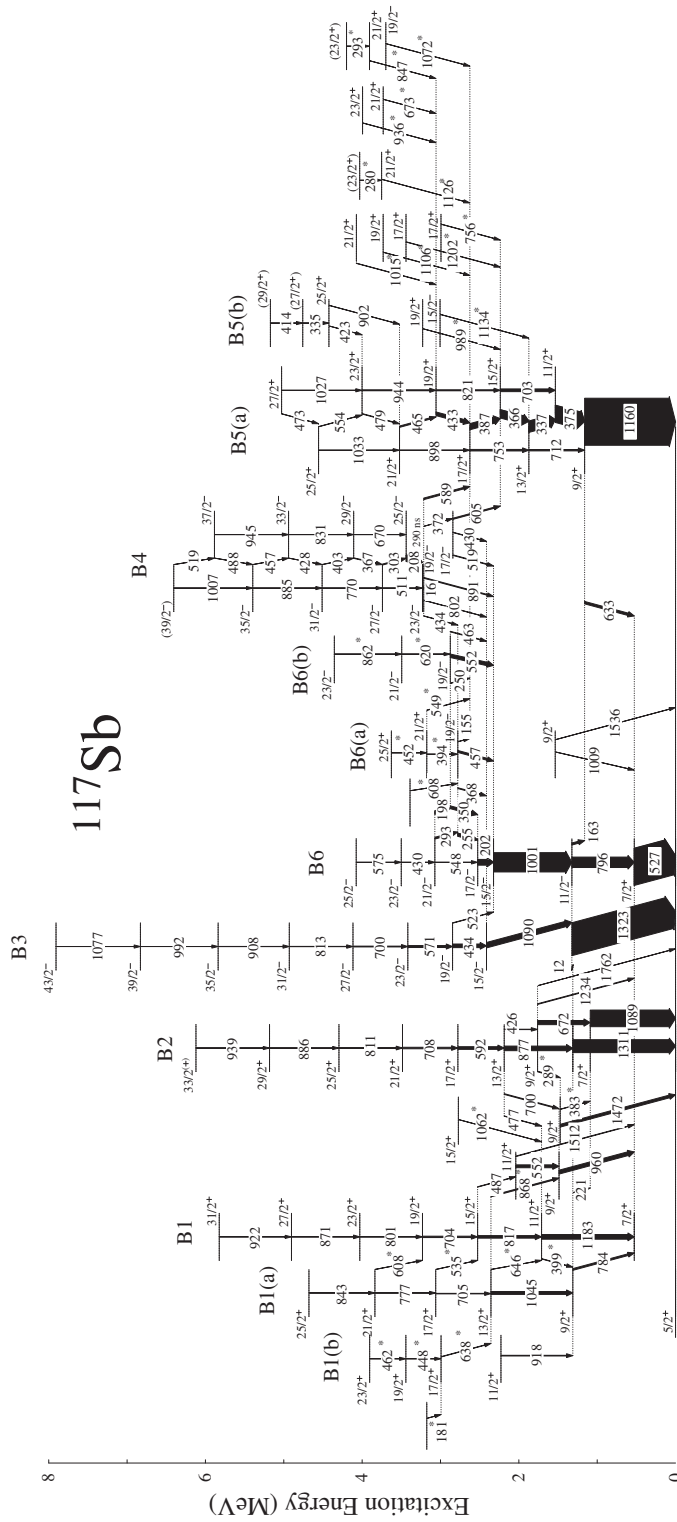


Figure 4.2: Proposed level scheme of  $^{117}\text{Sb}$ , as obtained from the present work. The new  $\gamma$  rays observed from the present work are marked with ‘\*’ on the right side of the  $\gamma$ -ray energy label.

B6(b) in the level scheme. 31 new  $\gamma$  rays are placed in the level scheme [29]. Band B1-B1(a) are established as signature partner bands by observing the interconnecting transitions. Other new non yrast states at the low and medium spin regime are also identified from the current measurements. The observed  $\gamma$  ray energies, level energies, their intensities along with their spin-parities are tabulated in Table 4.1. The  $\gamma$  rays having  $R_{DCO}$  values in the range of 0.5 to 0.7 in a quadrupole gate and from 0.9 to 1.1 in a dipole gate with negative  $\Delta_{PDCO}$  values, are considered as dominantly M1 with small E2 admixture and are assigned as M1(+E2). The  $\gamma$  rays having  $R_{DCO}$  values outside the abovesaid range and with negative  $\Delta_{PDCO}$  values are considered to be of mixed nature and assigned as M1+E2. The  $R_{DCO}$  *vs.*  $\Delta_{PDCO}$  plot of the newly observed  $\gamma$  rays, observed in the present work, along with few of the known  $\gamma$  rays are shown in Fig. 4.3. The reported nature of the known transitions (shown in red colour in Fig. 4.3) are reproduced well from the present measurements of  $R_{DCO}$  and  $\Delta_{PDCO}$  values. This establishes that the assignments of the spin-parities to the newly observed levels are correct. Fig. 4.4 shows the angular distribution of some of the stretched quadrupole and dipole transitions, observed in the present measurement. Fig. 4.4(a), (c), (e) and (g) shows the angular distribution of the 1160 (known), 817 (known), 843 (new) and 638 keV (new) transitions, respectively. These transitions are assigned as the quadrupole ones. On the other hand, Fig. 4.4(b), (d), (f) and (h) shows the angular distribution of the 527 (known), 163 (known), 394 (new) and 862 keV (new) transitions, respectively. These transitions are assigned as the dipole ones.

The present work reports the observation of the bands B1 and B1(a) upto spin  $31/2^+$  and  $25/2^+$ , respectively, with confirmed spin-parity assignments. These two bands are obtained as positive parity E2 bands. The interconnecting transitions between B1 and B1(a) are observed for the first time from the present work, which makes these two bands as the signature partners. Band B1(a) is found to decay to the band B1 via 608, 535, 646 keV M1 transitions. On the other hand, only one transition (399 keV) is found to decay from the  $11/2^+$  level of the band B1 to the  $9/2^+$  level of the band B1(a). Coincidence spectra corresponding to the gate of 817 and 1183 keV transitions of the band B1 are shown in Fig. 4.5(a) and (b), respectively. The insets of this figures show the expanded part of the corresponding coincidence gates, which show the

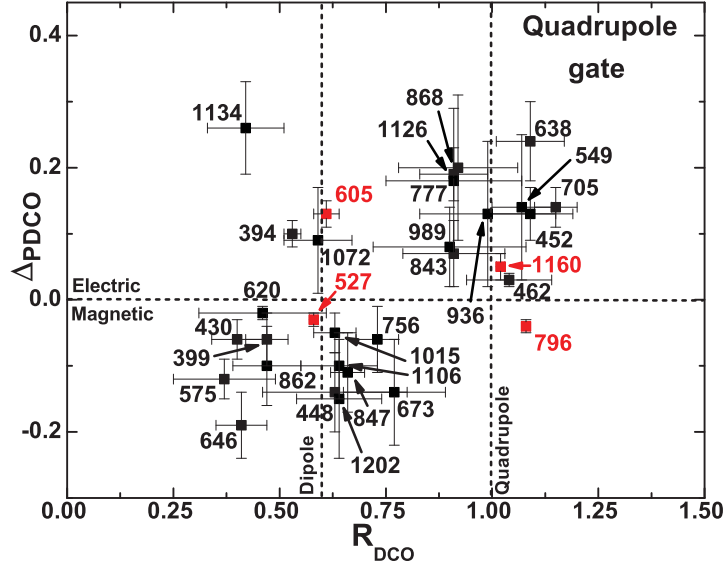


Figure 4.3: DCO ratio ( $R_{DCO}$ ) vs.  $\Delta_{PDCO}$  plot of various new (black) and known (red) transitions observed in  $^{117}\text{Sb}$  obtained in the present work. The dotted lines at X-axis are to guide the eye for the DCO ratios corresponding to the pure dipole and quadrupole transitions, respectively. The dotted line at Y-axis is to guide the eye for  $\Delta_{PDCO}$  values corresponding to the electric (+ve) and magnetic (-ve) nature of the transitions.

connecting M1 transitions between B1 and B1(a) clearly. Another new sequence of transitions of energies 638, 448 and 462 keV is observed above the 2356 keV level and marked as B1(b) in the level scheme (Fig. 4.2). The coincidence spectrum corresponding to the 1045 keV gate, showing the  $\gamma$  rays of B1(a) and the new transitions of B1(b), is shown in Fig. 4.5(c).

The band B2 is observed up to spin  $33/2^{(+)}$  in the present work. The 995 and 1068 keV transitions, which were reported [7] to be present in this band, could not be observed in the present data. Fig. 4.6(a) represents the coincidence spectrum corresponding to the 877 keV transition. The band, marked as B3 in the level scheme, is a negative parity band and is observed upto spin  $43/2^-$ . The spin-parity assignments of the 7908 ( $43/2^-$ ), 6831 ( $39/2^-$ ) and 5839 ( $35/2^-$ ) keV levels of the band B3 are confirmed from the present work, which were reported as tentative in Ref. [7]. Fig. 4.6(b) shows the coincidence spectrum corresponding to the 571 keV transition of band B3, showing the cascade  $\gamma$  rays of this band.

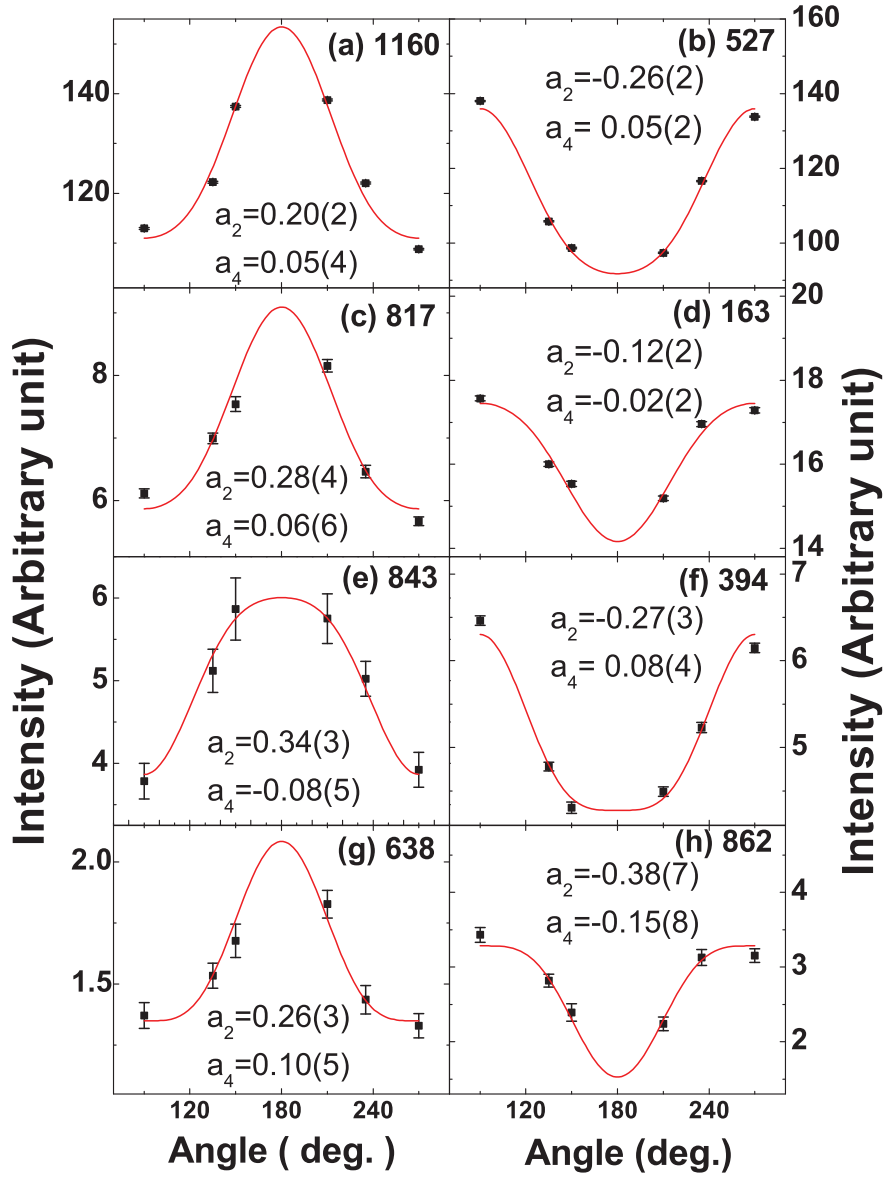


Figure 4.4: Angular distributions of various transitions of  $^{117}\text{Sb}$ , observed in the present work. The panels (a), (c), (e) and (g) represent the distribution for the quadrupole transitions and the panels (b), (d), (f) and (h) represent distribution corresponding to the dipole transitions in  $^{117}\text{Sb}$ , as obtained in the present work.

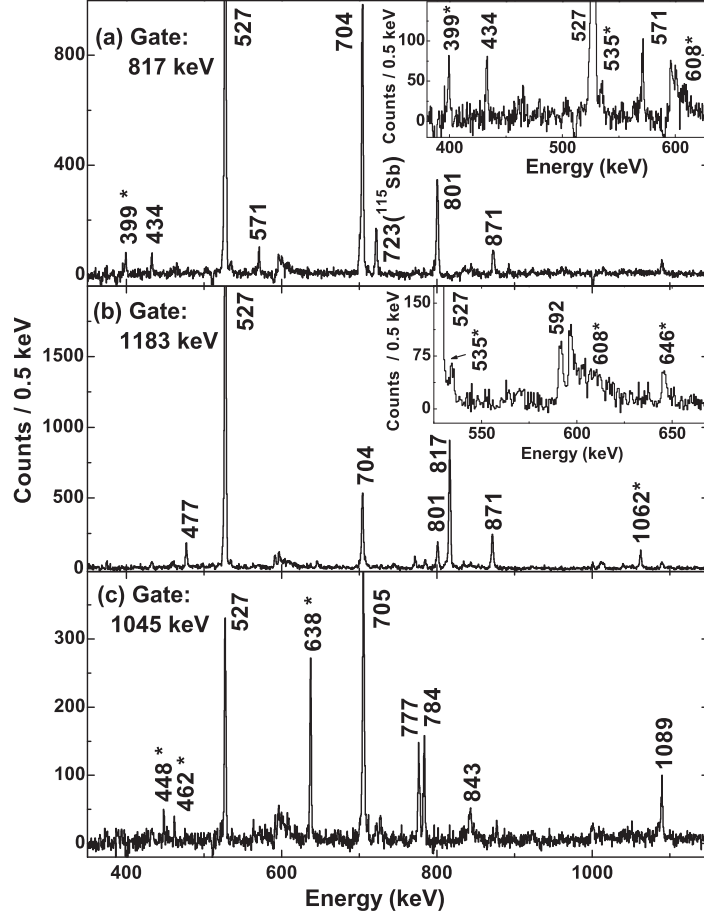


Figure 4.5: Coincidence spectra corresponding to the (a) 817 keV gate of the band B1, (b) 1183 keV gate of the band B1 and (c) 1045 keV gate of the band B1(a). The insets of (a) and (b) show the expanded view of the coincidence spectra of the 817 and 1183 keV gates respectively. The newly observed transitions are marked with ‘\*’.

A strongly coupled negative parity band, named as B4, is observed in the present work upto  $(39/2^-)$  level. This band is built above the reported 290 ns isomeric state [20]. The states beyond  $25/2^-$  of this band were only tentatively assigned [7]. From the present  $R_{DCO}$  and  $\Delta_{PDCO}$  measurements, the spin-parity to these states have been firmly assigned. The  $\Delta J = 1$  transitions of this band are found to be relatively stronger than the corresponding  $\Delta J = 2$  crossovers. The double gates of 208 and 303 keV transitions of band B4, obtained from  $E_\gamma$ -

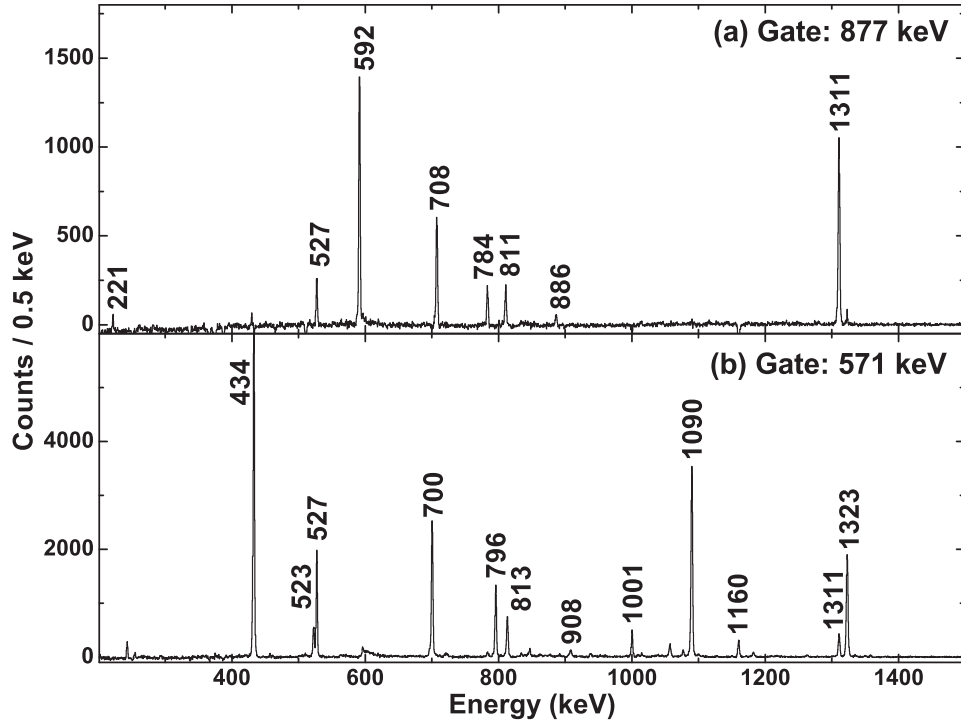


Figure 4.6: Coincidence spectra corresponding to the gates of (a) 877 keV  $\gamma$  ray of band B2 and (b) 571 keV  $\gamma$  ray of band B3.

$E_\gamma$ - $E_\gamma$  cube is shown in Fig. 4.7(a). The transitions of band B4 can be clearly seen from this figure.

The band B5(a) (see Fig. 4.2), is a strongly coupled positive parity band and is observed upto  $27/2^+$  level. The spin-parities of the top two levels of the band B5(a) are confirmed as  $25/2^+$  and  $27/2^+$  from the present measurements. The dipole transitions of this band are found to be of mixed (M1+E2) nature. Fig. 4.7(b) shows the double gated coincidence spectra of 1160 and 387 keV transitions of the band B5(a), showing the  $\gamma$  rays present in this band. The 159 keV  $\gamma$ -ray present in this coincidence spectrum is the decaying transition from the first excited state of  $^{117}\text{Sn}$ , which has a strong EC decay feeding from  $^{117}\text{Sb}$ . The sequence, B5(b), is connected to the band B5(a) at  $23/2^+$  level and is observed upto  $(29/2^+)$  in the present work. Fig. 4.7(c) shows the coincidence spectrum corresponding to the double gates of 1001 and 202 keV transitions, showing the  $\gamma$  rays corresponding to the negative parity sequence (B6)

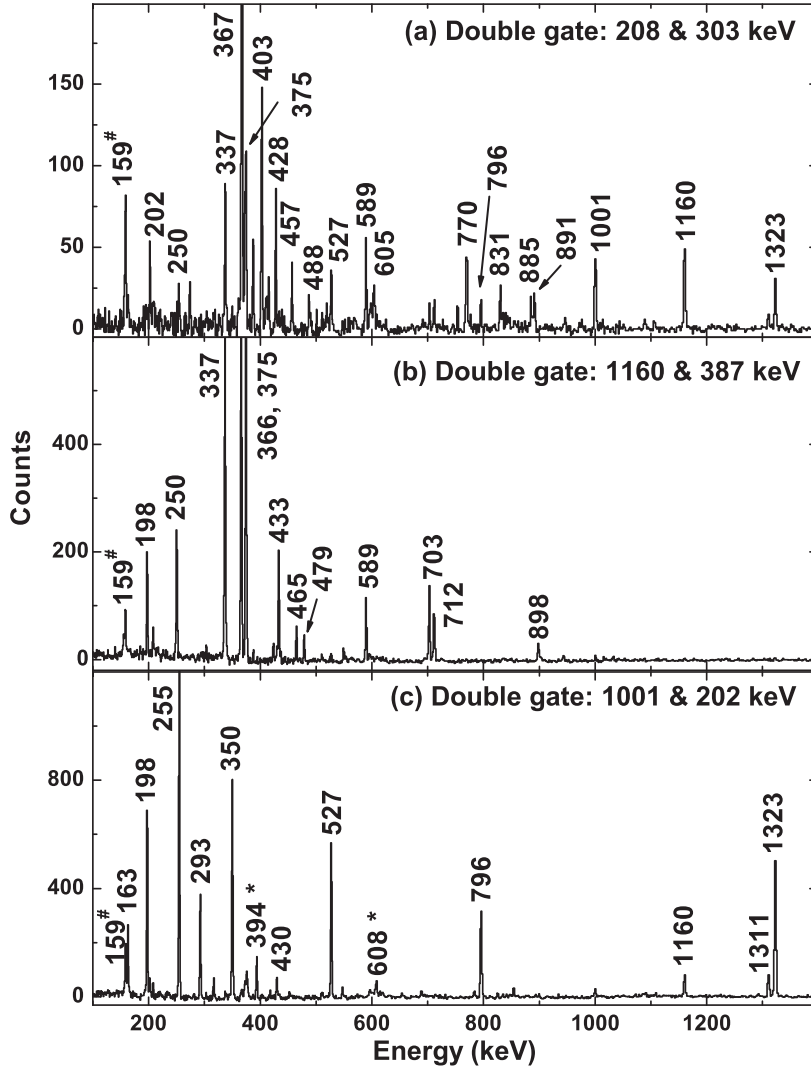


Figure 4.7: The coincidence spectra corresponding to the double gates of (a) 208 & 303 keV  $\gamma$  rays of B4, (b) 1160 & 387 keV  $\gamma$  rays of B5 and (c) 1001 & 202 keV  $\gamma$  rays of B6 from the  $E_\gamma$ - $E_\gamma$ - $E_\gamma$  cube. The new transitions observed in the current work are marked with '\*'. The 159 keV, marked with '#', is from  $^{117}\text{Sn}$ .

in the level scheme. The current  $R_{DCO}$  and  $\Delta_{PDCO}$  measurements of the 430 and 575 keV  $\gamma$  rays confirm the spin-parity of the corresponding levels, which were previously assigned tentatively.

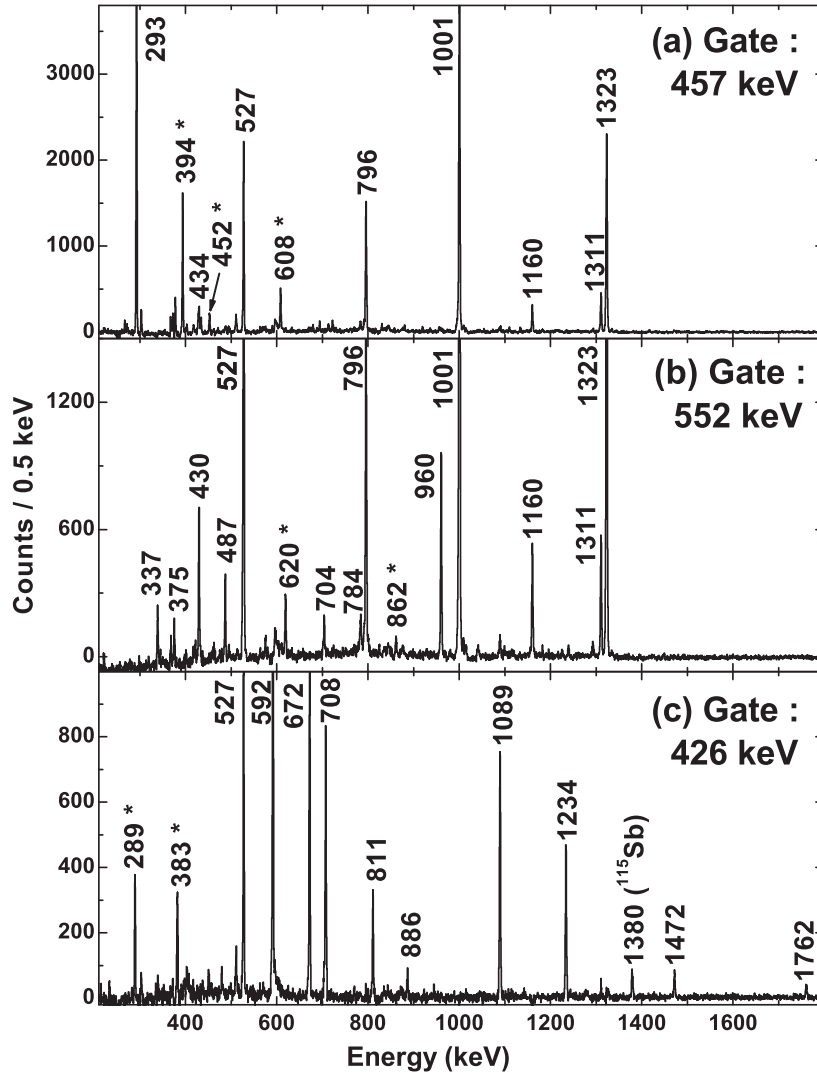


Figure 4.8: Coincidence spectra corresponding to the gates of (a) 457 keV  $\gamma$  ray of B6(a), (b) 552 keV  $\gamma$  ray of B6(b) and (c) 426 keV  $\gamma$  ray of B2. The new  $\gamma$  rays observed in the present work are marked with ‘\*’.

Band B6(a) and B6(b) are the newly observed short sequences built above the 2781 ( $19/2^-$ ) and 2876 keV ( $19/2^-$ ) levels, respectively. Two transitions of energy 394 and 452 keV are placed in B6(a) and 620 and 862 keV transitions are placed in B6(b). Fig. 4.8(a) and Fig. 4.8(b) represent the coincidence spectra corresponding to the gates of 457 keV of B6(a) and 552 keV of B6(b), respectively, as obtained from the  $E_\gamma$ - $E_\gamma$  matrix.

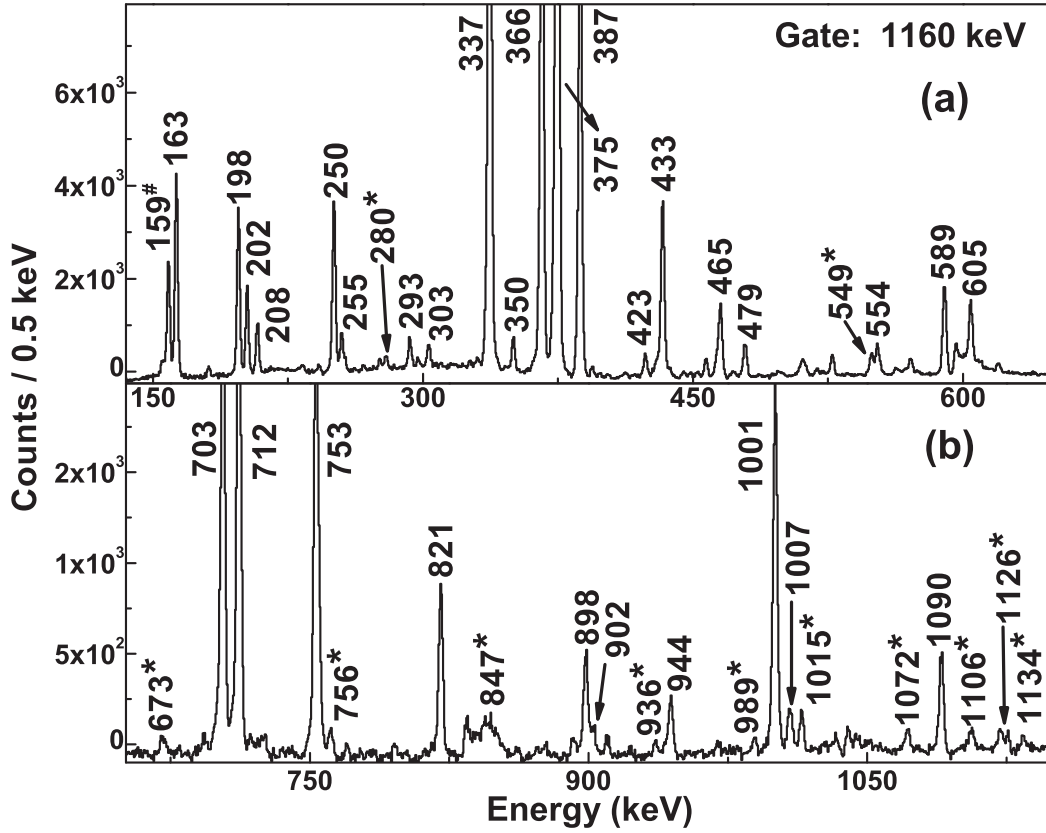


Figure 4.9: Coincidence spectra corresponding to the gate of 1160 keV transition of the band B5, (a) upto 625 keV; (b) above 625 keV. All the newly observed transitions are marked with ‘\*’.

Various non-yrast single particle positive parity states, as reported in Ref. [19, 7], are also observed in the present work. Several interconnecting transitions between these states, such as, 221, 289, 383, 868, 1234 and 1472 keV, are placed in the level scheme of  $^{117}\text{Sb}$ . Fig. 4.8(c) shows the coincidence spectra corresponding to the 426 keV gate, showing the new transitions observed in this work. The nature of the observed  $\gamma$  rays are tabulated in the table 4.1. The two higher energy  $\gamma$  rays of energy 1536 and 1762 keV were reported earlier from  $(p, n\gamma)$  reaction [19], but not from the heavy ion induced reaction [7]. These transitions are also observed in the present  $\alpha$  induced reaction.

Presence of a new set of transitions are observed in the present work, decaying to the various levels of the band B5(a), extending the level structure horizontally. Fig. 4.9 represents the coincidence spectrum corresponding to the 1160 keV gate. The newly observed  $\gamma$ -rays are marked with '\*' along with other known transitions of the band B5(a) in that figure. The 1134 keV transition is present in coincidence with the 337, 375 and 1160 keV transitions, but not with the transitions above the 1872 keV level. Thus it is placed above the 1872 keV level in parallel to the 366 keV transition. The 1202 and 756 keV transitions are placed above the 2238 keV level. Another E2 transition of energy 989 keV is placed above the 2238 keV level. Its E2 nature is established from the measured  $R_{DCO}$  and  $\Delta_{PDCO}$  values. The  $\gamma$  rays of energy 549, 1072, 1106 and 1126 keV are placed above the 2626 keV level. Another sequence of two  $\gamma$  rays of 847 and 293 keV is found to feed the 3059 keV level. The transitions of energy 673, 936 and 1015 keV are found in coincidence with the  $\gamma$  rays below 3059 keV level of band B5(a) but not with each other. Therefore, these transitions are placed on top of the 3059 keV level.

Table 4.1: The energies ( $E_\gamma$ ) and relative intensities ( $I_\gamma$ ) of the  $\gamma$  rays observed in  $^{117}\text{Sb}$  along with the spin and parity of the initial ( $J_i^\pi$ ) and the final ( $J_f^\pi$ ) states and the energy of the initial state ( $E_i$ ). The measured values of  $R_{DCO}$  and  $\Delta_{PDCO}$  are also shown along with the multipolarity of the  $\gamma$  rays.

$E_\gamma$ (keV)	$E_i$ (keV)	$J_i^\pi \rightarrow J_f^\pi$	$I_\gamma(\text{Err})^1$	$R_{DCO}(\text{Err})$	$\Delta_{PDCO}(\text{Err})$	Multipolarity
(12) <sup>2</sup>	1323.1	11/2 <sup>-</sup> $\rightarrow$ 9/2 <sup>+</sup>	-	-	-	(E1)
(16) <sup>3</sup>	3230.9	23/2 <sup>-</sup> $\rightarrow$ 19/2 <sup>-</sup>	-	-	-	(E2)
155.2(1)	2780.8	19/2 <sup>-</sup> $\rightarrow$ 17/2 <sup>+</sup>	0.27(2)	0.74(8) <sup>4</sup>	-	E1
163.0(1)	1323.1	11/2 <sup>-</sup> $\rightarrow$ 9/2 <sup>+</sup>	0.18(2)	0.65(1) <sup>4</sup>	-	E1
181.1(1)	3174.9	- $\rightarrow$ 17/2 <sup>+</sup>	0.05(2)	-	-	-
197.6(1)	3073.6	21/2 <sup>-</sup> $\rightarrow$ 19/2 <sup>-</sup>	6.83(47)	0.67(1) <sup>4</sup>	-0.05(3)	M1(+E2)
202.3(1)	2525.9	17/2 <sup>-</sup> $\rightarrow$ 15/2 <sup>-</sup>	11.24(78)	0.64(1) <sup>4</sup>	-0.04(2)	M1(+E2)
208.1(1)	3439.0	25/2 <sup>-</sup> $\rightarrow$ 23/2 <sup>-</sup>	12.80(64)	0.67(3) <sup>4</sup>	-	M1+E2

Table 4.1: Continued...

$E_\gamma$ (keV)	$E_i$ (keV)	$J_i^\pi \rightarrow J_f^\pi$	$I_\gamma(\text{Err})$ <sup>1</sup>	$R_{DCO}(\text{Err})$	$\Delta_{PDCO}(\text{Err})$	Multipolarity
221.4(1)	1310.8	$9/2^+ \rightarrow 7/2^+$	2.48(8)	$1.15(4)$ <sup>5</sup>	-	M1+E2
250.4(1)	2876.0	$19/2^- \rightarrow 17/2^+$	0.87(6)	$0.71(1)$ <sup>4</sup>	0.07(1)	E1
254.9(1)	2780.8	$19/2^- \rightarrow 17/2^-$	6.25(44)	$0.83(1)$ <sup>4</sup>	-0.09(1)	M1+E2
279.8(1)	4031.2	$(23/2^+) \rightarrow 21/2^+$	0.10(8)	$0.49(5)$ <sup>4</sup>	-	(M1+E2)
289.3(1)	1761.6	$9/2^+ \rightarrow 9/2^+$	1.27(5)	-	-	(M1+E2)
292.8(1)	3073.6	$21/2^- \rightarrow 19/2^-$	3.57(25)	$0.82(1)$ <sup>4</sup>	-0.07(1)	M1+E2
293.3(1)	4199.3	$(23/2^+) \rightarrow 21/2^+$	0.09(4)	$0.80(4)$ <sup>4</sup>	-	(M1+E2)
303.3(1)	3742.3	$27/2^- \rightarrow 25/2^-$	1.99(8)	$1.15(2)$ <sup>5</sup>	-0.13(1)	M1+E2
334.7(2)	4761.3	$(27/2^+) \rightarrow 25/2^+$	0.21(8)	-	-	(M1+E2)
337.1(1)	1872.2	$13/2^+ \rightarrow 11/2^+$	23(2)	$0.82(1)$ <sup>4</sup>	-0.09(1)	M1+E2
350.1(1)	2876.0	$19/2^- \rightarrow 17/2^-$	5.69(40)	$0.81(3)$ <sup>4</sup>	-0.08(1)	M1+E2
366.1(1)	2238.3	$15/2^+ \rightarrow 13/2^+$	17(1)	$0.81(2)$ <sup>4</sup>	-0.09(1)	M1+E2
366.9(1)	4109.2	$29/2^- \rightarrow 27/2^-$	1.16(5)	$1.20(2)$ <sup>5</sup>	-0.13(2)	M1+E2
367.5(1)	2780.8	$19/2^- \rightarrow 15/2^-$	1.64(12)	$1.08(3)$ <sup>4</sup>	0.09(2)	E2
371.9(1)	3214.9	$19/2^- \rightarrow 17/2^-$	0.88(16)	-	-	(M1+E2)
374.7(1)	1535.1	$11/2^+ \rightarrow 9/2^+$	35(2)	$0.88(1)$ <sup>4</sup>	-0.09(1)	M1+E2
382.9(1)	1472.3	$9/2^+ \rightarrow 7/2^+$	0.40(8)	-	-	M1+E2
387.3(1)	2625.6	$17/2^+ \rightarrow 15/2^+$	12.27(85)	$0.81(1)$ <sup>4</sup>	-0.07(1)	M1+E2
393.8(1)	3174.8	$21/2^+ \rightarrow 19/2^-$	0.64(11)	$0.53(2)$ <sup>4</sup>	0.10(2)	E1
399.3(1)	1710.1	$11/2^+ \rightarrow 9/2^+$	0.75(6)	$0.47(5)$ <sup>4</sup>	-0.06(4)	M1+E2
402.9(1)	4512.1	$31/2^- \rightarrow 29/2^-$	0.41(2)	$1.12(3)$ <sup>5</sup>	-0.18(4)	M1+E2
413.9(2)	5175.2	$(29/2^+) \rightarrow (27/2^+)$	0.16(2)	$0.50(11)$ <sup>4</sup>	-0.22(7)	M1(+E2)
423.4(1)	4426.6	$25/2^+ \rightarrow 23/2^+$	0.19(4)	$0.68(4)$ <sup>4</sup>	-0.19(4)	M1(+E2)
425.8(1)	2187.4	$13/2^+ \rightarrow 9/2^+$	0.75(3)	$1.02(2)$ <sup>4</sup>	0.08(2)	E2
428.1(1)	4940.2	$33/2^- \rightarrow 31/2^-$	0.17(2)	$1.10(12)$ <sup>5</sup>	-0.16(3)	M1(+E2)
429.6(1)	3503.2	$23/2^- \rightarrow 21/2^-$	0.76(6)	$0.40(6)$ <sup>4</sup>	-0.06(3)	M1+E2
429.7(1)	2843.0	$17/2^- \rightarrow 15/2^-$	0.66(6)	-	-	(M1+E2)
433.1(1)	3058.8	$19/2^+ \rightarrow 17/2^+$	4.45(35)	$0.81(1)$ <sup>4</sup>	-0.06(1)	M1+E2

Table 4.1: Continued...

$E_\gamma$ (keV)	$E_i$ (keV)	$J_i^\pi \rightarrow J_f^\pi$	$I_\gamma(\text{Err})$ <sup>1</sup>	$R_{DCO}(\text{Err})$	$\Delta_{PDCO}(\text{Err})$	Multipolarity
433.5(1)	2846.8	$19/2^- \rightarrow 15/2^-$	7.57(53)	$0.99(1)^4$	0.11(1)	E2
434.1(1)	3214.9	$19/2^- \rightarrow 19/2^-$	0.45(4)	-	-	(M1+E2) <sup>6</sup>
448.3(1)	3441.9	$19/2^+ \rightarrow 17/2^+$	0.21(7)	$0.63(17)^4$	-0.14(6)	M1(+E2)
452.1(1)	3626.9	$25/2^+ \rightarrow 21/2^+$	0.21(8)	$1.09(10)^4$	0.13(4)	E2
457.2(1)	2780.8	$19/2^- \rightarrow 15/2^-$	4.03(28)	$1.02(1)^4$	0.10(1)	E2
457.3(1)	5397.5	$35/2^- \rightarrow 33/2^-$	0.08(1)	$1.21(6)^5$	-0.16(4)	M1+E2
462.1(1)	3904.0	$23/2^+ \rightarrow 19/2^+$	0.12(3)	$1.04(10)^4$	0.03(1)	E2
462.7(1)	2876.0	$19/2^- \rightarrow 15/2^-$	1.17(8)	$0.90(9)^4$	0.02(1)	(E2)
465.3(1)	3524.2	$21/2^+ \rightarrow 19/2^+$	2.74(19)	$0.74(2)^4$	-0.12(2)	M1+E2
472.5(2)	5029.9	$27/2^+ \rightarrow 25/2^+$	0.19(5)	$0.39(13)^4$	-0.11(6)	M1+E2
477.3(1)	2187.4	$13/2^+ \rightarrow 11/2^+$	0.59(3)	$0.92(7)^5$	-0.08(4)	M1(+E2)
478.8(1)	4003.2	$23/2^+ \rightarrow 21/2^+$	0.94(7)	$0.66(2)^4$	-0.14(1)	M1(+E2)
487.4(1)	2526.6	$15/2^+ \rightarrow 11/2^+$	0.74(13)	$1.99(10)^5$	0.04(3)	E2
487.9(1)	5885.4	$37/2^- \rightarrow 35/2^-$	0.05(2)	$1.14(10)^5$	-0.29(5)	M1+E2
511.4(1)	3742.3	$27/2^- \rightarrow 23/2^-$	-	-	-	(E2)
518.9(1)	6404.3	$(39/2^-) \rightarrow 37/2^-$	0.04(2)	-	-	(M1+E2)
519.4(1)	2843.0	$17/2^- \rightarrow 15/2^-$	1.19(9)	-	-	(M1+E2) <sup>6</sup>
523.2(2)	2846.8	$19/2^- \rightarrow 15/2^-$	0.69(5)	$1.16(6)^4$	0.20(6)	E2
527.3(1)	527.3	$7/2^+ \rightarrow 5/2^+$	76(1)	$0.58(1)^4$	-0.03(1)	M1(+E2)
534.9(1)	3061.5	$17/2^+ \rightarrow 15/2^+$	0.05(3)	-	-	(M1+E2)
547.7(1)	3073.6	$21/2^- \rightarrow 17/2^-$	0.54(4)	$1.03(7)^4$	0.05(5)	E2
549.2(1)	3174.8	$21/2^+ \rightarrow 17/2^+$	0.56(4)	$1.07(7)^4$	0.14(11)	E2
551.5(1)	2039.2	$11/2^+ \rightarrow 9/2^+$	6.11(25)	$1.15(14)^5$	-0.05(4)	M1+E2
552.4(1)	2876.0	$19/2^- \rightarrow 15/2^-$	7.17(50)	$0.98(1)^4$	0.07(3)	E2
554.2(2)	4557.4	$25/2^+ \rightarrow 23/2^+$	0.36(12)	$0.76(17)^4$	-	(M1+E2)
570.8(1)	3417.6	$23/2^- \rightarrow 19/2^-$	4.15(29)	$1.06(2)^4$	0.12(6)	E2
574.9(1)	4078.1	$25/2^- \rightarrow 23/2^-$	0.25(3)	$0.37(12)^4$	-0.12(3)	M1+E2
589.3(1)	3214.9	$19/2^- \rightarrow 17/2^+$	3.22(23)	-	-	(E1) <sup>6</sup>

Table 4.1: Continued...

$E_\gamma$ (keV)	$E_i$ (keV)	$J_i^\pi \rightarrow J_f^\pi$	$I_\gamma(\text{Err})$ <sup>1</sup>	$R_{DCO}(\text{Err})$	$\Delta_{PDCO}(\text{Err})$	Multipolarity
591.5(1)	2778.9	17/2 <sup>+</sup> $\rightarrow$ 13/2 <sup>+</sup>	5.65(40)	0.99(3) <sup>4</sup>	0.07(3)	E2
604.7(1)	2843.0	17/2 <sup>-</sup> $\rightarrow$ 15/2 <sup>+</sup>	2.34(17)	-	-	(E1) <sup>6</sup>
607.5(1)	3838.4	21/2 <sup>+</sup> $\rightarrow$ 19/2 <sup>+</sup>	0.06(4)	-	-	(M1+E2)
608.2(1)	3389.0	- $\rightarrow$ 19/2 <sup>-</sup>	0.70(6)	-	-	-
619.8(1)	3495.8	21/2 <sup>-</sup> $\rightarrow$ 19/2 <sup>-</sup>	1.47(6)	0.46(15) <sup>4</sup>	-0.02(1)	M1+E2
632.8(1)	1160.4	9/2 <sup>+</sup> $\rightarrow$ 7/2 <sup>+</sup>	1.69(7)	1.12(3) <sup>5</sup>	-0.05(2)	M1+E2
637.5(1)	2993.6	17/2 <sup>+</sup> $\rightarrow$ 13/2 <sup>+</sup>	0.55(3)	1.09(8) <sup>4</sup>	0.24(6)	E2
646.0(1)	2356.1	13/2 <sup>+</sup> $\rightarrow$ 11/2 <sup>+</sup>	0.19(2)	0.41(6) <sup>4</sup>	-0.19(5)	M1+E2
670.2(1)	4109.2	29/2 <sup>-</sup> $\rightarrow$ 25/2 <sup>-</sup>	0.18(2)	1.72(6) <sup>5</sup>	0.07(3)	E2
672.2(1)	1761.6	9/2 <sup>+</sup> $\rightarrow$ 7/2 <sup>+</sup>	8.81(32)	1.12(2) <sup>5</sup>	-0.02(2)	M1+E2
672.6(2)	3731.4	21/2 <sup>+</sup> $\rightarrow$ 19/2 <sup>+</sup>	0.21(2)	0.77(12) <sup>4</sup>	-0.14(8)	M1+E2
699.7(1)	2187.4	13/2 <sup>+</sup> $\rightarrow$ 9/2 <sup>+</sup>	1.59(7)	0.90(7) <sup>4</sup>	0.11(3)	E2
700.2(1)	4117.8	27/2 <sup>-</sup> $\rightarrow$ 23/2 <sup>-</sup>	1.70(12)	1.02(2) <sup>4</sup>	0.05(3)	E2
703.2(1)	2238.3	15/2 <sup>+</sup> $\rightarrow$ 11/2 <sup>+</sup>	5.66(40)	1.04(1) <sup>4</sup>	0.04(1)	E2
704.3(1)	3230.9	19/2 <sup>+</sup> $\rightarrow$ 15/2 <sup>+</sup>	2.87(18)	1.10(3) <sup>4</sup>	0.08(3)	E2
705.4(1)	3061.5	17/2 <sup>+</sup> $\rightarrow$ 13/2 <sup>+</sup>	1.11(5)	1.15(5) <sup>4</sup>	0.14(3)	E2
707.5(1)	3486.4	21/2 <sup>+</sup> $\rightarrow$ 17/2 <sup>+</sup>	3.16(37)	1.05(7) <sup>4</sup>	0.08(2)	E2
711.8(1)	1872.2	13/2 <sup>+</sup> $\rightarrow$ 9/2 <sup>+</sup>	5.92(51)	1.01(1) <sup>4</sup>	0.07(1)	E2
753.4(1)	2625.6	17/2 <sup>+</sup> $\rightarrow$ 13/2 <sup>+</sup>	6.42(45)	0.95(2) <sup>4</sup>	0.05(1)	E2
755.5(1)	2993.8	17/2 <sup>+</sup> $\rightarrow$ 15/2 <sup>+</sup>	0.08(4)	0.73(5) <sup>4</sup>	-0.06(5)	M1+E2
769.8(1)	4512.1	31/2 <sup>-</sup> $\rightarrow$ 27/2 <sup>-</sup>	0.17(1)	1.74(6) <sup>5</sup>	0.04(3)	E2
776.9(1)	3838.4	21/2 <sup>+</sup> $\rightarrow$ 17/2 <sup>+</sup>	0.38(2)	0.91(8) <sup>4</sup>	0.19(4)	E2
783.5(1)	1310.8	9/2 <sup>+</sup> $\rightarrow$ 7/2 <sup>+</sup>	3.59(15)	1.03(2) <sup>5</sup>	-0.02(1)	M1(+E2)
795.8(1)	1323.1	11/2 <sup>-</sup> $\rightarrow$ 7/2 <sup>+</sup>	22(1)	1.08(1) <sup>4</sup>	-0.04(1)	M2
800.6(1)	4031.5	23/2 <sup>+</sup> $\rightarrow$ 19/2 <sup>+</sup>	1.08(5)	1.01(5) <sup>4</sup>	0.04(3)	E2
801.6(1)	3214.9	19/2 <sup>-</sup> $\rightarrow$ 15/2 <sup>-</sup>	0.36(3)	-	-	(E2)
811.1(1)	4297.5	25/2 <sup>+</sup> $\rightarrow$ 21/2 <sup>+</sup>	1.33(11)	1.22(12) <sup>4</sup>	0.07(6)	E2
813.1(1)	4930.9	31/2 <sup>-</sup> $\rightarrow$ 27/2 <sup>-</sup>	0.54(4)	0.96(4) <sup>4</sup>	0.10(3)	E2

Table 4.1: Continued...

$E_\gamma$ (keV)	$E_i$ (keV)	$J_i^\pi \rightarrow J_f^\pi$	$I_\gamma(\text{Err})$ <sup>1</sup>	$R_{DCO}(\text{Err})$	$\Delta_{PDCO}(\text{Err})$	Multipolarity
816.5(1)	2526.6	$15/2^+ \rightarrow 11/2^+$	5.36(22)	$1.02(2)^4$	0.09(1)	E2
820.5(1)	3058.8	$19/2^+ \rightarrow 15/2^+$	2.15(15)	$1.06(3)^4$	0.02(1)	E2
831.0(1)	4940.2	$33/2^- \rightarrow 29/2^-$	0.11(1)	$1.08(19)^4$	0.10(4)	E2
842.9(2)	4681.3	$25/2^+ \rightarrow 21/2^+$	0.23(2)	$0.91(12)^4$	0.07(5)	E2
847.2(1)	3906.0	$21/2^+ \rightarrow 19/2^+$	0.12(3)	$0.66(4)^4$	-0.11(6)	M1(+E2)
862.0(1)	4357.8	$23/2^- \rightarrow 21/2^-$	0.16(7)	$0.47(8)^4$	-0.10(6)	M1+E2
868.4(1)	2356.1	$13/2^+ \rightarrow 9/2^+$	2.25(9)	$0.92(14)^4$	0.20(11)	E2
871.4(1)	4902.9	$27/2^+ \rightarrow 23/2^+$	1.66(8)	$1.07(9)^4$	0.02(2)	E2
876.6(1)	2187.4	$13/2^+ \rightarrow 9/2^+$	9.76(69)	$1.06(2)^4$	0.07(1)	E2
885.4(1)	5397.5	$35/2^- \rightarrow 31/2^-$	0.09(1)	$1.05(13)^4$	0.04(4)	E2
886.0(1)	5183.5	$29/2^+ \rightarrow 25/2^+$	0.19(3)	$0.96(5)^4$	0.10(6)	E2
891.3(1)	3214.9	$19/2^- \rightarrow 15/2^-$	1.78(13)	-	-	(E2) <sup>6</sup>
898.4(1)	3524.2	$21/2^+ \rightarrow 17/2^+$	1.41(10)	$0.97(4)^4$	0.16(3)	E2
902.4(1)	4426.6	$25/2^+ \rightarrow 21/2^+$	0.27(2)	$1.00(11)^4$	0.11(6)	E2
907.8(1)	5838.7	$35/2^- \rightarrow 31/2^-$	0.18(2)	$1.05(13)^4$	0.05(4)	E2
917.6(1)	2228.4	$11/2^+ \rightarrow 9/2^+$	2.91(21)	$0.51(2)^4$	-0.05(3)	M1(+E2)
921.9(1)	5824.8	$31/2^+ \rightarrow 27/2^+$	0.09(3)	$1.13(26)^4$	0.14(7)	E2
935.8(1)	3994.6	$23/2^+ \rightarrow 19/2^+$	0.18(2)	$0.99(16)^4$	0.13(11)	E2
939.1(1)	6122.6	$33/2^{(+)} \rightarrow 29/2^+$	0.05(1)	$1.15(33)^4$	-	(E2)
944.4(1)	4003.2	$23/2^+ \rightarrow 19/2^+$	0.94(7)	$1.23(12)^4$	0.07(2)	E2
945.2(1)	5885.4	$37/2^- \rightarrow 33/2^-$	0.03(1)	$1.93(20)^5$	0.15(12)	E2
960.4(1)	1487.7	$9/2^+ \rightarrow 7/2^+$	7.99(32)	$0.89(2)^5$	-0.02(1)	M1+E2
989.4(1)	3227.7	$19/2^+ \rightarrow 15/2^+$	0.16(2)	$0.90(18)^4$	0.08(6)	E2
992.2(2)	6830.9	$39/2^- \rightarrow 35/2^-$	0.11(2)	$0.96(19)^4$	0.08(6)	E2
1000.5(1)	2323.6	$15/2^- \rightarrow 11/2^-$	41(3)	$0.94(2)^4$	0.03(1)	E2
1006.8(1)	6404.3	$(39/2^-) \rightarrow 35/2^-$	0.02(1)	-	-	(E2)
1008.9(1)	1536.2	$9/2^+ \rightarrow 7/2^+$	2.48(10)	$1.07(4)^5$	-0.07(2)	M1(+E2)
1014.7(1)	4073.5	$21/2^+ \rightarrow 19/2^+$	0.47(4)	$0.63(5)^4$	-0.05(3)	M1(+E2)

Table 4.1: Continued...

$E_\gamma$ (keV)	$E_i$ (keV)	$J_i^\pi \rightarrow J_f^\pi$	$I_\gamma(\text{Err})$ <sup>1</sup>	$R_{DCO}(\text{Err})$	$\Delta_{PDCO}(\text{Err})$	Multipolarity
1026.7(2)	5029.9	$27/2^+ \rightarrow 23/2^+$	0.12(4)	$1.21(34)^4$	0.26(14)	E2
1033.2(1)	4557.4	$25/2^+ \rightarrow 21/2^+$	0.27(8)	$0.90(24)^4$	0.20(8)	E2
1045.3(1)	2356.1	$13/2^+ \rightarrow 9/2^+$	6.14(44)	$1.05(3)^4$	0.05(2)	E2
1061.9(1)	2772.0	$15/2^+ \rightarrow 11/2^+$	0.06(2)	$0.92(5)^4$	0.18(12)	E2
1072.1(1)	3697.7	$19/2^- \rightarrow 17/2^+$	0.33(2)	$0.59(8)^4$	0.09(8)	E1
1076.8(1)	7907.7	$43/2^- \rightarrow 39/2^-$	0.11(3)	$0.95(13)^4$	0.23(6)	E2
1089.4(1)	1089.4	$7/2^+ \rightarrow 5/2^+$	35(2)	$0.30(2)^4$	-0.06(2)	M1+E2
1090.2(1)	2413.3	$15/2^- \rightarrow 11/2^-$	11.20(78)	$0.98(2)^4$	0.04(1)	E2
1106.2(1)	3731.8	$19/2^+ \rightarrow 17/2^+$	0.34(3)	$0.64(9)^4$	-0.10(5)	M1(+E2)
1125.8(2)	3751.4	$21/2^+ \rightarrow 17/2^+$	0.18(2)	$0.91(16)^4$	0.18(11)	E2
1133.5(2)	3005.7	$15/2^- \rightarrow 13/2^+$	0.19(2)	$0.42(9)^4$	0.26(7)	E1
1160.4(1)	1160.4	$9/2^+ \rightarrow 5/2^+$	100(1)	$1.02(1)^4$	0.05(2)	E2
1182.8(1)	1710.1	$11/2^+ \rightarrow 7/2^+$	9.90(40)	$1.10(3)^4$	0.02(1)	E2
1201.9(1)	3440.2	$17/2^+ \rightarrow 15/2^+$	0.51(4)	$0.64(10)^4$	-0.15(9)	M1(+E2)
1234.3(1)	1761.6	$9/2^+ \rightarrow 7/2^+$	1.42(6)	$0.93(3)^5$	-0.06(2)	M1(+E2)
1310.8(1)	1310.8	$9/2^+ \rightarrow 5/2^+$	27.73(29)	$0.96(2)^4$	0.04(2)	E2
1323.1(1)	1323.1	$11/2^- \rightarrow 5/2^+$	67.62(94)	$1.19(1)^4$	0.05(3)	E3
1472.3(1)	1472.3	$9/2^+ \rightarrow 5/2^+$	5.89(11)	$1.27(19)^4$	0.11(6)	E2
1511.9(2)	2039.2	$11/2^+ \rightarrow 7/2^+$	1.02(5)	$1.11(9)^4$	0.07(3)	E2
1536.2(1)	1536.2	$9/2^+ \rightarrow 5/2^+$	0.47(4)	-	-	(E2)
1761.6(1)	1761.6	$9/2^+ \rightarrow 5/2^+$	0.11(2)	$1.26(22)^4$	-	(E2)

<sup>1</sup>Relative  $\gamma$ -ray intensities are estimated from the relevant coincidence gates of transitions feeding to the ground state and then normalized to the intensity of 1160.4-keV  $\gamma$ -ray in prompt singles spectrum.

<sup>2</sup>Transition not observed in present work, adopted from Ref. [8].

<sup>3</sup>Transition not observed in present work, adopted from Ref. [20].

<sup>4</sup>From quadrupole gate.

<sup>5</sup>From dipole gate.

<sup>6</sup>Adopted from Ref. [20].

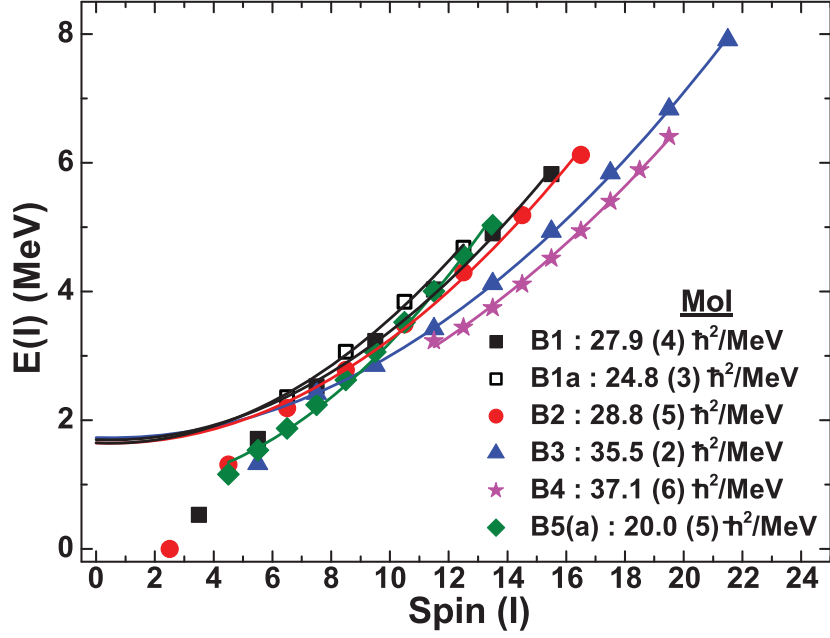


Figure 4.10: Excitation energy ( $E(I)$ ) as a function of level spin ( $I$ ) for the bands of  $^{117}\text{Sb}$ .

## 4.4 Discussion

The nucleus  $^{117}\text{Sb}$ , with one proton above the Sn core ( $Z = 50$ ) and neutrons at the middle of the  $N = 50 - 82$  shell, reveals various single particle structures as well as deformed bands. The various low-lying states in  $^{117}\text{Sb}$  are mainly attributed as to arise due to the odd valence proton occupying the available orbitals above  $Z = 50$  shell (*i.e.*  $\pi g_{7/2}$ ,  $\pi d_{5/2}$ ,  $\pi h_{11/2}$ ). The ground state ( $5/2^+$ ) and the first excited state ( $7/2^+$ ) of  $^{117}\text{Sb}$  result from the coupling of odd proton in  $\pi d_{5/2}$  and  $\pi g_{7/2}$  orbital with the ground state of  $^{116}\text{Sn}$ . On the other hand, the observed decoupled rotational band structures are interpreted as the coupling of the valence proton with the  $2p - 2h$  deformed structures in  $^{116}\text{Sn}$ . The present work mainly reports the observation of signature partner bands (bands B1 and B1(a)) having the configuration involving  $\pi g_{7/2}$ . Moreover, a number of new non-yrast states have been reported in the low and medium spin region. Other than these, a band-like sequence B1(b) on  $13/2^+$  state and two short sequences B6(a) and B6(b) on top of the  $15/2^-$  state, involving mainly  $\pi h_{11/2}$  contribution, have been identified for the first time.

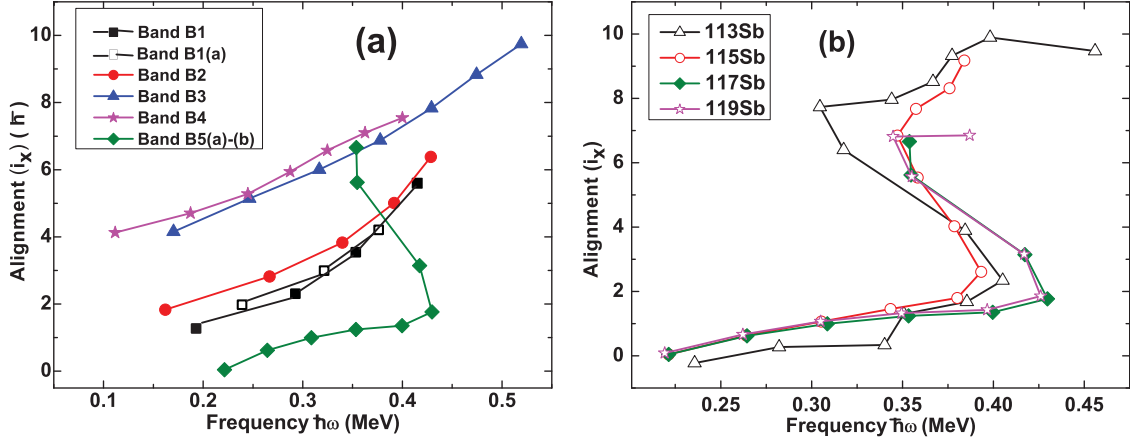


Figure 4.11: Aligned angular momentum ( $i_x$ ) of (a) various band structures in  $^{117}\text{Sb}$  and (b) the band B5(b) of  $^{117}\text{Sb}$  and same band of similar configurations in odd mass Sb isotopes as a function of rotational frequency  $\hbar\omega$ . Harris reference parameters of  $J_0 = 17$  and  $J_1 = 12$  have been taken from Ref. [11].

The  $E(I)$  (level energy) *vs.*  $I$  (level spin) of band B1 and B1(a) along with the other observed band structures in  $^{117}\text{Sb}$  are plotted in Fig. 4.10, which shows their rotational character. All the band structures are well fitted with the parabolic rotational model formula,  $E(I) = E_0 + (\hbar^2/2\mathcal{J}) * I * (I + 1)$ , where,  $\mathcal{J}$  is the moment of inertia of the band and  $E_0$  is a parameter corresponding to the initial energy of the band. Different slopes of the parabolas of different band structures correspond to the different moments of inertia of the bands. It can be seen from the Fig. 4.10, that the lower spin members of the bands B1 and B1(a) do not follow the same fitted parabola which indicate rotational nature of these bands develops from slightly higher spins. The pure band like structure of the band B1 and B1(a) develops after the  $11/2^+$  level which corresponds to the coupling of the  $\pi g_{7/2}$  orbital with the  $2^+$  state of the even-even  $^{116}\text{Sn}$  core. This nature is also evident for the bands B2 and B3 which involve  $\pi d_{5/2}$  and  $\pi h_{11/2}$  configurations, respectively. These two bands show band-like sequences beyond  $13/2^+$  and  $15/2^-$  levels, respectively. It is also found that the bands B1, B2 and B5, involving single protons in  $\pi g_{7/2}$ ,  $\pi d_{5/2}$  and  $\pi g_{9/2}$  orbitals, respectively, have similar and smaller Moment of Inertia (MoI), as expected. On the other hand, the band B3 having single proton in  $\pi h_{11/2}$  orbital, show relatively higher MoI, indicating higher deformation and consequently, larger

shape driving effect of the high-j  $\pi h_{11/2}$  orbital. The band B4 is built on the  $23/2^-$  isomer with the configuration of  $[(\pi g_{7/2} d_{5/2})^2 \otimes (\pi g_{9/2})^{-1}] \otimes \nu 7^-$ ,  $\nu 7^-$  representing the  $(\nu h_{11/2} d_{3/2})$  configuration of the  $7^-$  state in  $^{116}\text{Sn}$  core [20].

The variation of the aligned angular momentum ( $i_x$ ) as a function of the rotational frequency ( $\hbar\omega$ ) of the bands B1 and B1(a) along with the other bands is shown in Fig. 4.11(a). The bands B1 and B1(a) have similar aligned angular momentum ( $i_x$ ), which is expected for the signature partner bands. The initial alignment of the band B5 is much less since it is based on a high- $\Omega$  orbital, whereas, the initial alignment of band B3 has been found to be higher and similar to that of the 5-qp band B5, as the band B3 is built on the low- $\Omega$  component of the high-j,  $\pi h_{11/2}$  orbital.

The aligned angular momentum of the band B5(b) of odd mass Sb isotopes, mass ranging from 113 to 119, is plotted in Fig. 4.11(b). It is found that  $^{117}\text{Sb}$  and  $^{119}\text{Sb}$  show identical bending frequency ( $\hbar \sim 0.43$  MeV) with similar alignment gain. But the lower mass isotopes show bending at a little lower frequency compared to the  $^{117,119}\text{Sb}$ . The observed alignment gain in  $^{117,119}\text{Sb}$  of  $\sim 7\hbar$  in this band can be explained as neutron alignment in  $h_{11/2}$  orbital. Such kind of alignment in this  $2p - 1h$  band is already reported in  $Z = 53, 55$  isotones.

The variation of the kinematic moments of inertia ( $\vartheta^{(1)}$ ) as a function of the rotational frequency ( $\hbar\omega$ ) of the signature partner bands along with the other band structures in  $^{117}\text{Sb}$  are plotted in Fig. 4.12. It can be seen from the Fig. 4.12 that the bands B1 and B1(a), involving  $\pi g_{7/2}$ , have similar  $\vartheta^{(1)}$ , as expected for the signature partner bands. The  $\vartheta^{(1)}$  of bands B2 and B5 are also close to that of B1 and B1(a), except the fact that the particle alignment of band B5 is reflected at a frequency of  $\hbar\omega \sim 0.45$  MeV. The  $\vartheta^{(1)}$  of the bands B3 and B4 are found to be higher compared to the other band structures, due to the involvement of the  $\pi h_{11/2}$  orbital in B3 and five quasiparticle configuration of the band B4. The sharp decreasing trend of  $\vartheta^{(1)}$  with frequency for the band B4 indicates that the dominant contribution to the total angular momentum comes from the multi-quasiparticle alignment rather than collective rotation.

The new positive parity states observed below 2 MeV are mostly due to the single particle excitations involving the odd proton above  $Z = 50$  and its coupling to the corresponding

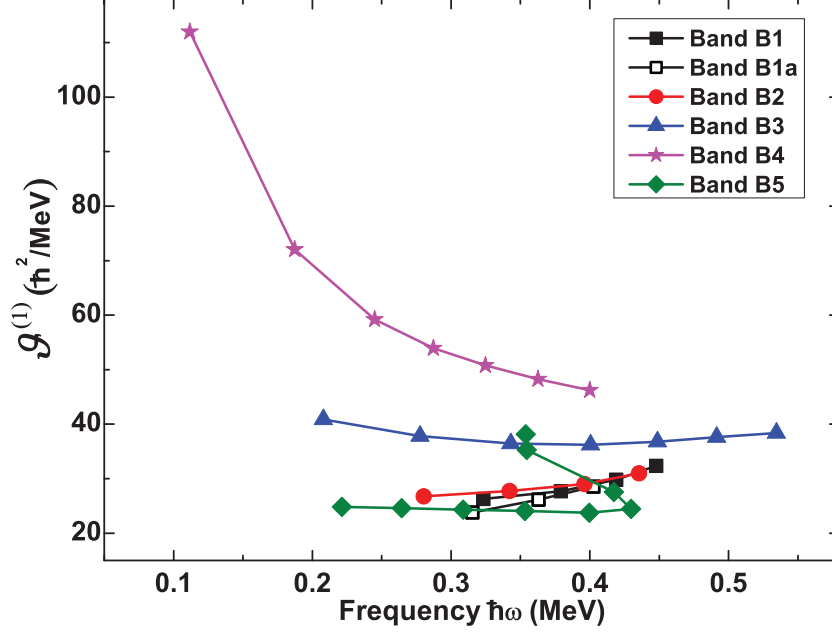


Figure 4.12: Kinematic moment of inertia ( $\mathcal{I}^{(1)}$ ) of various band structures in  $^{117}\text{Sb}$  as a function of rotational frequency  $\hbar\omega$ .

spherical single particle states in the  $^{116}\text{Sn}$  core. These states also connect to the lower spin members of the decoupled bands B1 and B2 based on the  $\pi g_{7/2}$  and  $\pi d_{5/2}$  proton coupled to the  $2p - 2h$  structure of  $^{116}\text{Sn}$ , respectively. The connections between the states originating from the single particle excitations and the states of the decoupled bands indicate mixing of various configurations at low spin. The two short sequences B6(a) and B6(b) are developed on the  $15/2^-$  state, involving mainly the  $\pi h_{11/2}$  contribution. The other set of levels at higher excitation, reported in the present work, are the non-yrast excitations decaying to the band B5 by various parallel transitions. As the band B5 is known to have  $2p - 1h$  configuration involving  $\pi g_{9/2}$  hole excitation [8] across the  $Z = 50$  core, so the single particle states connecting to the band B5 also expected to involve the  $\pi g_{9/2}$  hole excitation.

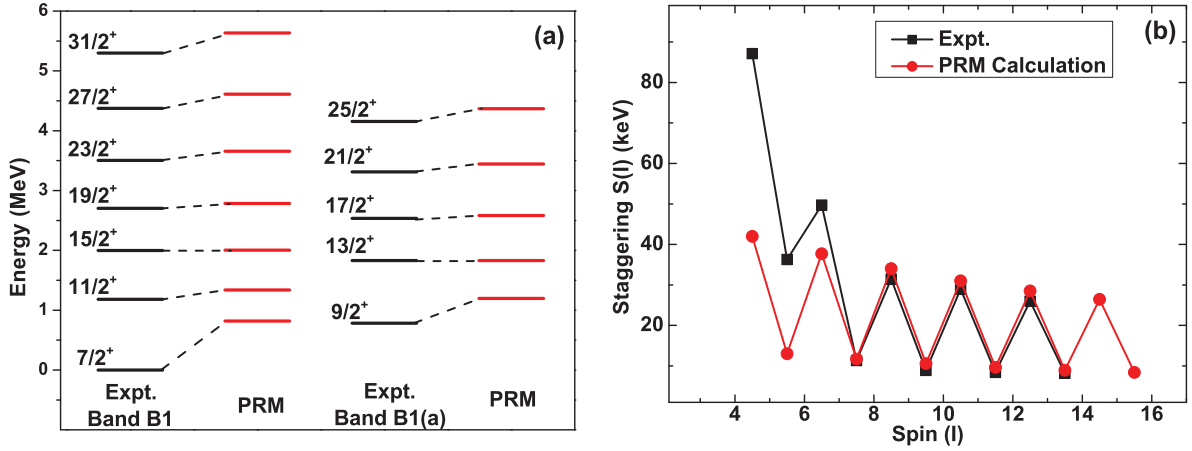


Figure 4.13: Comparison of the experimental (a) energy levels and (b) the energy staggering of the band B1 and B1(a) with that obtained from present PRM calculations. The energy levels are plotted with respect to the  $13/2^+$  state.

## 4.5 PRM calculations

In an attempt to understand the character of the bands B1 and B1(a) and to investigate the observed signature splitting between these two partner bands, Particle Rotor Model (PRM) calculations using PRM code [31], incorporating the Variable Moment of Inertia (VMI) formalism, have been carried out. The theoretical study shows that the bands are based on the low- $\Omega$  Nilsson orbital, dominated largely by the  $\pi g_{7/2}$  with deformation  $\beta_2 \sim 0.15$ . The parameters  $\mu$  and  $\kappa$ , have been suitably chosen [32], to obtain the best fit in this mass region. The Fermi level has been chosen close to  $1/2[431]$ , a down-sloping (for prolate deformation) Nilsson orbital. The obtained value of the elastic constant of the VMI model is  $0.8 \times 10^7 \text{ keV}^3$ , which signifies that the nucleus is not particularly soft towards deformation.

The theoretically obtained levels have been compared with the experimental ones in Fig. 4.13(a). The calculated level energies are plotted in Fig. 4.13(a) with a normalization in the  $13/2^+$  state. It can be seen that the theory overestimates the low-lying levels but it is extremely successful to reproduce the experimental data above the  $11/2^+$  state. This is also consistent with the fact that the lower spin members of this bands, B1 and B1(a), have significant mixing of

different configurations. The large signature splitting (*i.e.* staggering) between the signature partner bands is also supported by the theoretical PRM calculations. It indicates strong Coriolis interaction between the valence particle with the core. The energy staggering parameter, defined by,  $S(I) = [E(I) - E(I - 1)]/2I$ , where,  $E(I)$  is the level energy of the state with spin  $I$ , is plotted as a function of the spin ( $I$ ) for the bands B1 and B1(a) in the Fig. 4.13(b). It can be seen from the figure that an excellent agreement is obtained between the experimental results and the calculated data, only except for the first few state. Therefore, it can be concluded that the  $\pi g_{7/2}$  orbital induces axial deformation to the even-even Sn core.

## 4.6 Shell model calculations

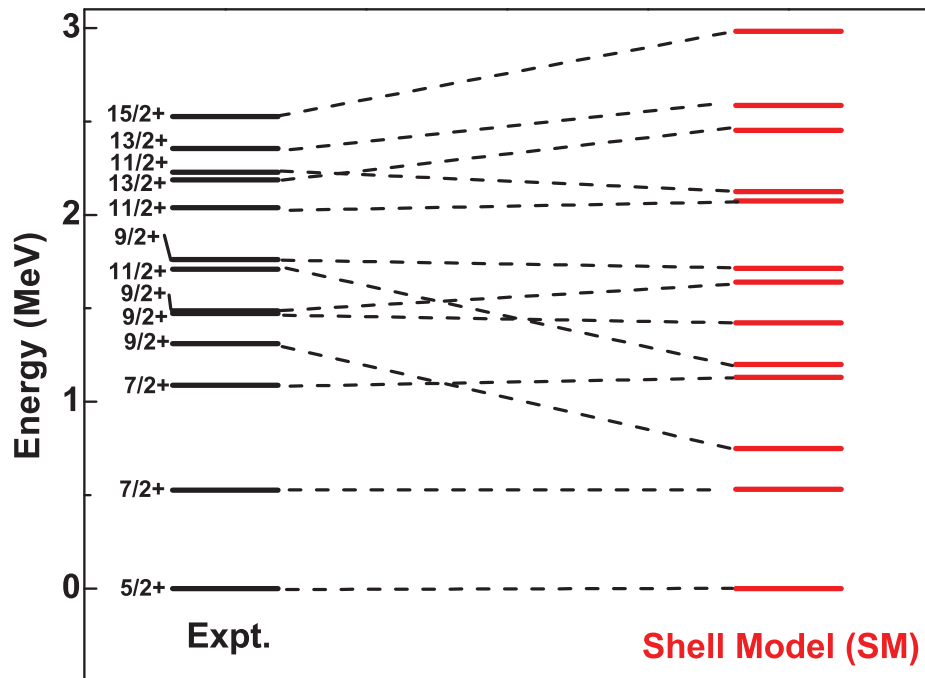


Figure 4.14: Comparison of the experimentally observed low-lying states with that of the Shell Model calculation.

Table 4.2: Experimental excitation energy ( $E_x$ ), spin ( $J^\pi$ ) and their calculated configurations with % contribution of the positive parity low lying states in  $^{117}\text{Sb}$ , as obtained from the shell model calculations. Contributions above 10% of the configurations are only tabulated.

Spin ( $J^\pi$ )	$E_x$ (Expt.) (in keV)	Configuration	Contribution
5/2 <sup>+</sup>	0	$\pi(d_{5/2})^1 \otimes \nu[(d_{5/2})^6(s_{1/2})^2]$	37%
		$\pi(d_{5/2})^1 \otimes \nu[(d_{5/2})^6(d_{3/2})^2]$	36%
7/2 <sup>+</sup>	527	$\pi(g_{7/2})^1 \otimes \nu[(d_{5/2})^6(s_{1/2})^2]$	51%
		$\pi(g_{7/2})^1 \otimes \nu[(d_{5/2})^6(d_{3/2})^2]$	27%
7/2 <sup>+</sup>	1089	$\pi(d_{5/2})^1 \otimes \nu[(d_{5/2})^6(d_{3/2})^1(s_{1/2})^1]$	69%
		$\pi(d_{5/2})^1 \otimes \nu[(d_{5/2})^5(d_{3/2})^2(s_{1/2})^1]$	19%
9/2 <sup>+</sup>	1311	$\pi(d_{5/2})^1 \otimes \nu[(d_{5/2})^6(d_{3/2})^1(s_{1/2})^1]$	64%
		$\pi(d_{5/2})^1 \otimes \nu[(d_{5/2})^6(d_{3/2})^2]$	16%
9/2 <sup>+</sup>	1472	$\pi(g_{7/2})^1 \otimes \nu[(d_{5/2})^6(d_{3/2})^1(s_{1/2})^1]$	78%
		$\pi(g_{7/2})^1 \otimes \nu[(d_{5/2})^5(d_{3/2})^2(s_{1/2})^1]$	10%
9/2 <sup>+</sup>	1488	$\pi(d_{5/2})^1 \otimes \nu[(d_{5/2})^6(d_{3/2})^2]$	43%
		$\pi(g_{7/2})^1 \otimes \nu[(d_{5/2})^6(d_{3/2})^1(s_{1/2})^1]$	20%
		$\pi(d_{5/2})^1 \otimes \nu[(d_{5/2})^6(d_{3/2})^1(s_{1/2})^1]$	12%
9/2 <sup>+</sup>	1762	$\pi(g_{7/2})^1 \otimes \nu[(d_{5/2})^6(d_{3/2})^1(s_{1/2})^1]$	30%
		$\pi(g_{7/2})^1 \otimes \nu[(d_{5/2})^6(d_{3/2})^2]$	20%
		$\pi(d_{5/2})^1 \otimes \nu[(d_{5/2})^6(d_{3/2})^2]$	16%
		$\pi(g_{7/2})^1 \otimes \nu[(d_{5/2})^5(d_{3/2})^2(s_{1/2})^1]$	10%
11/2 <sup>+</sup>	1710	$\pi(g_{7/2})^1 \otimes \nu[(d_{5/2})^6(d_{3/2})^1(s_{1/2})^1]$	66%
		$\pi(g_{7/2})^1 \otimes \nu[(d_{5/2})^6(d_{3/2})^2]$	16%
11/2 <sup>+</sup>	2039	$\pi(g_{7/2})^1 \otimes \nu[(d_{5/2})^6(d_{3/2})^2]$	70%
		$\pi(g_{7/2})^1 \otimes \nu[(d_{5/2})^6(d_{3/2})^1(s_{1/2})^1]$	15%
11/2 <sup>+</sup>	2228	$\pi(d_{5/2})^1 \otimes \nu[(d_{5/2})^5(d_{3/2})^1(s_{1/2})^2]$	67%
		$\pi(d_{5/2})^1 \otimes \nu[(d_{5/2})^5(d_{3/2})^3]$	12%
13/2 <sup>+</sup>	2187	$\pi(d_{5/2})^1 \otimes \nu[(d_{5/2})^5(d_{3/2})^1(s_{1/2})^2]$	71%
		$\pi(d_{5/2})^1 \otimes \nu[(d_{5/2})^5(d_{3/2})^2(s_{1/2})^1]$	10%
13/2 <sup>+</sup>	2356	$\pi(g_{7/2})^1 \otimes \nu[(d_{5/2})^5(d_{3/2})^1(s_{1/2})^2]$	72%
		$\pi(g_{7/2})^1 \otimes \nu[(d_{5/2})^5(d_{3/2})^2(s_{1/2})^1]$	10%
15/2 <sup>+</sup>	2526	$\pi(g_{7/2})^1 \otimes \nu[(d_{5/2})^5(d_{3/2})^1(s_{1/2})^2]$	78%
		$\pi(g_{7/2})^1 \otimes \nu[(d_{5/2})^5(d_{3/2})^2(s_{1/2})^1]$	11%

The new positive parity states below 2 MeV, observed in this work, are dominantly generated from the single particle excitations of the valence proton above the  $Z = 50$  core and its coupling to the spherical and deformed states of the  $^{116}\text{Sn}$  core. To understand the single particle configurations of this states, large basis shell model calculations are carried out using OXBASH [23]. The  $\text{sn100pn}$  effective interaction [24] with  $^{100}\text{Sn}$  as a core is used for current calculations. The model space, used for this calculation, consists of the orbitals  $g_{7/2}$ ,  $d_{5/2}$ ,  $d_{3/2}$ ,  $s_{1/2}$  and  $h_{11/2}$  for both protons and neutrons. As the  $\pi g_{9/2}$  orbital, situated in the other shell, has not been considered in the model space, the  $9/2^+$  state in the band B5(a) can not be characterised in the present calculation. The calculations have been carried out with no restriction in the proton model space but the neutrons are restricted such that the  $\nu g_{7/2}$  orbital is always filled whereas no particle excitation is considered in the  $\nu h_{11/2}$  orbital. This restriction in neutron space is justified as the valence proton is expected to play the major role in generating the low spins.

Fig. 4.14 shows the comparison between the experimentally observed low spin positive parity levels with those obtained from the present Shell Model (SM) calculations. It is evident from Fig. 4.14 that the experimental positive parity states match quite well with the shell model calculations, except the first  $9/2^+$  and the first  $11/2^+$  states. These states are under predicted by  $\sim 500$  keV. It should be noted that, these two states are also part of the rotational bands and discussed in terms of mixed configurations of spherical and deformed shapes in the previous sections. The major contributions (above 10%) of the configurations for a particular state are tabulated in Table 4.2. It is clear from the table that the ground state has a dominant  $\pi d_{5/2}^1$  proton configuration which couples with the spherical Sn core. The first excited state  $7/2^+$  (527 keV) is found to have dominant contribution of  $\pi g_{7/2}$  orbital.

The other set of levels, decaying to the various states of the band B5(a), are not possible to obtain in the present shell model calculations. The band B5(a) is known to have the  $2p - 1h$  configuration of  $[(\pi g_{7/2})^2 \otimes (\pi g_{9/2})^{-1}]$ . Thus, the new set of levels, connecting to the band B5, are expected to involve the above  $2p - 1h$  configuration. Such particle-hole excitation across the  $Z = 50$  shell is not within the scope of the present SM calculation.

## 4.7 Summary

Excited states of  $^{117}\text{Sb}$  have been studied by populating it using  $\alpha$  induced fusion evaporation reaction. The existing level scheme is extended with the placement of 31 new transitions. Several new non-yrast transitions are also identified. The spin-parities of the excited states are determined. The signature partner of the band, having configuration  $\pi g_{7/2}$ , is observed for the first time. Particle Rotor Model (PRM) calculations have been carried out to explain the large signature splitting of the observed signature partner bands. A weak coupling nature involving the low- $\Omega$  component of the  $\pi g_{7/2}$  band is established from this work. The lower-spin levels are interpreted on the basis of large-scale shell-model calculations using OXBASH.

# Bibliography

- [1] K. Heyde, P. Van Isacker, M. Waroquier, J. L. Wood and R. A. Meyer, Phys. Rep., **102**, 291 (1983).
- [2] K. Heyde, M. Waroquier, H. Vincx and P. Van Isacker, Phys. Lett., **64B**, 135 (1976).
- [3] A. Savelius *et al.*, Nucl. Phys. **A637**, 491 (1998).
- [4] D.R. LaFosse *et al.*, Phys. Rev. C, **50**, 1819 (1994).
- [5] P. Banerjee *et al.*, Phys. Rev. C, **87**, 034321 (2013).
- [6] R. S. Chakrawarthy and R. G. Pillay, Phys. Rev. C, **54**, 2319 (1996).
- [7] D. R. LaFosse *et al.*, Phys. Rev. C **56**, 760 (1997).
- [8] R. E. Shroy, A. K. Gaigalas, G.Schatz and D.B.Fossan, Phys. Rev. C, **19**, 1324 (1979).
- [9] A. K. Gaigalas, R. E. Shroy, G. Schatz and D. B. Fossan, Phys. Rev. Lett., **35**, 555 (1975).
- [10] J. Bron *et al.*, Nucl. Phys. A **318**, 335 (1979).
- [11] V. P. Janzen *et al.*, Phys. Rev. Lett. **70**, 1065 (1993).
- [12] D. R. LaFosse *et al.*, Phys. Rev. Lett. **69**, 1332, (1992).
- [13] S. Tormanen *et al.*, Nucl. Phys. A **613**, 282 (1997).
- [14] S. Ohya, Nuclear Data Sheet, **111**, 1619 (2010).
- [15] G. Berzins *et al.*, Nucl. Phys. A, **104**, 241 (1967)

- [16] W. D. Fromm *et al.*, Nucl. Phys. A, **243**, 9 (1975).
- [17] Yu. N. Lobach, D. Bucurescu, Phys. Rev. C, **58**, 1515 (1998).
- [18] Yu. N. Lobach and V. V. Trishin, Phys. Atomic Nuclei **58**, 1079 (1995).
- [19] D. Bucurescu *et al.*, Phys. Rev. C, **52**, 616 (1995).
- [20] M. Ionescu-Bujor *et al.*, Nucl. Phys. A, **466**, 317 (1987).
- [21] Soumik Bhattacharya *et al.*, Proc. of DAE-BRNS Symp. on Nucl. Phys. **61**, 98 (2016).
- [22] Soumik Bhattacharya *et al.*, Phys. Rev. C **98**, 044311 (2018).
- [23] S. Das *et al.*, Nucl. Instr. and Methods in Phys. Res. A, **893**, 138 (2018).
- [24] D. C. Radford, Nucl. Instrum. Methods Phys. Res. A, **361**, 297 (1995).
- [25] <http://www.tifr.res.in/~pell/lamps.html>
- [26] A. Kramer-Flecken *et al.*, Nucl. Instrum. Methods Phys. Res. A **275**, 333 (1989).
- [27] K. Starosta *et al.*, Nucl. Instrum. Methods Phys. Res. A **423**, 16 (1999).
- [28] Ch. Droste *et al.*, Nucl. Instrum. Methods Phys. Res. A **378**, 518 (1996).
- [29] R. Banik *et al.*, Phys. Rev. C **101**, 014322 (2020).
- [30] R. Bengtsson and S. Frauendorf, *et al.*, Nucl. Phys. A **327**, 139 (1979).
- [31] S. Bhattacharya, S. Sen and R. K. Guchhait, Phys. Rev. C, **32**, 1026, (1985).
- [32] Jing-ye Zhang, N. Xu, D. B. Fossan, Y. Liang, R. Ma and E. S. Paul, Phys. Rev. C **39**, 714 (1989).
- [33] Oxbash for Windows, B. A. Brown *et al.*, MSU-NSCL report number 1289 (2004).
- [34] B. A. Brown, N. J. Stone, J. R. Stone, I. S. Towner and M. Hjorth-Jensen, Phys. Rev. C **71**, 044317 (2005).

# Chapter 5

## Yrast and non-yrast band structures in $^{131}\text{Xe}$

### 5.1 Introduction

Nuclei in the mass 130 – 140 region are known to have variety of nuclear shapes and exhibit different exotic modes of excitations. The transitional nuclei in  $A \sim 130$  region, having proton number above the  $Z = 50$  shell and neutron number below the  $N = 82$  shell, provide rich variety of single particle and collective structures and their coexistence [1, 2, 3]. Near the  $N = 82$  shell closure, vibrational bands are more prominent, signifying spherical structures while addition of neutron holes induces deformation to the system and rotational bands are observed. Transitional nature is seen for the nuclei having few numbers of neutron holes and proton particles with respect to the  $^{132}\text{Sn}$  core. The structures of these transitional nuclei are determined by the shape driving effect of the available orbitals. Most of the even-even nuclei in this transitional region are known to depict  $\gamma$  softness [4]. It is, therefore, possible that the addition of an extra nucleon drives the structure of an odd- $A$  nucleus towards different shapes, depending upon the shape driving effect of the valence orbital. In this context, it is very interesting to study the various band structures of odd- $A$  nuclei in the transitional  $A \sim 130$

region, which will provide important information about the shape driving effects of different orbitals. Such effects of some of the neutron orbitals have been reported in this region from the observation of different rotational band structures [5, 6]. Moreover, the Fermi surfaces of both proton and neutron of the nuclei in this mass region lie within the same major shell *i.e.*  $Z, N = 50 - 82$ . Hence, proton particles and neutron holes can occupy different (*e.g.* low- $\Omega$  and high- $\Omega$ ) components of the same, high- $j$ ,  $h_{11/2}$  orbital. Therefore, different polarizing effects of these components should be manifested in the level structure of the same nucleus. The unique-parity, high- $j$   $h_{11/2}$  orbital plays key role in generating the high spin states and is also responsible for the presence of long lived isomers at low exciting energy, in these odd-A nuclei. Various theoretical models have been employed to explain the different aspects of the level structures of nuclei, such as, Strutinsky mean-field methods [7], Interacting Boson Model [8, 9], Pair Truncated Shell Model [10], Large Scale Shell Model [11, 12] *etc.*

The Xe ( $Z = 54$ ) isotopes, with four proton particles above the  $Z = 50$  core and neutron numbers just below the  $N = 82$  core, are thus suitable candidates to study the various interesting features of transitional nuclei in this region. Particularly, the odd-A Xe isotopes are of interest to understand the coupling of the odd neutron to the rotational structure of the corresponding even-even core and other possible multi-qp band structures. Rotational bands with large quadrupole moments have been reported in  $^{125}\text{Xe}$  [13] at high spins and rotational band on a three quasi-neutron isomer with a rotational alignment of a pair of neutron in the  $h_{11/2}$  orbital have been observed in  $^{127}\text{Xe}$  [14, 15]. Also triaxial band structures were demonstrated in  $^{129}\text{Xe}$  [16]. On the other hand, in  $^{123}\text{Xe}$  [17], a dipole band was proposed to have Magnetic Rotational (MR) character and explained by tilted axis configuration  $\pi h_{11/2}^1 \otimes \nu h_{11/2}^{-1}$ . Although, such MR bands are more probable as the neutron number approaches the  $N = 82$  shell closure, but such bands could not be seen in  $^{125,129}\text{Xe}$ . This could be possible either if the particular configuration for such MR band is not populated or because the shapes of these nuclei are not near spherical. For heavier isotopes of Xe, close to the  $N = 82$  shell closure, near-spherical shapes are expected, which could result into MR bands, but the high spin spectroscopic information are very limited. Therefore, in order to investigate the various coupling and to understand the systematics of the different multi-qp configurations of the odd-A  $^{131}\text{Xe}$

isotope, it is necessary to have detailed spectroscopic information of both yrast and non-yrast states.

The population of  $^{131}\text{Xe}$  is difficult due to the unavailability of suitable stable target and heavy-ion projectile combination. The structure of  $^{131}\text{Xe}$  was first studied using offline decay spectroscopy technique [4, 19] and Coulomb excitation measurements [20]. Angular correlation measurements were also carried out for a few states of  $^{131}\text{Xe}$  [21] to assign the spin and parity to some of these states. The first in-beam measurements of the high spin states of  $^{131}\text{Xe}$  were performed using  $(\alpha, 3n)$  [22] and  $(\alpha, n)$  [3] reactions with a few Ge(Li) detectors, where, one- and three-qp states at low spins were identified. Detailed spectroscopic information about  $^{131}\text{Xe}$  could not be obtained in these studies, mainly due to the limitation of the detection systems. Recently, excited states in  $^{131}\text{Xe}$  at higher spins have been reported by Kaya *et al.* [12], using multi-nucleon transfer reaction involving  $^{136}\text{Xe}$  beam and the  $^{124}\text{Sn}(^{11}\text{B}, p3n)$  reaction. The yrast negative parity band, built on the  $11/2^-$  long lived isomer, in  $^{131}\text{Xe}$  was extended up to 4.9 MeV by Kaya *et al.*, with the placement of three new  $\gamma$  transitions. No other band structures could be identified by them. The spin and parity of few states were also assigned tentatively in Ref. [12].

In the present thesis work, the yrast and non-yrast states of  $^{131}\text{Xe}$  have been populated via  $\alpha$ -induced fusion-evaporation reaction and are studied using Indian National Gamma Array (INGA). The present study reports various new yrast and non-yrast band structures in  $^{131}\text{Xe}$  involving different single- and multi-qp configurations.

## 5.2 Experiment and Data Analysis

In the present work,  $^{131}\text{Xe}$  have been populated using the reaction  $^{130}\text{Te}(\alpha, 3n)^{131}\text{Xe}$  at an beam energy of 38 MeV delivered from the K-130 cyclotron at Variable Energy Cyclotron Centre, Kolkata (India). An enriched  $^{130}\text{Te}$  target of thickness  $2\text{ mg/cm}^2$ , with a  $600\text{ }\mu\text{g/cm}^2$  Mylar backing, was used. The Indian National Gamma Array (INGA) having seven Compton suppressed Clover HPGe detector at VECC [23], Kolkata, was used for detecting the emitted  $\gamma$

rays from the produced nuclei. Time stamped list mode data were acquired using the PIXIE-16 250 MHz 12-bit digitizer modules [24] in both coincidence ( $M_\gamma \geq 2$ ) and singles ( $M_\gamma \geq 1$ ) mode. Details of the setup and data acquisition can be found in Chapter 3 of this thesis. Standard  $^{133}\text{Ba}$  and  $^{152}\text{Eu}$  radioactive sources, were used for energy and efficiency calibration of the setup.

The data from all the detectors were gain matched to 0.5 keV/channel and then sorted using the IUCPIX [24] data sorting package to construct the symmetric and angle dependent  $E_\gamma$ - $E_\gamma$  matrices and the  $E_\gamma$ - $E_\gamma$ - $E_\gamma$  cube. The RADWARE [25] and LAMPS [26] analysis packages were then used to analyze these matrices and the cube to develop the new level scheme.

The spin-parities of the excited states of  $^{131}\text{Xe}$  have been assigned from the measured  $R_{DCO}$  [27] and  $\Delta_{PDCO}$  [28, 29] values. In this study, the typical  $R_{DCO}$  value is found to be  $\sim 1.9$  (0.6) for a stretched quadrupole (dipole) transition, when gated by a stretched dipole (quadrupole) transition. One dimensional projection of the symmetric  $E_\gamma$ - $E_\gamma$  matrix, as obtained in the present work, is shown in Fig. 5.1. In this figure, the marked  $\gamma$ -rays are mostly from  $^{131}\text{Xe}$ , which indicates the unique property of  $\alpha$ -induced reaction that it produces mostly a particular channel with large cross-section.

### 5.3 Results

The new level scheme of  $^{131}\text{Xe}$ , as obtained from the current measurements, is shown in Fig. 5.2. The level structure is significantly extended, compared to the previous studies [22, 12], with the observation and placement of 72 new  $\gamma$  rays in the level scheme of  $^{131}\text{Xe}$  [30]. It is evident from Fig. 5.2 that the level scheme has been expanded above the  $11/2^-$  isomer (11.84 days) at 164 keV excitation, as well as above the  $3/2^+$  ground state. The various sequences in the level scheme are marked with  $B1$  to  $B7$  for the convenience of describing them. The  $R_{DCO}$  and  $\Delta_{PDCO}$  values of the new transitions, identified from the present work, along with some of the representative known transitions, are plotted as a function of the  $\gamma$ -ray energy and shown in the Fig. 5.3(a) and 5.3(b), respectively. The  $\gamma$ -ray energies ( $E_\gamma$ ) along with the corresponding level energies ( $E_i$ ), relative intensities ( $I_\gamma$ ),  $R_{DCO}$ ,  $\Delta_{PDCO}$  values and the assigned multipolarities are

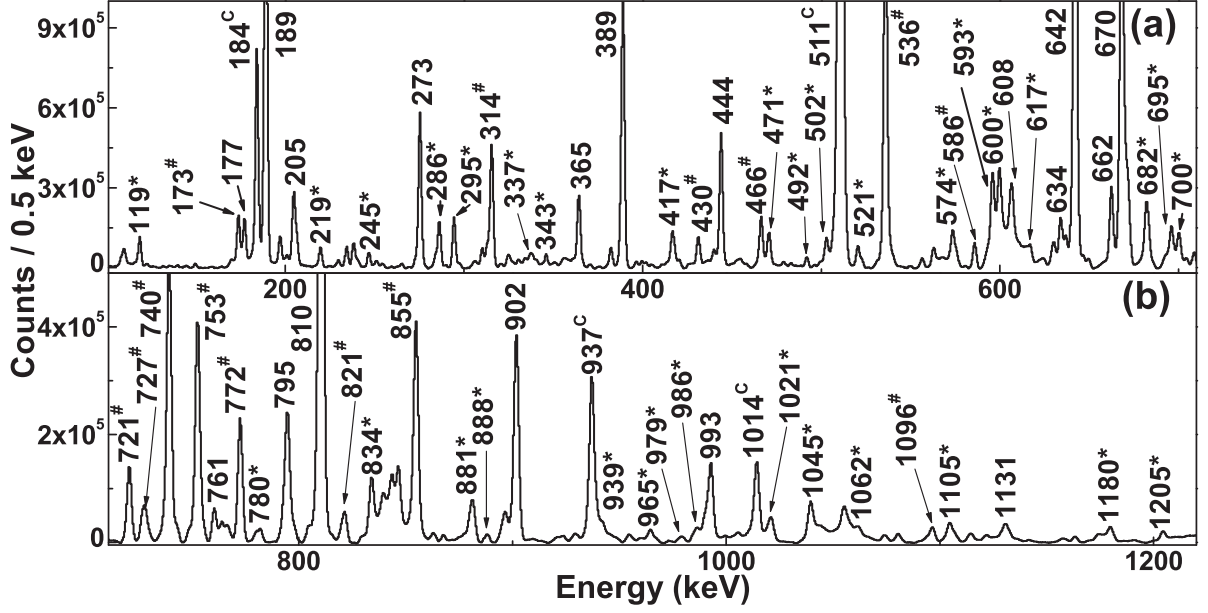


Figure 5.1: Total projection of the symmetric  $E_\gamma$ - $E_\gamma$  matrix. Energy of the observed  $\gamma$ -rays are marked and the new transitions of  $^{131}\text{Xe}$ , are marked with '\*'. Energy upto 710 keV is shown in (a) and above 710 keV is shown in (b). The transitions of neighbouring nuclei produced in the same reaction are marked as '#' and the  $\gamma$  rays marked with 'c' are the contaminant  $\gamma$  rays coming from the reactions with Mylar backing and Al frame.

tabulated in Table 5.1. The  $\gamma$  rays having  $R_{DCO}$  values in the range of 0.5 to 0.7, obtained in a quadrupole gate and 0.9 to 1.1 in a dipole gate, with negative  $\Delta_{PDCO}$  values, are considered as dominantly of M1 nature with possible small E2 admixture and are mentioned as M1(+E2). The  $\gamma$  rays with  $R_{DCO}$  other than the above values and with negative  $\Delta_{PDCO}$  values are considered to be of mixed nature and mentioned as M1+E2 in Table 5.1.

Band  $B1$  in the level scheme is the negative parity yrast band, which is observed upto 4945 keV ( $35/2 \hbar$ ) in the present work. The top three transitions of this band have also been reported by Kaya *et al.* [12], but the spin-parities of the 3815 and 4945 keV levels were assigned tentatively. From the present work, these two states are assigned as  $31/2^-$  and  $35/2^-$  respectively, from the deduced  $R_{DCO}$  and  $\Delta_{PDCO}$  measurements. Fig. 5.4(a) shows the double gated spectrum of 642 and 902 keV transitions of the yrast band  $B1$  from  $E_\gamma - E_\gamma - E_\gamma$  cube. Other than the main



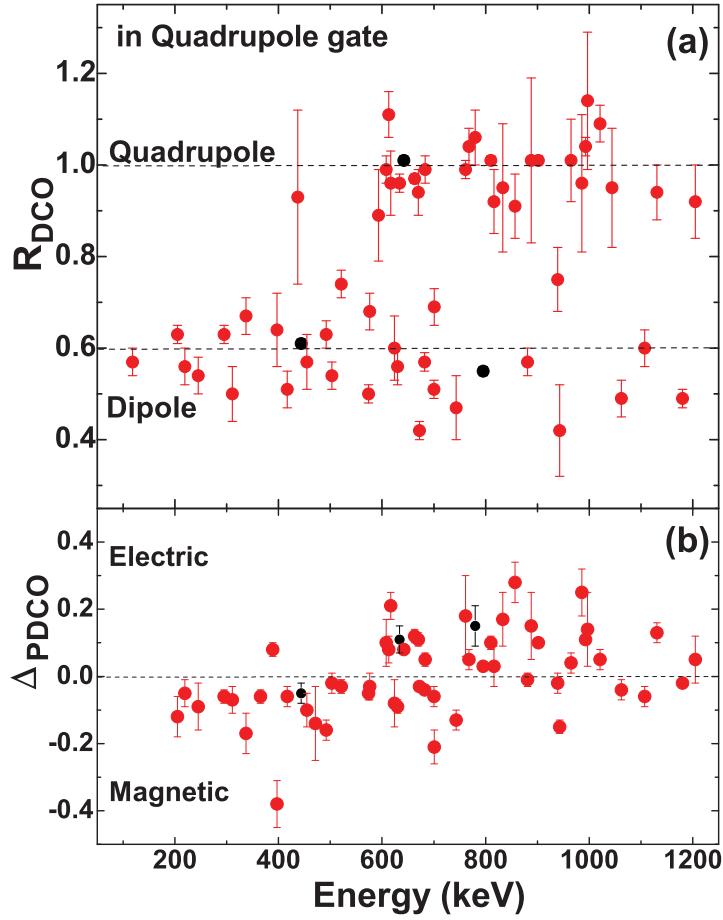


Figure 5.3: (a) The DCO ratio ( $R_{DCO}$ ) and (b) the polarization asymmetry ( $\Delta_{PDCO}$ ) of the new  $\gamma$  rays (in red), and those of some of the known  $\gamma$  rays (in black), as obtained in the present work, are plotted as a function of  $\gamma$ -ray energy. The dotted lines at Y-axis in (a) are to guide the eye for the DCO ratio corresponding to pure dipole and quadrupole transitions respectively. The dotted line at Y-axis in (b) is to guide the eye for  $\Delta_{PDCO}$  values corresponding to the electric (+ve) and magnetic (-ve) nature of the transitions.

yrast band, presence of several new transitions in coincidence with the 642-902 cascade can be seen from Fig. 5.4(a). A new band structure is identified, which decays to the main yrast band by M1 transitions of energy 682, 574, 881 and 834 keV. This band is identified as the possible signature partner band of the main yrast sequence and marked as  $B1(a)$  in the level scheme. The presence of this band is evident from the Fig. 5.4(b) and (c), which show the coincidence

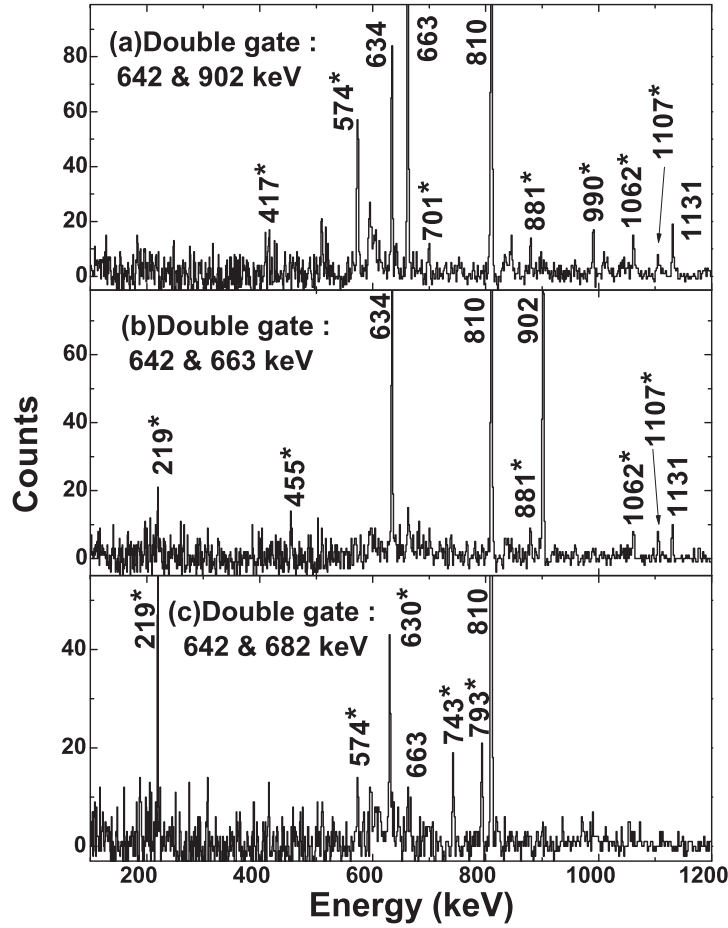


Figure 5.4: Coincidence spectra corresponding to the double gates of (a) 642 & 902 keV, (b) 642 & 663 keV and (c) 642 & 682 keV transitions of band  $B1$  from  $E_\gamma$ - $E_\gamma$ - $E_\gamma$  cube. The new transitions observed in the present work are marked with ‘\*’.

spectra of the double gates of 642 & 663 keV and 642 & 682 keV transitions, respectively. Other than the transitions of these two bands, various other new transitions can also be seen from the Fig. 5.4(a)-(c). These transitions are placed in the level scheme depending on their coincidence relationships.

In the present work, it is observed that, there are two parallel branches present above the 1806 keV ( $19/2^+$ ) level, which are marked as  $B3$  and  $B4$  in the level scheme (Fig. 5.2). One of them is in coincidence with the 444 keV (M1) transition and the other is in coincidence with

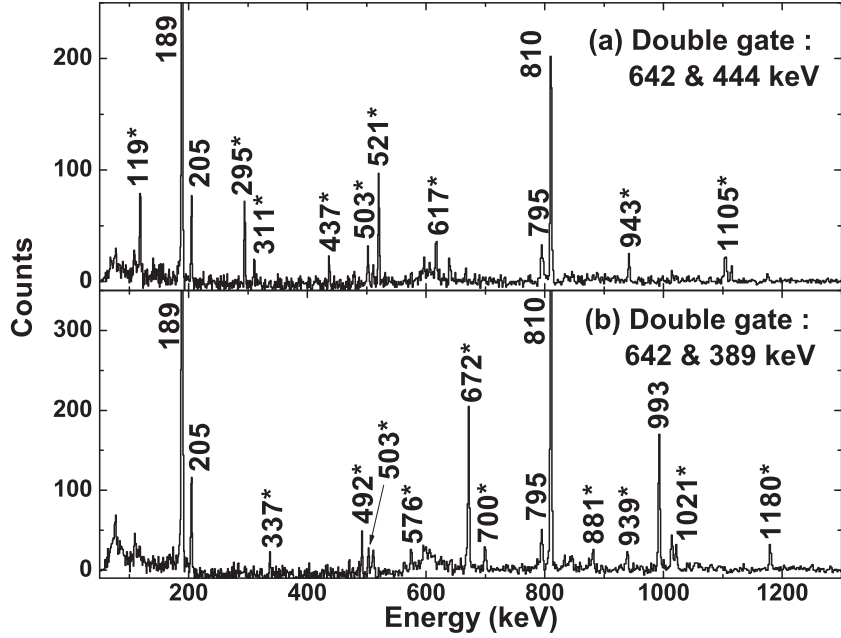


Figure 5.5: Coincidence spectra corresponding to the double gates of (a) 642 & 444 keV and (b) 642 & 389 keV transitions from the  $E_\gamma$ - $E_\gamma$ - $E_\gamma$  cube. The new transitions observed in the present work are marked with ‘\*’.

the 389 keV (E2) transition. The double gated coincidence spectra corresponding to the 642 & 444 keV and 642 & 389 keV are shown in Fig. 5.5(a) and (b), respectively. It is evident from the figure, that two completely different set of  $\gamma$  rays are present in coincidence with the 444 and 389 keV transitions.

The sequence B3 is built above the 2249 keV ( $21/2^+$ ) level and is extended upto the 5172 keV ( $33/2^+$ ) level. From the present measurements, 1105, 295, 503, 119, 311 and 592 keV transitions are placed above the 2249 keV ( $21/2^+$ ) level, which are in coincidence with the 444 keV transition as can be seen from Fig. 5.5(a). The ordering of these transitions are determined on the basis of their relative intensities. The multipolarities of these transitions were obtained from their  $R_{DCO}$  values. Also the deduced negative  $\Delta_{PDCO}$  for these transitions make them of M1 character. The polarization asymmetry ( $\Delta_{PDCO}$ ) of the 119 keV low energy transition could not be determined, since it has less Compton scattering probability. However, the dipole

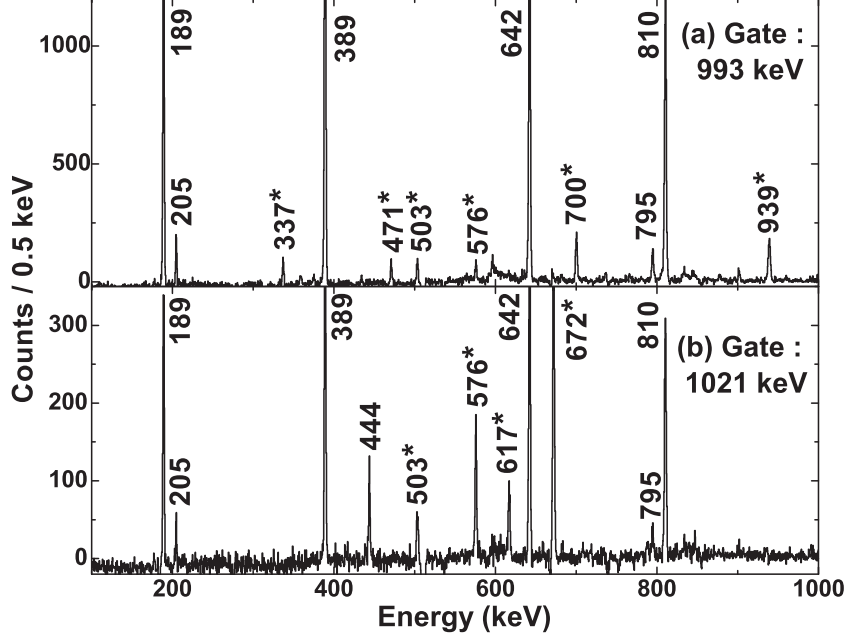


Figure 5.6: Coincidence spectra corresponding to the gates of (a) 993 and (b) 1021 keV transitions of band  $B4$  obtained from the  $E_\gamma$ - $E_\gamma$  matrix. The new transitions observed in the present work are marked with ‘\*’.

nature of this transition is confirmed from the deduced  $R_{DCO}$  value 0.57(3) in the quadrupole gate.

Table 5.1: The energies ( $E_\gamma$ ) and relative intensities ( $I_\gamma$ ) of the  $\gamma$  rays observed in  $^{131}\text{Xe}$  along with the spin and parity of the initial ( $J_i^\pi$ ) and the final ( $J_f^\pi$ ) states and the energy of the initial state ( $E_i$ ). The measured values of  $R_{DCO}$  and  $\Delta_{PDCO}$  are also shown along with the proposed multiplicity of the  $\gamma$  rays.

$E_\gamma$ (in keV)	$E_i$ (in keV)	$J_i^\pi \rightarrow J_f^\pi$	$I_\gamma(\text{Err})$ <sup>1</sup>	$R_{DCO}(\text{Err})$	$\Delta_{PDCO}(\text{Err})$	Deduced Multipolarity
118.5(1)	4270.0	$29/2^{(+)} \rightarrow 27/2^{+}$	0.37(3)	0.57(3) <sup>2</sup>	-	(M1+E2)
170.3(1)	1826.3	$15/2^{(+)} \rightarrow 13/2^{+}$	0.15(6)	0.59(9) <sup>3</sup>	-	(M1+E2)
177.1(1)	341.1	$9/2^{-} \rightarrow 11/2^{-}$	3.36(17)	0.57(2) <sup>4</sup>	-	(M1+E2) <sup>13</sup>

Table 5.1: Continued...

$E_\gamma$ (in keV)	$E_i$ (in keV)	$J_i^\pi \rightarrow J_f^\pi$	$I_\gamma(\text{Err})$ <sup>1</sup>	$R_{DCO}(\text{Err})$	$\Delta_{PDCO}(\text{Err})$	Deduced Multipolarity
186.8(1)	1585.8	13/2 <sup>+</sup> → 11/2 <sup>+</sup>	0.11(2)	-	-	(M1+E2)
188.9(1)	1805.5	19/2 <sup>+</sup> → 19/2 <sup>-</sup>	31(2)	0.82(2) <sup>5</sup>	0.11(3)	E1
204.6(1)	1805.5	19/2 <sup>+</sup> → 17/2 <sup>+</sup>	3.24(16)	0.63(2) <sup>5</sup>	-0.12(6)	M1(+E2)
204.7(1)	2693.8	(19/2 <sup>+</sup> ) → 17/2 <sup>+</sup>	-	-	-	(M1+E2)
219.4(1)	2518.3	23/2 <sup>-</sup> → 21/2 <sup>-</sup>	0.86(5)	0.56(4) <sup>5</sup>	-0.05(4)	M1(+E2)
244.7(1)	2407.8	17/2 <sup>+</sup> → 15/2 <sup>+</sup>	0.22(8)	0.54(4) <sup>6</sup>	-0.09(7)	M1(+E2)
273.2(1)	637.9	7/2 <sup>+</sup> → 5/2 <sup>+</sup>	1.07(6)	0.86(9) <sup>6</sup>	-	M1+E2
286.2(1)	952.5	- → 7/2 <sup>-</sup>	0.08(1)	-	-	-
294.5(1)	3648.7	25/2 <sup>+</sup> → 23/2 <sup>+</sup>	1.09(9)	0.63(2) <sup>2</sup>	-0.06(2)	M1(+E2)
310.6(1)	4580.6	31/2 <sup>(+)</sup> → 29/2 <sup>(+)</sup>	0.22(2)	0.50(6) <sup>2</sup>	-0.07(4)	M1(+E2)
315.5(1)	1268.0	- → -	0.07(1)	-	-	-
320.8(1)	3187.2	27/2 <sup>+</sup> → 25/2 <sup>+</sup>	0.08(1)	0.68(10) <sup>7</sup>	-	(M1+E2)
325.2(1)	666.3	7/2 <sup>-</sup> → 9/2 <sup>-</sup>	0.67(3)	1.21(5) <sup>8</sup>	-0.03(2)	M1+E2
334.2(1)	675.3	11/2 <sup>(-)</sup> → 9/2 <sup>-</sup>	0.55(3)	1.08(7) <sup>8</sup>	-	(M1+E2)
334.9(1)	972.8	9/2 <sup>+</sup> → 7/2 <sup>+</sup>	0.48(4)	0.55(3) <sup>9</sup>	-	(M1+E2)
337.1(1)	4463.4	31/2 <sup>+</sup> → 29/2 <sup>+</sup>	0.11(1)	0.67(4) <sup>7</sup>	-0.17(6)	M1(+E2)
342.6(1)	1998.6	15/2 <sup>+</sup> → 13/2 <sup>+</sup>	1.34(15)	0.76(5) <sup>3</sup>	-0.18(9)	M1+E2
364.7(1)	364.7	5/2 <sup>+</sup> → 3/2 <sup>+</sup>	7.30(91)	0.69(3) <sup>6</sup>	-0.06(2)	M1(+E2)
389.0(1)	2194.5	23/2 <sup>+</sup> → 19/2 <sup>+</sup>	24(1)	1.09(2) <sup>5</sup>	0.08(2)	E2
396.6(1)	2013.2	21/2 <sup>-</sup> → 19/2 <sup>-</sup>	0.88(4)	0.64(8) <sup>5</sup>	-0.38(7)	M1(+E2)
416.8(1)	3508.7	27/2 <sup>-</sup> → 25/2 <sup>-</sup>	1.35(8)	0.51(4) <sup>5</sup>	-0.06(3)	M1(+E2)
426.2(1)	1399.0	11/2 <sup>+</sup> → 9/2 <sup>+</sup>	0.71(6)	-	-	(M1+E2)
436.9(1)	2686.3	25/2 <sup>+</sup> → 21/2 <sup>+</sup>	0.37(3)	0.93(19) <sup>2</sup>	-	(E2)
443.9(1)	2249.4	21/2 <sup>+</sup> → 19/2 <sup>+</sup>	12.42(62)	0.61(1) <sup>5</sup>	-0.05(3)	M1(+E2)
454.7(2)	5376.5	35/2 <sup>-</sup> → 33/2 <sup>-</sup>	0.52(4)	0.57(6) <sup>10</sup>	-0.10(5)	M1(+E2)
470.8(1)	3658.0	27/2 <sup>+</sup> → 27/2 <sup>+</sup>	0.08(1)	0.71(9) <sup>7</sup>	-0.14(11)	M1+E2
483.1(1)	2068.9	15/2 <sup>+</sup> → 13/2 <sup>+</sup>	1.66(14)	0.71(16) <sup>3</sup>	-0.09(6)	M1+E2
491.8(1)	2686.3	25/2 <sup>+</sup> → 23/2 <sup>+</sup>	0.19(3)	0.63(3) <sup>7</sup>	-0.16(3)	M1(+E2)

Table 5.1: Continued...

$E_\gamma$ (in keV)	$E_i$ (in keV)	$J_i^\pi \rightarrow J_f^\pi$	$I_\gamma(\text{Err})$ <sup>1</sup>	$R_{DCO}(\text{Err})$	$\Delta_{PDCO}(\text{Err})$	Deduced Multipolarity
496.4(1)	2152.4	$17/2^{(+)} \rightarrow 13/2^+$	0.55(7)	1.01(13) <sup>6</sup>	-	(E2)
502.3(1)	666.3	$7/2^- \rightarrow 11/2^-$	2.81(31)	-	-	(E2) <sup>14</sup>
502.8(1)	4151.5	$27/2^+ \rightarrow 25/2^+$	0.58(5)	1.09(17) <sup>11</sup>	-0.15(4)	M1(+E2)
503.2(1)	4966.6	$33/2^{(+)} \rightarrow 31/2^+$	0.19(1)	0.54(3) <sup>7</sup>	-0.02(3)	M1+E2
507.1(1)	2163.1	$15/2^+ \rightarrow 13/2^+$	0.32(4)	0.71(8) <sup>6</sup>	-0.10(3)	M1+E2
520.8(2)	2770.2	$23/2^+ \rightarrow 21/2^+$	2.23(18)	0.74(3) <sup>2</sup>	-0.03(2)	M1+E2
573.6(2)	3091.9	$25/2^- \rightarrow 23/2^-$	0.77(13)	0.50(2) <sup>5</sup>	-0.05(2)	M1(+E2)
575.7(1)	2770.2	$23/2^+ \rightarrow 23/2^+$	0.27(3)	0.68(4) <sup>7</sup>	-0.01(2)	M1+E2
575.9(1)	4463.4	$31/2^+ \rightarrow 29/2^+$	0.10(2)	0.63(4) <sup>12</sup>	-0.03(4)	M1+E2
591.5(1)	5172.1	$33/2^{(+)} \rightarrow 31/2^{(+)}$	0.22(2)	1.05(17) <sup>11</sup>	-	(M1+E2)
593.3(1)	2606.5	$25/2^{(-)} \rightarrow 21/2^-$	0.48(10)	0.89(10) <sup>5</sup>	-	(E2)
599.6(1)	1998.6	$15/2^+ \rightarrow 11/2^+$	0.81(10)	0.96(8) <sup>9</sup>	0.08(7)	E2
601.7(1)	1268.0	$- \rightarrow 7/2^-$	0.42(8)	-	-	-
608.1(1)	972.8	$9/2^+ \rightarrow 5/2^+$	4.32(22)	0.99(3) <sup>6</sup>	0.10(7)	E2
611.4(1)	952.5	$- \rightarrow 9/2^-$	0.34(3)	-	-	-
613.0(1)	1585.8	$13/2^+ \rightarrow 9/2^+$	3.79(31)	1.11(5) <sup>3</sup>	0.08(4)	E2
615.1(1)	5078.5	$33/2^+ \rightarrow 31/2^+$	0.06(4)	-	-	(M1+E2)
617.0(1)	2866.4	$25/2^+ \rightarrow 21/2^+$	1.09(9)	0.96(7) <sup>2</sup>	0.21(4)	E2
624.1(1)	4371.7	$29/2^+ \rightarrow 27/2^+$	0.07(2)	0.60(7) <sup>7</sup>	-0.08(7)	M1(+E2)
630.2(2)	2929.1	$23/2^- \rightarrow 21/2^-$	1.83(11)	0.56(4) <sup>5</sup>	-0.09(2)	M1(+E2)
633.9(1)	3814.7	$31/2^- \rightarrow 27/2^-$	6.46(33)	0.96(2) <sup>5</sup>	0.11(4)	E2
637.9(1)	637.9	$7/2^+ \rightarrow 3/2^+$	7.87(94)	1.01(2) <sup>13</sup>	0.04(2)	E2
642.2(1)	806.2	$15/2^- \rightarrow 11/2^-$	100(6)	1.01(1) <sup>2</sup>	0.08(1)	E2
662.5(1)	3180.8	$27/2^- \rightarrow 23/2^-$	11.69(58)	0.97(1) <sup>5</sup>	0.12(2)	E2
669.9(1)	2068.9	$15/2^+ \rightarrow 11/2^+$	0.56(9)	0.94(5) <sup>9</sup>	0.11(2)	E2
671.9(1)	2866.4	$25/2^+ \rightarrow 23/2^+$	1.62(8)	0.42(2) <sup>7</sup>	-0.03(1)	M1+E2
682.3(1)	2298.9	$21/2^- \rightarrow 19/2^-$	8.61(43)	0.57(2) <sup>5</sup>	-0.04(1)	M1(+E2)
683.2(1)	1656.0	$13/2^+ \rightarrow 9/2^+$	3.51(21)	0.99(2) <sup>3</sup>	0.05(2)	E2

Table 5.1: Continued...

$E_\gamma$ (in keV)	$E_i$ (in keV)	$J_i^\pi \rightarrow J_f^\pi$	$I_\gamma(\text{Err})$ <sup>1</sup>	$R_{DCO}(\text{Err})$	$\Delta_{PDCO}(\text{Err})$	Deduced Multipolarity
695.2(1)	2693.8	(19/2 <sup>+</sup> ) $\rightarrow$ 15/2 <sup>+</sup>	0.57(3)	-	-	(E2)
700.3(1)	3887.5	29/2 <sup>+</sup> $\rightarrow$ 27/2 <sup>+</sup>	0.26(2)	0.51(2) <sup>7</sup>	-0.06(3)	M1(+E2)
700.5(1)	3792.4	27/2 <sup>-</sup> $\rightarrow$ 25/2 <sup>-</sup>	1.14(26)	0.69(4) <sup>10</sup>	-0.21(5)	M1(+E2)
704.6(1)	1045.7	13/2 <sup>-</sup> $\rightarrow$ 9/2 <sup>-</sup>	1.99(10)	1.89(5) <sup>8</sup>	0.02(1)	E2
737.2(1)	3431.0	(23/2 <sup>+</sup> ) $\rightarrow$ (19/2 <sup>+</sup> )	0.38(8)	0.93(14) <sup>9</sup>	0.08(6)	E2
743.4(2)	3042.3	23/2 <sup>+</sup> $\rightarrow$ 21/2 <sup>-</sup>	0.65(5)	0.47(7) <sup>5</sup>	-0.13(3)	M1+E2
761.1(1)	1399.0	11/2 <sup>+</sup> $\rightarrow$ 7/2 <sup>+</sup>	0.97(8)	0.99(2) <sup>9</sup>	0.18(12)	E2
768.0(1)	2167.0	15/2 <sup>+</sup> $\rightarrow$ 11/2 <sup>+</sup>	0.16(5)	1.04(4) <sup>9</sup>	0.05(3)	E2
780.2(1)	2436.2	17/2 <sup>+</sup> $\rightarrow$ 13/2 <sup>+</sup>	1.15(26)	1.06(6) <sup>6</sup>	0.15(6)	E2
793.0(1)	3091.9	25/2 <sup>-</sup> $\rightarrow$ 21/2 <sup>-</sup>	2.26(6)	1.09(15) <sup>2</sup>	0.05(12)	E2
794.7(1)	1600.9	17/2 <sup>+</sup> $\rightarrow$ 15/2 <sup>-</sup>	12.56(21)	0.55(1) <sup>5</sup>	0.03(1)	E1
810.4(1)	1616.6	19/2 <sup>-</sup> $\rightarrow$ 15/2 <sup>-</sup>	81(4)	1.01(1) <sup>5</sup>	0.10(2)	E2
815.7(1)	1861.4	17/2 <sup>(-)</sup> $\rightarrow$ 13/2 <sup>-</sup>	1.04(5)	0.92(7) <sup>4</sup>	0.03(6)	(E2)
833.1(1)	2489.1	17/2 <sup>+</sup> $\rightarrow$ 13/2 <sup>+</sup>	0.95(21)	0.95(14) <sup>3</sup>	0.17(8)	E2
834.3(1)	4649.0	33/2 <sup>-</sup> $\rightarrow$ 31/2 <sup>-</sup>	0.21(8)	0.55(9) <sup>5</sup>	-0.07(5)	M1(+E2)
850.1(1)	1191.2	11/2 <sup>-</sup> $\rightarrow$ 9/2 <sup>-</sup>	0.20(2)	0.96(8) <sup>8</sup>	-0.09(5)	M1+E2
857.3(1)	1903.0	17/2 <sup>-</sup> $\rightarrow$ 13/2 <sup>-</sup>	0.31(2)	0.91(7) <sup>4</sup>	0.28(6)	E2
880.9(1)	4061.7	29/2 <sup>-</sup> $\rightarrow$ 27/2 <sup>-</sup>	2.69(14)	0.57(3) <sup>5</sup>	-0.10(3)	M1(+E2)
881.2(1)	3747.6	27/2 <sup>+</sup> $\rightarrow$ 25/2 <sup>+</sup>	0.24(2)	0.54(3) <sup>7</sup>	-0.01(2)	M1+E2
887.8(1)	3658.0	27/2 <sup>+</sup> $\rightarrow$ 23/2 <sup>+</sup>	0.28(2)	1.01(18) <sup>2</sup>	0.15(10)	E2
901.7(1)	2518.3	23/2 <sup>-</sup> $\rightarrow$ 19/2 <sup>-</sup>	21(1)	1.01(1) <sup>5</sup>	0.10(1)	E2
901.8(1)	3390.9	21/2 <sup>(+)</sup> $\rightarrow$ 17/2 <sup>+</sup>	0.21(12)	0.98(17) <sup>3</sup>	-	(E2)
939.1(1)	4126.3	29/2 <sup>+</sup> $\rightarrow$ 27/2 <sup>+</sup>	0.26(2)	0.75(7) <sup>7</sup>	-0.02(3)	M1+E2
942.5(1)	3191.9	23/2 <sup>+</sup> $\rightarrow$ 21/2 <sup>+</sup>	1.23(10)	0.42(10) <sup>2</sup>	-0.15(2)	M1+E2
964.7(1)	2770.2	23/2 <sup>+</sup> $\rightarrow$ 19/2 <sup>+</sup>	1.11(11)	1.01(9) <sup>5</sup>	0.04(3)	E2
969.8(1)	4061.7	29/2 <sup>-</sup> $\rightarrow$ 25/2 <sup>-</sup>	-	-	-	(E2)
978.7(1)	3585.2	29/2 <sup>(-)</sup> $\rightarrow$ 25/2 <sup>(-)</sup>	0.37(4)	1.04(27) <sup>5</sup>	0.05(15)	(E2)
979.2(1)	2024.9	15/2 <sup>(-)</sup> $\rightarrow$ 13/2 <sup>-</sup>	0.29(2)	0.62(7) <sup>4</sup>	-	(M1+E2)

Table 5.1: Continued...

$E_\gamma$ (in keV)	$E_i$ (in keV)	$J_i^\pi \rightarrow J_f^\pi$	$I_\gamma(\text{Err})$ <sup>1</sup>	$R_{DCO}(\text{Err})$	$\Delta_{PDCO}(\text{Err})$	Deduced Multipolarity
986.2(1)	2791.7	23/2 <sup>+</sup> → 19/2 <sup>+</sup>	1.43(9)	0.96(15) <sup>5</sup>	0.25(7)	E2
990.4(1)	3508.7	27/2 <sup>-</sup> → 23/2 <sup>-</sup>	2.79(23)	0.94(3) <sup>10</sup>	0.24(3)	E2
992.7(1)	3187.2	27/2 <sup>+</sup> → 23/2 <sup>+</sup>	1.56(9)	1.04(2) <sup>7</sup>	0.11(1)	E2
997.4(1)	3191.9	23/2 <sup>+</sup> → 23/2 <sup>+</sup>	0.08(2)	1.14(15) <sup>7</sup>	0.14(11)	E2
1021.2(1)	3887.5	29/2 <sup>+</sup> → 25/2 <sup>-</sup>	0.34(2)	1.09(4) <sup>7</sup>	0.05(3)	E2
1044.5(1)	2090.2	17/2 <sup>(-)</sup> → 13/2 <sup>-</sup>	0.09(1)	0.95(13) <sup>4</sup>	-	(E2)
1061.8(1)	4242.6	29/2 <sup>-</sup> → 27/2 <sup>-</sup>	1.72(11)	0.49(4) <sup>10</sup>	-0.04(3)	M1+E2
1104.8(1)	3354.2	23/2 <sup>+</sup> → 21/2 <sup>+</sup>	1.52(8)	1.04(15) <sup>11</sup>	-0.03(2)	M1(+E2)
1107.1(1)	4921.8	33/2 <sup>-</sup> → 31/2 <sup>-</sup>	0.27(11)	0.60(4) <sup>10</sup>	-0.06(3)	M1(+E2)
1130.6(1)	4945.3	35/2 <sup>-</sup> → 31/2 <sup>-</sup>	1.49(8)	0.94(6) <sup>2</sup>	0.13(3)	E2
1179.8(1)	3374.3	25/2 <sup>+</sup> → 23/2 <sup>+</sup>	0.42(2)	0.49(2) <sup>7</sup>	-0.02(1)	M1+E2
1191.0(1)	5078.5	33/2 <sup>+</sup> → 29/2 <sup>+</sup>	0.12(3)	0.96(21) <sup>7</sup>	0.17(12)	E2
1205.1(2)	3108.1	21/2 <sup>(-)</sup> → 17/2 <sup>-</sup>	0.26(3)	0.92(8) <sup>4</sup>	0.05(7)	(E2)
1276.2(1)	4463.4	31/2 <sup>+</sup> → 27/2 <sup>+</sup>	-	-	-	(E2)
1561.8(1)	5376.5	35/2 <sup>-</sup> → 31/2 <sup>-</sup>	-	-	-	(E2)

<sup>1</sup>Relative  $\gamma$ -ray intensities are normalized to 100 for the total intensity of 642.2-keV  $\gamma$ -ray.

<sup>2</sup>From 810.4 keV (E2) DCO gate;

<sup>3</sup>From 608.1 keV (E2) DCO gate;

<sup>4</sup>From 704.6 keV (E2) DCO gate;

<sup>5</sup>From 642.2 keV (E2) DCO gate;

<sup>6</sup>From 683.2 keV (E2) DCO gate;

<sup>7</sup>From 389.0 keV (E2) DCO gate;

<sup>8</sup>From 177.1 keV (M1) DCO gate;

<sup>9</sup>From 637.9 keV (E2) DCO gate;

<sup>10</sup>From 901.7 keV (E2) DCO gate;

<sup>11</sup>From 794.7 keV (E1) DCO gate;

<sup>12</sup>From 1021.1 keV (E2) DCO gate;

<sup>13</sup>From 761.1 keV (E2) DCO gate;

<sup>14</sup>adopted from Ref. [31];

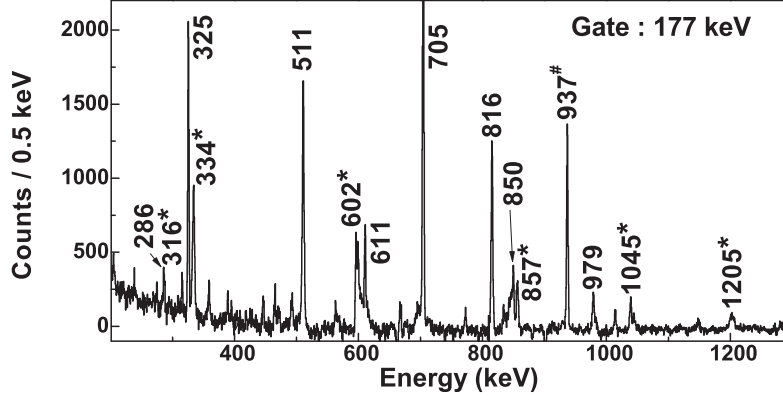


Figure 5.7: Coincidence spectra corresponding to the gate of 177 keV transition of sequence *B5* from the  $E_\gamma$ - $E_\gamma$  matrix. The new transitions observed in the present work are marked with ‘\*’. The  $\gamma$ -ray marked with ‘#’ is the contaminant  $\gamma$ -ray coming from reactions with the Mylar backing.

A new band, called band *B4*, is observed above the 2194 keV ( $23/2^+$ ) level. From the present work, the band *B4* has been established upto 5079 keV ( $33/2^+$ ) excitation energy. Few levels are also found at 3374 ( $25/2^+$ ), 4126 ( $29/2^+$ ) and 4967 ( $33/2^+$ ) keV, which are connected to the band *B4* by  $\Delta J = 1$  transitions. The coincidence spectra corresponding to the 993 and 1021 keV  $\gamma$ -ray gates are shown in Fig. 5.6(a) and (b), respectively. Transitions pertaining to this band can be seen from this figure. Another two new levels are observed at 2770 and 3658 keV which decay to the band *B4* by non-stretched transitions of energy 576 and 471 keV, respectively.

Another sequence of levels, marked as *B5*, built above the  $11/2^-$  isomer is observed and placed parallel to the yrast band *B1* in the level scheme (Fig. 5.2). In the present work, seven new transitions of energies 316, 334, 602, 857, 1045 and 1205 keV have been placed in that sequence. The coincidence spectrum corresponding to the gate of 177 keV  $\gamma$ -ray is shown in Fig. 5.7. The new transitions are clearly seen from this figure. The 316 and 602 keV  $\gamma$  rays are found to be in coincidence with 177 keV, but not with the 705 keV and therefore placed accordingly. Three new transitions of energies 857, 1045 and 1205 keV are seen in coincidence with both 177 keV

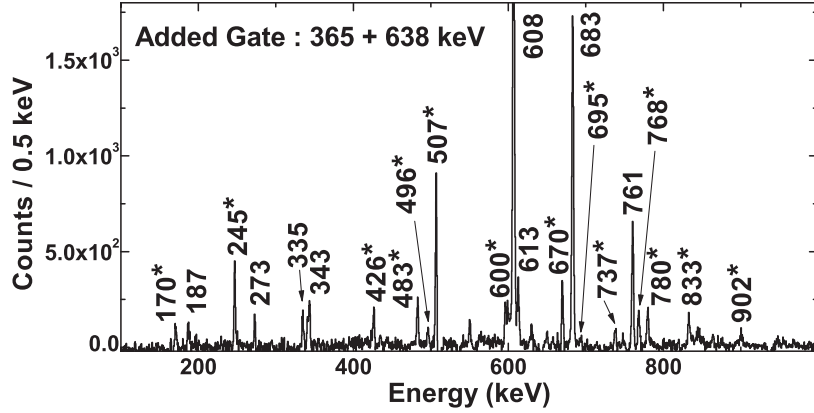


Figure 5.8: Coincidence spectra corresponding to the added gates of 365 and 638 keV transitions of band  $B6$  obtained from the  $E_\gamma$ - $E_\gamma$  matrix. The new transitions observed in the present work are marked with ‘\*’.

and 705 keV transitions and thus are placed above the 1046 keV level. The spin-parities of the 341 and 666 keV levels are adopted from Ref. [31].

The positive parity level structure, marked as  $B6$  in the level scheme (Fig. 5.2), is built on the  $3/2^+$  ground state. This sequence has been extended upto an excitation energy of 3431 keV ( $23/2^+$ ) by placing 16 new transitions. Fig. 5.8 shows the coincidence spectra of the added gates of the two lowest transitions of energies 365 and 638 keV, where the new transitions are clearly visible.

## 5.4 Discussion

The ground state spin parity of  $^{131}\text{Xe}$  is determined by the odd valence neutron occupying available orbitals. The ground state ( $3/2^+$ ) and the 164 keV ( $11/2^-$ ) level of this nucleus are originated from the odd neutron occupying the available  $d_{3/2}$  and  $h_{11/2}$  orbitals. The large spin difference between these two states makes the  $11/2^-$  state to be a long lived isomer (11.8 days) in  $^{131}\text{Xe}$ . Such long lived isomers having  $\nu h_{11/2}$  configuration can be seen systematically in the neighbouring isotone and isotopes [2, 5, 6, 13, 14, 16]. The neutron Fermi level of the Xe

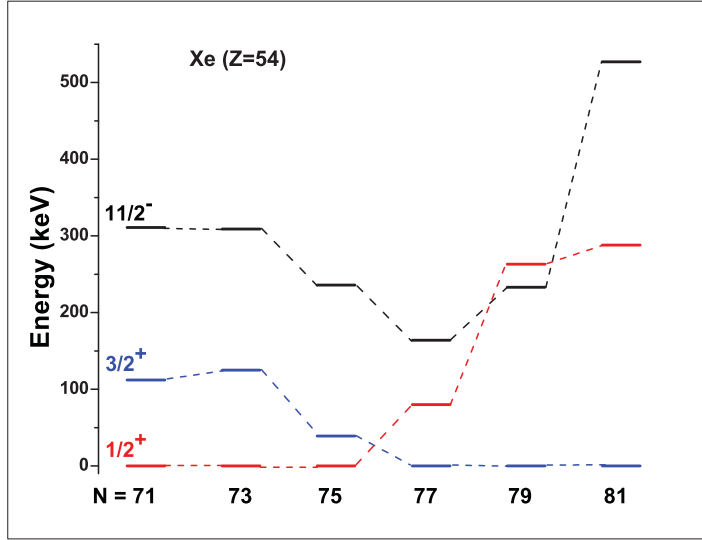


Figure 5.9: Evolution of the low-lying 1-qp states in Xe isotopes.

isotopes in  $A \sim 130$  region is situated just below the  $N = 82$  shell closure. The evolution of the excitation energies of the single particle configurations in the Xe isotopic chain are shown in Fig. 5.9. It can be clearly seen from the figure that the ground states of the lighter Xe isotopes change at  $N = 77$  ( $^{131}\text{Xe}$ ) from  $1/2^+$  to  $3/2^+$  and continues to be  $3/2^+$  until  $N = 81$ . Moreover, the  $11/2^-$  state, corresponding to the  $h_{11/2}$  orbital, shows a minimum for the  $N = 77$  ( $^{131}\text{Xe}$ ) isotope. This clearly shows the transitional nature of  $^{131}\text{Xe}$ . It is worth mentioning in this context, that, the transitional nature of the neutron number  $N = 77$  is also reported for Cs ( $Z = 55$ ) isotopes [32] as well. Therefore,  $N = 77$  seems to play crucial role in determining the high spin structure of nuclei in this  $A \sim 130$  region.

The band  $B1$  in  $^{131}\text{Xe}$  is a rotational band based on the  $\nu h_{11/2}$  configuration. The total aligned angular momenta ( $I_x$ ) of  $B1$  shows a pronounced backbending for the  $N = 77$  isotope, whereas lighter odd-A Xe isotopes show upbend [12] (see Fig. 5.10, where alignment gain  $i_x$  of the  $\nu h_{11/2}$  band is plotted for various Xe isotopes). It also suggests the transitional nature of the Xe isotopes around  $N = 77$ . The band crossing in this band is due to the alignment of a pair of proton in the  $\pi h_{11/2}$  orbital. In order to get an idea on the involved single particle orbitals, the aligned single particle angular momenta  $i_x$  are plotted for the  $\nu h_{11/2}$  band of the neighbouring

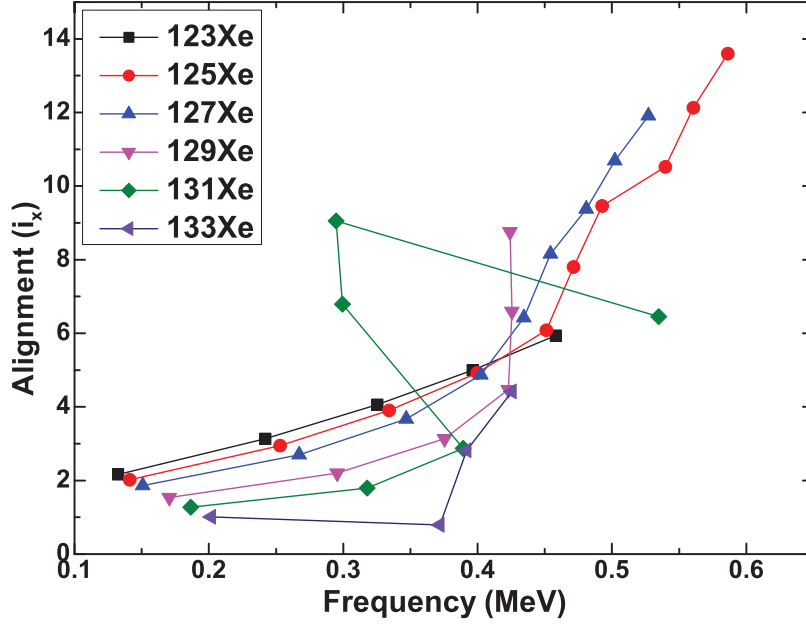


Figure 5.10: Alignment plot of the  $\nu h_{11/2}$  band of Xe ( $Z = 54$ ) isotopes. The Harris parameters of  $J_0 = 16 \hbar^2/\text{MeV}$  and  $J_1 = 7 \hbar^4/\text{MeV}^3$  are used [15]. Filled and open circles are used for two different signatures.

odd-A and even-even nuclei in Fig. 5.11. It is observed that both the  $N = 77$  isotones have similar initial single particle alignments, which are about  $3 \hbar$  more than that of the even-even isotopes. This indicates the involvement of the  $\Omega = 9/2$  component of the  $\nu h_{11/2}$  orbital ( $9/2[514]$  Nilsson configuration) for this band in the  $N = 77$  isotones. This comparatively higher  $\Omega$  component would result a small or no signature splitting in this band. But, the  $11/2^-$  bands in Xe isotopes and in the  $N = 77$  isotones are observed with a reasonably large signature splitting. This indicated a possible  $\Omega$  mixing. In the case of  $^{129}\text{Xe}$ , it was reported to have triaxial shape [16], giving the required  $\Omega$  mixing and resulted in large signature splitting. In the present work, a signature partner band above the  $19/2^-$  state has been identified (band  $B1(a)$ ) for the first time in  $^{131}\text{Xe}$ . This band also shows large signature splitting as in case of  $^{129}\text{Xe}$ . The staggering parameter,  $S(I)$ , as defined in Ref. [16], as a function of  $2I$ , is plotted in Fig. 5.12(a) and 5.12(b) for  $^{131}\text{Xe}$  with its neighbouring isotopes and isotones. The excellent agreement of the general trend and the amount of signature splitting is observed for the isotopes

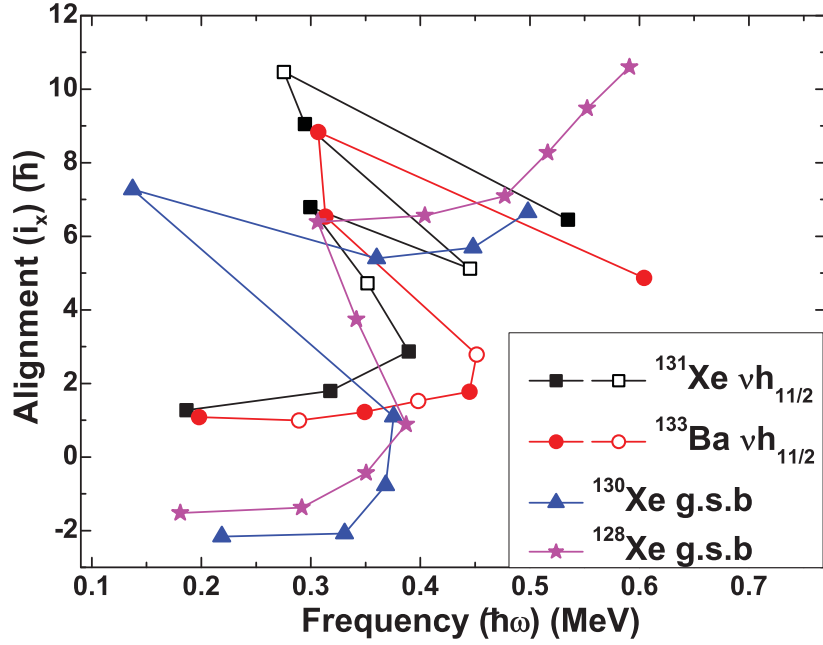


Figure 5.11: Alignment plot of the  $\nu h_{11/2}$  band of the  $N = 77$  isotones and the ground state band (g.s.b) of neighbouring even-even nuclei. The Harris parameters of  $J_0 = 16 \hbar^2/\text{MeV}$  and  $J_1 = 7 \hbar^4/\text{MeV}^3$  are used [15]. Filled and open circles are used for two different signatures.

and isotones, which indicates that the structure of  $^{131}\text{Xe}$  is similar to that of its neighbouring isotopes and isotones that is a triaxial or a gamma-soft shape. A set of states, marked as  $B1(b)$ , has also been identified in  $^{131}\text{Xe}$  in this work, which decays to the main band  $B1$ . These states might correspond to the excitation of gamma phonons in  $^{131}\text{Xe}$ . However, the intra-band transitions between the states in  $B1(b)$  could not be observed as they are of weak intensity.

The  $21/2^-$  state (2013 keV) has been observed for the first time in this work having a band like structure  $B2$  built above it. This band decays to the  $19/2^-$  state of the  $\nu h_{11/2}$  band. This  $21/2^-$  state was not observed in the neighbouring isotope  $^{129}\text{Xe}$ , but could be identified in the  $N = 77$  isotone  $^{129}\text{Te}$  [33] at an excitation energy of 1958 keV. Considering the similar excitation energy and decay pattern of this state, this state has been assigned a configuration of  $\pi g_{7/2}^2 \otimes \nu h_{11/2}$ .

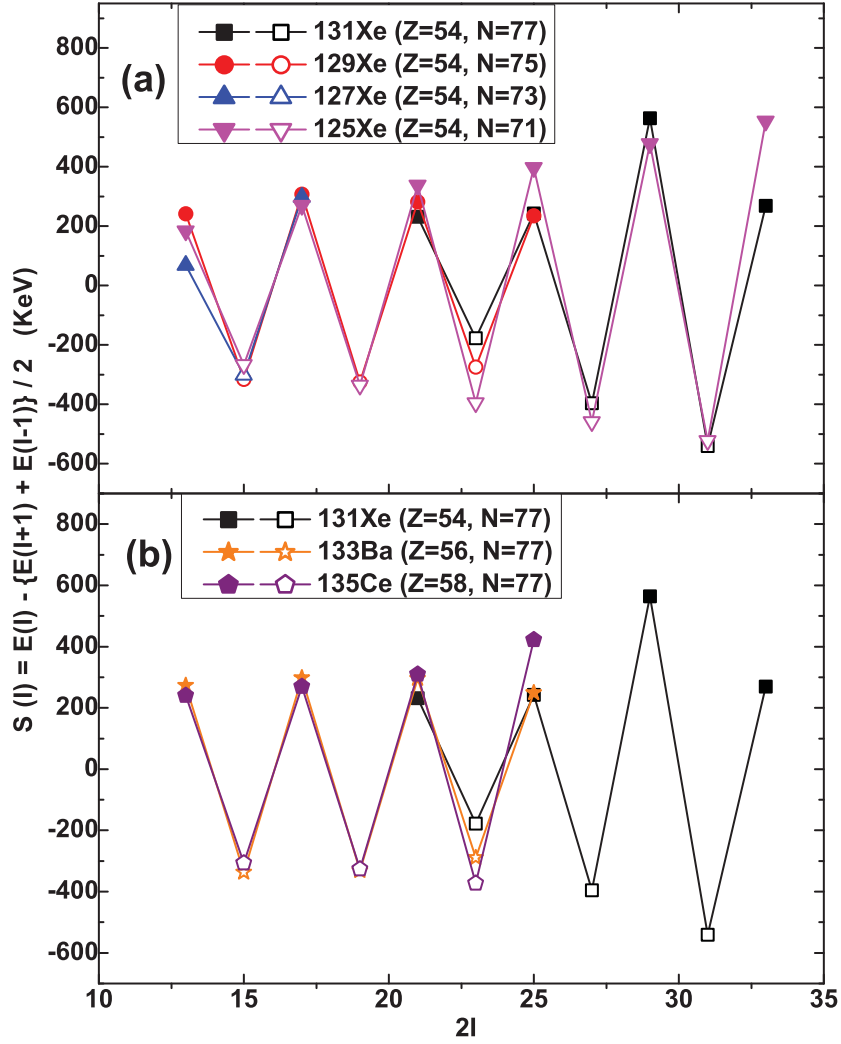


Figure 5.12: Staggering of the  $11/2^-$  band in  $^{131}\text{Xe}$  are plotted as a function of spin,  $I$ , and compared with the same band of other isotopes (a) and isotones (b). Filled and open circles are used for two different signatures.

The  $17/2^+$  and the  $19/2^+$  states at 1.6 and 1.8 MeV excitation energies in the lower part of the band  $B4$  assigned a 3-qp configuration of  $\pi g_{7/2} h_{11/2} \otimes \nu h_{11/2}^{-1}$ , similar to that of  $^{129}\text{Xe}$ . The upper part of the band  $B3$  decays to the lower part of it through a high energy (1105 keV) transition. Also these states do not decay to the band  $B1$  of configuration of  $\pi h_{11/2}^2 \otimes \nu h_{11/2}$ . In  $^{130}\text{Xe}$ , there is a  $5^+$  state at  $\sim 2.4$  MeV of excitation energy, which has been assigned a two

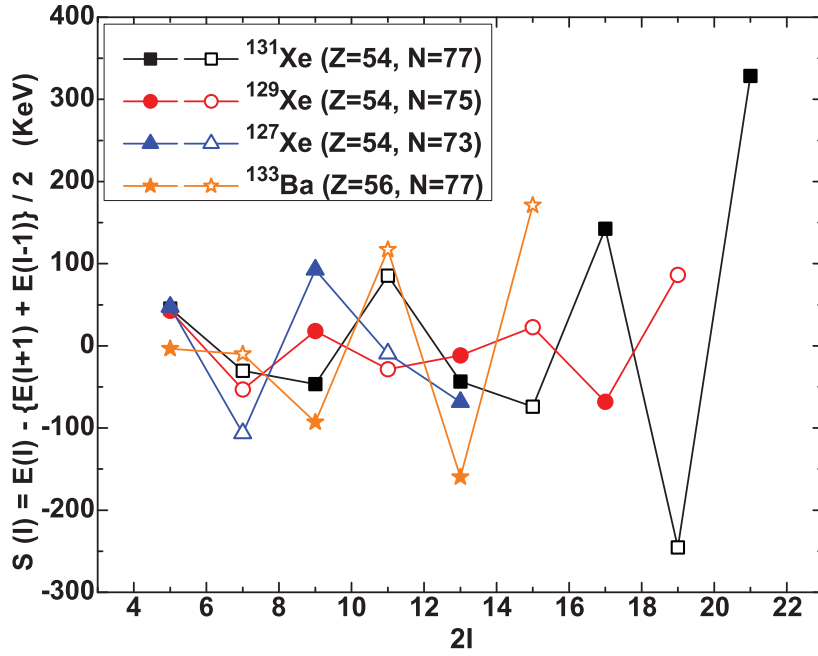


Figure 5.13: The staggering,  $S(I)$ , plot as a function of spin,  $I$ , for the low-lying positive parity band  $B6$  of  $^{131}\text{Xe}$  along with the neighbouring isotopes and isotone. Filled and open circles are used for two different signatures.

qp configuration of  $\pi d_{5/2}g_{7/2}$  [34, 35]. Thus, the  $27/2^+$  state of  $B3$  might have formed by the coupling of this  $5^+$  state with the 3-qp configuration of the lower part of it. Therefore, a high- $j$ , configuration of  $\pi(d_{5/2}g_{7/2})^3 h_{11/2} \otimes \nu h_{11/2}^{-1}$  is assigned to the upper part of  $B3$ .

A low lying  $23/2^+$  state at an excitation energy of about 2.2 MeV was reported in  $^{131}\text{Xe}$  [12]. A new band structure,  $B4$ , has been identified built on this state in the present work having a large signature splitting. This band is similar to the 3-qp band in  $^{129}\text{Xe}$  involving a deformation driving low- $\Omega$  orbital. Therefore, the band  $B4$  in  $^{131}\text{Xe}$  has been assigned with a 3-qp configuration of  $\pi(g_{7/2}h_{11/2})^2 \otimes \nu f_{7/2}$ . The  $[541]1/2^-$  component of the  $\nu f_{7/2}$  orbital provides the required large Coriolis force which generates the large signature splitting. The signature spitting of this band is shown in Fig. 5.14. As it is already mentioned that a large signature splitting may also corresponds to a triaxial or  $\gamma$  deformed shape, a non-axial deformation or  $\gamma$ -softness can again be expected for the band  $B4$ . This kind of  $\gamma$ -soft shape should cause a

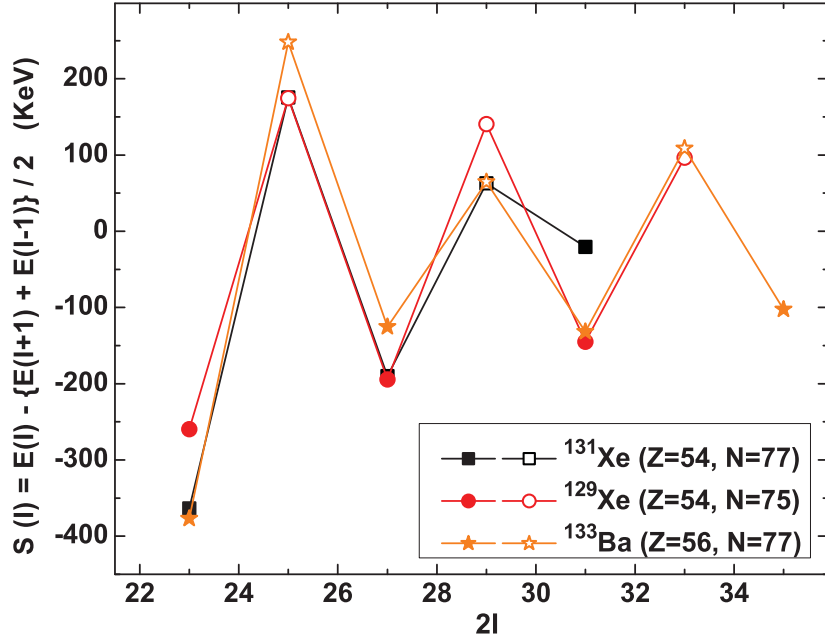


Figure 5.14: The staggering,  $S(I)$ , plot as a function of spin,  $I$ , for the band  $B4$  of  $^{131}\text{Xe}$  along with the similar bands in the neighbouring isotope and isotone. Filled and open circles are used for two different signatures.

$\gamma$  band. Another set of states,  $23/2^+$ ,  $25/2^+$ ,  $29/2^+$ ,  $33/2^+$ , has been identified in this work which decays to the band  $B4$ . This states may constitute the expected  $\gamma$  vibrational band of  $B4$ . However, transitions between the states of this side band could not be identified in this work.

Most of the low-lying non-yrast states above the  $11/2^-$  isomeric state were known [22]. The band-like sequence  $B5$  built on the  $13/2^-$  (1046 keV) state has been identified in the present work. The possible configuration of this state is  $(2^+)_{130\text{Xe}} \otimes \nu h_{11/2}$ .

A low-lying positive parity band based on the  $1/2^+$  or  $3/2^+$  ground state, as the band  $B6$  in  $^{131}\text{Xe}$ , has been identified systematically in the odd-A isotopes of Xe and Ba nuclei. In the lighter mass isotopes, this band was described as a  $s_{1/2}/d_{3/2}$  mixed configuration. In  $^{131}\text{Xe}$ , the ground state becomes  $3/2^+$  (Fig. 5.9) indicating a more pure  $d_{3/2}$  configuration for this state and for the band  $B6$  in  $^{131}\text{Xe}$ . The band  $B6$  is extended upto  $23/2 \hbar$  from the present work.

The signature splitting (Staggering parameter  $S(I)$ ), for this band is compared with the other isotopes and isotones in Fig. 5.13. It is found that the staggering in the Xe isotopes decreases with increasing mass number indicating less contribution from low- $\Omega$  orbitals. The  $S(I)$  values for the  $N = 77$  isotones,  $^{131}\text{Xe}$  and  $^{133}\text{Ba}$  are found to be very similar. A signature inversion at  $I = 15/2\hbar$  has been observed in  $^{131}\text{Xe}$  analogous to that of  $^{129}\text{Xe}$  but in opposite phase. It can be seen that, for  $^{131}\text{Xe}$ , after the inversion, the signature splitting increases rapidly. This indicates a change in shape to an oblate or a triaxial deformation.

## 5.5 TRS calculations

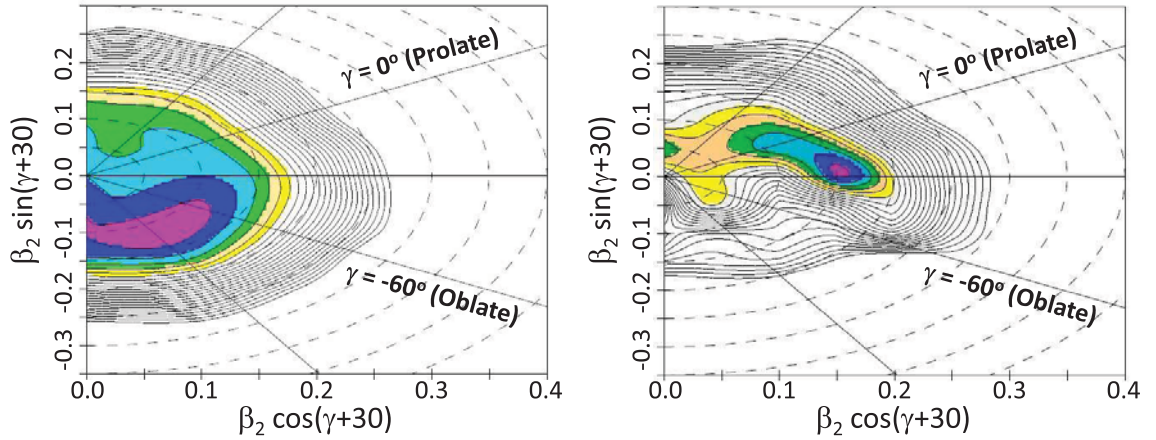


Figure 5.15: Contour plots of total Routhian surfaces in the  $\beta_2 - \gamma$  deformation mesh calculated for the lowest negative parity configuration corresponding to the  $\nu h_{11/2}$  band (band B1) in  $^{131}\text{Xe}$  at the rotational frequencies ( $\hbar\omega$ ) = 0.11 MeV (left) and 0.26 MeV (right).

In order to understand the different configurations of  $^{131}\text{Xe}$ , Total Routhian surface (TRS) calculations have been performed using Strutinski shell correction method. The formalism of Nazarewicz *et al.* [36, 37] has been used. The procedure as described in Ref.[38] has been followed.

The TRSs for the  $h_{11/2}$  band (band B1) are shown in Fig. 5.15(left) and 5.15(right) for two different rotational frequencies of  $\hbar\omega = 0.11$  and 0.26 MeV, respectively. It is found that

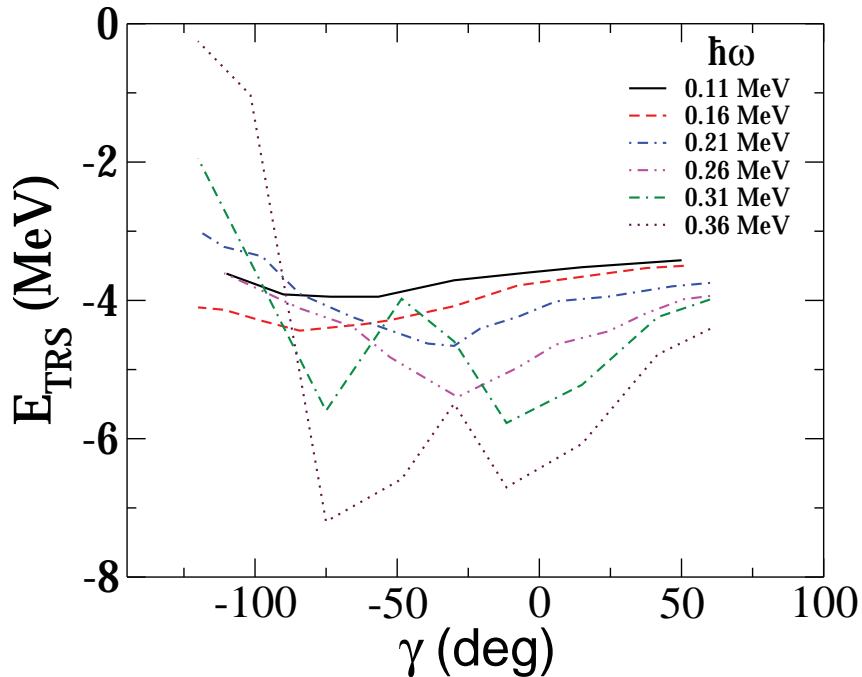


Figure 5.16: Plot of total Routhian surface energies ( $E_{TRS}$ ) as a function of the deformation parameter,  $\gamma$  calculated for the 1-qp, negative parity configuration corresponding to the  $\nu h_{11/2}$  band in  $^{131}\text{Xe}$  at different values of rotational frequencies ( $\hbar\omega$ ).

the minimum is spread over a region of  $\gamma$  around  $\gamma \sim -75^\circ$  that is, the nucleus displays  $\gamma$ -softness close to the ground state for lower rotational frequencies. However, at a slightly higher frequency of  $\hbar\omega \sim 0.26$  MeV, a triaxial shape emerges. This corresponds to the lower part of the band  $B1$ . This prediction of triaxial shape for the  $\nu h_{11/2}$  band in  $^{131}\text{Xe}$  is analogous to that of its neighbouring isotope  $^{129}\text{Xe}$  [16]. The variation of the total Routhian energies ( $E_{TRS}$ ) as a function of the deformation parameter ( $\gamma$ ) is shown in Fig.5.16 for  $h_{11/2}$  band for different rotational frequencies ( $\hbar\omega$ ). The  $\beta_2$  parameters were fixed around the minimum of the TRS as obtained for each  $\hbar\omega$ . At low rotational frequencies ( $\hbar\omega = 0.11$  and  $0.16$  MeV),  $E_{TRS}$  show some  $\gamma$ -softness. At mid frequencies, ( $\hbar\omega = 0.21$  and  $0.26$  MeV), the minima of  $E_{TRS}$  shift to a triaxial deformation ( $\gamma \sim -26^\circ$ ). At higher frequencies ( $\hbar\omega = 0.31$  and  $0.36$  MeV), the minima appear at  $\gamma \sim -12^\circ$  and at  $\gamma \sim -75^\circ$ . This indicates an interesting structural

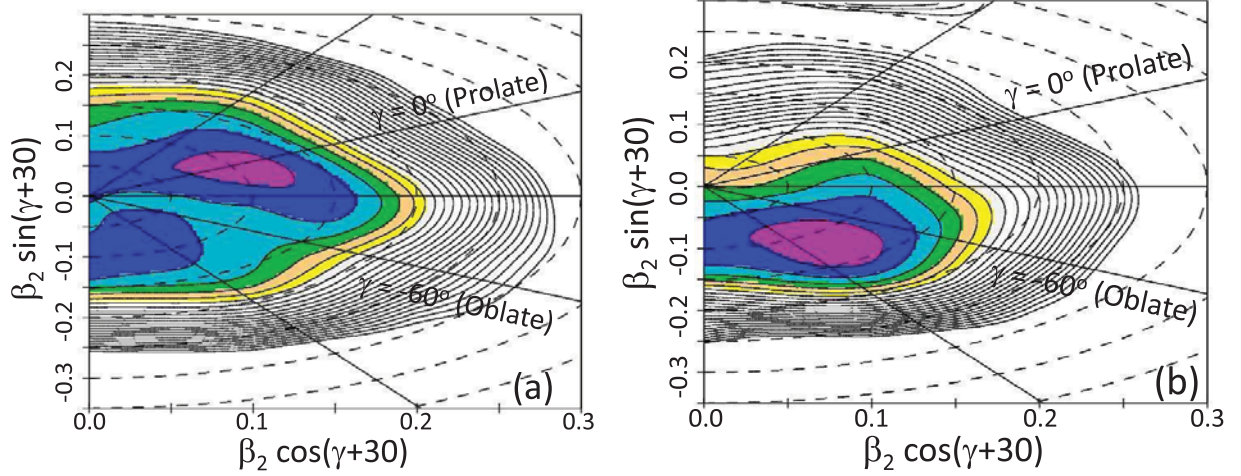


Figure 5.17: Same as Figure 5.15 but for the lowest positive parity configuration, corresponding to the  $\nu d_{3/2}$  band (band B6) in  $^{131}\text{Xe}$  at rotational frequencies ( $\hbar\omega$ ) = 0.16 MeV (a) and 0.36 MeV (b).

evolution, from gamma-soft to triaxial shape coexistence with increasing rotational frequency for the  $h_{11/2}$  band.

The TRS plots for the positive parity  $\nu d_{3/2}$  configuration (band B6) are shown in Fig. 5.17 for two rotational frequencies ( $\hbar\omega = 0.16$  MeV and 0.36 MeV). The calculations predict a near prolate shape at lower rotational frequency and a triaxial shape with near oblate deformation at higher rotational frequency. These results corroborate well with the observed increase in the staggering parameter at higher spins for this band after the signature inversion (Fig. 5.13).

The TRSs for the 3-qp configuration band (B4) are shown in Fig. 5.18(a). The plots show a minimum at an oblate deformation ( $\beta_2 \sim 0.15$  and  $\gamma \sim -60^\circ$ ) and a large extent of gamma-softness. The variation of the TRS energy ( $E_{TRS}$ ) around the minimum for this surface has been plotted in Fig. 5.18(b) as a function of  $\gamma$ . The gamma-softness can be clearly visible in this plot. The minimum value of  $E_{TRS}$  remains within 100 keV for the variation of  $\gamma$  in the range  $-86^\circ \leq \gamma \leq -45^\circ$ . The observed large staggering and a possible gamma-band with B4 in  $^{131}\text{Xe}$  is thus in good agreement with the above prediction.

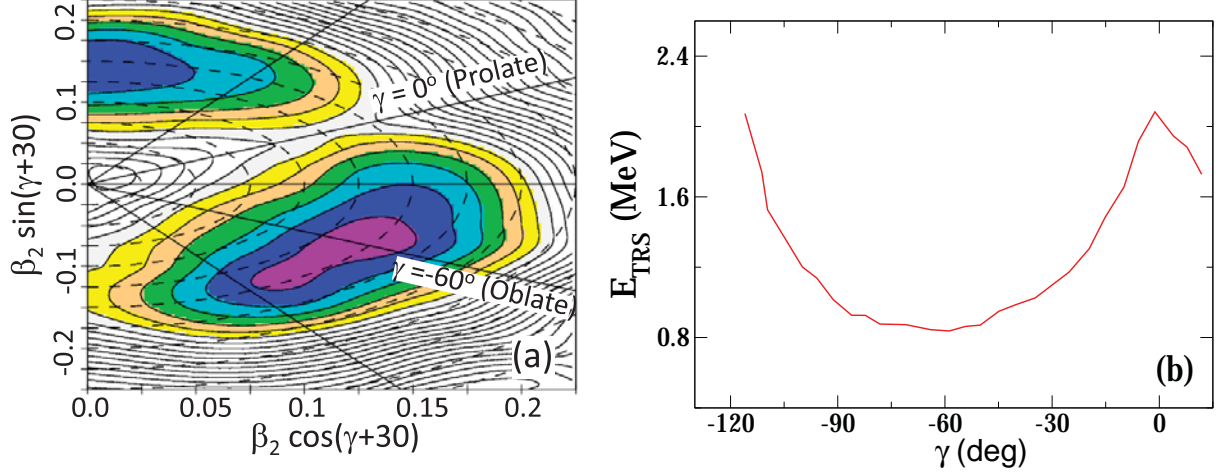


Figure 5.18: (a) Same as Figure 5.15 but for the 3-qp configuration, corresponding to the band  $B4$  in  $^{131}\text{Xe}$ . (b) The TRS energies as a function of the deformation parameter  $\gamma$  for  $\beta_2$  value around the minimum of the TRS.

## 5.6 SPAC and semi-empirical calculations of the Shears band

The upper part of the band  $B3$  above the  $27/2^+$  (4152 keV) state in  $^{131}\text{Xe}$  has been described in the framework of Shears mechanism with the Principal Axis Cranking (SPAC) [39]. This dipole band has a small dynamical moment of inertia ( $J^2 \approx 4 - 5 \hbar^2 \text{MeV}^{-1}$ ) which indicates a weakly deformed shape. Similar dipole bands in the  $A \sim 100$  region have been identified as Magnetic Rotation (MR) bands [40] with the theoretical support within the framework of the Shears mechanism [41, 42].

In the present work, the calculations have been performed with the configuration  $\pi(g_{7/2}d_{5/2})^3 h_{11/2} \otimes \nu h_{11/2}^{-1}$  for the band  $B3$  assuming an oblate deformed shape. The angular momenta are taken as  $j_\pi = 12 \hbar$ ,  $j_\nu = 5.5 \hbar$  and the interaction strength as  $V_2 = 1.90 \text{ MeV}$  for the calculation. Under these assumptions the energy level and the spins (I) for the dipole band above the  $27/2^+$  state were well reproduced as shown in Fig. 5.19(a). The spin dependence of  $\theta_1$  (angle between the proton angular momentum and the neutron angular momentum) and

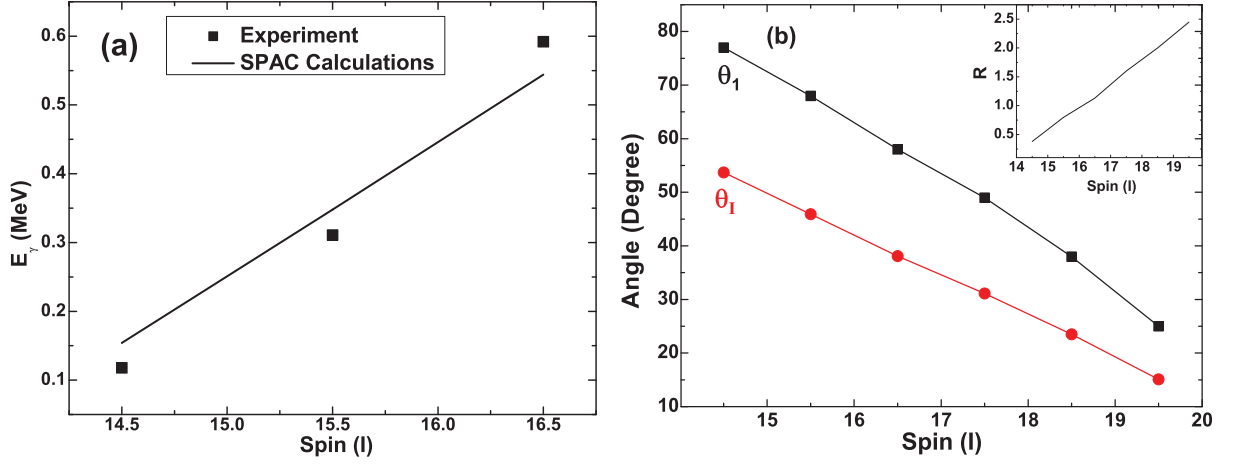


Figure 5.19: (a) Variation of the observed  $\gamma$ -ray energy with spin (I), which is compared with the SPAC calculation (solid line). (b) Variation of  $\theta_1$  and  $\theta_I$  with spin (I) as obtained from the present SPAC calculations. Inset shows the variation of core angular momentum contribution (R) with spin.

$\theta_I$  (angle of the total angular momentum with the rotational axis) are shown in Fig. 5.19(b) while the variation of R (core contribution) with spin is shown in the inset of Fig. 5.19(b). Present SPAC calculations determines the parameter  $\chi$  defined as  $\chi = \frac{J(I)}{j_\pi^2/3V_2}$  to be +0.10. This indicates that almost 91% of the total angular momentum is generated due to the shears mechanism.

The semi-empirical description for the shears bands, prescribed by Clark and Machiavelli [42] is also used to investigate the properties of the levels above the  $27/2^+$  level of this band. According to this model the shears angle between proton and neutron angular momenta blades can be written as,

$$\cos \theta = \frac{I(I+1) - j_\pi(j_\pi+1) - j_\nu(j_\nu+1)}{2\sqrt{j_\pi(j_\pi+1)j_\nu(j_\nu+1)}} \quad (5.1)$$

According to this prescription [42], the proton and neutron angular momentum interacts with the total angular momentum via a factor  $V_2P_2(\cos\theta)$ . The variation in the level energies of the MR band is thus due to this angular momentum couplings and can be expressed as,

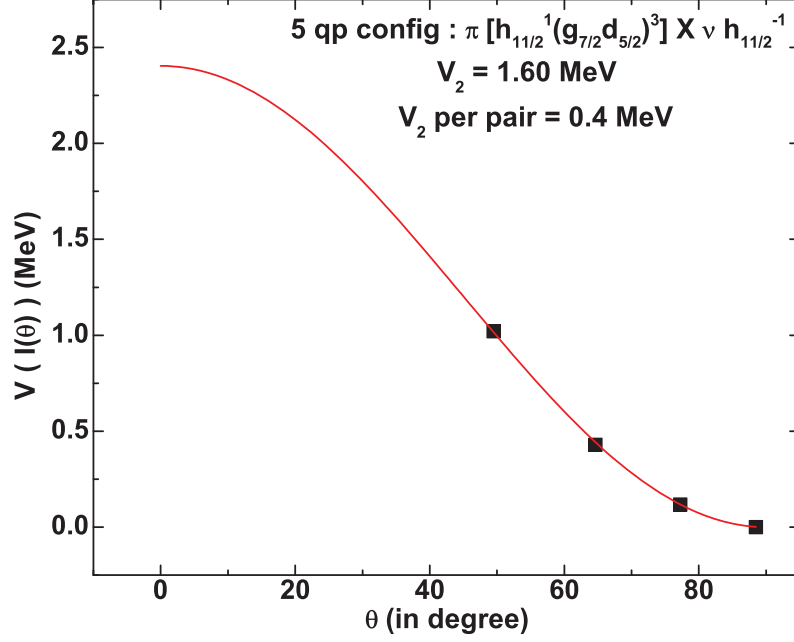


Figure 5.20: Variation of  $V[I(\theta)]$  as a function of the shears angle ( $\theta$ ) for the MR band in  $^{131}\text{Xe}$ . The solid line is the fit to the data points from which the effective interaction ( $V_2$ ) between the proton and neutron angular momentum vectors has been obtained.

$$V[I(\theta)] = E_I - E_B = (3/2)V_2 \cos^2 \theta \quad (5.2)$$

where,  $E_I$  and  $E_B$  are the energies of the levels with spin  $I$  and band head, respectively. The  $\theta$  is called the shears angle and  $V_2$  is the interaction strength. The experimentally obtained  $V[I(\theta)]$  and the shears angle  $\theta$  for each state from and above  $27/2^+$  of  $B3$  are plotted in Fig. 5.20. These experimental data points are fitted using the Eq. 5.2 to extract the interaction strength  $V_2$ . A value of  $V_2 = 1.60$  MeV is obtained for this 5-qp MR band. This leads to the interaction strength per pair is 0.4 MeV which is in very good agreement with the mass scaled interaction strength in this  $A \sim 130$  region [49]. Thus, the present shears mechanism and SPAC model calculations can describe successfully the angular momentum generation of the band  $B3$  of  $^{131}\text{Xe}$ .

## 5.7 Shell Model calculations

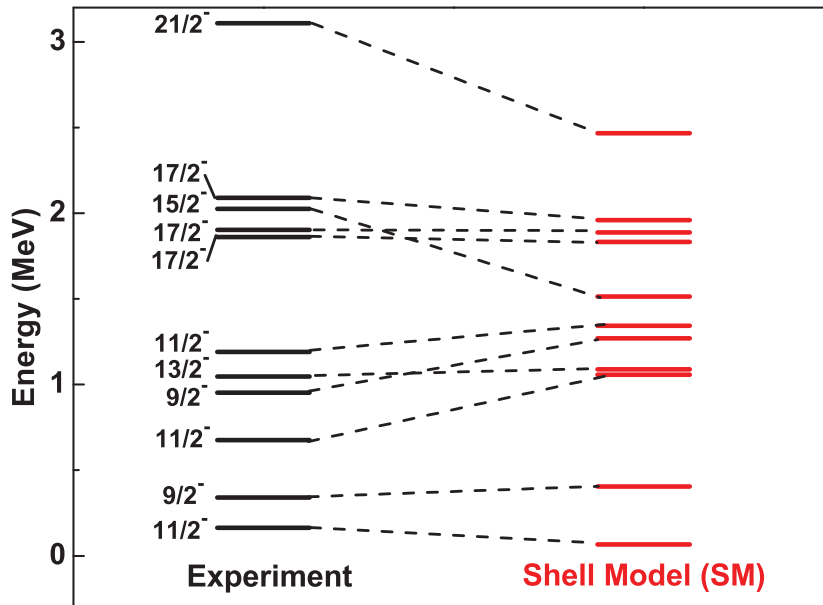


Figure 5.21: Comparison of the calculated energy levels (red) using the shell model calculations with the experimental levels (black) in  $^{131}\text{Xe}$ .

The levels in the non-yrast sequence, marked as  $B5$  in the level scheme, are found to decay via various non-stretched transitions, indicating these states to be of single particle origin. Shell Model calculations are carried out to characterize these states employing the code NUSHELLX [50] in the  $gdsh$  model space with the  $jj55pna$  Hamiltonian, referred as SN100PN interaction [51]. The available orbitals are consisting of  $g_{7/2}$ ,  $d_{5/2}$ ,  $d_{3/2}$ ,  $s_{1/2}$  and  $h_{11/2}$ , for both protons and neutrons in the shell  $N, Z = 50 - 82$ . The calculations are carried out without any restriction in the proton and neutron model space. The comparison between the calculated energy levels and the experimental levels of the sequence  $B5$  is shown in Fig. 5.21. For this purpose, the experimental levels with increasing order of excitation energy for a given spin are compared with the corresponding states of the shell model calculations. A good agreement between the experimental states and the shell model calculations for sequences  $B5$  is obtained.

## 5.8 Summary

The excited states in  $^{131}\text{Xe}$  are studied with the Compton suppressed clover detector setup of INGA, coupled to digital data acquisition system. The level structure of  $^{131}\text{Xe}$  has been significantly extended, compared to the previous studies, with the observation and placement of 72 new  $\gamma$ -ray transitions. The yrast negative-parity band is seen up to  $35/2^-$  spin and the signature partner of this band is identified for the first time. The positive-parity ground state band, built on the  $3/2^+$  ground state, is extended up to  $23/2^+$  spin, with the observation of a signature inversion, which signifies a pair of particle alignment around the spin of  $15/2\hbar$ . A dipole band, consisting of M1 transitions, is identified and interpreted in terms of shears mechanism, having a 5-qp configuration. A new band structure, built on the 3-qp  $23/2^+$  state, is also observed with a large signature splitting. A comparison of the excited states in the isotopic and isotonic chains reveals the transitional nature of the  $N = 77$  nuclei. Total Routhian Surface calculations predicts a  $\gamma$ -soft nature of this nucleus at higher spin.

# Bibliography

- [1] R. Wyss *et al.*, Nucl. Phys. A **505**, 337 (1989).
- [2] S. Juutinen *et al.*, Phys. Rev. C **51**, 1699 (1995).
- [3] T. Lönnroth *et al.*, Physica Scripta. **27**, 228, (1983).
- [4] N.V. Zamfir and R.F. Casten, Phys. Lett. B **260**, 265 (1991).
- [5] A.P. Byrne *et al.*, Nucl. Phys. A **548**, 131 (1992).
- [6] R. Ma *et al.*, Phys. Rev. C, **41**, 2624 (1990).
- [7] A. Granderath *et al.*, Nucl. Phys. A **597**, 427 (1996).
- [8] R.F. Casten and P. von Brentano, Phys. Lett. B **152**, 22 (1985).
- [9] K. Nomura, T. Niksic and D. Vretenar, Phys. Rev. C **96**, 014304 (2017).
- [10] E. Teruya *et al.*, Phys. Rev. C, **92**, 034320 (2015).
- [11] A. Astier *et al.*, Eur. Phys. J. A **50**, 2 (2014).
- [12] L. Kaya *et al.*, Phys. Rev. C **98**, 014309 (2018).
- [13] A. Al-Khatib *et al.*, Phys. Rev. C **83**, 024306 (2011).
- [14] S. Chakraborty *et al.*, Phys. Rev. C **97**, 054311 (2018).
- [15] S. Chakraborty *et al.*, Braz. Jour. of Phys. **47**, 406 (2017).

- [16] Y. Huang *et al.*, Phys. Rev. C **93**, 064315 (2016).
- [17] G. Rainovski *et al.*, Phys. Rev. C **66**, 014308 (2002).
- [18] R.A. Meyer *et al.*, F. Momyer and W. B. Walters, Z. Physik **268**, 387 (1974).
- [19] A.D. Irving *et al.*, P.D. Forsyth, I. Hall and D.G.E Martin, J. Phys. G: Nucl. Phys. **5**, 1595 (1979).
- [20] D.C. Palmer *et al.*, A.D. Irving, P.D. Forsyth, I. Hall, D.G.E. Martin and M.J Maynard, J. Phys. G: Nucl. Phys. **4**, 1143 (1978).
- [21] Chr. Bargholtz *et al.*, S. Beshai and L. Gidefeldt, Nucl. Phys. A **270**, 189 (1976).
- [22] A. Kerek *et al.*, A. Luukko, M. Grecescu and J. Sztarkier, Nucl. Phys A **172**, 603 (1971).
- [23] Soumik Bhattacharya *et al.*, Proceedings of the DAE Symp. on Nucl. Phys. **63**, 1156 (2018).
- [24] S. Das, S. Samanta *et al.*, Nucl. Instrum. and Methods in Phys. Res. A, 893, 138 (2018).
- [25] D. C. Radford, Nucl. Instrum. Methods Phys. Res. A, 361, 297 (1995).
- [26] <http://www.tifr.res.in/~pell/lamps.html>
- [27] A. Krämer-Flecken *et al.*, Nucl. Instrum. Methods Phys. Res. A **275**, 333 (1989).
- [28] K. Starosta *et al.*, Nucl. Instrum. Methods Phys. Res. A **423**, 16 (1999).
- [29] Ch. Droste *et al.*, Nucl. Instrum. Methods Phys. Res. A **378**, 518 (1996).
- [30] R. Banik *et al.*, Phys. Rev. C **101**, 044306 (2020).
- [31] Yu. Khazov *et al.*, Nucl. Data Sheet **107**, 2715 (2006).
- [32] H. Pai *et al.*, Phys. Rev. C **84**, 041301(R) (2011).
- [33] C.T. Zhang *et al.*, Nucl. Phys. **A628**, 386 (1998).
- [34] L. Goettig *et al.*, Nucl. Phys. **A 357**, 109 (1981).

- [35] T. Lönnroth *et al.*, Nucl. Phys. **A431**, 256 (1984).
- [36] W. Nazarewicz, J. Dudek, R. Bengtsson, T. Bengtsson and I. Ragnarsson, Nucl. Phys. **A 435**, 397 (1985).
- [37] W. Nazarewicz, M.A. Riley and J.D. Garrett, Nucl. Phys. **A 512**, 61 (1990).
- [38] G. Mukherjee, P. Joshi, R.K. Bhowmik, S.N. Roy, S. Dutta, S. Muralithar and R.P. Singh, Nucl. Phys. **A 829**, 137 (2009).
- [39] R. Banik *et al.*, EPJ Web of Conferences, **232**, 04001 (2020).
- [40] Amita, A. K. Jain, and B. Singh, At. Data and Nucl. Data Tables 74, 283 (2000).
- [41] S. Frauendorf, Rev. Mod. Phys. 73, 463 (2001).
- [42] R.M. Clark, A.O. Macchiavelli, Annu. Rev. Nucl. Part. Sci.**50**, 1 (2000).
- [43] A.A. Pasternak *et al.*, Eur. Phys. J. **A 23**, 191 (2005).
- [44] E.O. Podsvirova *et al.*, Eur. Phys. J. **A 21**, 1 (2004).
- [45] A.A.Pasternak *et al.*, Eur. Phys. J. **A 37**, 279 (2008).
- [46] S. Rajbanshi *et al.*, Phys. Rev. C **89**, 014315 (2014).
- [47] S. Rajbanshi *et al.*, Phys. Rev. C **90**, 024318 (2014).
- [48] A. A. Pasternak, E. O. Liedera and R. M. Liederb, Acta Phys. Pol. **B 40**, 647 (2009).
- [49] R.M. Clark *et al.*, Phys. Rev. Lett. **82**, 3220 (1999).
- [50] B. A. Brown and W. D. M. Rae, Nucl. Data Sheets, **120**, 115 (2014).
- [51] B. A. Brown, N. J. Stone, J. R. Stone *et al.*, Phys. Rev. C, **71**, 044317 (2005).

# Chapter 6

## Prompt-delayed spectroscopy of neutron-rich Iodine nuclei near $N = 82$

### 6.1 Introduction

The nuclei having odd numbers of valence protons or neutrons near a major shell closure are always of special interests, as their level structures carry an important link to the nucleon-nucleon effective interactions [1, 2, 3] of that major shell. Thus, the single particle excitations, particle-hole interactions and mixing of various single particle configurations in nuclei with few valence particles/holes around the doubly magic nucleus  $^{132}\text{Sn}$  have been the subject of contemporary interest, both experimentally [4, 5, 6, 7, 8] and theoretically [2, 9]. In particular, nuclei with a few odd valence protons outside the  $Z = 50$  shell closure provide important information about the proton single particle energies and multiplets of various particle-hole configurations. Also, these nuclei with few odd neutron holes in the  $N = 82$  shell, provide key inputs in understanding the effective proton-neutron interactions used for the large scale shell model calculations. The presence of high- $j$ , unique parity  $h_{11/2}$  orbital in the  $Z, N = 50 - 82$  shell, for both protons and neutrons, plays the major role in generating the high spin states for nuclei in  $A = 130$  region. Configurations involving  $h_{11/2}$  neutron holes are also

responsible for systematic occurrence of the isomers in odd- $A$  as well as in odd-odd nuclei in this region [10]. It would be, thus, interesting to investigate the level structures above these isomers to understand the involvement of the  $h_{11/2}$  orbital and the relative contribution of proton and neutron occupancies in this high- $j$  orbital, in generating the high spin states above the isomers.

The Iodine ( $Z = 53$ ) isotopes with three protons outside the  $Z = 50$  core and few neutron holes/particles in vicinity of the  $N = 82$  core have attracted attention of several recent studies [11, 12]. The importance of several structures based on the  $\pi g_{7/2}$ ,  $\pi d_{5/2}$  and  $\nu h_{11/2}$  orbitals has been reported systematically in the odd-odd Iodine isotopes till  $N = 75$  [13, 14, 11, 12]. In the odd- $A$  Iodine isotopes,  $^{127,129}\text{I}$ , collective bands based on the  $\pi g_{7/2}$ ,  $\pi d_{5/2}$  and  $\pi h_{11/2}$  configurations have been reported. At higher spins, the states associated with a neutron pair breaking, involving orbitals  $\pi g_{7/2}$  and  $\nu h_{11/2}$ , have also been observed [15, 16]. Towards the  $N = 82$ , isomeric states ( $19/2^-$  and  $23/2^+$ ) dominated by two neutron-hole configurations coupled to the odd number of protons have been identified in  $^{131,133}\text{I}$  ( $N = 78, 80$ ) [18].

The information on high spin states above the isomers of neutron-rich Iodine isotopes towards the  $N = 82$ , is very limited. This is mainly because of the fact that these nuclei are at the limit of population using the fusion evaporation reactions, which could be used to produce the isotopes till  $^{129}\text{I}$ . On the other hand, for the heavier isotopes towards the neutron-rich side, either multi-nucleon transfer reactions [18] or spontaneous fission of  $^{252}\text{Cf}$  [19] or  $^{248}\text{Cm}$  [20, 21, 22] were used to study the high spin excitations. Studies of the spontaneous fission of Actinides utilize the prompt high-fold  $\gamma$ - $\gamma$  coincidence techniques to identify the high spin states. With this technique, it is difficult to obtain the  $\gamma$ - $\gamma$  correlations across a long lived isomer. Neutron-rich Iodine nuclei, above the  $N = 82$  shell closure, could be studied using spontaneous fission of  $^{252}\text{Cf}$  and  $^{248}\text{Cm}$  [21, 22]. In contrast, for neutron-rich Iodine isotopes  $^{130,132}\text{I}$ , just below the  $N = 82$ , almost no information on the high spin states is available. Low lying long lived high spin isomers ( $6^-, 8^-$ ) have been identified systematically in the odd-odd neutron-rich Iodine isotopes. Few states above the ( $8^-$ ) isomer ( $T_{1/2} = 3.52$  min) in  $^{134}\text{I}$  [19], have been identified, but no excited states above the corresponding ( $8^-$ ) isomers ( $T_{1/2} = 1.38$  hr in  $^{132}\text{I}$  and  $T_{1/2} = 315$  ns in  $^{130}\text{I}$ ) were reported.

In this work, the neutron-rich Iodine isotopes  $^{130-134}\text{I}$  were produced as fission fragments and excited states have been characterized from the in-beam prompt-delayed  $\gamma$ -ray spectroscopy after the isotopic identifications ( $A, Z$ ). The high spin excitations above the  $(8^-)$  isomer and the corresponding  $\gamma$ -ray transitions in the odd-odd Iodine nuclei  $^{130,132}\text{I}$  have been observed for the first time. A new isomer in  $^{132}\text{I}$  has been identified and the half-life has been measured from the corresponding  $\gamma$ -ray decay. New prompt  $\gamma$ -ray transitions above the isomeric states,  $19/2^-$ , in  $^{131,133}\text{I}$  and  $(8^-)$  in  $^{134}\text{I}$  have also been identified. The contribution of the neutron hole occupancy of the  $\nu h_{11/2}$  orbital to the high spin negative parity states is analyzed using the large scale shell model calculations.

## 6.2 Experiment and Data Analysis

The excited states of the neutron rich Iodine isotopes were populated via fusion-fission and transfer induced fission reactions in inverse kinematics, using the  $^{238}\text{U}$  beam at the energy of 6.2 MeV/u, bombarding on two different  $^9\text{Be}$  targets of thicknesses 1.6  $\mu\text{m}$  and 5  $\mu\text{m}$  each at Grand Accélérateur National d'Ions Lourds (GANIL), France. The isotopic identification ( $A, Z$ ) of the fission fragments was obtained using the large acceptance magnetic spectrometer VAMOS++, placed at an angle of  $20^\circ$  with respect to the beam axis [23, 24, 25, 26, 27]. The  $Z$  identification was obtained by a  $\Delta E - E$  measurement using the ionization chamber placed at the focal plane of VAMOS++. Time of Flight of each fragment was measured using the Dual Position-Sensitive multi-wire proportional counter (DPS-MWPC) [26], placed at the entrance of the VAMOS++ and the MWPC placed at the focal plane. The focal plane detector system also consisted of two drift chambers (DC) for tracking. The mass number ( $A$ ), atomic number ( $Z$ ), atomic charge ( $Q$ ) and the velocity vector of the fission fragments were determined on an event-by-event basis. The  $(M/Q)$  parameter was obtained from the reconstructed magnetic rigidity ( $B\rho$ ) and the velocity of the fragment. The isotopic identification for the Iodine isotopes obtained from the two-dimensional plot of  $Q$  and  $M/Q$  is shown in Fig. 6.1. The narrow gates were applied to obtain the corresponding  $\gamma$ -ray spectra. The possible contaminations of the  $\gamma$ -ray spectra by the nuclei associated with the neighboring  $Z$ ,  $A$ , and  $Q$  were individually

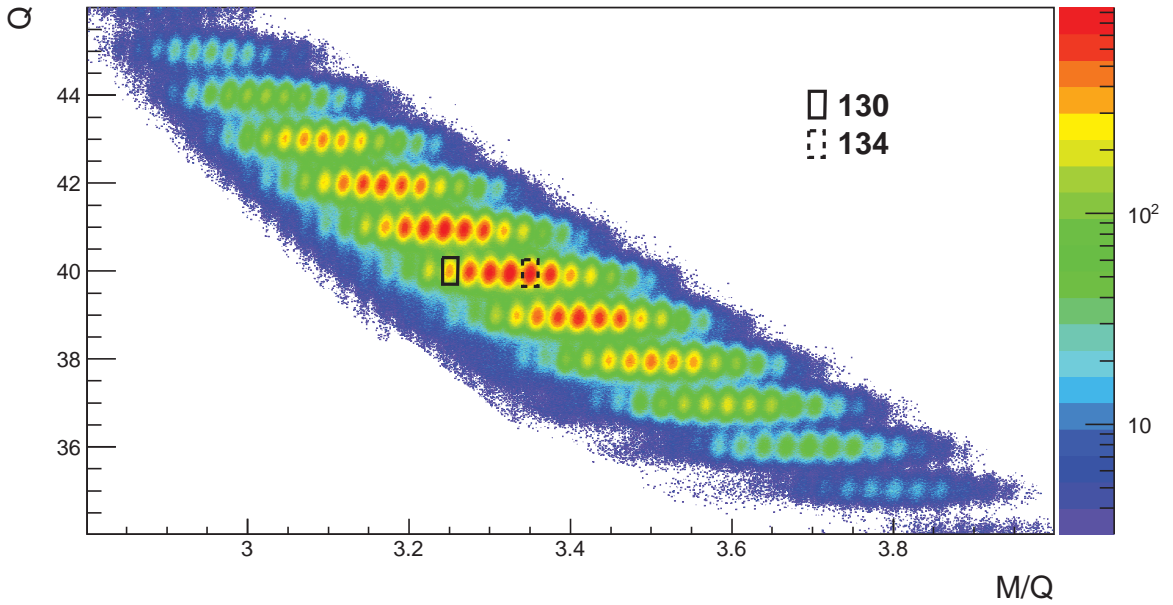


Figure 6.1: Charge state ( $Q$ ) as a function of the mass over charge ( $M/Q$ ) after the selection of Iodine ( $Z = 53$ ). The Iodine isotopes are obtained from various charge states and the identification of  $A = 130$  and  $134$  are marked for charge state  $Q = 40$ .

examined. The analysis of the corresponding  $\gamma$ -ray spectra allowed to evaluate any possible small contamination and perform the suitable background subtraction case by case.

The prompt  $\gamma$  rays ( $\gamma_P$ ) emitted from the recoiling fission products at the target position were detected using the  $\gamma$ -ray tracking array AGATA [28]. In the current experimental setup, the AGATA consisted of 32 crystals and was placed at 13.5 cm away from the target. An array of seven EXOGAM segmented Clover detectors [29] was also placed after the focal plane of the VAMOS++ to detect the delayed  $\gamma$  rays ( $\gamma_D$ ). Further details of the experimental setup consisting VAMOS++, AGATA and EXOGAM can be found in Chapter 3 of this thesis.

Coincidence matrices were constructed between the prompt  $\gamma$  rays ( $\gamma_P$ - $\gamma_P$ ), prompt-delayed  $\gamma$  rays ( $\gamma_P$ - $\gamma_D$ ) and any two delayed  $\gamma$  rays ( $\gamma_D$ - $\gamma_D$ ) [27]. Also small corrections for isobaric and isotopic contamination (if any) were taken into account for each of the Iodine isotopes in both prompt and delayed spectra following the procedure described in Chapter 3. Intensity

determination and corrections for the half-lives calculations have also been carried out, as described in Ref. [27].

## 6.3 Results

### 6.3.1 $^{130}\text{I}$

Prior to the present study, the spectroscopic information of  $^{130}\text{I}$  was limited only to low spin excitations up to 1 MeV, investigated via  $(n, \gamma)$  and  $(d, p)$  reactions using two Ge(Li) detectors [30]. Some of the  $\gamma$ -ray transitions reported in Ref. [30] were also previously identified in  $(p, n)$  reaction [31]. Half-lives of four isomeric states at 39.95 keV ( $8.3 \pm 1$  min), 69.59 keV ( $133 \pm 7$  ns), 82.39 keV ( $315 \pm 15$  ns) and 85.11 keV ( $254 \pm 4$  ns) were also reported in Ref. [30] with probable spin-parity assignments as  $2^+$ ,  $6^-$ ,  $8^-$  and  $6^-$  respectively. The 82.39 keV level was assigned as  $8^-$  in Ref. [30] from the observed coincidences. However, this  $8^-$  assignment for the 82.39 keV level is not adopted in Ref. [32]. No high spin states above the ( $6^-$ ) or ( $8^-$ ) isomers have been reported for  $^{130}\text{I}$  prior to the present work.

Fig. 6.2 shows the proposed level scheme of  $^{130}\text{I}$ , obtained using the prompt-delayed coincidence in the present work [33]. All the transitions placed in the level scheme above the isomeric state are observed for the first time and are marked in red. The relative placements of these  $\gamma$ -ray transitions in the level scheme are done based on their mutual coincidence relationships and relative intensities. The details of the  $\gamma$  rays of  $^{130}\text{I}$  with tentative spin and parity of the initial ( $J_i^\pi$ ) and the final ( $J_f^\pi$ ) states are given in Table 6.1. Fig. 6.3(a) shows the prompt singles  $\gamma$ -ray spectrum ( $\gamma_P$ ) after Doppler correction, in coincidence with the  $^{130}\text{I}$  fragments, detected at the focal plane of the VAMOS++ spectrometer. A coincidence spectrum corresponding to the sum of gates on 748, 922 and 971 keV transitions is shown in Fig. 6.3(b). The 748, 922, 135 and 971 keV  $\gamma$  rays are found to be in mutual coincidence, whereas, the 588 and 812 keV  $\gamma$  rays are observed only in coincidence with the 748 keV. This is evident from the coincidence spectra corresponding to 588 and 922 keV transitions shown in Fig. 6.3(c) and Fig. 6.3(d), respectively.

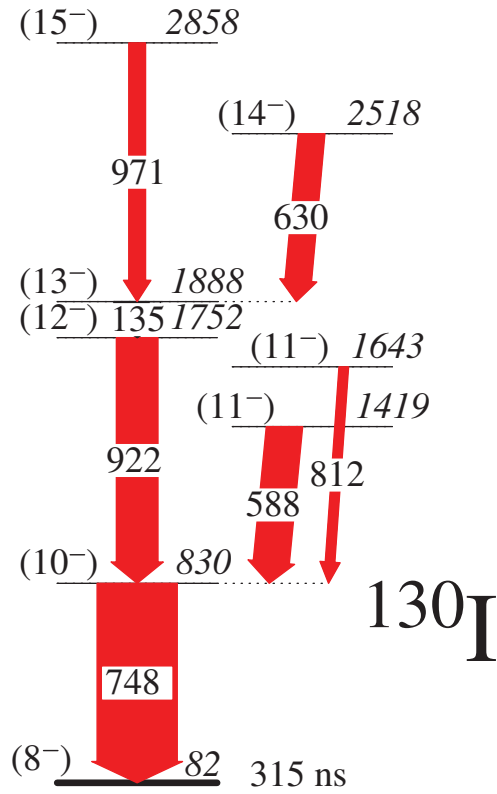


Figure 6.2: Level scheme of  $^{130}\text{I}$  above the  $(8^-)$  isomeric level, as obtained in the present work. The newly observed  $\gamma$  rays are displayed in red. The thickness of the  $\gamma$  rays represents their relative intensities.

Similarly, the 630 keV  $\gamma$ -ray is found to be in coincidence with the 748-922-135 keV cascade, but not with the 971, 588 and 812 keV  $\gamma$  rays. A coincidence spectrum corresponding to the 630 keV  $\gamma$ -ray gate is also shown in Fig. 6.3(e), where the presence of the 748, 922 and 135 keV  $\gamma$  rays is clearly visible. Other transitions, *i.e.*, 397, 465, 607 keV  $\gamma$  rays are also observed in prompt spectrum and are marked in Fig. 6.3(a), but no coincidence could be obtained with other prompt  $\gamma$  rays in  $^{130}\text{I}$ , observed in the present work. These transitions were also previously reported in Ref. [30], but the  $\gamma$  rays which were reported to be in coincidence with these transitions in Ref. [30], are not observed in the present work. There are few more  $\gamma$  rays of energies 340, 375, 444, 557, 738 and 1091 keV, which are identified as belonging to  $^{130}\text{I}$  and marked in the total singles spectrum (Fig. 6.3(a)), but could not be placed in the level scheme due to lack of coincidence information.

Table 6.1: Energies ( $E_\gamma$ ) and relative intensities ( $I_\gamma$ ) of the  $\gamma$  rays observed in  $^{130}\text{I}$  along with tentative spin and parity of the initial ( $J_i^\pi$ ) and the final ( $J_f^\pi$ ) states and the energy of the initial state ( $E_i$ ).

$E_\gamma$ (keV)	$E_i$ (keV)	$I_\gamma$	$J_i^\pi \rightarrow J_f^\pi$
135.3(2)	1887.5	44(9)	$(13^-) \rightarrow (12^-)$
588.1(1)	1418.5	45(10)	$(11^-) \rightarrow (10^-)$
630.1(3)	2517.6	31(11)	$(14^-) \rightarrow (13^-)$
748.4(2)	830.4	100	$(10^-) \rightarrow (8^-)$
812.5(1)	1642.9	12(7)	$(11^-) \rightarrow (10^-)$
921.8(1)	1752.2	52(10)	$(12^-) \rightarrow (10^-)$
970.9(1)	2858.4	21(6)	$(15^-) \rightarrow (13^-)$

The isomers in  $^{130}\text{I}$  decay via low energy  $\gamma$ -ray transitions. The lower cutoff of the delayed  $\gamma$ -ray spectra of the present setup was around 80-100 keV, and thus the low energy decay  $\gamma$  rays from these low lying isomers could not be observed in the delayed spectrum obtained in the present work. Therefore, the definite placement of the observed prompt transitions above particular isomeric state is not possible. Following the systematics of neighboring even- $A$  Iodine isotopes, the observed prompt  $\gamma$  rays from the present work are tentatively placed above the existing  $(8^-)$  isomer.

### 6.3.2 $^{131}\text{I}$

Low lying states of  $^{131}\text{I}$  were previously studied using  $\beta$ -decay of  $^{131}\text{Te}$  [34, 35, 36] and  $(^3\text{He}, d)$  [37] reaction. An isomeric level at  $15/2^-$  with half-life 5.9 ns was reported from the  $\beta$ -decay studies [34]. The only in-beam spectroscopic study of  $^{131}\text{I}$ , prior to the present work, was carried out using multi-nucleon transfer reaction [18], where new isomers at  $19/2^-$

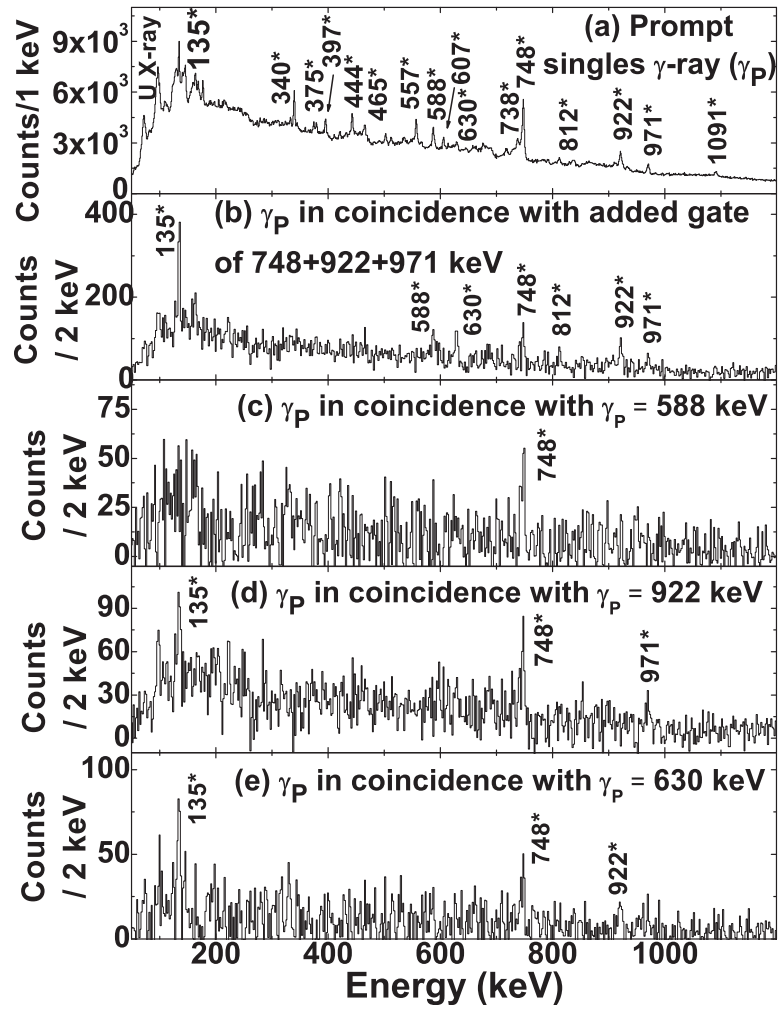


Figure 6.3: (a) The prompt singles  $\gamma$ -ray spectrum ( $\gamma_P$ ) of  $^{130}\text{I}$ . (b) Prompt  $\gamma$  rays ( $\gamma_P$ ) in coincidence with added gates of  $\gamma_P = 748+922+971$  keV. (c) Prompt  $\gamma$  rays ( $\gamma_P$ ) in coincidence with  $\gamma_P = 588$  keV. (d) Prompt  $\gamma$  rays ( $\gamma_P$ ) in coincidence with  $\gamma_P = 922$  keV. (e) Prompt  $\gamma$  rays ( $\gamma_P$ ) in coincidence with  $\gamma_P = 630$  keV. The new  $\gamma$ -transitions are marked with ‘\*’ in all the cases.

( $24 \mu\text{s}$ ),  $23/2^+$  (42 ns) and ( $31/2^-$ ,  $33/2^-$ ) (25 ns) were identified along with their depopulating transitions.

The proposed level scheme of  $^{131}\text{I}$ , as obtained from the present work [33], is shown in Fig. 6.4. The details of the  $\gamma$  rays of  $^{131}\text{I}$  with tentative spin and parity of the initial ( $J_i^\pi$ ) and the

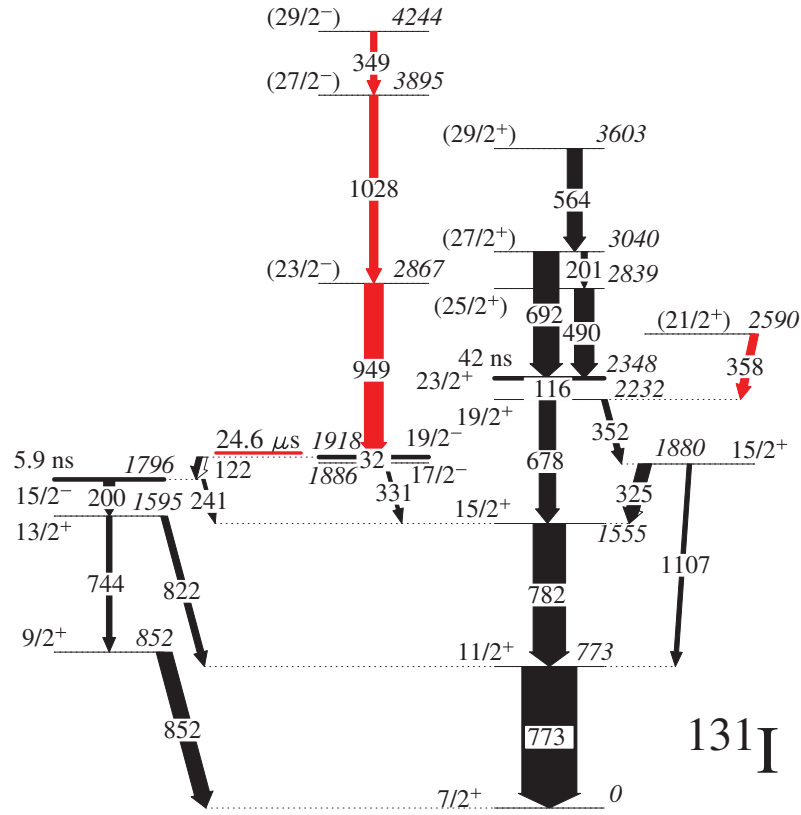


Figure 6.4: Level scheme of  $^{131}\text{I}$  as obtained in the present work. The newly observed  $\gamma$  rays are displayed in red. Isomeric state is indicated with a thick line and the half-life remeasured in this work is underlined by a red line. The thickness of the  $\gamma$  rays represent their relative intensities.

final ( $J_f^\pi$ ) states are given in Table 6.2. The Doppler corrected prompt singles  $\gamma$ -ray spectrum ( $\gamma_P$ ), in coincidence with the  $^{131}\text{I}$  fragments, is shown in Fig. 6.5(a). The newly observed  $\gamma$ -ray transitions from the present measurement are marked with '\*'. All the other identified  $\gamma$  rays were previously reported in Ref. [18]. Fig.6.5(b) represents the added coincidence gates of prompt  $\gamma$  rays of energies 773 and 782 keV. All the  $\gamma$  rays which are in prompt coincidence with 773 and 782 keV are present in this spectrum. The expanded energy range of 300-400 keV of this prompt coincidence spectrum is shown in the inset of Fig. 6.5(b). The presence of 325, 331, 352 and 358 keV prompt  $\gamma$  rays is clearly visible from the inset. The 358 keV  $\gamma$ -ray is the new transition observed in the present work and placed in the level scheme (Fig. 6.4) between

Table 6.2: Energies ( $E_\gamma$ ) and relative intensities ( $I_\gamma$ ) of the  $\gamma$  rays observed in  $^{131}\text{I}$  along with tentative spin and parity of the initial ( $J_i^\pi$ ) and the final ( $J_f^\pi$ ) states and the energy of the initial state ( $E_i$ ). The top and bottom panels, separated by a line, are for the prompt and delayed transitions, respectively. The low energy transitions which could not be detected with the present setup are adopted from Ref.[18] and are put within parenthesis.

$E_\gamma$ (keV)	$E_i$ (keV)	$I_\gamma$	$J_i^\pi \rightarrow J_f^\pi$
201.1(1)	3039.8	10(1)	(27/2 <sup>+</sup> ) $\rightarrow$ (25/2 <sup>+</sup> )
240.8(3)	1795.5	6(2)	15/2 <sup>-</sup> $\rightarrow$ 15/2 <sup>+</sup>
325.2(2)	1879.9	23(9)	15/2 <sup>+</sup> $\rightarrow$ 15/2 <sup>+</sup>
330.9(2)	1885.6	6(2)	17/2 <sup>-</sup> $\rightarrow$ 15/2 <sup>+</sup>
348.6(2)	4243.7	11(3)	(31/2 <sup>-</sup> ) $\rightarrow$ (27/2 <sup>-</sup> )
352.3(2)	2232.2	10(1)	19/2 <sup>+</sup> $\rightarrow$ 15/2 <sup>+</sup>
358.2(3)	2590.4	14(2)	(21/2 <sup>+</sup> ) $\rightarrow$ 19/2 <sup>+</sup>
490.5(1)	2838.7	35(1)	(25/2 <sup>+</sup> ) $\rightarrow$ 23/2 <sup>+</sup>
563.6(1)	3603.4	27(2)	(29/2 <sup>+</sup> ) $\rightarrow$ (27/2 <sup>+</sup> )
677.5(1)	2232.2	30(3)	19/2 <sup>+</sup> $\rightarrow$ 15/2 <sup>+</sup>
691.6(1)	3039.8	46(2)	(27/2 <sup>+</sup> ) $\rightarrow$ 23/2 <sup>+</sup>
773.1(1)	773.1	100	11/2 <sup>+</sup> $\rightarrow$ 7/2 <sup>+</sup>
781.6(2)	1554.7	59(2)	15/2 <sup>+</sup> $\rightarrow$ 11/2 <sup>+</sup>
822.3(1)	1595.4	12(2)	13/2 <sup>+</sup> $\rightarrow$ 11/2 <sup>+</sup>
851.9(1)	851.9	28(2)	9/2 <sup>+</sup> $\rightarrow$ 7/2 <sup>+</sup>
949.1(1)	2866.7	34(1)	(23/2 <sup>-</sup> ) $\rightarrow$ 19/2 <sup>-</sup>
1028.4(1)	3895.1	15(2)	(27/2 <sup>-</sup> ) $\rightarrow$ (23/2 <sup>-</sup> )
1106.8(3)	1879.9	8(1)	15/2 <sup>+</sup> $\rightarrow$ 11/2 <sup>+</sup>
(32)	1917.6	-	19/2 <sup>-</sup> $\rightarrow$ 17/2 <sup>-</sup>
(116)	2348.2	-	23/2 <sup>+</sup> $\rightarrow$ 19/2 <sup>+</sup>
122.1(1)	1917.6	34(5)	19/2 <sup>-</sup> $\rightarrow$ 15/2 <sup>-</sup>
199.9(2)	1795.5	14(4)	15/2 <sup>-</sup> $\rightarrow$ 13/2 <sup>+</sup>
743.7(1)	1595.6	15(2)	13/2 <sup>+</sup> $\rightarrow$ 9/2 <sup>+</sup>

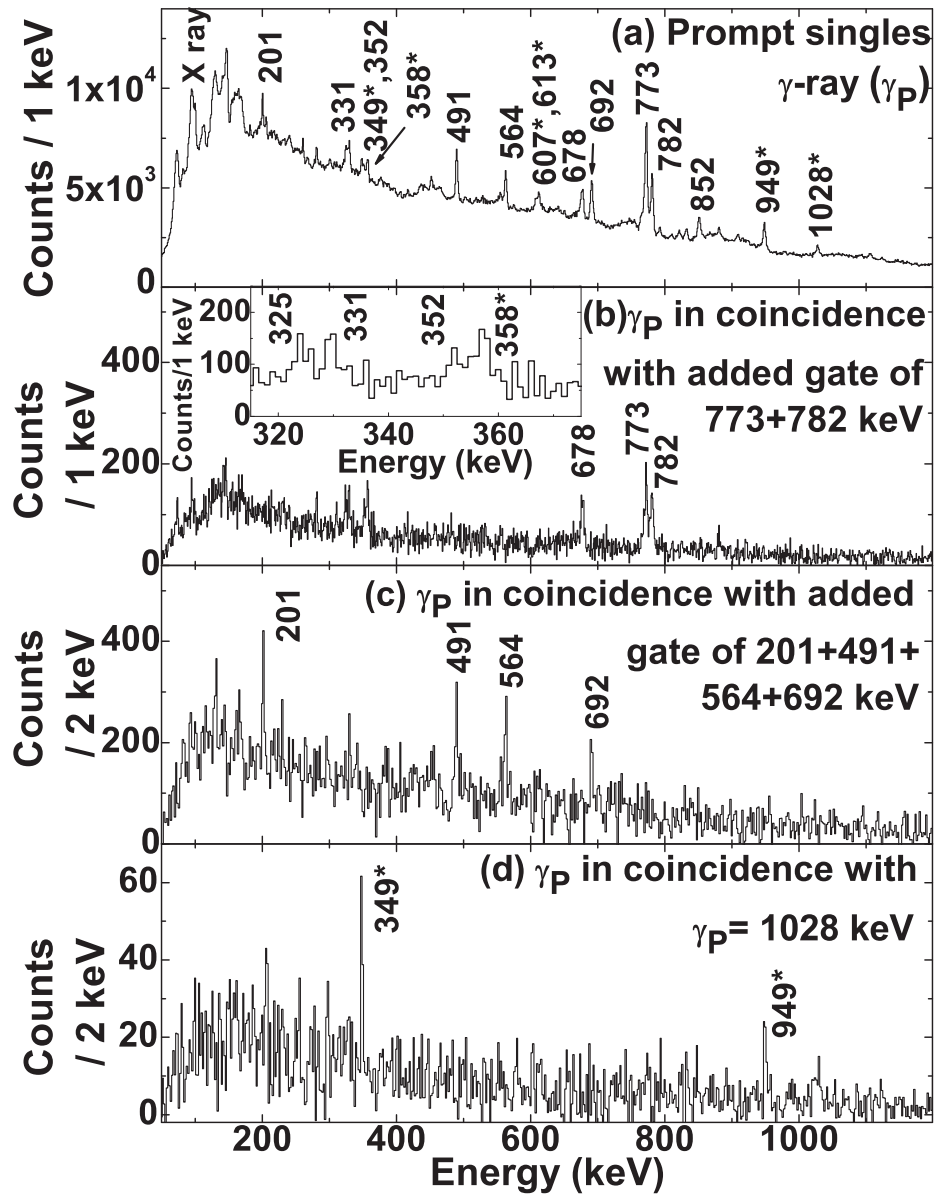


Figure 6.5: (a) The prompt singles  $\gamma$ -ray spectrum of  $^{131}\text{I}$ . (b) Prompt  $\gamma$  rays ( $\gamma_P$ ) in coincidence with added gates of  $\gamma_P = 773 + 782$  keV. The inset shows the expanded energy range of 300-400 keV. (c) Prompt  $\gamma$  rays ( $\gamma_P$ ) in coincidence with added gates of  $\gamma_P = 201 + 491 + 564 + 692$  keV. The new  $\gamma$ -transitions are marked with ‘\*’.

the 2590 and 2232 keV levels. The other two new  $\gamma$  rays of energies 607 and 613 keV, observed in the present work, could not be placed in the level scheme, as no coincidence of these  $\gamma$  rays

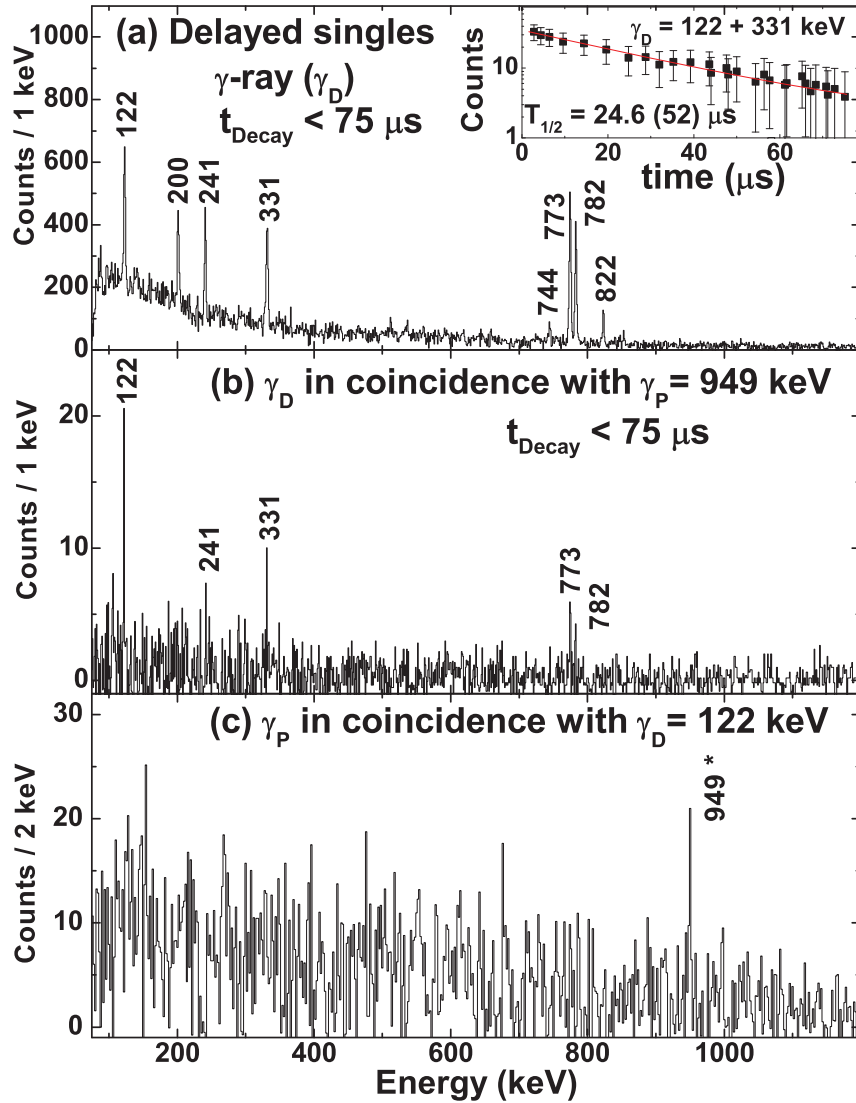


Figure 6.6: (a) The delayed singles  $\gamma$ -ray ( $\gamma_D$ ) spectrum of  $^{131}\text{I}$  for  $t_{\text{Decay}} < 75 \mu\text{s}$ . The inset shows the decay curve of  $\gamma_D = 122 + 331 \text{ keV}$  delayed transitions with exponential fit. (b) Delayed  $\gamma$  rays ( $\gamma_D$ ) within the time window  $t_{\text{Decay}} < 75 \mu\text{s}$  in coincidence with  $\gamma_P = 949 \text{ keV}$ . (c) Prompt  $\gamma$  rays ( $\gamma_P$ ) in coincidence with  $\gamma_D = 122 \text{ keV}$ . The new  $\gamma$ -transitions are marked with ‘\*’.

are found with other known transitions of  $^{131}\text{I}$ . It is also evident that though the 949, 1028 and 349 keV new  $\gamma$  rays are observed in prompt singles  $\gamma$  ( $\gamma_P$ ) spectrum (Fig. 6.5(a)), but are not

present in prompt coincidence with 773 and 782 keV (fig. 6.5(b)). Prompt  $\gamma$  rays in coincidence with the added gates of 692, 491, 201 and 564 keV  $\gamma$  rays, confirming the transitions placed above the  $23/2^+$  (42 ns) isomeric level, are shown in Fig. 6.5(c). Fig. 6.5(d) represents the coincidence gate of the 1028 keV transition, which shows that the 949 and 349 keV  $\gamma$  rays are in prompt coincidence with the 1028 keV. But these  $\gamma$  rays are not in prompt coincidence with any other transitions placed in  $^{131}\text{I}$ .

Fig. 6.6(a) shows the delayed singles  $\gamma$ -ray ( $\gamma_D$ ) spectrum obtained with the EXOGAM detectors within the delayed time window of  $t_{Decay} < 75 \mu\text{s}$ . All the delayed  $\gamma$  rays below the 1918 ( $19/2^-$ ) isomeric level are seen in this spectrum. The decay curve corresponding to the 122 + 331 keV delayed  $\gamma$  rays is shown in the inset of Fig. 6.6(a) within the same time window. An exponential fit to the time decay corresponding to the gate of 122 and 331 keV  $\gamma$  rays yield a half-life of  $T_{1/2} = 24.6(5.2) \mu\text{s}$  for the 1918 keV ( $19/2^-$ ) level from the present measurements. The measured half-life of the 1918 keV ( $19/2^-$ ) level corroborates the reported value of  $24(1) \mu\text{s}$  [18]. The delayed  $\gamma$ -ray ( $\gamma_D$ ) spectrum for the time window of  $t_{Decay} < 75 \mu\text{s}$  in coincidence with the newly observed prompt transition of the 949 keV is shown in Fig. 6.6(b). The delayed  $\gamma$  rays de-exciting the  $19/2^-$  isomeric level are seen in this spectrum. This confirms the placement of the 949 keV prompt  $\gamma$ -ray above the 1918 keV ( $19/2^-$ ) isomeric level. Fig. 6.6(c) shows the prompt  $\gamma$ -ray ( $\gamma_P$ ) spectrum corresponding to the gate on the delayed  $\gamma$ -ray 122 keV. The presence of the 949 keV  $\gamma$ -ray in this coincidence spectrum and the mutual prompt coincidence among the 949, 1028 and 349 keV  $\gamma$  rays (as shown in Fig. 6.5(d)) establishes the placement of prompt  $\gamma$ -ray cascade of 949-1028-349 keV above the 1918 keV ( $19/2^-$ ) isomeric level.

### 6.3.3 $^{132}\text{I}$

Low spin excited states of  $^{132}\text{I}$  were studied earlier using  $\beta$ -decay of  $^{132}\text{Te}$ , produced from the  $\alpha$ -induced fission [38]. The lifetime and magnetic moment measurements of low spin states have been reported in various investigations [39, 40, 41]. The presence of an isomeric state ( $(8^-)$ ,  $T_{1/2} = 83.6 \pm 1.7 \text{ min}$ ) at 120 keV excitation was also reported in Ref. [38, 40], it was



Table 6.3: Energies ( $E_\gamma$ ) and relative intensities ( $I_\gamma$ ) of the  $\gamma$  rays observed in  $^{132}\text{I}$  along with probable spin and parity of the initial ( $J_i^\pi$ ) and the final ( $J_f^\pi$ ) states and the energy of the initial state ( $E_i$ ). The total intensity of the 762 keV doublet (d) is normalized to 100.

$E_\gamma$ (keV)	$E_i$ (keV)	$I_\gamma$	$J_i^\pi \rightarrow J_f^\pi$
143.2(2)	1944.6	12(2)	(12 <sup>-</sup> ) $\rightarrow$ (11 <sup>-</sup> )
296.9(1)	1941.3	12(1)	(13 <sup>-</sup> ) $\rightarrow$ (12 <sup>-</sup> )
484.6(1)	1366.8	10(1)	(11 <sup>-</sup> ) $\rightarrow$ (10 <sup>-</sup> )
605.4(1)	605+x	44(1)	(12 <sup>+</sup> ) $\rightarrow$ (11 <sup>+</sup> )
703.0(1)	2644.3	11(2)	(14 <sup>-</sup> ) $\rightarrow$ (13 <sup>-</sup> )
755.7(2)	1361+x	2(1)	(13 <sup>+</sup> ) $\rightarrow$ (12 <sup>+</sup> )
762.2(4)	1644.4		(12 <sup>-</sup> ) $\rightarrow$ (10 <sup>-</sup> )
762.2(4)	882.2	100 <sup>d</sup>	(10 <sup>-</sup> ) $\rightarrow$ (8 <sup>-</sup> )
919.2(3)	1801.4	21(2)	(11 <sup>-</sup> ) $\rightarrow$ (10 <sup>-</sup> )
1062.4(2)	1944.6	14(1)	(12 <sup>-</sup> ) $\rightarrow$ (10 <sup>-</sup> )
1147.8(2)	1753+x	4(1)	(14 <sup>+</sup> ) $\rightarrow$ (12 <sup>+</sup> )
1200.9(2)	2845.3	5(2)	(13 <sup>-</sup> ) $\rightarrow$ (12 <sup>-</sup> )

AGATA, in coincidence with the  $^{132}\text{I}$  fragments is shown in Fig. 6.8(a). A prompt coincidence spectrum corresponding to the gate of the 762 keV  $\gamma$ -ray is shown in Fig. 6.8(b). Presence of a 762 keV transition in the 762 keV gate establishes 762 keV as a doublet transition. Other than the 762 keV, the 143, 297, 485, 703, 919, 1062 and 1201 keV transitions are also found to be in coincidence with the 762 keV  $\gamma$ -ray. The 762 keV doublet and the other transitions observed in the 762 keV gate are placed in the level scheme of  $^{132}\text{I}$  (Fig. 6.7) according to their relative intensities. Among the transitions observed in the 762 keV gate, the 297, 485, 919, 1062 and 1201 keV are not found to be in coincidence with each other. The 143 keV transition is found to be in coincidence with the 762 keV and 919 keV transitions, but not with the 1062 keV. Thus, the 919-143 keV cascade is placed in parallel with the 1062 keV from coincidence relationship, intensities and energy sum. The observed intensity of the 762 keV in the coincidence spectra of 297, 919, 1062 and 1201 keV gates is compared to understand the relative placements of these transitions in the level scheme. The intensity of the 762 keV is found to be more in the coincidence spectra of the 297 and 1201 keV gates than that in the

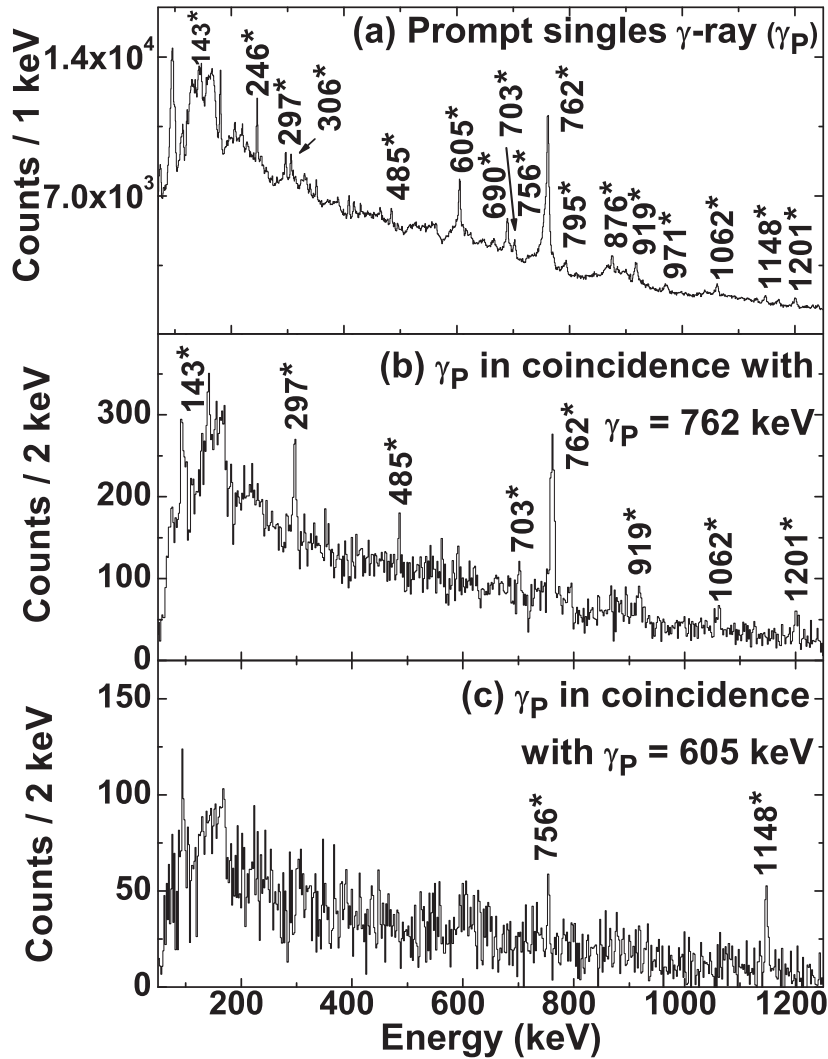


Figure 6.8: (a) The prompt singles  $\gamma$ -ray spectrum of  $^{132}\text{I}$ . (b) Prompt  $\gamma$  rays ( $\gamma_P$ ) in coincidence with  $\gamma_P = 762$  keV. (c) Prompt  $\gamma$  rays ( $\gamma_P$ ) in coincidence with  $\gamma_P = 605$  keV. The new  $\gamma$ -transitions are marked with ‘\*’.

coincidence spectra of the 1062 and 919 keV gates, after appropriate intensity normalization of the gating transitions. Thus, it is clear that the 1062 and 919 keV  $\gamma$  rays are in coincidence with one of the transitions of the 762 keV doublet, whereas, the 297 and 1201 keV are in coincidence with both the transitions of the 762 keV doublet. Also the 605, 756 and 1148 keV  $\gamma$  rays are seen in the prompt singles ( $\gamma_P$ ) spectrum (Fig. 6.8(a)), but are not in coincidence

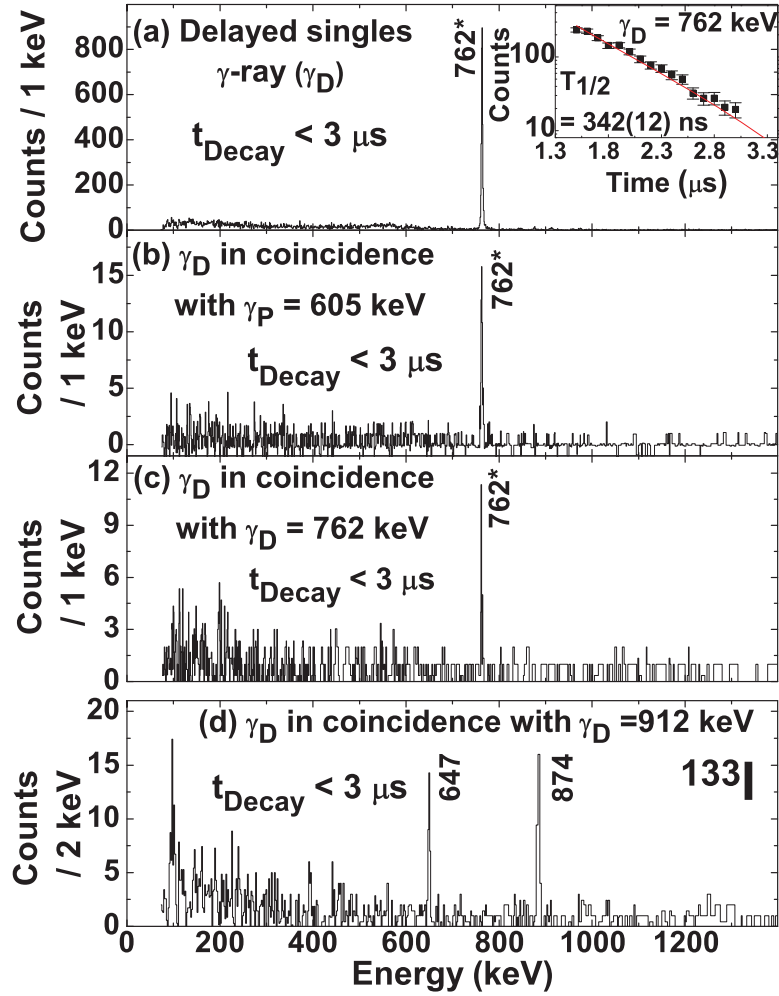


Figure 6.9: (a) The delayed singles  $\gamma$ -ray ( $\gamma_D$ ) spectrum of  $^{132}\text{I}$  in the time window  $t_{\text{Decay}} < 3 \mu\text{s}$ . The inset shows the decay pattern of delayed  $\gamma$ -ray 762 keV with exponential fitting. (b) Delayed  $\gamma$  rays ( $\gamma_D$ ) within the time window  $t_{\text{Decay}} < 3 \mu\text{s}$  in coincidence with  $\gamma_P = 605 \text{ keV}$ . (c) Delayed  $\gamma$  rays ( $\gamma_D$ ) within the time window  $t_{\text{Decay}} < 3 \mu\text{s}$  in coincidence with  $\gamma_D = 762 \text{ keV}$ . (d) Delayed  $\gamma$  rays ( $\gamma_D$ ) within the time window  $t_{\text{Decay}} < 3 \mu\text{s}$  in coincidence with  $\gamma_D = 912 \text{ keV}$  of  $^{133}\text{I}$ . The new  $\gamma$ -transitions are marked with ‘\*’.

with the 762 keV (Fig. 6.8(b)). The 756 and 1148 keV transitions are found to be present in the coincidence spectrum corresponding to the 605 keV gate as shown in Fig. 6.8(c). On the other hand, no coincidence could be found between the 756 and 1148 keV transitions and hence

these are placed in parallel with each other. The set of transitions of 605, 756 and 1148 keV do not have any prompt coincidence with any other  $\gamma$  rays of the prompt sequence. The  $\gamma$  rays of energies 246, 306, 690, 795 and 876 keV, observed in the prompt singles  $\gamma$ -ray spectrum (Fig. 6.8(a)), could not be placed in the level scheme of  $^{132}\text{I}$ , as no coincidences are found of these with any other  $\gamma$  rays of  $^{132}\text{I}$ .

The delayed singles  $\gamma$ -ray ( $\gamma_D$ ) spectrum obtained with the EXOGAM detectors within the delayed time window of  $t_{Decay} < 3 \mu\text{s}$  is shown in Fig. 6.9(a). Only the 762 keV transition is found to be in this delayed coincidence. The inset of Fig. 6.9(a) shows the fitting of the decay curve of the 762 keV transition, from which the half-life is obtained as  $T_{1/2} = 342(12)$  ns. The delayed  $\gamma$  rays ( $\gamma_D$ ) within the same time window, in coincidence with the prompt transition  $\gamma_P = 605$  keV is shown in Fig. 6.9(b). Thus, the 605, 756 and 1148 keV transitions which are in prompt coincidence with each other, must be placed as prompt transitions above this isomer. Fig. 6.9(c) shows the delayed  $\gamma$  rays observed in coincidence with the delayed transition  $\gamma_D = 762$  keV. It is evident from this spectrum, that, the transitions of 762 keV doublet form a cascade below the isomer. To verify the correctness of the  $\gamma_D$ - $\gamma_D$  procedure, the gate is put on the delayed  $\gamma$ -ray of 912 keV of  $^{133}\text{I}$  with a known cascade below the 478 ns,  $23/2^+$ , isomer at the 2492 keV energy (see text in the next section also). From Fig. 6.9(d), the presence of the known  $\gamma$  rays of this cascade is evident. The 59 keV  $\gamma$ -ray decaying from the isomer could not be observed due to the low energy threshold. Since, in  $^{132}\text{I}$ , the 762 keV doublet, 297 and 703 keV transitions are in prompt coincidence (see Fig. 6.9(b)), neither of the corresponding depopulated levels are isomeric. Therefore, the isomer is likely to be depopulated by a low energy unobserved transition.

### 6.3.4 $^{133}\text{I}$

Spectroscopic information of low spin states of  $^{133}\text{I}$  were first extracted from the  $\beta$ -decay measurements [42, 43]. High spin spectroscopy of  $^{133}\text{I}$  was carried out via multi-nucleon transfer reaction [18]. In these studies three isomers of half-lives 170 ns, 9 sec and 469 ns have been reported at 1729.1 keV ( $15/2^-$ ), 1634.1 keV ( $19/2^-$ ) and 2493.7 keV ( $23/2^+$ ) respectively.

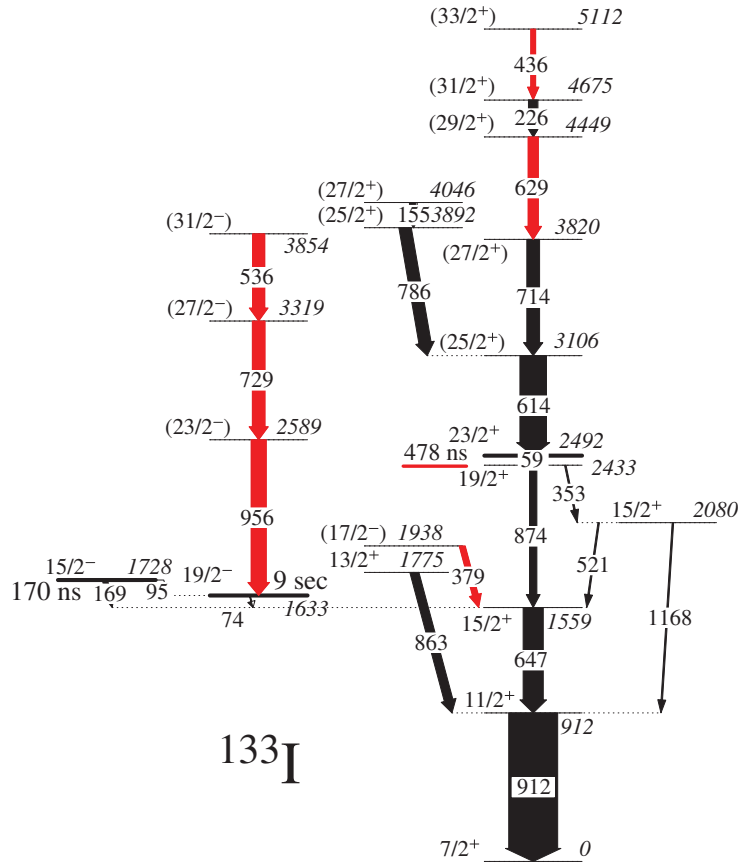


Figure 6.10: Level scheme of  $^{133}\text{I}$  as obtained in the present work. The newly observed  $\gamma$  rays are displayed in red. Isomeric state is indicated with a thick line and the half-life remeasured in this work has been underlined by a red line. The thickness of the  $\gamma$  rays represents their relative intensities.

The proposed level scheme of  $^{133}\text{I}$ , from the present work [33], is shown in Fig. 6.10. The details of the  $\gamma$  rays of  $^{133}\text{I}$  with probable spin and parity of the initial ( $J_i^\pi$ ) and the final ( $J_f^\pi$ ) states are tabulated in Table 6.4. Doppler corrected prompt singles  $\gamma$ -ray ( $\gamma_P$ ) spectrum, obtained with the AGATA, in coincidence with the  $^{133}\text{I}$  fragments, after ( $A, Z$ ) selection at the focal plane of the VAMOS++ spectrometer is shown in Fig. 6.11(a). The new  $\gamma$  rays observed in the present work are marked with '\*'. The higher energy part of the prompt singles  $\gamma$ -ray ( $\gamma_P$ ) spectrum is shown in an expanded scale in the inset of Fig. 6.11(a). The presence of the 1168 keV  $\gamma$ -ray, placed in the level scheme from previous measurements [18], is clear from this

Table 6.4: Energies ( $E_\gamma$ ) and relative intensities ( $I_\gamma$ ) of the  $\gamma$  rays observed in  $^{133}\text{I}$  along with probable spin and parity of the initial ( $J_i^\pi$ ) and the final ( $J_f^\pi$ ) states and the energy of the initial state ( $E_i$ ). The top and bottom panels, separated by a line, are for the prompt and delayed transitions, respectively. The low energy transitions which could not be detected with the present setup are adopted from Ref.[18] and are put within parenthesis.

$E_\gamma$ (keV)	$E_i$ (keV)	$I_\gamma$	$J_i^\pi \rightarrow J_f^\pi$
154.6(1)	4046.3	12(2)	(27/2 <sup>+</sup> ) $\rightarrow$ (25/2 <sup>+</sup> )
226.2(1)	4675.3	18(1)	(31/2 <sup>+</sup> ) $\rightarrow$ (29/2 <sup>+</sup> )
352.7(2)	2433.2	3(1)	19/2 <sup>+</sup> $\rightarrow$ 15/2 <sup>+</sup>
378.5(1)	1937.6	12(1)	(17/2 <sup>-</sup> ) $\rightarrow$ 15/2 <sup>+</sup>
436.2(2)	5111.5	10(1)	(33/2 <sup>+</sup> ) $\rightarrow$ (31/2 <sup>+</sup> )
521.4(1)	2080.5	3(1)	15/2 <sup>+</sup> $\rightarrow$ 15/2 <sup>+</sup>
535.6(2)	3854.2	25(3)	(31/2 <sup>-</sup> ) $\rightarrow$ (27/2 <sup>-</sup> )
614.0(1)	3105.9	54(1)	(25/2 <sup>+</sup> ) $\rightarrow$ 23/2 <sup>+</sup>
629.2(1)	4449.1	21(1)	(29/2 <sup>+</sup> ) $\rightarrow$ (27/2 <sup>+</sup> )
647.0(1)	1559.1	41(2)	15/2 <sup>+</sup> $\rightarrow$ 11/2 <sup>+</sup>
714.0(1)	3819.9	26(1)	(27/2 <sup>+</sup> ) $\rightarrow$ (25/2 <sup>+</sup> )
729.2(1)	3318.6	26(2)	(27/2 <sup>-</sup> ) $\rightarrow$ (23/2 <sup>-</sup> )
785.8(1)	3891.7	25(1)	(25/2 <sup>+</sup> ) $\rightarrow$ (25/2 <sup>+</sup> )
862.7(1)	1774.8	18(2)	13/2 <sup>+</sup> $\rightarrow$ 11/2 <sup>+</sup>
874.1(1)	2433.2	15(1)	19/2 <sup>+</sup> $\rightarrow$ 15/2 <sup>+</sup>
912.1(1)	912.1	100	11/2 <sup>+</sup> $\rightarrow$ 7/2 <sup>+</sup>
956.3(1)	2589.4	31(2)	(23/2 <sup>-</sup> ) $\rightarrow$ 19/2 <sup>-</sup>
1168.4(1)	2080.5	3(1)	15/2 <sup>+</sup> $\rightarrow$ 11/2 <sup>+</sup>
(59)	2491.9	-	23/2 <sup>+</sup> $\rightarrow$ 19/2 <sup>+</sup>
(74)	1633.1	-	19/2 <sup>-</sup> $\rightarrow$ 15/2 <sup>+</sup>
(95)	1728.1	-	15/2 <sup>-</sup> $\rightarrow$ 19/2 <sup>-</sup>
(169)	1728.1	-	15/2 <sup>-</sup> $\rightarrow$ 15/2 <sup>+</sup>

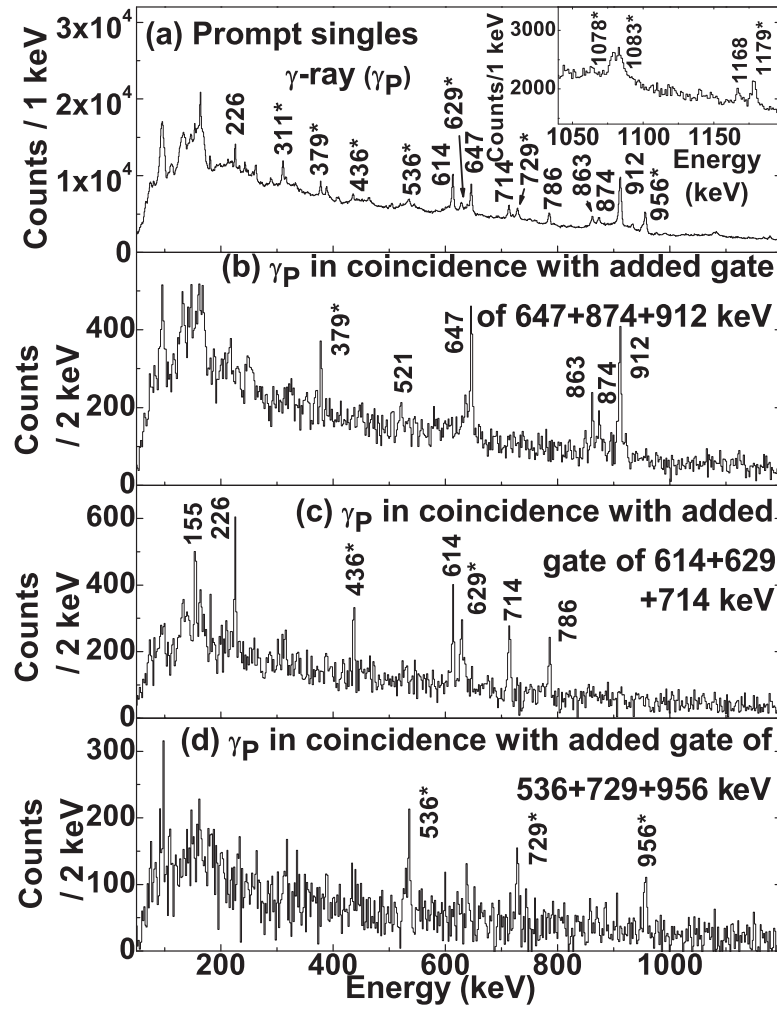


Figure 6.11: (a) The prompt singles  $\gamma$ -ray spectrum of  $^{133}\text{I}$ . The higher energy part of this spectrum is shown in an expanded scale in the inset. (b) Prompt  $\gamma$  rays ( $\gamma_P$ ) in coincidence with the added gate of  $\gamma_P = 912 + 647 + 874$  keV. (c) Prompt  $\gamma$  rays ( $\gamma_P$ ) in coincidence with added gate of  $\gamma_P = 614 + 714 + 629$  keV. (d) Prompt  $\gamma$  rays ( $\gamma_P$ ) in coincidence with added gate of  $\gamma_P = 956 + 729 + 536$  keV. The new  $\gamma$ -transitions are marked with ‘\*’ in all the cases.

spectrum. Four of the new  $\gamma$  rays of energies 311, 1078, 1083 and 1179 keV, observed from the present work (marked with ‘\*’ in Fig. 6.11(a)), could not be placed in the level scheme due to the low statistics in the corresponding coincidence spectra. However, their assignment to  $^{133}\text{I}$  is confirmed as the prompt singles  $\gamma$ -ray ( $\gamma_P$ ) spectrum is obtained with ( $A, Z$ ) gating condition.

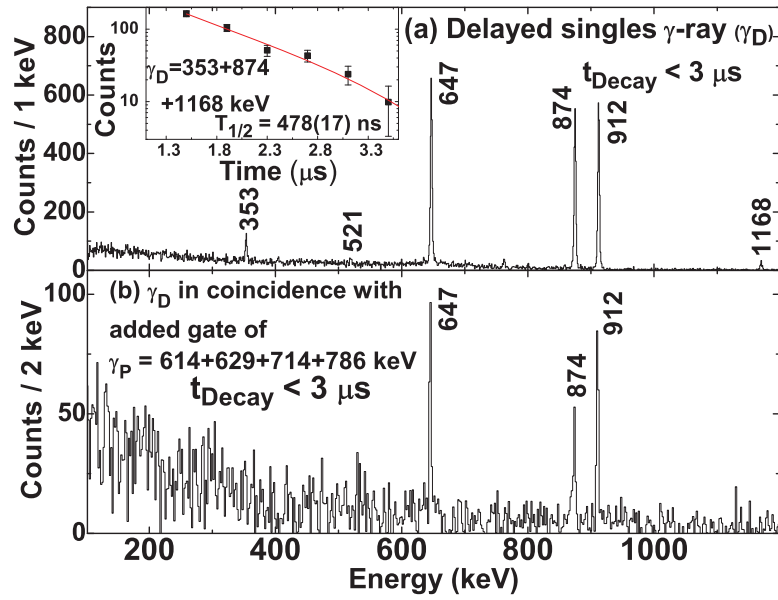


Figure 6.12: (a) Delayed  $\gamma$ -ray ( $\gamma_D$ ) spectrum of  $^{133}\text{I}$  within time window  $t_{\text{Decay}} < 3 \mu\text{s}$ . Inset of the figure shows the decay pattern of delayed  $\gamma$  rays  $\gamma_D = 874 + 353 + 1168 \text{ keV}$  with exponential fitting. (b) Delayed  $\gamma$  rays ( $\gamma_D$ ) in coincidence with the added prompt gate of  $\gamma_P = 614 + 714 + 629 + 786 \text{ keV}$ .

The prompt coincidence spectra corresponding to the added gates of 912, 647 and 874 keV  $\gamma$  rays below the isomeric levels, is shown in Fig. 6.11(b). The 379 keV  $\gamma$ -ray is newly observed from the present work and on the basis of the coincidence relations, it has been placed above the 1559 keV level. In the present work, the high spin states of  $^{133}\text{I}$  above the  $23/2^+$  isomer are extended with addition of two new transitions of energies 629 and 436 keV. A prompt  $\gamma$ - $\gamma$  coincidence spectrum corresponding to the sum gates of 614, 714 and 629 keV, decaying to the  $23/2^+$  isomeric level, is shown in Fig. 6.11(c). The new  $\gamma$  rays of energies 629 and 436 keV, placed in the proposed level scheme above the  $23/2^+$  isomer, are clearly seen in this coincidence spectrum. The placement of the previously reported 226 keV transition has also been changed on the basis of measured relative intensities in the present work. The other new  $\gamma$  rays, *i.e.*, 956, 729 and 536 keV, observed in the prompt singles spectrum (Fig. 6.11(a)), are found to be in coincidence with each other, but not with any other known prompt  $\gamma$ -ray transitions of  $^{133}\text{I}$ . This is evident from the added coincidence gates of 956, 729 and 536 keV  $\gamma$  rays, shown

in Fig. 6.11(d). However, the assignment of these  $\gamma$  rays to  $^{133}\text{I}$  could be confirmed, as these are present in the prompt  $\gamma$  spectrum (Fig. 6.11(a)), obtained after isotopic ( $A, Z$ ) selection of the  $^{133}\text{I}$  fragments. It may be noted, that, a similar set of prompt  $\gamma$  rays have been observed in the neighboring odd- $A$   $^{131}\text{I}$ , above the  $19/2^-$  isomer ( $24.6 \mu\text{s}$ ). Thus, it is possible that the new cascade of prompt transitions of 956-729-536 keV, observed in  $^{133}\text{I}$  may also decay to the  $19/2^-$  (9 sec) isomeric state. As the upper limit ( $200 \mu\text{s}$ ) of the delayed time window for the present setup is much lower than the half-life of the  $19/2^-$  (9 sec) isomeric state in  $^{133}\text{I}$ , therefore, the prompt-delayed correlation across the isomer could not be observed. Therefore, the cascade of prompt transitions of 956-729-536 keV is placed above the  $19/2^-$  (9 sec) isomeric state at 1633 keV in  $^{133}\text{I}$ .

Fig. 6.12(a) shows the delayed singles  $\gamma$ -ray ( $\gamma_D$ ) spectrum within the decay time range of  $t_{Decay} < 3 \mu\text{s}$ . All the known delayed  $\gamma$  rays of  $^{133}\text{I}$ , *i.e.*, 912, 647, 874, 1168 and 353 keV, are observed in this time gated delayed spectrum. The other known delayed low energy  $\gamma$  rays of 59, 74, 95, 169 keV could not be observed in this delayed spectrum, either due to their weak intensities or due to the low energy threshold of the present setup to detect the delayed  $\gamma$  rays. The time decay curve for the 874 + 353 + 1168 keV transitions, decaying out from the  $23/2^+$  isomer is shown in the inset of Fig. 6.12(a). An exponential decay fit of this curve yields a value of  $T_{1/2} = 478(17)$  ns, which matches well with the reported [18] value of 469(15) ns. Fig. 6.12(b) shows the delayed  $\gamma$  rays observed in coincidence with the prompt transitions of 614, 714, 629 and 785 keV above the  $23/2^+$  isomer. The known delayed transitions of energies 912, 647 and 874 keV below the isomer is clearly seen in this spectrum. The other  $\gamma$  rays of 353, 521 and 1168 keV could not be seen in this spectrum due to their weak intensities.

### 6.3.5 $^{134}\text{I}$

Low lying excited states of  $^{134}\text{I}$  were previously studied from  $\beta$ -decay of  $^{134}\text{Te}$  [44, 45]. A high spin isomer ( $8^-$ ) of  $T_{1/2} \sim 3.8$  min (adopted in NNDC as 3.52 min [46]) at an excitation energy of 316 keV was also identified in Ref. [47]. High spin states above the ( $8^-$ ) isomer in  $^{134}\text{I}$  were

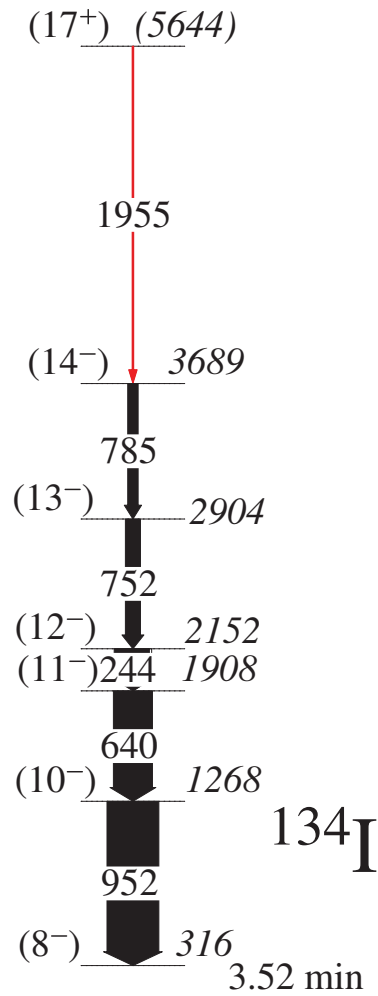


Figure 6.13: Level scheme of  $^{134}\text{I}$  as obtained in the present work. The newly observed  $\gamma$  rays are displayed in red. The thickness of the  $\gamma$  rays represents their relative intensity.

recently investigated using prompt spectroscopy of fission fragments [19], where five excited states were identified.

The level scheme of  $^{134}\text{I}$ , as obtained from the present measurements [33], is shown in Fig. 6.13. In the present work, the level scheme above the reported  $8^-$  isomer of  $^{134}\text{I}$ , as reported by [19], is extended with the placement of one new  $\gamma$ -ray transition  $(17^+) \rightarrow (14^-)$  above the 3689 keV level (see discussions Section 6.4.2). The assignment of the earlier known  $\gamma$  rays and the newly observed  $\gamma$ -ray from the present work are confirmed after unambiguous isotopic ( $A, Z$ )

Table 6.5: Energies ( $E_\gamma$ ) and relative intensities ( $I_\gamma$ ) of the  $\gamma$  rays observed in  $^{134}\text{I}$  along with probable spin and parity of the initial ( $J_i^\pi$ ) and the final ( $J_f^\pi$ ) states and the energy of the initial state ( $E_i$ ).

$E_\gamma$ (keV)	$E_i$ (keV)	$I_\gamma$	$J_i^\pi \rightarrow J_f^\pi$
243.5(1)	2150.9	68(1)	$(12^-) \rightarrow (11^-)$
639.6(1)	1907.4	75(1)	$(11^-) \rightarrow (10^-)$
752.0(1)	2902.9	29(2)	$(13^-) \rightarrow (12^-)$
785.2(1)	3688.1	20(1)	$(14^-) \rightarrow (13^-)$
951.8(1)	1267.8	100	$(10^-) \rightarrow (8^-)$
1955.1(1)	5643.2	3(1)	$(17^+) \rightarrow (14^-)$

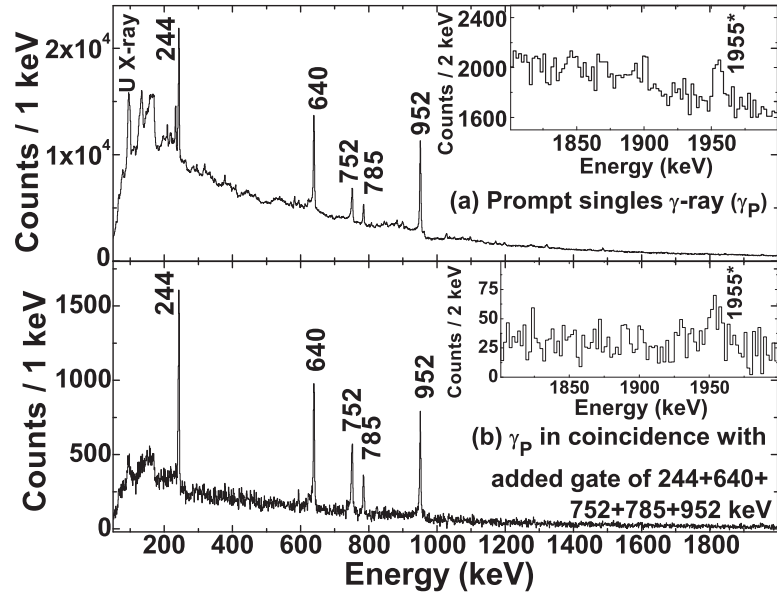


Figure 6.14: (a) The prompt singles  $\gamma$ -ray spectrum of  $^{134}\text{I}$ . (b) Prompt  $\gamma$  rays ( $\gamma_P$ ) in coincidence with added gate of  $\gamma_P = 962 + 640 + 244 + 752 + 785$  keV. (c) Prompt  $\gamma$  rays ( $\gamma_P$ ) in coincidence with  $\gamma_P = 952$  keV. The new  $\gamma$ -transitions are marked with '\*' in all the cases.

identification of  $^{134}\text{I}$ . The details of the  $\gamma$  rays of  $^{134}\text{I}$  with probable spin and parity of the initial ( $J_i^\pi$ ) and the final ( $J_f^\pi$ ) states are tabulated in Table 6.5. A Doppler corrected prompt singles  $\gamma$ -ray spectrum ( $\gamma_P$ ), obtained with the AGATA, in coincidence with the  $^{134}\text{I}$  fragments detected at the focal plane of the VAMOS++ spectrometer, is shown in Fig. 6.14(a). The previously known  $\gamma$ -ray transitions of energies 244, 640, 752, 785 and 952 keV are marked along with one new  $\gamma$ -ray of energy 1955 keV (marked with '\*'), observed from the present work. The prompt  $\gamma$ - $\gamma$  coincidence spectrum corresponding to the added prompt gates on 952, 640, 244, 752 and 785 keV transitions is shown in Fig. 6.14(b). All the previously assigned transitions along with the 1955 keV (marked with '\*') are seen in that figure. The presence of the 1955 keV  $\gamma$ -ray in this added spectrum is clear from the inset of Fig. 6.14(b), where the higher energy part of the coincidence spectrum is shown in an expanded energy scale. The new transition is placed in the level scheme of  $^{134}\text{I}$  on the basis of its mutual coincidence relationship and intensity balance.

## 6.4 Discussion

### 6.4.1 Systematics

The systematics of the energy difference between low lying  $\Delta I = 2$  the states are plotted for the isotopes of Sn ( $Z = 50$ ), Sb ( $Z = 51$ ), Te ( $Z = 52$ ) and I ( $Z = 53$ ) as a function of neutron number in Fig. 6.15(a) for even- $N$  and in Fig. 6.15(b) for odd- $N$ . One can observe the change in the energy differences as one, two and three protons are added to the corresponding Tin core ( $\text{Sn}_N$ ). In Sb, the energy differences  $E(11/2^+) - E(7/2^+)$  and  $E(10^-) - E(8^-)$  follow closely the corresponding  $E(2^+) - E(0^+)$  and  $E(15/2^-) - E(11/2^-)$  in Sn, respectively. This reflects the fact that the energy difference results from the neutron excitation, *i.e.*  $2^+$ , in both Sn and Sb, since there is no valence proton present in Sn ( $Z = 50$ ) and only one present in Sb ( $Z = 51$ ). It can be also seen that in I the energy differences  $E(11/2^+) - E(7/2^+)$  and  $E(10^-) - E(8^-)$  follow the corresponding  $E(2^+) - E(0^+)$  and  $E(15/2^-) - E(11/2^-)$  in Te, respectively. The significant drop in the energy difference in Te and I, relative to that in Sn and Sb, results from the strong mixing, between the proton and neutron excitations due to the neutron-proton

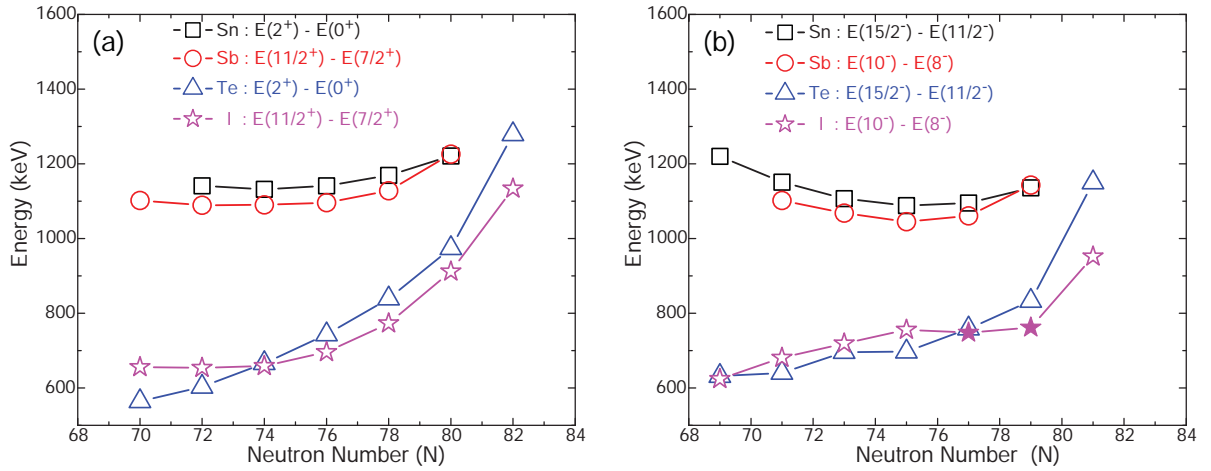


Figure 6.15: Systematics of experimental energy differences for the lowest states with  $\Delta I = 2$  for: (a) even- $N$  isotopes of Sn ( $E(2^+) - E(0^+)$ ), Sb ( $E(11/2^+) - E(7/2^+)$ ), Te ( $E(2^+) - E(0^+)$ ) and I ( $E(11/2^+) - E(7/2^+)$ ). (b) odd- $N$  isotopes of Sn ( $E(15/2^-) - E(11/2^-)$ ), Sb ( $E(10^-) - E(8^-)$ ), Te ( $E(15/2^-) - E(11/2^-)$ ) and I ( $E(10^-) - E(8^-)$ ). The new states observed in the present measurements are shown by filled symbols.

interaction. The decrease of the energy differences in Te and I, towards the neutron mid-shell can be seen from the figure. The systematic energy drop, *i.e.*  $(Z, Z + 1), (Z + 2, Z + 3), \dots$  with  $Z = 50$ , related to the increase of the collectivity, and an energy inheritance, for odd- $Z$  from even- $Z$  isotones, could be also observed for other isotopes from the known data while more protons are added, towards the proton mid-shell.

## 6.4.2 Shell Model Calculations

To understand the basic configurations and contribution of various single particle orbitals to the excited states of the Iodine isotopes in the mass region  $A = 130 - 134$ , observed in the present work, large scale shell model calculations have been performed using the code NUSHELLX [48]. The calculations are carried out using the model space involving  $1g_{7/2}, 2d_{5/2}, 2d_{3/2}, 3s_{1/2}, 1h_{11/2}$  single particle orbitals, for both protons and neutrons. The calculations used the SN100PN interaction [49]. The results of the shell model calculations are compared with the experimental

levels, obtained in the present work, for even- $A$  and odd- $A$  Iodine isotopes in Fig. 6.16(a-c) and Fig. 6.16(d-e), respectively. An overall good agreement is observed between the experimental and calculated levels for all the Iodine isotopes.

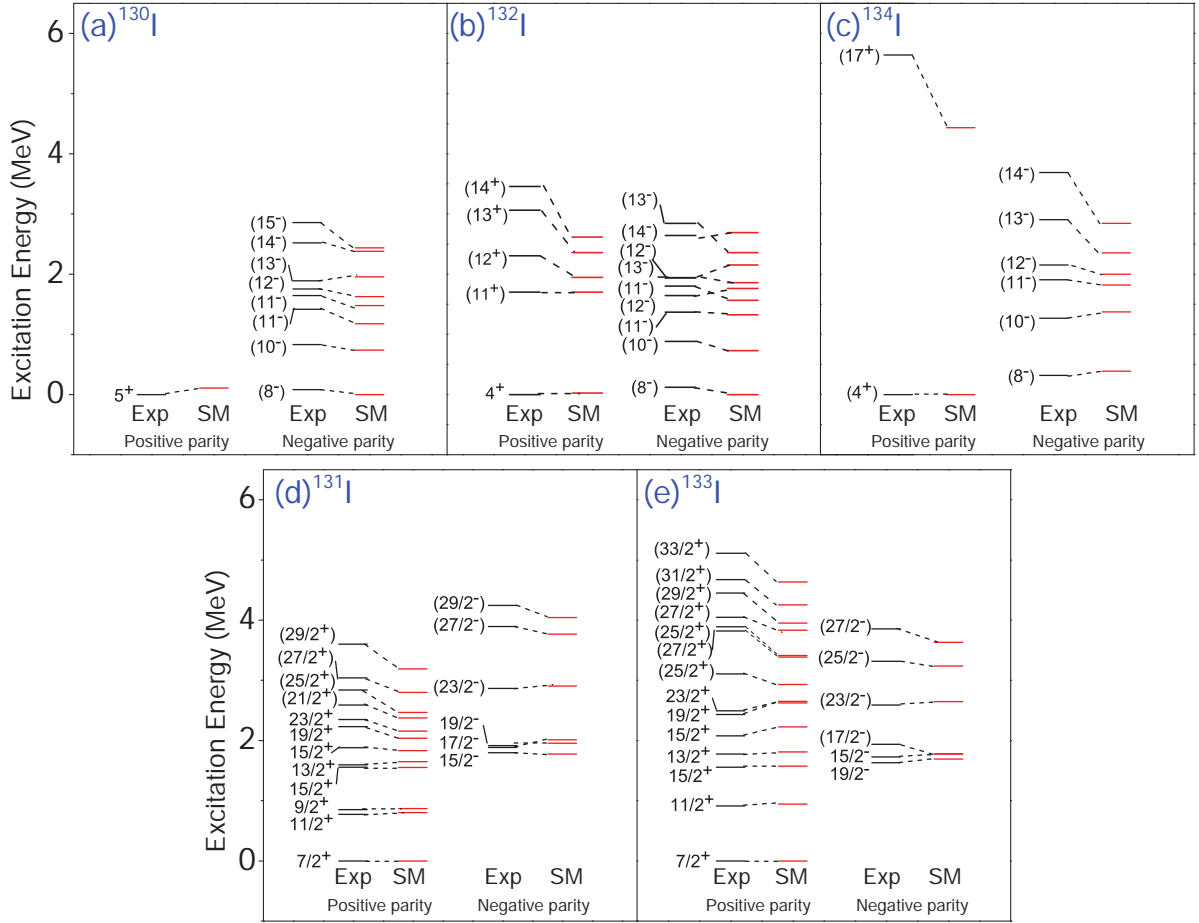


Figure 6.16: The comparison of experimental ((Exp) shown in black) and theoretical ((SM) shown in red) level schemes for even- $A$   $^{130,132,134}\text{I}$  (a-c) and odd- $A$   $^{131,133}\text{I}$  (d-e) isotopes for both positive and negative parities. The experimental and shell model states of the same spin-parity have been joined with dotted lines to guide the eye.

In the present shell model calculation of the even mass isotopes  $^{130}\text{I}$  ( $N = 77$ ) and  $^{132}\text{I}$  ( $N = 79$ ), the  $8^-$  level is predicted as the ground state, instead for the experimentally known ground states of  $5^+$  and  $4^+$ , respectively. But, the energy difference between the calculated and experimental

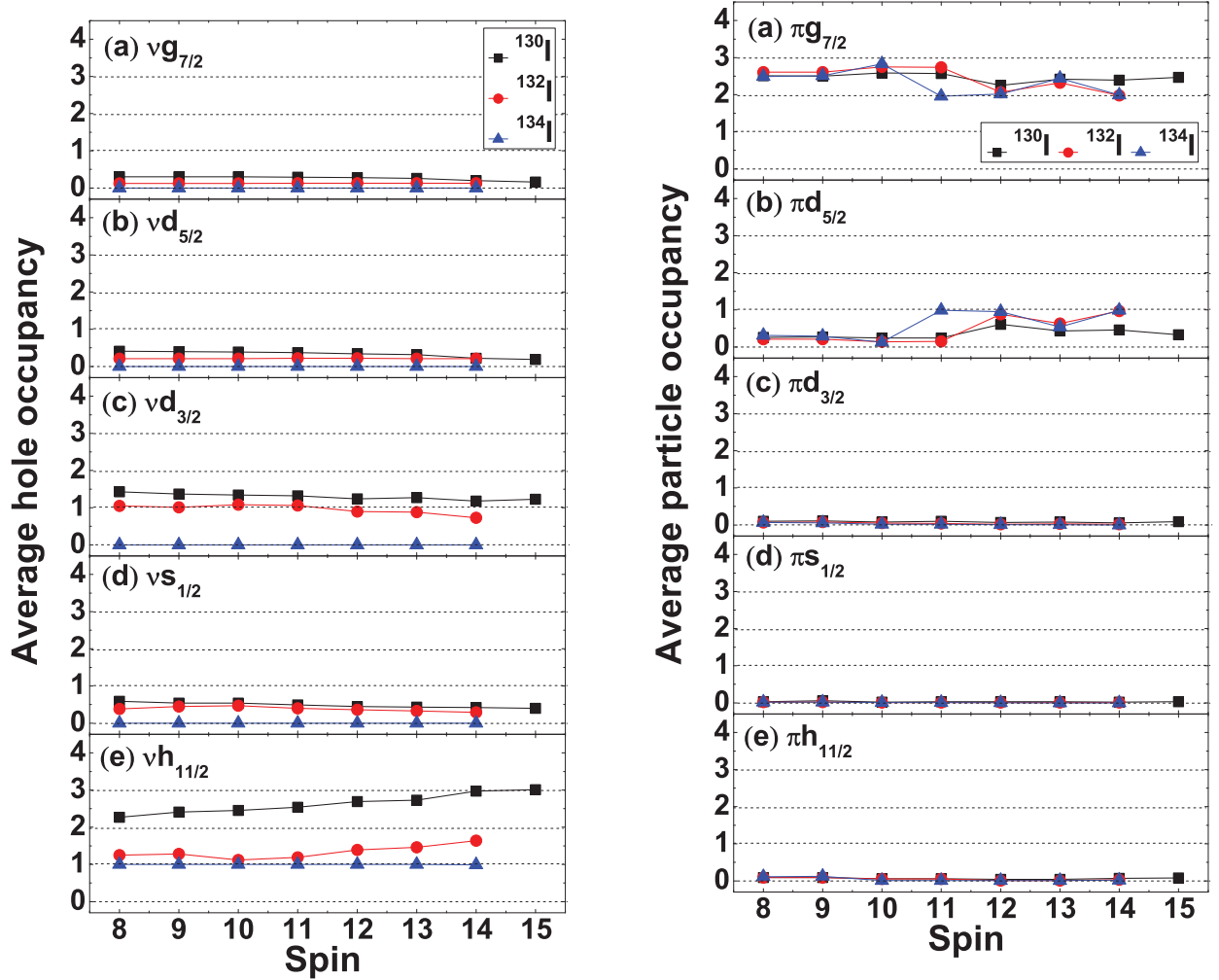


Figure 6.17: The variation in average hole occupancy (for neutron) and particle occupancy (for proton) in all the available orbitals for even mass  $^{130,132,134}\text{I}$  isotopes.

ground states are found to be within 120 keV for both the nuclei. In the case of  $^{134}\text{I}$  ( $N = 81$ ), the measured ground state is reproduced in the shell model calculation as  $4^+$ .

The higher spin negative parity states above the  $(8^-)$  state in  $^{130,132}\text{I}$ , newly observed in the present work, could be reproduced well in the shell model calculations, as can be seen from Fig. 6.16(a) and (b), respectively. The spin assignments to the negative parity levels above the  $8^-$  isomeric state in both  $^{130,132}\text{I}$  are based on the comparison with the present shell model calculation and the systematics of the even mass Iodine isotopes. The relative excitation energies

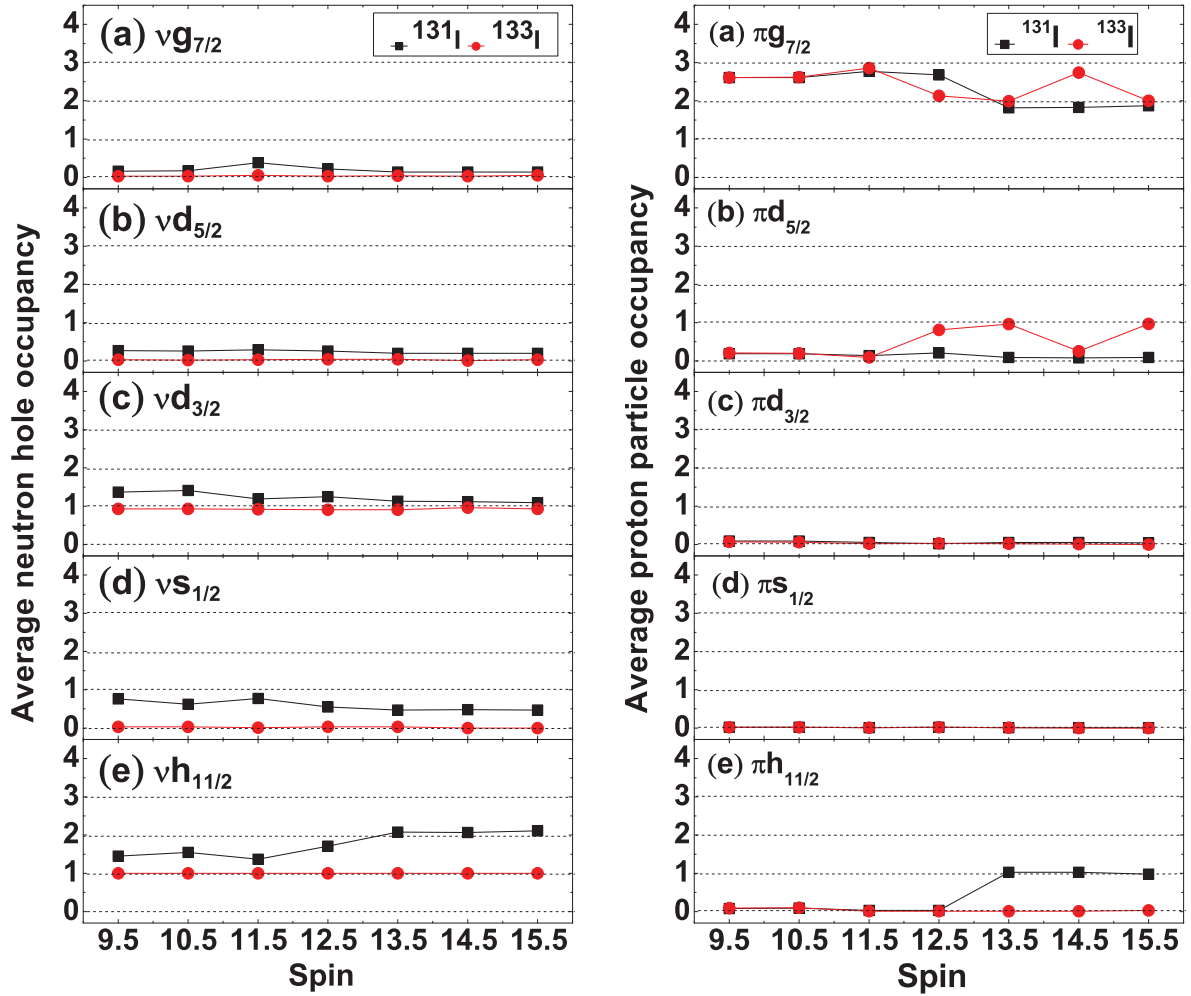


Figure 6.18: The variation in average hole occupancy (for neutron) and particle occupancy (for proton) in all the available orbitals for odd mass  $^{131,133}\text{I}$  isotopes.

and the sequence  $8^-$ - $10^-$ - $11^-$ - $12^-$  with respect to the  $8^-$  state in  $^{130,132}\text{I}$  follow a smooth pattern and is very similar to the corresponding states in  $^{128}\text{I}$  ( $N = 75$ ) and  $^{134}\text{I}$  ( $N = 81$ ). Thus the excited states at 830, 1419 and 1752 keV in  $^{130}\text{I}$  and the states at 882, 1367 and 1644 keV in  $^{132}\text{I}$  are assigned as  $(10^-)$ ,  $(11^-)$  and  $(12^-)$  respectively. This relative energy spacing increases for higher mass number towards the  $N = 82$ . The yrast sequence  $12^-$ - $10^-$ - $8^-$  in  $^{130}\text{I}$  and  $^{132}\text{I}$  also closely follow the analogous sequence of  $15/2^+$ - $11/2^+$ - $7/2^+$  in the odd- $A$  neighbours  $^{129}\text{I}$  and  $^{131}\text{I}$ , respectively.

The variation of occupancy of proton particle and neutron holes in the available orbitals for the even mass and odd mass Iodine isotopes are shown in Fig. 6.17 and 6.18, respectively. For the even mass  $^{130,132,134}\text{I}$  isotopes, it is found that only the  $\pi g_{7/2}$  and  $\pi d_{5/2}$  in the proton space and the  $\nu d_{3/2}$ ,  $\nu s_{1/2}$  and  $\nu h_{11/2}$  in the neutron space are responsible in generating the experimentally observed spins. All the other orbitals remain inactive in spin generation for the even mass Iodine isotopes. On the other hand, it is observed that the  $\pi g_{7/2}$ ,  $\pi d_{5/2}$  and  $\pi d_{5/2}$  orbitals in the proton space actively contribute in spin generation in the odd mass Iodine isotopes. The new 342 ns isomeric state in  $^{132}\text{I}$ , reported in the present work, is tentatively assigned as  $(11^+)$ , following the systematics of similar isomers observed in the even- $A$  Sb isotopes [51]. The three new excited states observed above the  $(11^+)$  isomer in  $^{132}\text{I}$  are assigned as  $(12^+)$ ,  $(13^+)$  and  $(14^+)$ , respectively, following the similar pattern of spin sequence above the  $(11^+)$ , 600 ns isomer, in  $^{130}\text{Sb}$ . The excitation energy of the  $(11^+)$  isomer in  $^{132}\text{I}$  could not be determined experimentally. Shell model calculation predicts the  $\pi g_{7/2}^3 \nu d_{3/2}^{-1} \nu h_{11/2}^{-2}$  configuration as the main component of those positive parity states with an admixture of  $\pi g_{7/2}^3 \nu s_{1/2}^{-1} \nu h_{11/2}^{-2}$  configuration. The excitation energy differences of the positive parity states, above the  $(11^+)$  isomer are not well reproduced by the shell model calculations (Fig. 6.16(b)).

In  $^{134}\text{I}$ , the yrast states, *i.e.*  $(8^-)$  to  $(14^-)$  were understood as built from the  $\pi g_{7/2}^3 \nu h_{11/2}^{-1}$  and  $\pi g_{7/2}^2 \pi d_{5/2} \nu h_{11/2}^{-1}$  configurations [19, 52]. In this work, the newly observed state at (5644) keV decaying by the emission of the 1955 keV transition, is proposed as  $(17^+)$ , resulting from the  $\pi g_{7/2}^2 \pi h_{11/2}^1 \nu h_{11/2}^{-1}$  configuration, based on the following considerations. In the neighboring nucleus  $^{135}\text{I}$ , having the closed  $N = 82$  shell, the low-lying positive parity states,  $(7/2^+, 11/2^+, 15/2^+, 17/2^+)$ , are mainly from the  $\pi g_{7/2}^3$  and  $\pi g_{7/2}^2 \pi d_{5/2}^1$  configurations [53]. The higher-lying yrast states,  $(19/2^-, 21/2^-, 23/2^-)$ , have a negative parity and are understood as resulting from one proton excitation to the  $\pi h_{11/2}$  orbital, leading to a  $\pi g_{7/2}^2 \pi h_{11/2}$  configuration. The strongest decay of these states to the positive parity states is of  $E3$  nature, corresponding to the  $\pi h_{11/2} \rightarrow \pi d_{5/2}$  stretched  $E3$  transition. An analogous pattern can be also observed in  $^{134}\text{Te}$  [53, 20]. In  $^{134}\text{I}$ , the model calculations further under predict the excitation energy of the  $13^-, 14^-$  and  $17^+$  states (Fig. 6.16(c)).

For the odd- $A$  Iodine isotopes,  $^{131,133}\text{I}$ , the previously known positive parity states below the  $23/2^+$ ,  $19/2^-$  and  $15/2^-$  isomers have been reproduced well in the present shell model calculations (Fig. 6.16(d-e)). The excited states above the  $19/2^-$  isomer, in both  $^{131,133}\text{I}$ , are reported for the first time in the present work. The three levels above the  $19/2^-$  state are assigned as  $(23/2^-)$ ,  $(27/2^-)$  and  $(29/2^-)$  in  $^{131}\text{I}$  and as  $(23/2^-)$ ,  $(25/2^-)$  and  $(27/2^-)$  in  $^{133}\text{I}$ , based on the agreement of the experimental results with the shell model calculation. The level at 1938 keV in  $^{133}\text{I}$  is newly observed in the current work and is connected to the  $15/2^+$  level via 378 keV transition. This state is assigned as  $(17/2^-)$ , following a similar assignment of a level, reported earlier in  $^{131}\text{I}$  [18].

The present shell model calculations show that the proton particles in the  $\pi g_{7/2}$ ,  $\pi d_{5/2}$ ,  $\pi h_{11/2}$  and neutron holes in the  $\nu d_{3/2}$ ,  $\nu s_{1/2}$ ,  $\nu h_{11/2}$  have a leading contribution to the structure of the negative parity excited states. All the other orbitals remain relatively inactive. This work shows that the neutron hole occupancy in the  $\nu h_{11/2}$  orbital varies as a function of increasing spin. But, all the states with the relevant spins in  $^{134}\text{I}$  are generated with only one neutron hole in the  $\nu h_{11/2}$  [19, 52]. In left panel of Fig. 6.19(a) and right panel of 6.19(a), the probability of neutron hole occupancy in  $\nu h_{11/2}$  orbital is shown as a function of the total spin ( $J$ ) and ( $2J$ ) of the negative parity states, for  $^{130,132}\text{I}$  and  $^{131,133}\text{I}$ , respectively. It can be seen from the figures that:

- $^{132}\text{I}$  : (three neutron holes) the main contribution is from the  $\nu h_{11/2}^{-1}$ , which slightly decreases at higher spin in favor of the  $\nu h_{11/2}^{-3}$  configuration,
- $^{130}\text{I}$  : (five neutron holes) there is a large contribution of  $\nu h_{11/2}^{-1}$  and  $\nu h_{11/2}^{-3}$  at lower spin, while the  $\nu h_{11/2}^{-3}$  dominates at higher spin, the contribution of  $\nu h_{11/2}^{-5}$  is negligible,
- $^{133}\text{I}$  : (two neutron holes) the  $\nu h_{11/2}^{-1}$  configuration is almost pure,
- $^{131}\text{I}$  : (four neutron holes) the  $\nu h_{11/2}^{-1}$  configuration dominates until  $25/2^-$ , beyond which the  $\nu h_{11/2}^{-2}$  takes over, implying the contribution of the proton  $\pi h_{11/2}$  excitation.

The average contribution of proton ( $2J_\pi$ ) and neutron ( $2J_\nu$ ) to the total spin of the negative parity states, for the configurations involving different occupancy of the  $\nu h_{11/2}$  orbital, are

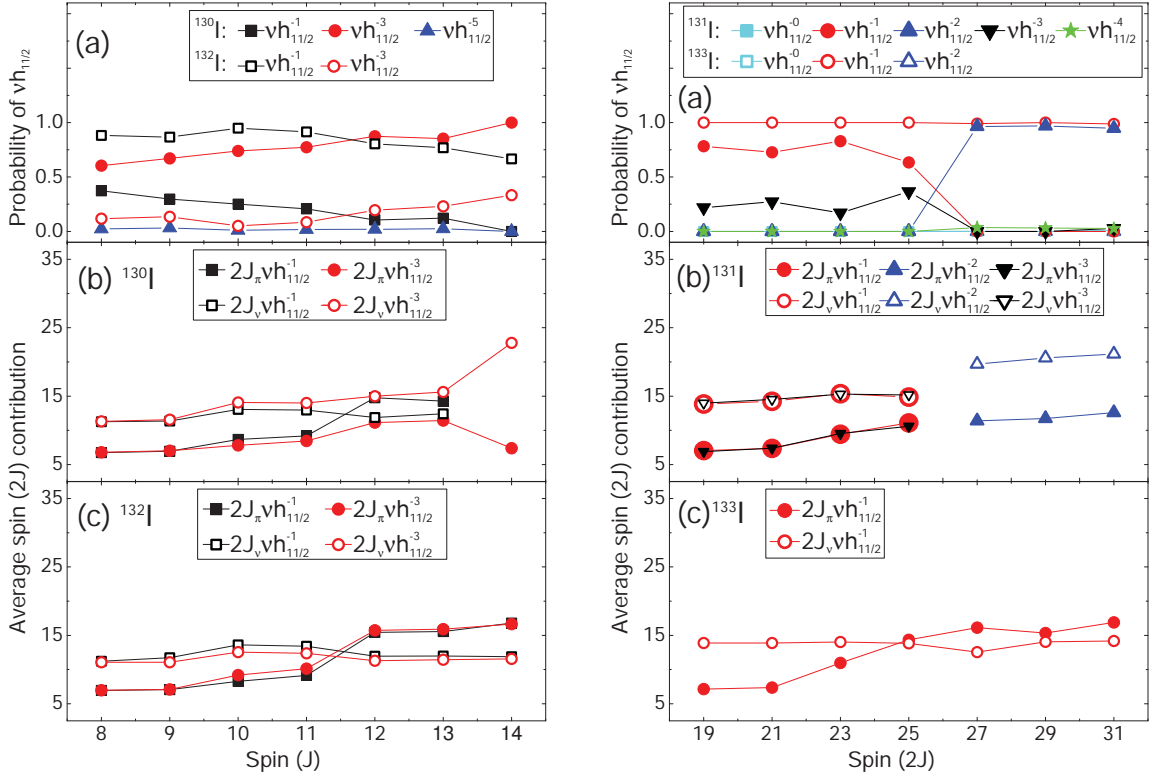


Figure 6.19: **(Left)** (a) Probability of neutron hole occupancy in  $\nu h_{11/2}$  orbital for  $^{130,132}\text{I}$  as a function of the total spin ( $J$ ) of the negative parity states, (b) Average spin contribution of proton ( $2J_\pi$ ) and neutron ( $2J_\nu$ ) to the total spin ( $J$ ) of the negative parity states in  $^{130}\text{I}$  for different number of hole occupancy in the  $\nu h_{11/2}$  orbital and (c) Same as (b), but for  $^{132}\text{I}$ . **(Right)** (a) Probability of neutron hole occupancy in  $\nu h_{11/2}$  orbital for  $^{131,133}\text{I}$  as a function of the total spin ( $2J$ ) of the negative parity states, (b) Average spin contribution of proton ( $2J_\pi$ ) and neutron ( $2J_\nu$ ) to the total spin ( $2J$ ) of the negative parity states in  $^{131}\text{I}$  for different number of hole occupancy in the  $\nu h_{11/2}$  orbital and (c) Same as (b), but for  $^{133}\text{I}$ .

shown in Fig. 6.19(b) (left panel) for  $^{130}\text{I}$  and (c) (left panel)  $^{132}\text{I}$  and in Fig. 6.19(b) (right panel) for  $^{131}\text{I}$  and (c) (right) for  $^{133}\text{I}$ . In  $^{132}\text{I}$ , at low spin, the average  $J_\pi^\pi$  is  $7/2^+$  and  $J_\nu^\pi$  is  $11/2^-$ . With increasing spin  $J$ , the average neutron spin remains almost constant, while the proton spin gradually increases towards the full spin alignment ( $17/2^+$ ) of the three protons

in the  $\pi g_{7/2}$  and  $\pi d_{5/2}$  orbitals, *i.e.*  $\left| (\pi g_{7/2}^2; 6^+) \times (\pi d_{5/2}; 5/2^+); 17/2^+ \right\rangle$ . A similar behavior is also observed in  $^{134}\text{I}$ , where the spin contribution of the single neutron hole in  $\nu h_{11/2}$  is  $11/2^-$ . The average spin contributions for the dominant ( $\nu h_{11/2}^{-1}$ ) configuration and that for the admixture ( $\nu h_{11/2}^{-3}$ ) closely follow each other. In  $^{130}\text{I}$ , the trends are similar for the admixture ( $\nu h_{11/2}^{-1}$ ), which has only a negligible contribution to the  $14^-$  state. For the leading component ( $\nu h_{11/2}^{-3}$ ), the proton spin contribution is smaller, which is compensated by the corresponding increase of the spin of the neutrons. In  $^{133}\text{I}$ , at low spin, the average  $J_\pi^\pi$  is  $7/2^+$  and  $J_\nu^\pi$  is  $7^-$ . The configuration of the  $J_\nu^\pi = 7^-$  corresponds to the  $\nu d_{3/2}^{-1} \nu h_{11/2}^{-1}$ . With the increase of the final spin  $J$ , similarly to the  $^{132}\text{I}$ , the average neutron spin remains almost constant while the proton spin gradually increases towards the full spin alignment. In  $^{131}\text{I}$ , the average spin contribution of protons and neutrons, below  $25/2^-$  is similar to that observed for  $^{133}\text{I}$ . The contributions from the dominant ( $\nu h_{11/2}^{-1}$ ) configuration and the admixture ( $\nu h_{11/2}^{-3}$ ) follow each other. The crossing between the average neutron and proton spin doesn't occur. At  $27/2^-$ , the configuration changes to  $\nu h_{11/2}^{-2}$  and one proton is promoted to the  $\pi h_{11/2}$  orbital. The average spin of protons  $J_\pi^\pi$  is  $11/2^-$  and that of neutrons  $J_\nu^\pi$  is  $10^+$ . The predicted, sudden change of the configuration, involving the  $\pi h_{11/2}$  excitation could however occur at too low excitation energy in the model, as already discussed earlier for  $^{134}\text{I}$ .

## 6.5 Summary

Excited states of the neutron-rich Iodine isotopes,  $^{130-134}\text{I}$ , are studied using prompt-delayed coincidence technique across the isomer by direct identification of the neutron-rich fission fragments at the focal plane of a magnetic spectrometer. The AGATA  $\gamma$ -ray tracking array was used for prompt  $\gamma$ -ray measurements at the target position, the EXOGAM segmented clover detectors were used to detect the delayed  $\gamma$ -rays after complete  $(A, Z)$  identification using the large acceptance magnetic spectrometer VAMOS++. New prompt transitions are placed above the high spin isomers, for the first time. A new isomer is identified in  $^{132}\text{I}$  from the prompt-delayed coincidence. The new states are characterized using the large scale shell model calculations. The new negative parity states of  $^{130-134}\text{I}$  are discussed in terms of their neu-

tron and proton occupancies and spins using these calculations. The importance of the hole occupancy of  $\nu h_{11/2}$  orbital in generation of the high spin negative parity states in these Iodine isotopes is investigated.

# Bibliography

- [1] J. P. Schiffer and W. W. True, Rev. Mod. Phys. 48, 191 (1976).
- [2] L. Coraggio, et al., Phys. Rev. C 66, 64311 (2002).
- [3] L. Coraggio, et al., Nucl. Phys. A 805, 424 (2008).
- [4] K. L. Jones *et al.*, Nature **465**, 454 (2010).
- [5] M. Rejmund, *et al.*, Phys. Lett. B **753**, 86 (2016).
- [6] S. Biswas *et al.*, Phys. Rev. C **93**, 034324 (2016).
- [7] J. Genevey *et al.*, Phys. Rev. C **65**, 034322 (2002).
- [8] P. Bhattacharyya *et al.*, Phys. Rev. Lett. **87**, 062502 (2001).
- [9] L. Coraggio *et al.*, Phys. Rev. C **87**, 034309 (2013).
- [10] S. Biswas *et al.*, Phys.Rev. C **99**, 064302 (2019).
- [11] Bhushan Kanagalekar *et al.*, Phys. Rev. C **88**, 054306 (2013).
- [12] B. Ding *et al.*, Phys. Rev. C **86**, 034302 (2012).
- [13] H. Kaur *et al.*, Phys. Rev. C **55**, 512 (1997).
- [14] Harjeet Kaur *et al.*, Phys. Rev. C **55**, 2234 (1997).
- [15] B. Deleanu *et al.*, Phys. Rev. C **85**, 044306 (2012).

- [16] D. Deleanu *et.al.*, Phys. Rev. C **87**, 014329 (2013).
- [17] A. Astier *et. al.*, Eur.Phys.J. **A 50**, 2 (2014).
- [18] H. Watanabe *et.al.*, Phys. Rev. C **79**, 064311 (2009).
- [19] S. H. Liu *et.al.*, Phys. Rev. C **79**, 067303 (2009).
- [20] S. K. Saha *et.al.*, Phys. Rev. C **65**, 017302 (2001).
- [21] W. Urban *et.al.*, Eur. Phys. J A **27**, 257 (2006).
- [22] T. Rzaca-Urban *et.al.*, Phys. Rev. C **75**, 054319 (2007).
- [23] A. Navin, *et al.*, Phys. Lett. B **728**, 136 (2014).
- [24] M. Rejmund, *et al.*, Nucl. Instrum. Methods A **646**, 184 (2011).
- [25] N. Alahari and M. Rejmund, Gamma-ray spectroscopy of neutron-rich fission fragments,(2019).
- [26] M. Vandebrouck *et. al.*, Nucl. Instr. and Meth. A **812**, 112 (2016).
- [27] Y. H. Kim *et. al.*, Eur. Phys. J. A **53**, 162 (2017).
- [28] S. Akkoyun, *et al.*, Nucl. Instrum. Methods A **668**, 26 (2012).
- [29] J. Simpson, *et al.*, Act. Phys. Hung. Ser. Heavy Ion Phys. **11**, 159 (2000).
- [30] S.L. Sakharov *et.al.*, Nuclear Physics A **494**, 36 (1989).
- [31] M. M. Musthafa *et.al.*, Phys. Rev. C, **52**, xxxx (1995).
- [32] B. Singh, Nuclear Data Sheets, **93** 33 (2001).
- [33] R. Banik *et al.* Phys. Rev. C **102**, 044329 (2020).
- [34] S. V. Jackson *et. al.*, Phys. Rev. C, **11**, 1323 (1975).
- [35] G. Lhersonneau *et. al.*, Phys. Rev. C, **12**, 2 (1975).

- [36] E. S. Macias *et. al.*, Nuclear Physics A, **161**, 471 (1971).
- [37] R. L. Auble *et. al.*, Phys. Rev., **169**, 4 (1969).
- [38] M. Diksic *et.al.*, Phys. Rev. C, **10**, No. 3 (1974).
- [39] S. K. Das *et.al.*, Eur. Phys. J. A **4**, 1 (1999).
- [40] S. Bhattacharyya *et.al.*, EPJ Web of Conferences **66**, 02009 (2014).
- [41] M. Tanigaki *et.al.*, Phys. Rev. C **80**, 034304 (2009).
- [42] H. G. Hicks *et. al.*, Phys. Rev. C, **27**, 5 (1983).
- [43] W. B. Walters *et. al.*, Phys. Rev. C, **29**, 3 (1984).
- [44] R. A. Meyer *et. al.*, Phys. Rev. C, **13**, 4 (1976).
- [45] V. Berg *et.al.*, Nucl. Phys. A **175**, 495 (1971).
- [46] A. A. Sonzogni, Nuclear Data Sheets, **103** 1 (2004).
- [47] C. D. Coryell *et.al.*, Nucl. Phys. A **179**, 689 (1972).
- [48] B. A. Brown and W. D. M. Rae, Nucl. Data Sheets **120**, 115 (2014).
- [49] B. A. Brown, N.J. Stone, J.R. Stone, I.S. Towner and M. Hjorth-Jensen, Phys. Rev. C **71**, 044317 (2005).
- [50] P. Bhattacharyya *et. al.*, Phys. Rev. C **64**, 54312 (2001).
- [51] S. Biswas, *et al.*, Phys. Rev. C **99**, 64302 (2019).
- [52] L. Coraggio, *et al.*, Phys. Rev. C **80**, 061303 (2009).
- [53] C. T. Zhang, *et al.*, Phys. Rev. Lett. **77**, 3743 (1996).

# Chapter 7

## Low lying level structure of $^{134}\text{Xe}$ from decay spectroscopy of fission fragments

### 7.1 Introduction

Nuclei around the doubly magic shell closure give the opportunity to understand the basic natures of the single particle orbitals along with the interactions between the pair of nucleons available in the valence nucleon space. The behaviour of the core coupled quasi-particles, can also be explained by the study of these kind of near shell closure nuclei. In the region near  $^{132}\text{Sn}$ , the single particle excitations and the collective structure compete at low energy. In all the even-even nuclei starting from mass 132 to 138 [1, 2, 3, 4, 5], the first excited  $4^+$  state is at twice in energy than the first  $2^+$  state, which can be interpreted as vibrational excitations. But in case of  $^{134}\text{Xe}$ , the presence of the  $\gamma$ -ray transition from the second  $2^+$  state to the ground state, as well as to the first  $2^+$  state makes it of  $\gamma$ -soft nature. Thus, it becomes evident that spherical shape and simple phonon vibrational model is not capable to explain completely the low lying structure of this nucleus. Lower excitation is thus expected to have a coupling of neutron holes with the vibrational core. Only a complete low lying spectroscopy can give light on the actual structures of the nuclei in this region.

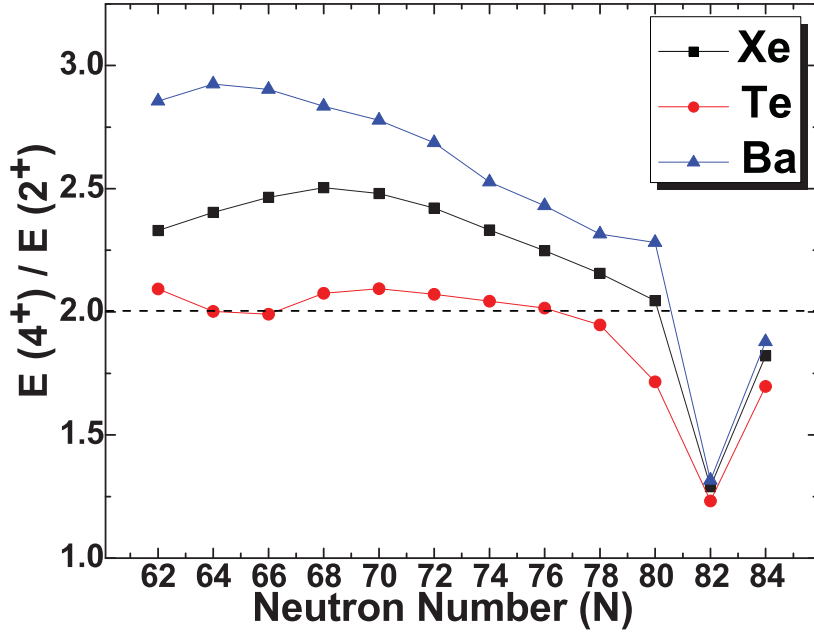


Figure 7.1: Variation of  $E_{4^+}/E_{2^+}$  with neutron number (N) for Te, Xe and Ba.

The Xe isotopes having four proton particles and few neutron holes with respect to the  $^{132}\text{Sn}$  core, are known for their shape variations with increasing neutron number. In neutron deficient Xe isotopes ( $A = 110 - 114$ ), octupole deformation was predicted [6] and experimentally addressed [7], whereas, deformed rotational structures dominate in the neutron mid-shell nuclei  $^{116,118,120}\text{Xe}$  [8, 9]. A systematic study of the shapes across the Xe chain from  $A = 118$  to 130 [10], indicates the change in shape from prolate to oblate. Fig. 7.1 shows the variation of the  $E_{4^+}/E_{2^+}$  with neutron number for Te ( $Z = 52$ ), Xe ( $Z = 54$ ) and Ba ( $Z = 56$ ) isotopes. It can be clearly seen from the figure that this ratio for Xenon isotopes is between 2 (pure vibrational) and 3.33 (pure rotational). This implies only vibrational model is not enough to describe the structure of Xenon. The nucleus of our interest,  $^{134}\text{Xe}$ , having four proton particles and two neutron holes about the  $^{132}\text{Sn}$  core has also shown deviation from the expected vibrational model.

The first study of  $^{134}\text{Xe}$  from the  $\beta$ -decay of  $^{134}\text{I}$  was reported in Ref. [11]. More detailed  $\gamma$ - $\gamma$  coincidence analysis of this nuclei, populated from the  $\beta$ -decay of  $^{134}\text{I}$ , has been carried out using only two NaI detectors [12], two Ge(Li) detectors [2], and one NaI and one Ge(Li) [13]. The spin

assignments to the levels were done on the basis of the conversion coefficient measurement [12, 14], and angular correlation measurements [15]. But these studies are limited by their detector resolution and efficiency. Availability of new generation detectors provides the scope to study this nucleus in more detail. A detailed prompt spectroscopy of the high spin states above the  $7^-$  isomeric state (290 ms) in  $^{134}\text{Xe}$  have been studied [16, 17], from fission fragment spectroscopy. In the present work, the low lying excited states of  $^{134}\text{Xe}$ , produced from the  $\beta$ -decay of the ground state,  $(4)^+$ , of  $^{134}\text{I}$ , have been investigated by offline decay spectroscopy using high resolution detectors. The lifetime of the ground state of  $^{134}\text{I}$  is 52.5 minutes, which makes it possible to study its  $\beta$ -decay in offline setup. The shell model calculations are carried out to characterize the levels at low spin.

## 7.2 Experiment and Data Analysis

Production of nuclei in the medium mass region ( $A = 130 - 136$ ) around  $^{132}\text{Sn}$  is difficult via widely used fusion evaporation reactions. Nuclear fission has significant cross section, in producing these nuclei around the  $^{132}\text{Sn}$  region. In this present work, Xenon ( $Z = 54$ ) isotopes were produced from the  $\beta$ -decay of Iodine ( $Z = 53$ ), whose ground state has a reasonable half-life for offline study. The Iodine isotopes were produced by the  $\alpha$  induced fission of  $^{nat}\text{U}$ , using 32 MeV beam delivered from the K-130 cyclotron at VECC, Kolkata (India). A stack of  $^{nat}\text{U}$  targets of thicknesses  $1 \text{ mg/cm}^2$ , which is electro-deposited on the Aluminum foils and separated by Aluminum catcher foils of thicknesses  $50 \mu\text{m}$ , have been used for experiment. There was also a catcher foil in front of the target stack, which was placed to collect the fission fragments going to the backward direction. Also the irradiation of the target was restricted to about 2 hour to optimize the activity of  $^{134}\text{I}$ , which has a ground state half-life about an hour. After the fission reaction, the Al catcher foils, containing fission products, were removed from the stack. Iodine isotopes were then radiochemically separated from all other fission products by solvent extraction method using Iodine as carrier.

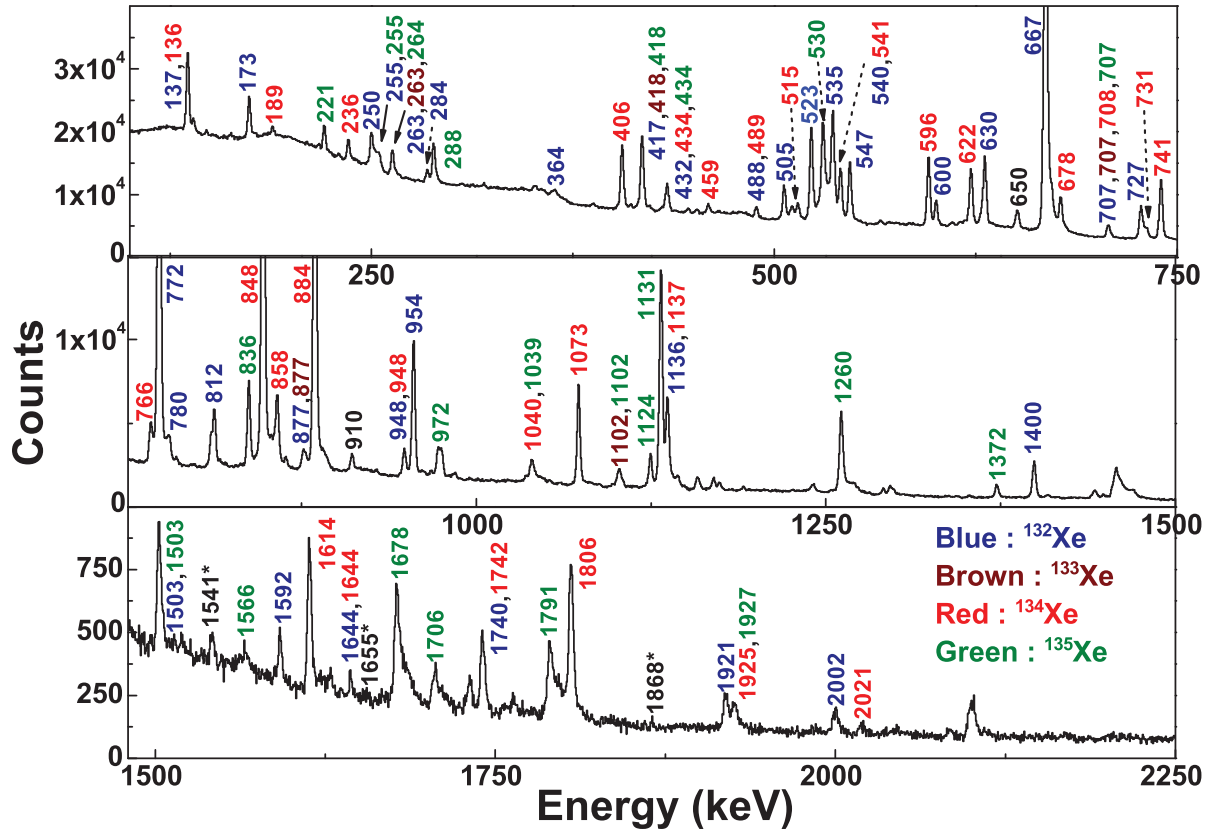


Figure 7.2: Total projected spectrum from the  $\gamma$ - $\gamma$  matrix as obtained in the present experiment indicating various  $\gamma$ -transitions coming from the corresponding excited nuclei.  $\gamma$  rays for different nuclei are indicated with different colour code.

The singles and coincidence measurements were carried out in an offline setup of four Clover HPGe detectors and two Low Energy Photon Spectrometer (LEPS) detectors. The detectors were placed at a distance 10.5 cm from the source position. Sixteen channel amplifiers and other standard NIM electronics were used to collect the LIST mode data with a VME based data acquisition system in LAMPS [18]. The singles data ( $M_\gamma \geq 1$ ) have been stored in files of each 10 minutes to follow the decay half-lives of observed  $\gamma$  transitions to confirm their identification in the spectrum. The raw data were collected and sorted to generate the symmetric  $E_\gamma$ - $E_\gamma$  matrix and the coincidence relationships between various transitions were obtained using the

analysis package RADWARE [19] and LAMPS [18]. The spin-parity assignments to the excited states were carried out using the angular correlation technique.

## 7.3 Results

### 7.3.1 Identification

Fig. 7.2 represents the projection of the  $E_\gamma$ - $E_\gamma$  matrix as obtained in the present experiment. It can be clearly seen from Fig. 7.2 that the transitions present in the spectrum are coming from various Xe isotopes having mass ranging from 132 to 135. It confirms that the radiochemically separated sample contains only Iodine isotopes. The  $\gamma$ -rays coming from the  $\beta$ -decay branch of the ( $8^-$ ) high spin isomer (1.39 hours) [20] in  $^{132}\text{I}$  have been observed, whereas, the decay transitions from the same high spin isomer (3.52 min) in  $^{134}\text{I}$  could not be observed. Since the half lives of other Iodine isotopes are much larger than the irradiation time of U foils, so their production was negligible and the decay transition from those isotopes are not present in the spectrum.

The ground state of the Iodine isotopes undergoes  $\beta$ -decay to the low lying excited states in daughter Xenon isotopes. The  $\beta$ -decay half lives of I isotopes, having mass ranging from  $A = 132 - 135$ , are from few minutes to few hours, which make it convenient to study these isotopes offline. The ground state half lives of these I isotopes can be estimated by plotting the variation in intensity of the decaying  $\gamma$ -rays as a function of time and then fitting that data with the exponential decay curve. The decay patterns of various  $\gamma$  rays, observed in this work, have been plotted in order to obtain their half lives and to suitably assign them to the proper Xenon isotopes. Left panel of Fig. 7.3 represents the decay curve of various transitions, which are present in the total projection. Presence of different nuclei produced in the present experiment can be seen for this figure.

The property of having similar lifetimes of the decaying  $\gamma$  rays from the excited states of  $^{134}\text{I}$ , has been utilized to confirm the presence of the new transitions observed in this work. The first

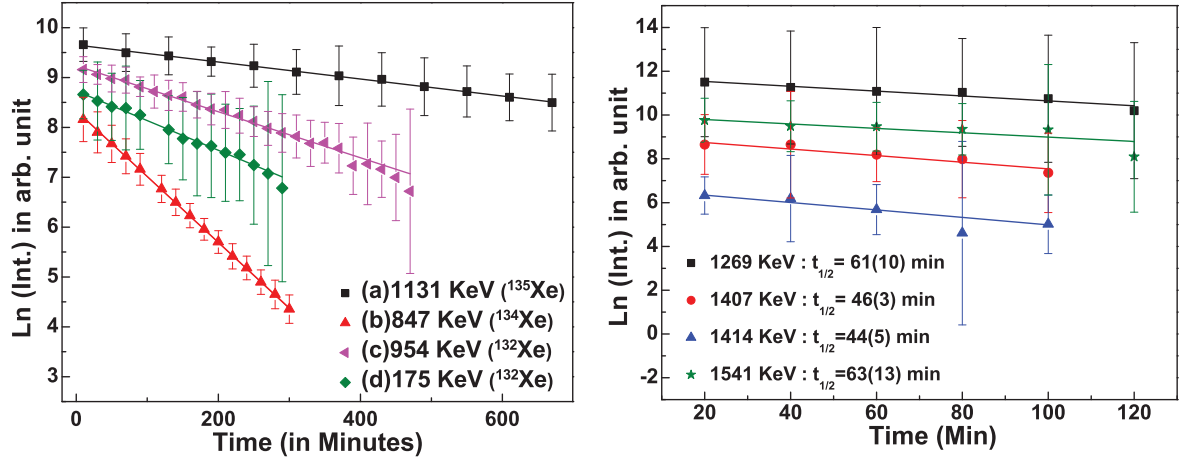
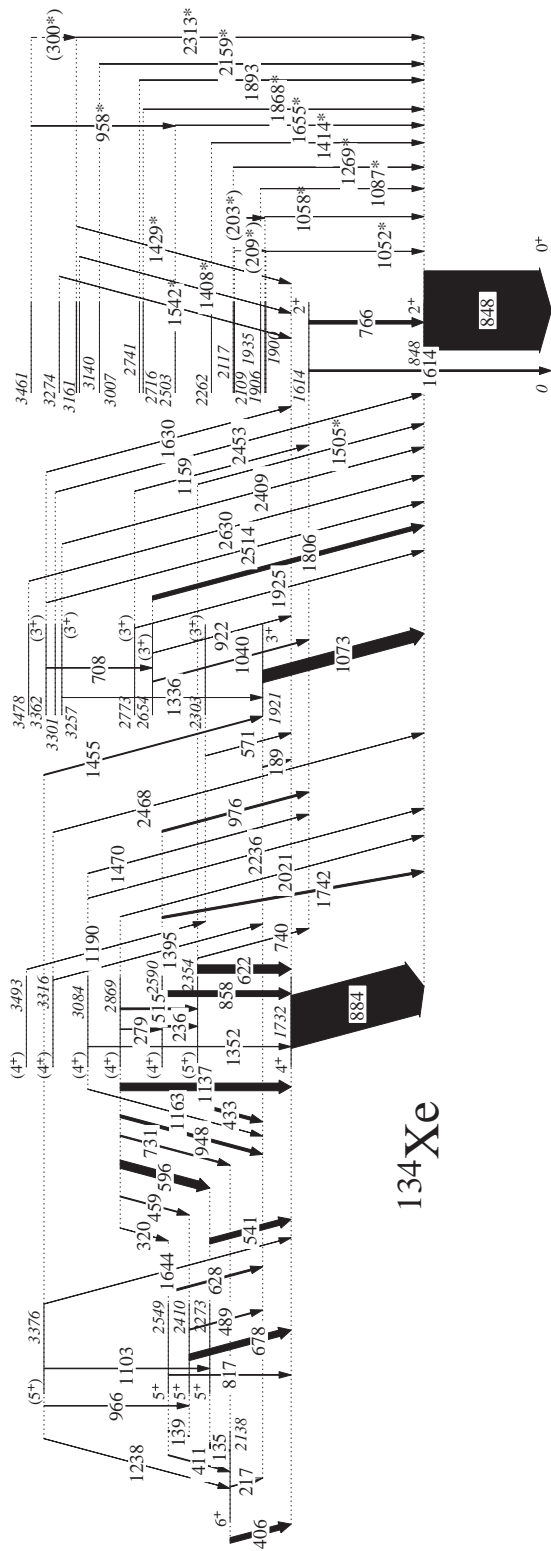


Figure 7.3: **(Left)** Decay half-life plots of (a) 1131 keV of  $^{135}\text{Xe}$  ( $t_{1/2} = 398(6)$  min) (b) 847 keV of  $^{134}\text{Xe}$  ( $t_{1/2} = 52.5(2)$  min) (c) 954 keV of  $^{132}\text{Xe}$  ( $t_{1/2} = 149(3)$  min) produced from ground state decay of  $^{132}\text{I}$  and (d) 175 keV of  $^{132}\text{Xe}$  ( $t_{1/2} = 94(9)$  min) populated from isomeric decay of  $^{132}\text{I}$ . Their deduced half-lives are in good agreement with the reported values. **(Right)** Decay plots of various newly observed  $\gamma$ -rays. Deduced half lives confirms them as decaying from  $^{134}\text{I}$  to  $^{134}\text{Xe}$ .

indication of the new transitions, belonging to  $^{134}\text{Xe}$ , comes from their decay half-lives. New transitions, which has half-lives near to the half-lives of the ground state of  $^{134}\text{I}$  (*i.e.* 52.5 min) can be identified as a part of  $^{134}\text{Xe}$  decay scheme. Thus, the presence of the new transitions in  $^{134}\text{Xe}$  is confirmed using the method of decay plots also. Right panel of Fig. 7.3 represents the decay plots of few new  $\gamma$  rays.

### 7.3.2 Coincidence Analysis

The level scheme of  $^{134}\text{Xe}$  is extended with the observation of 17 new  $\gamma$ -ray transitions. Fig. 7.4 represents the proposed new level scheme from this work. The presence and placement of the new transitions are confirmed from the coincidence relationships as well as following their decay half-lives [21].



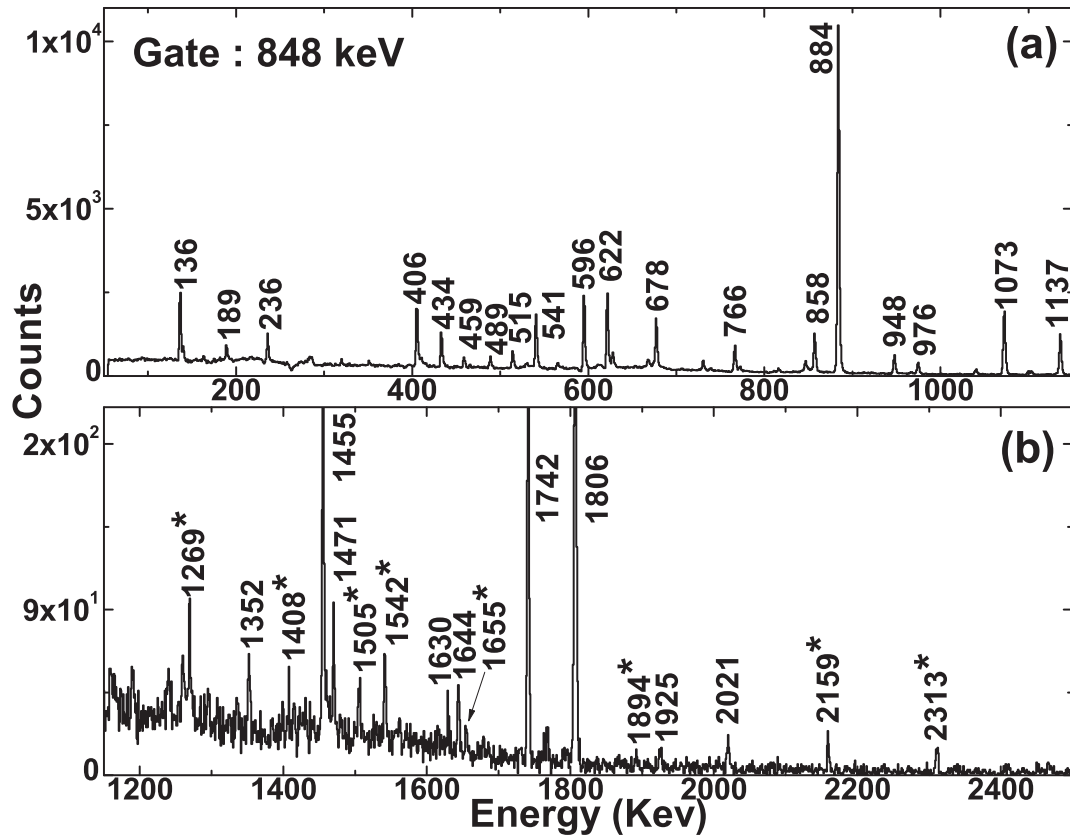


Figure 7.5: Coincidence spectra corresponding to the gate of 848 keV  $\gamma$ -ray of  $^{134}\text{Xe}$ . The newly observed transitions in the present work are marked with '\*'. (a) low energy part, (b) higher energy part.

Coincidence spectrum corresponding to the ground state transition of 848 keV of  $^{134}\text{Xe}$  is shown in Fig. 7.5. Most of the newly observed transitions, marked with "\*", can be seen in Fig. 7.5. Details of the  $\gamma$  rays, observed in this work, are tabulated in the Table 7.1. The ground state cascade ( $4^+ \rightarrow 2^+ \rightarrow 0^+$ ) of  $^{134}\text{Xe}$  is of 884 and 848 keV, respectively. The  $\gamma$  rays having energies 2313, 2159, 1894, 1868, 1505, 1414, 1087, 1059, 1052 and 1655 keV are seen only in coincidence with the 848 keV  $\gamma$ -ray, not with the 884 keV. These transitions are placed above the 848 keV level, in parallel with the 884 keV transition. On the other hand, 1429, 1408 and 1542 keV transitions are in coincidence with both 848 and 884 keV  $\gamma$  rays. These  $\gamma$  rays are placed in the level scheme accordingly. From the coincidence spectrum corresponding to the 2313 keV  $\gamma$ -ray (shown in Fig. 7.6(a)), it can be seen that only 848 keV is present, not the

884 keV. Presence of another new transition of energy 300 keV can also be seen in the gate of the 2313 keV  $\gamma$ -ray. Another cascade of  $\gamma$ -rays 958-1655 keV is also placed above the 848 keV level. The coincidence relationships between 958, 1655 and 848 keV can clearly be seen from the gate of 1655 keV, as shown in Fig. 7.6(b). The relative placement of the 958 and 1655 keV  $\gamma$  rays are carried out on the basis of their relative intensities. Fig. 7.6(c) shows the coincidence spectrum corresponding to the gate of 1541 keV  $\gamma$ -ray, which is found to be in coincidence with both the 848 and 884 keV transitions. Coincidences are also found between the 848 keV and 1052 keV  $\gamma$  rays, which confirms the presence of a new level at 1900 keV. Another new  $\gamma$ -ray of energy 209 keV is found to be in coincidence with both the 1052 and 848 keV transitions. Other new transitions of energies 2159, 1894, 1868, 1414 and 1087 keV are in coincidence with only the 848 keV and thus they are placed in the level scheme as decaying from the 3007, 2741, 2716, 2262 and 1935 keV levels to the 848 keV level, respectively. The 1429 keV  $\gamma$ -ray is present in the gate of both 848 and 884 keV transitions and thus placed above them. The 1505 and 1408 keV  $\gamma$  rays are seen in the coincidence with both the 884 and 848 keV  $\gamma$  rays.

In the previous work [2], the 1455 and 1073 keV transitions are placed as parallel transitions in the level scheme, decaying to the same 848 keV level. But in the present study, these two transitions are found to be in coincidence with each other (Fig. 7.7(a) and (b)). Thus, the placement of these two transitions are modified from this work. The 1455 keV transition is placed as decaying from the 3376 keV level to the 1921 keV level. And the 1073 keV transition is placed as decaying from the 1921 keV level. The 406 and 217 keV transitions are found to have coincidence with the 884-848 keV cascade and thus placed in the level scheme accordingly.

Table 7.1: The  $\gamma$ -ray energies ( $E_\gamma$ ) observed in the decay of  $^{134}\text{I}$  to  $^{134}\text{Xe}$  and their relative intensities ( $I_\gamma$ ) along with the corresponding angular correlation coefficients ( $a_{kk}$ ) and the energy of the initial state ( $E_i$ ). The new observed  $\gamma$  rays are marked with ‘\*’.

$E_\gamma$ (in keV)	$E_i$ (in keV)	$J_i^\pi \rightarrow J_f^\pi$	$I_\gamma(\text{Err})$ <sup>1</sup>	$a_{22}(\text{Err})$	$a_{44}(\text{Err})$
135.6(1)	2273.5	$5^+ \rightarrow 6^+$	5.26(21)	-	-

Table 7.1: Continued...

$E_\gamma$ (in keV)	$E_i$ (in keV)	$J_i^\pi \rightarrow J_f^\pi$	$I_\gamma(\text{Err})$ <sup>1</sup>	$a_{22}(\text{Err})$	$a_{44}(\text{Err})$
139.2(1)	2549.0	$4^+, 5^+ \rightarrow (5)^+$	1.00(8)	-	-
188.5(1)	1920.7	$3^+ \rightarrow 4^+$	0.99(15)	-	-
202.9(1)*	2109.2	$- \rightarrow -$	0.03(1)	-	-
209.2(1)*	2109.2	$- \rightarrow -$	0.04(2)	-	-
216.9(1)	2137.6	$- \rightarrow 3^+$	0.22(9)	-	-
235.7(1)	2590.1	$(4)^+ \rightarrow (4)^+$	1.94(20)	-	-
279.0(1)	2869.1	$(4)^+ \rightarrow (4)^+$	0.33(13)	-	-
300.2(1)*	3460.9	$- \rightarrow -$	-	-	-
320.1(1)	2869.1	$(4)^+ \rightarrow 4^+, 5^+$	0.39(9)	-	-
405.7(1)	2137.9	$6^+ \rightarrow 4^+$	6.72(46)	0.133(14)	-0.048(16) <sup>3</sup>
411.1(1)	2549.0	$4^+, 5^+ \rightarrow 6^+$	1.04(17)	-	-
433.7(1)	2354.4	$(4)^+ \rightarrow 3^+$	3.76(35)	-	-
459.3(1)	2869.1	$(4)^+ \rightarrow (5)^+$	1.15(24)	-	-
489.1(1)	2409.8	$(5)^+ \rightarrow 2^+$	1.27(16)	-	-
514.7(1)	2869.1	$(4)^+ \rightarrow (4)^+$	2.23(16)	-	-
541.2(1)	2273.4	$5^+ \rightarrow 4^+$	7.03(49)	0.090(9)	-0.002(9) <sup>2</sup>
570.7(1)	2303.1	$(3, 4)^+ \rightarrow 4^+$	0.33(9)	-	-
595.7(1)	2869.1	$(4)^+ \rightarrow 5^+$	10.07(77)	-	-
622.2(1)	2354.4	$(4)^+ \rightarrow 4^+$	10.56(56)	0.124(29)	-0.04(3) <sup>2</sup>
628.3(1)	2549.0	$4^+, 5^+ \rightarrow 3^+$	2.24(21)	-	-
677.6(1)	2409.8	$(5)^+ \rightarrow 4^+$	8.02(38)	-0.282(11)	-0.116(15) <sup>2</sup>
707.8(1)	3361.7	$(3, 4)^+ \rightarrow (3)^+$	0.20(9)	-	-
740.6(1)	2354.4	$(4)^+ \rightarrow (2)^+$	0.41(7)	-	-
731.2(1)	2869.1	$(4)^+ \rightarrow 6^+$	1.63(14)	-	-
766.4(1)	1613.8	$2^+ \rightarrow 2^+$	4.37(27)	0.403(98)	0.041(87) <sup>3</sup>
816.8(1)	2549.0	$4^+, 5^+ \rightarrow 4^+$	0.67(8)	-	-
847.8(2)	847.8	$2^+ \rightarrow 0^+$	100(4)	-	-
857.9(1)	2590.1	$(4)^+ \rightarrow 4^+$	7.33(42)	0.259(9)	-0.079(9) <sup>2</sup>

Table 7.1: Continued...

$E_\gamma$ (in keV)	$E_i$ (in keV)	$J_i^\pi \rightarrow J_f^\pi$	$I_\gamma(\text{Err})$ <sup>1</sup>	$a_{22}(\text{Err})$	$a_{44}(\text{Err})$ <sup>3</sup>
884.3(2)	1732.2	$4^+ \rightarrow 2^+$	65(2)	0.078(4)	-0.031(5) <sup>3</sup>
921.7(1)	2653.9	$3^+ \rightarrow 4^+$	0.23(11)	-	-
948.4(1)	2869.1	$(4)^+ \rightarrow 3^+$	3.64(23)	-	-
957.8(1)*	3460.9	- $\rightarrow$ -	0.03(1)	-	-
966.2(1)	3376.0	$(4, 5)^+ \rightarrow (5)^+$	0.33(12)	-	-
976.3(1)	2590.3	$(4)^+ \rightarrow 2^+$	2.44(13)	-	-
1040.1(1)	2653.9	$3^+ \rightarrow 2^+$	1.18(13)	-	-
1052.2(1)*	1900.0	- $\rightarrow$ $2^+$	0.04(1)	-	-
1058.5(1)*	1906.3	- $\rightarrow$ $2^+$	0.19(7)	-	-
1072.9(1)	1920.7	$3^+ \rightarrow 2^+$	15.25(68)	0.149(30)	-0.073(32) <sup>3</sup>
1087.1(1)*	1934.9	- $\rightarrow$ $2^+$	0.05(1)	-	-
1102.6(1)	3376.0	$(4, 5)^+ \rightarrow 5^+$	0.72(8)	-	-
1136.9(1)	2869.1	$(4)^+ \rightarrow 4^+$	9.66(49)	-	-
1159.2(1)	2773.0	$(3, 4)^+ \rightarrow 2^+$	0.29(5)	-	-
1163.6(1)	3084.3	$(3, 4)^+ \rightarrow 3^+$	0.32(6)	-	-
1190.1(1)	3493.2	$(3, 4)^+ \rightarrow (3, 4)^+$	0.39(19)	-	-
1238.1(1)	3376.0	$(4, 5)^+ \rightarrow 6^+$	0.30(10)	-	-
1269.4(1)*	2117.2	- $\rightarrow$ $2^+$	0.04(2)	-	-
1336.2(1)	3256.9	$(3, 4)^+ \rightarrow 3^+$	0.19(11)	-	-
1352.1(1)	3084.3	$(3, 4)^+ \rightarrow 4^+$	0.44(9)	-	-
1395.2(1)	3315.9	$(3, 4)^+ \rightarrow 3^+$	0.06(1)	-	-
1407.6(1)*	3139.8	- $\rightarrow$ $4^+$	0.13(9)	-	-
1414.3(1)*	2262.1	- $\rightarrow$ $2^+$	0.15(7)	-	-
1428.5(1)*	3160.7	- $\rightarrow$ $4^+$	0.08(2)	-	-
1455.3(2)	3376.0	- $\rightarrow$ $3^+$	2.06(20)	-	-
1470.5(1)	3084.3	$(3, 4)^+ \rightarrow 2^+$	0.55(8)	-	-
1505.1(1)*	2352.9	- $\rightarrow$ $2^+$	0.27(7)	-	-
1541.8(1)*	3274.0	- $\rightarrow$ $4^+$	0.50(9)	-	-

Table 7.1: Continued...

$E_\gamma$ (in keV)	$E_i$ (in keV)	$J_i^\pi \rightarrow J_f^\pi$	$I_\gamma(\text{Err})$ <sup>1</sup>	$a_{22}(\text{Err})$	$a_{44}(\text{Err})$
1613.8(1)	1613.8	$2^+ \rightarrow 0^+$	2.28(7)	-	-
1629.5(1)	3361.7	$(3, 4)^+ \rightarrow 4^+$	0.13(11)	-	-
1643.8(1)	3376.0	$(4, 5)^+ \rightarrow 4^+$	0.41(6)	-	-
1655.3(1)*	2503.1	$- \rightarrow 2^+$	0.16(6)	-	-
1742.3(2)	2590.1	$(4)^+ \rightarrow 2^+$	2.63(24)	-0.097(147)	-0.227(202) <sup>3</sup>
1806.1(1)	2653.9	$3^+ \rightarrow 2^+$	5.36(28)	-0.390(37)	0.057(47) <sup>3</sup>
1868.1(1)*	2715.9	$- \rightarrow 2^+$	0.05(1)	-	-
1893.6(1)*	2741.4	$- \rightarrow 2^+$	0.08(4)	-	-
1925.2(2)	2773.0	$(3, 4)^+ \rightarrow 2^+$	0.17(5)	-	-
2021.3(1)	2869.1	$(4)^+ \rightarrow 2^+$	0.28(7)	-	-
2159.4(2)*	3007.2	$- \rightarrow 2^+$	0.24(5)	-	-
2236.5(1)	3084.3	$(3, 4)^+ \rightarrow 2^+$	0.07(4)	-	-
2312.9(1)*	3160.7	$- \rightarrow 2^+$	0.24(5)	-	-
2409.1(2)	3256.9	$(3, 4)^+ \rightarrow 2^+$	0.13(5)	-	-
2452.9(1)	3300.7	$- \rightarrow 2^+$	0.08(3)	-	-
2468.1(1)	3315.9	$(3, 4)^+ \rightarrow 2^+$	0.08(3)	-	-
2513.9(1)	3361.7	$(3, 4)^+ \rightarrow 2^+$	0.05(1)	-	-
2629.9(2)	3477.7	$- \rightarrow 2^+$	0.08(2)	-	-

### 7.3.3 Spin assignments

The spin assignments of the excited levels are carried out using the angular correlation analysis technique [22]. Angular correlation plots for various  $\gamma$  rays, observed in this work, are shown

<sup>1</sup>Relative  $\gamma$ -ray intensities are calculated from raw spectra and normalized to 100 for the total intensity of 847.8-keV  $\gamma$ -ray.

<sup>2</sup>From 884.3 keV (E2) gate;

<sup>3</sup>From 847.8 keV (E2) gate;

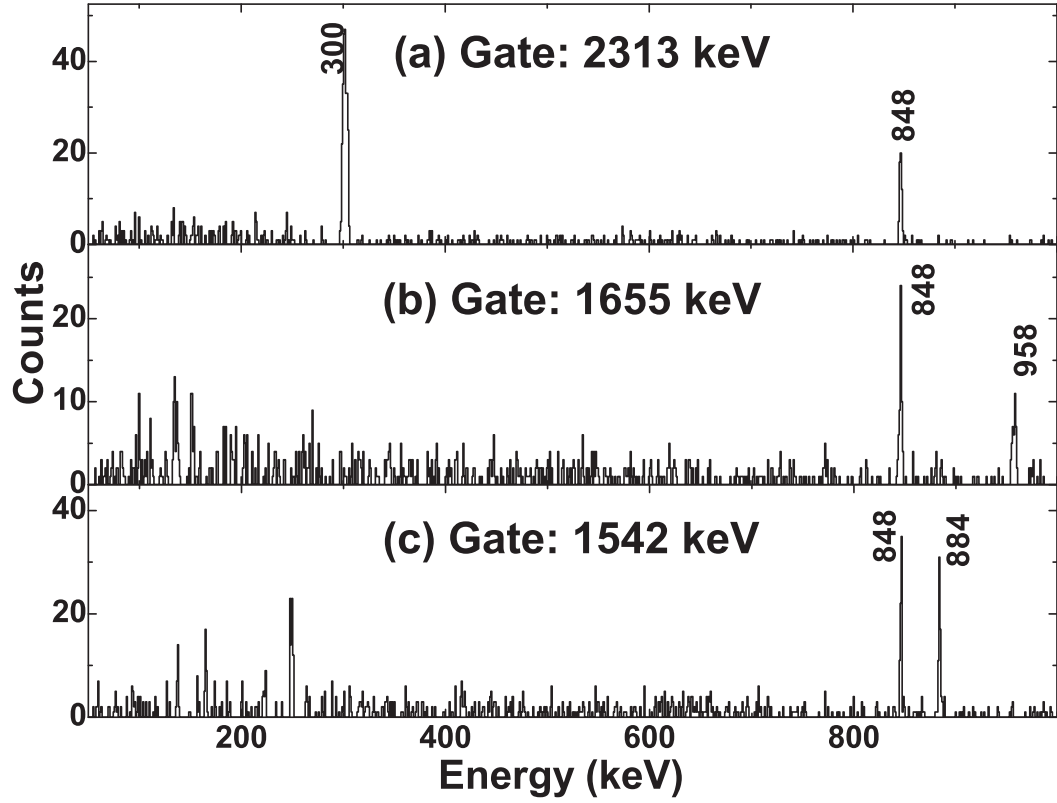


Figure 7.6: Coincidence spectra corresponding to the newly observed  $\gamma$  rays of energy (a)2313, (b)1655 and (c)1542 keV.

in Fig. 7.8. The contour plots between the  $a_{22}$  and  $a_{44}$  coefficients with varying  $\delta$  are shown in Fig. 7.9. These contours are plotted for five possible spin sequences as indicated in the figure. Experimentally obtained  $a_{kk}$  coefficients (as mentioned in Table 7.1) are also plotted in the same plot in order to compare with the theoretical values. The 1614 keV level was previously assigned with a tentative spin of  $(2^+)$ . The spin of the 1614 keV level is confirmed to be  $2^+$  from this work. The deduced  $a_{kk}$  coefficients of the 766 keV in the gate of 847 keV (E2) transition confirms the spin of the 1614 keV level to be  $2^+$ . The 1732 keV level has the spin  $4^+$  since the decaying transition from this level, 884 keV, is of pure E2 nature. The nature of the 884 keV transition corroborates with the angular correlation analysis result also. Angular correlation result for the 1806 keV transition in the 848 keV (E2) gate shows that this transition is a

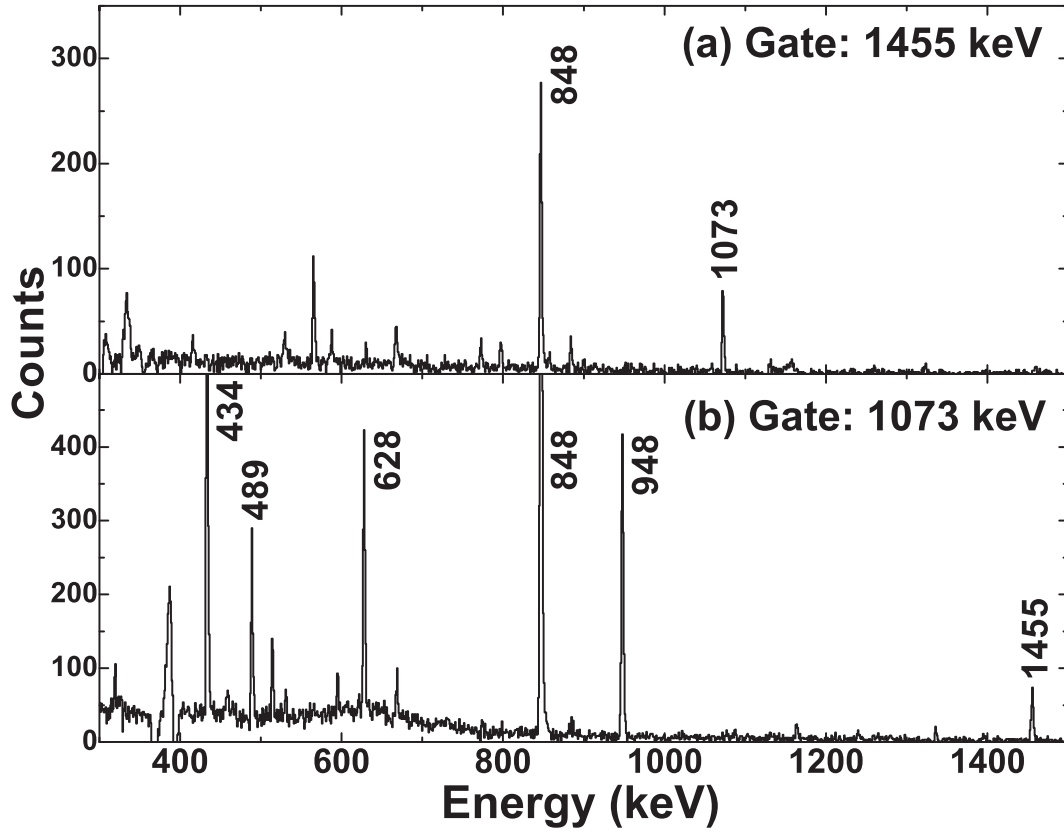


Figure 7.7: Coincidence spectra corresponding to the  $\gamma$  rays of energies (a)1455 keV and (b)1073 keV.

$3^+ \rightarrow 2^+$  one, which is in good agreement with the previously reported result. The nature of the 1073 keV transition is deduced as dipole with high mixing of quadrupole in it. The multipolarity of the 1073 keV transition is obtained as dipole ( $3^+ \rightarrow 2^+$ ) from the angular correlation measurement (in 848 keV, E2 gate) and hence the 1921 keV level is assigned as  $3^+$ . The spin of the 2273 keV level is assigned as  $4^+$  from the angular correlation measurement of the 541 keV transition. The spin of the 2410 keV level is also confirmed as  $5^+$  from the present measurements, which was tentatively assigned earlier. From the angular correlation plot of the 622 keV  $\gamma$ -ray, which is decaying from the 2354 keV level, shows that this transition is of dipole nature and decays as  $5^+ \rightarrow 4^+$ . This fixes the spin of the 2354 keV level as  $5^+$ .

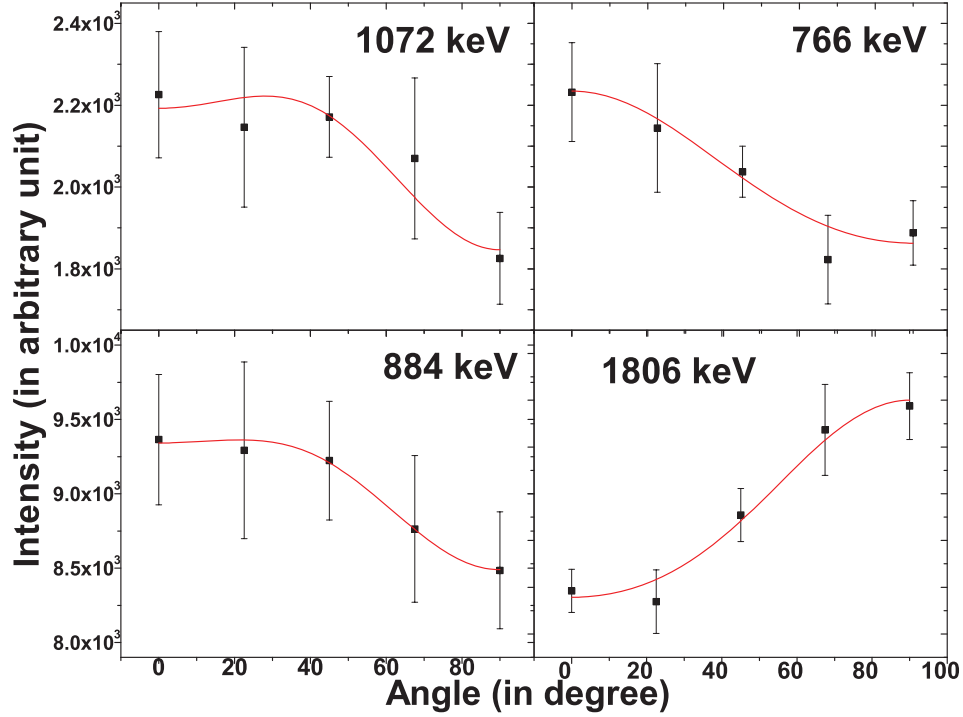


Figure 7.8: Variation of intensities of different transitions as a function of angle. These intensities are fitted with angular correlation function.

## 7.4 Discussion

Fig. 7.10 shows the evolution of the low lying excited states as a function of neutron number for Xenon ( $Z = 54$ ) isotope. A smooth increase in energy for every state is observed upto  $^{136}\text{Xe}$ . It is obvious that  $^{136}\text{Xe}$  will possess higher first excited state,  $2^+$ , as it has neutron number  $N = 82$ . It can also be concluded that as one goes away from the shell closure, the state comes down in excitation energy due to the effect of collectivity.

### 7.4.1 Shell Model Calculations

The configurations of the observed levels along with the previously reported levels in  $^{134}\text{Xe}$  are interpreted using shell model calculations. The large basis shell model calculations are carried

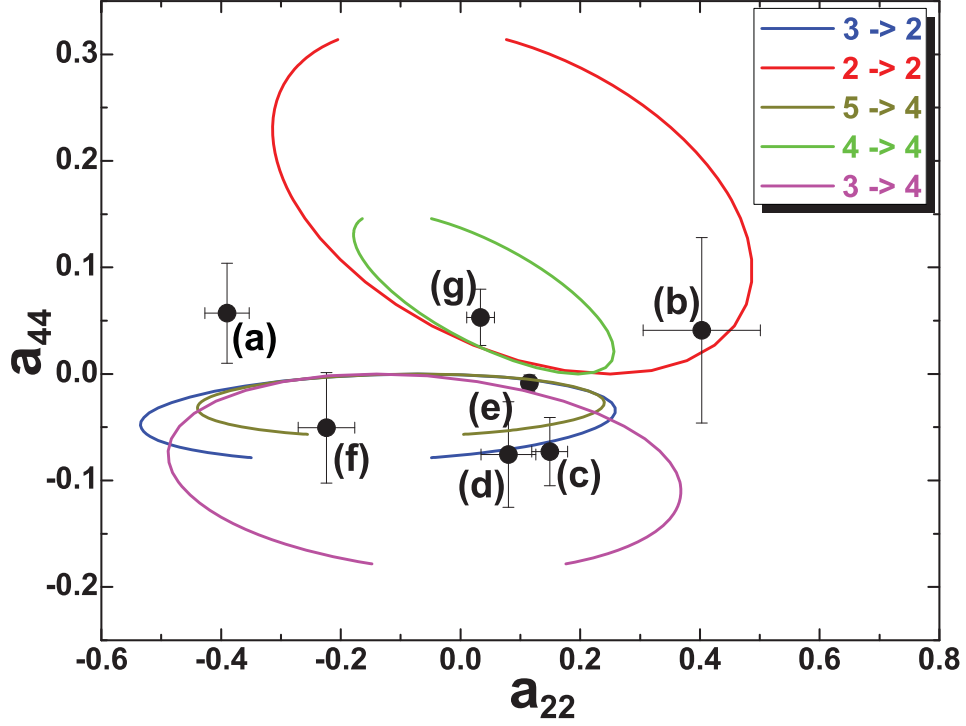


Figure 7.9: Comparison between experimental  $a_{kk}$  coefficients with the theoretical calculations. The contours shown are plotted for varying  $\delta$  values. (a) 1806, (a) 766, (a) 1073, (a) 817, (a) 622, (a) 678 and (a) 541 keV transitions are shown in the figure.

out using the code OXBASH [23]. The SN100PN effective interaction [24], is used to carry out the calculations. This SN100PN is a realistic interaction which is widely used for the shell model calculations of the nuclei near  $^{132}\text{Sn}$ . In this calculation,  $^{100}\text{Sn}$  is considered as core. The two body matrix elements (TBME) used in this interaction was developed by using the well known CD Bonn interaction [24]. This interaction is in n-p formalism, which has different single particle energies for protons and neutrons. The calculations are carried out using the complete available valence space without any restriction. The model space consists of orbitals between the magic numbers 50 and 82 which are  $g_{7/2}$ ,  $d_{5/2}$ ,  $d_{3/2}$ ,  $s_{1/2}$  and  $h_{11/2}$  for both neutrons and protons. Fig. 7.11 shows the comparison between theoretically calculated levels with the experimentally observed levels in  $^{134}\text{Xe}$  for the low lying spin. A overall good agreement is achieved between the experimentally observed levels and shell model calculations. Only the

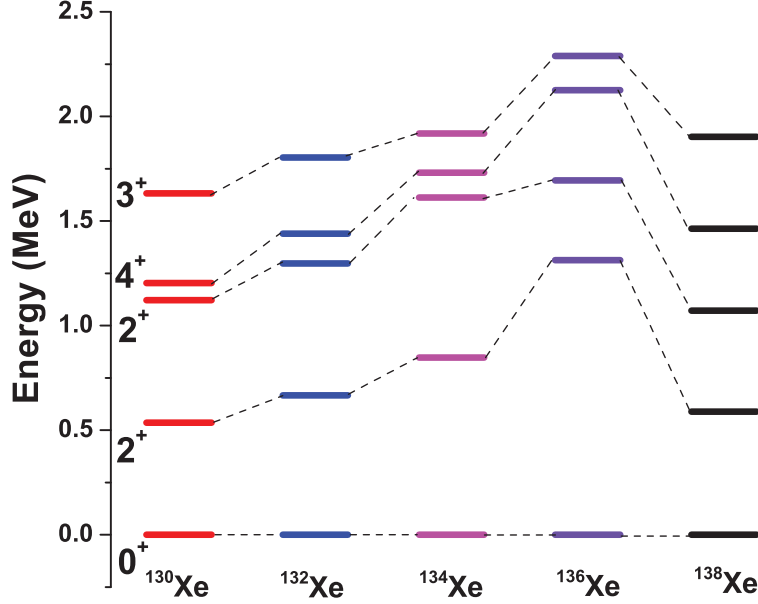


Figure 7.10: Evolution of the lower lying levels in Xe ( $Z = 54$ ) isotonic chain.

odd spin states are calculated to have enhanced energy compared to that of experiment. The calculated configurations of the lower lying states, whose contributions are  $\geq 10\%$ , are tabulated in Table 7.2.

The calculation shows a good agreement between the calculated level energies and the experimental values for the lower excitation states. It is evident from the Table 7.2 that the yrast  $0^+$ ,  $2^+$ ,  $4^+$  and  $6^+$  states have the maximum contribution from the configuration  $\pi g_{7/2}^4 \otimes \nu d_{3/2}^{-2}$ . The intense connecting transitions between these yrast states also supports the fact that they have same configurations. As these states are having same configurations, it can be stated that they are of same vibrational multiplets. The ratio of the first  $4^+$  state to the first  $2^+$  state also validates this claim. Still there is a scope for vibrational symmetry breaking, which is indicated by the presence of transitions from second  $2^+$  state to the first  $2^+$  state. But for conclusive evidence of the same, life time measurements of the observed states are needed, which is out of the scope of the present experimental setup. It will obviously be a challenge to measure the level life times in this mass region. But for the yrast odd spin,  $3^+$  state, the calculated value comes

Table 7.2: Configurations of various states as obtained from the present shell model calculations.

Contribution greater than 10 % is only mentioned.

$J^\pi$	$E_{level}$ (Exp) (in keV)	$E_{level}$ (Theory) (in keV)	Configuration	%
$0^+$	0	0	$\pi g_{7/2}^4 \otimes \nu d_{3/2}^{-2}$	20
			$\pi g_{7/2}^4 \otimes \nu h_{11/2}^{-2}$	12
$2^+$	848	910	$\pi g_{7/2}^4 \otimes \nu d_{3/2}^{-2}$	18
			$\pi g_{7/2}^4 \otimes \nu d_{3/2}^{-1} s_{1/2}^{-1}$	13
$2^+$	1614	1741	$\pi g_{7/2}^4 \otimes \nu d_{3/2}^{-1} s_{1/2}^{-1}$	16
			$\pi g_{7/2}^4 \otimes \nu d_{3/2}^{-2}$	13
			$\pi g_{7/2}^4 \otimes \nu h_{11/2}^{-1}$	11
$3^+$	1921	2321	$\pi g_{7/2}^3 d_{5/2}^1 \otimes \nu d_{3/2}^{-2}$	25
			$\pi g_{7/2}^3 d_{5/2}^1 \otimes \nu h_{11/2}^{-2}$	24
			$\pi g_{7/2}^3 d_{5/2}^1 \otimes \nu s_{1/2}^{-2}$	10
$4^+$	1732	1789	$\pi g_{7/2}^4 \otimes \nu d_{3/2}^{-2}$	23
			$\pi g_{7/2}^4 \otimes \nu h_{11/2}^{-2}$	14
$5^+$	2273	2174	$\pi g_{7/2}^3 d_{5/2}^1 \otimes \nu d_{3/2}^{-2}$	27
			$\pi g_{7/2}^3 d_{5/2}^1 \otimes \nu h_{11/2}^{-2}$	21
			$\pi g_{7/2}^3 d_{5/2}^1 \otimes \nu s_{1/2}^{-2}$	11
$6^+$	2138	1972	$\pi g_{7/2}^4 \otimes \nu d_{3/2}^{-2}$	18
			$\pi g_{7/2}^4 \otimes \nu h_{11/2}^{-2}$	10
			$\pi g_{7/2}^3 d_{5/2}^1 \otimes \nu h_{11/2}^{-2}$	10



# Bibliography

- [1] R. O. Hughes *et al.*, Phys. Rev. C **69**, 051303 (R)(2004).
- [2] W. G. Winn *et al.*, Phys. Rev., Vol. 184, No. 4 (1969).
- [3] B. Fogelberg *et al.*, Phys. Rev. C, Vol. 41, No. 3, (1990).
- [4] R. A. Meyer *et al.*, Phys. Rev., Vol. 186, No. 4 (1969).
- [5] Glenn M. Julian, Phys. Rev. C, Vol. 3, No. 2 (1971).
- [6] J. Skalski, Phys. Lett. B, **238**, 6 (1990).
- [7] S. L. Rugari *et al.*, Phys. Rev. C, **48**, 2078 (1993).
- [8] J. M. Sears *et al.*, Phys. Rev. C, Vol. 57, No. 6 (1998).
- [9] P. Chowdhury *et al.*, Phys. Rev. C, Vol. 25, No. 2 (1982).
- [10] R. Wyss *et al.*, Nucl. Phys. A, **505**, 337 (1989).
- [11] M. McKeown and S. Katcoff, Phys. Rev., **94**, 965 (1954).
- [12] N. R. Johnson *et al.*, Phys. Rev. C, Vol. 122, No. 5, (1961).
- [13] E. Takekoshi *et al.*, Nucl. Phys. A, **133**, 493 (1969).
- [14] E. Achterberg *et al.*, Phys. Rev., Vol. 4, No. 1, (1971).
- [15] J. M. Gualda *et al.*, Nucl. Phys. A, **234**, 357 (1974).

- [16] A. Shrivastava *et al.*, Phys. Rev. C, **80**, 051305 (R)(2009).
- [17] A. Vogt *et al.*, Phys. Rev. C, **93**, 054325 (2016).
- [18] <http://www.tifr.res.in/~pell/lamps.html>.
- [19] D. C. Radford, Nucl. Instrum. Methods Phys. Res. A, **361**, 297 (1995).
- [20] M. Diksic *et al.*, Phys. Rev. C, Vol. 10, No. 3 (1974).
- [21] R. Banik *et al.*, Proc. of the DAE Symposium on Nucl. Phys., **60**, 244 (2015).
- [22] R. Banik *et al.*, Proc. of the DAE Symposium on Nucl. Phys., **61**, 76 (2016).
- [23] Oxbash for Windows, B. A. Brown *et al.*, MSU-NSCL report number 1289 (2004).
- [24] B. A. Brown *et al.*, Phys. Rev. C, **71**, 044317 (2005).

## Abstract

The present thesis reports the single particle and collective excitations of nuclei, both near stability as well as towards the neutron-rich side, having atomic number around the  $Z = 50$  shell closure. Nuclei, having few proton particles above  $Z = 50$ , with few neutron holes in the  $N = 82$  shell provide valuable information about the effective nucleon-nucleon interactions and various coupling schemes between the valence protons and neutrons. The presence of the unique parity, high-j  $h_{11/2}$  orbital, in both  $Z, N = 50 - 82$  shell, makes these nuclei more fascinating in order to explore the shape driving effects of the  $h_{11/2}$  orbital over a chain of isotopes from near stability to neutron-rich side of the nuclear chart. The contribution of the  $h_{11/2}$  orbital in the high spin generation mechanism is also one of the major interests of this thesis. The study of the nuclei, having proton number near  $Z = 50$ , also helps to understand the competition between the collective and the single particle excitations. On the contrary, if one moves towards  $N \geq 82$ , with  $Z \sim 50$ , the exciting domain of neutron rich nuclei around  $^{132}\text{Sn}$  becomes accessible. The present thesis also aims to explore the deformation driving behavior of the  $vh_{11/2}$  orbital in the neutron rich domain.

This thesis reports the results from the study of the excited level structures of  $^{117}\text{Sb}$  ( $Z = 51$ ), having single proton above  $Z = 50$  and neutron in mid-shell of  $N = 50-82$ , and  $^{131,134}\text{Xe}$  ( $Z = 54$ ),  $^{130-134}\text{I}$  ( $Z = 53$ ) which have few neutron holes in the  $N = 82$  shell closure. It, therefore, helps to understand the evolution of the  $vh_{11/2}$  orbital over a mass region. In this work, different reactions mechanisms, such as fusion evaporation, fission and  $\beta$ -decay have been employed to populate the nuclei in its excited states. The measurements, related to the present thesis, are carried out using different high resolution HPGe detector arrays, namely, VECC Array for Nuclear Spectroscopy (VENUS) at VECC, India, Indian National Gamma Array (INGA) at VECC, India and Advanced Gamma Ray Tracking Array (AGATA), coupled with VAMOS++ magnetic spectrometer and segmented clover HPGe detectors (EXOAM), at GANIL, France.

The new results, obtained for the first time, manifest various new structural phenomena in the nuclei of interest. The competition between the collective and single particle degrees of freedom is explored in detail. Such competition is observed in both mid shell nucleus  $^{117}\text{Sb}$  ( $N = 66$ ) and near shell closure nucleus  $^{131}\text{Xe}$  ( $N = 77$ ). The core polarizing effects, leading to the deformation originating from the effect of the mid shell neutrons are also explored from the observation of strongly coupled  $g_{9/2}$  and weakly coupled  $g_{7/2}$  bands in the same nucleus  $^{117}\text{Sb}$ . The weak coupling scheme of the  $g_{7/2}$  orbital with the core, due to the involvement of the low-component, is established, for the first time, from the observation of its signature partner band and Particle Rotor Model (PRM) calculation. The deformation driving effect of the high-j  $h_{11/2}$  orbital is also studied from the observation of rotational band based on this orbital in  $^{131}\text{Xe}$ . Triaxial nature of this band at higher spin is also observed. The involvement of this orbital, both in proton and neutron valence space, gives rise to exotic excitation modes, such as Magnetic Rotational (MR) band, as observed in  $^{131}\text{Xe}$ , in the present work. The  $\gamma$ -soft nature of  $^{131}\text{Xe}$  at the higher spin is established from the observation of new 3 quasi-particle band and several new states, along with Total Routhian Surface (TRS) calculation. The orbital  $h_{11/2}$  is also found to be responsible for generation of high spin states in the near spherical neutron-rich systems,  $^{130-134}\text{I}$ . Towards the neutron rich side, the single particle excitations are found to dominate, as is seen in  $^{130-134}\text{I}$ , above the high spin isomers and in the low lying structures of  $^{134}\text{Xe}$ . It is found that, the hole occupancy in the  $vh_{11/2}$  orbital plays a crucial role in generating the high spin negative parity states as a function of the increasing neutron number in these neutron rich Iodine isotopes.

## Thesis Highlight

**Name of the Student:** Ranabir Banik

**Name of the CI/OCC:** Variable Energy Cyclotron Centre

**Enrolment No.:** PHYS04201404012

**Thesis Title:** Single particle and collective excitations near Z=50

**Discipline:** Physical Sciences

**Sub-Area of Discipline:** Nuclear structure

**Date of viva voce:** 07/05/2021

The present thesis reports the single particle and collective structures of nuclei, both near stability and towards the neutron-rich side, near  $Z = 50$ . Nuclei, having few particles above  $Z = 50$  and few neutron holes in the  $N = 82$  shell provide valuable information about the effective nucleon-nucleon interactions near  $^{132}\text{Sn}$ . The presence of the unique parity, high- $j$   $h_{11/2}$  orbital, makes these nuclei more fascinating in order to explore the shape driving nature of this orbital over a chain of isotopes. The contribution of this unique parity  $h_{11/2}$  orbital in the high spin generation is also one of the major interests of the present thesis.

Both odd and even  $Z$  nuclei,  $^{117}\text{Sb}$  ( $Z=51$ ),  $^{130-134}\text{I}$  ( $Z=53$ ) and  $^{131,134}\text{Xe}$  ( $Z=54$ ), are studied using  $\gamma$ -ray spectroscopic techniques. The measurements are carried out using different state-of-art high resolution HPGe detector arrays, namely, VECC Array for Nuclear Spectroscopy (VENUS) and Indian National Gamma Array (INGA) at VECC, India. Fission fragment spectroscopy followed by complete isotopic identification is also carried out using VAMOS++ magnetic spectrometer coupled with Advanced Gamma Ray Tracking Array (AGATA), and EXOGAM segmented clover HPGe detectors, at GANIL, France. Prompt as well as prompt-delayed coincidences are obtained to construct the new level schemes above the high spin isomers.

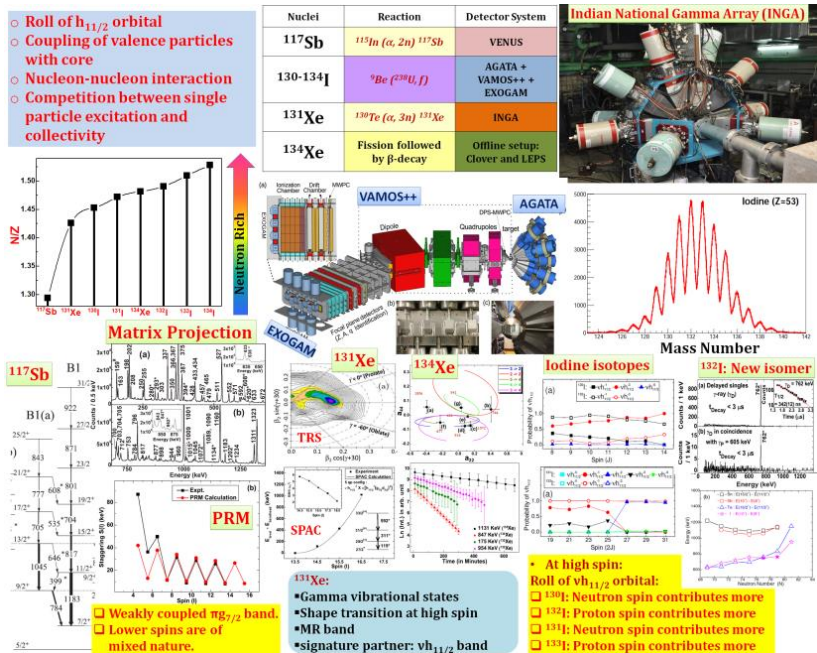


Figure 1.  $^{117}\text{Sb}$ ,  $^{130-134}\text{I}$  and  $^{131,134}\text{Xe}$  are studied using different detector arrays. New structural information, such as, signature partner bands, gamma softness, MR band and roll of high- $j$   $h_{11/2}$  orbital are shown.

prompt as well as prompt-delayed coincidences are obtained to construct the new level schemes above the high spin isomers.

The new results, obtained for the first time, manifest various new structural phenomena in the nuclei of interest. The competition between the collective and single particle degrees of freedom is explored in both mid shell nucleus  $^{117}\text{Sb}$  ( $N = 66$ ) and near shell closure nucleus  $^{131}\text{Xe}$  ( $N = 77$ ). The role of high- $j$  unique parity  $h_{11/2}$  orbital in inducing deformation is also studied. This orbital is also found to be responsible for generation of high spin states in the near spherical neutron-rich systems,  $^{130-134}\text{I}$  and  $^{134}\text{Xe}$ . The involvement of this orbital, both in proton and neutron valence spaces, gives rise to exotic excitation modes, such as Magnetic Rotational band, as observed in  $^{131}\text{Xe}$ , in the present work. It is also found that, the variation of neutron hole occupancy in the  $vh_{11/2}$  orbital plays a crucial role in generating the high spin negative parity states as a function of the increasing neutron number in these neutron rich Iodine isotopes.